An Experimental Approach into the Degradation of Wind Turbine Blade Coating Systems due to Rain and Weathering

PhD Thesis

Grant Leishman

Supervisor – Professor David Nash

Wind & Marine Energy Systems CDT,
Department of Electronic & Electrical Engineering,
University of Strathclyde, Glasgow

February 2023

This thesis is the result of the author's original research. It has been composed by the author and has not been previously submitted for examination which has led to the award of a degree.

Signed:

Grant Leishman

Date: 25/02/2023

Abstract

Leading edge erosion of wind turbine blades is an issue which is increasing in prevalence due to the ever-growing installed capacity of wind turbines globally. Leading edge erosion causes a reduction in the aerodynamic efficiency of a wind turbine blade, in turn reducing the turbine's energy yield and therefore also the annual energy production. Furthermore, leading edge erosion can lead to structural degradation, resulting in premature failure of the blade.

This thesis looks to define a quantitative experimental methodology to assess and characterise erosion on wind turbine blades. Furthermore, this thesis goes on to include weathering as a factor in wind turbine blade coating system assessment. Accelerated tests were used to mimic the effects of years of in-situ rain erosion and weathering on test specimens. A suite of analytical laboratory tools was used to measure the effects of rain erosion and weathering, both individually and as a combined study on, industrially relevant and operationally used, wind turbine blade coating systems.

It was found that coating systems from different manufacturers were unique in their response and degradation behaviour. A novel methodology, using surface gloss, was used to quantify erosion and then categorise the specimen into one of the developed erosion stages. Additionally, this approach provides a greater accuracy in erosion quantification than the current method of mass loss measurement and the gloss methodology can be used in-situ, whereas mass loss cannot. Another key finding from this thesis is that weathering has a measurable effect on erosion, increasing mass loss by 1.5% and gloss loss by up to 15% for one of the coating systems tested.

Acknowledgements

Firstly, I would like to express my deepest appreciation to my academic supervisor Professor David Nash. David has been an invaluable source of knowledge, guidance, and mentorship throughout my studies. David encouraged me to grow and develop as an engineer and to that, I am very grateful.

I wish to thank Dr Kirsten Dyer from Offshore Renewable Energy Catapult. Kirsten is a world-renowned expert in leading edge erosion and has contributed greatly to my research work, publications, and conference contributions. Kirsten arranged and managed the joint industry project which supplied the materials and industrial partners for this work. Without Kirsten, this work would not have been possible.

I also am grateful to Dr Liu Yang for his expertise in materials analysis and providing access to the Advanced Composite Group analytical laboratory and facilities.

Furthermore, I would like to thank the Wind and Marine Energy Systems CDT for providing a stimulating learning environment and for funding this work under grant number EP/L016680/1.

Finally, a special thanks to my wife, Kirsty, and my parents, Ian & Jennifer, for their encouragement and support. Without them, I’m sure this Thesis would remain unwritten.

Publications and Conference Contributions

From the work detailed within this thesis, two journal publications and four conference presentations have been disseminated. These are listed below.

I. A staged approach to erosion analysis of wind turbine blade coatings. Nash, D., Leishman, G., MacKie, C., Dyer, K. & Yang, L., In: Coatings. 11, 6, 11 p., 681., 5 Jun 2021

II. A novel approach for wind turbine blade erosion characterization: an investigation using surface gloss measurement. Leishman, G., Nash, D., Yang, L. & Dyer, K., In: Coatings. 12, 7, 18 p., 928., 30 Jun 2022,

III. Creation of a single water droplet FEA model for rain erosion and observations of coating property changes during rain erosion testing. Nash, D., and Leishman, G. 1st International Symposium on Leading Edge Erosion of Wind Turbine Blades, DTU Risø Campus. 5 Feb 2020.

IV. Quantification of leading edge erosion using surface gloss and applications to long term weathering. Nash, D., Leishman, G., Dyer, K. & Yang, L., 2nd International Symposium on Leading Edge Erosion of Wind Turbine Blades, DTU Risø Campus. 2 Feb 2021.

V. A novel approach to combined rain and weathering testing of wind turbine blade coating systems. Nash, D., Leishman, G., Dyer, K. & Yang, L., 3rd International Symposium on Leading Edge Erosion of Wind Turbine Blades, DTU Risø Campus. 3 Feb 2022.

VI. Weathering and rain erosion testing of wind blade coating systems. Nash, D. & Leishman, G., 4th International Symposium on Leading Edge Erosion of Wind Turbine Blades, DTU Risø Campus. 8 Feb 2023.

Table of Contents

Nomenclature

Term	Units	Definition
P_{wind}	W	Power available in the wind
ρ	kg/m^3	Density
A	m^2	Area
u	m/s	Velocity
v_t	m/s	Tip speed
ω	s^{-1}	Rotational velocity
R	m	Blade length
P_{wh}	Pa	Water hammer pressure
u_i	m/s	Impact velocity
ρ_l	kg/m^3	Density of liquid droplet
ρ_s	kg/m^3	Density of solid surface
C_l	m/s	Speed of sound in the liquid droplet
C_s	m/s	Speed of sound in the solid surface
c_L	m/s	Velocity of the compressional longitudinal wave
c_T	m/s	Velocity of the shear transverse wave
c_R	m/s	Velocity of the surface Rayleigh wave
E	Pa	Young's modulus

ν		Poisson's ratio
v_{dt}	m/s	Damage threshold velocity
K_{ic}	MPa/m	Fracture toughness of the solid
c_l	m/s	Compressional wave speed within the liquid droplet
d_l	m	Diameter of liquid droplet
$\tan\delta$		Phase lag of resultant force to an impact force
E'	Pa	Storage modulus
E''	Pa	Loss modulus
L*		Lightness position
a*		Red/green position
b*		Blue/yellow position
ΔE*		Colour change
E_k	J	Kinetic energy
m	kg	Mass
V	m^3	Volume
r	m	Radius

Chapter 1 - Introduction

The demand for renewable energy is greater than ever due to the understanding, and also increasing acceptance, that past methods of power generation such as fossil fuels and coal are destructive to the environment. Renewable energy technologies are now playing a growing role in the power generation mix. Figure 1.1 shows Europe's electricity mix by generation source from 2000 to 2050, the figure was produced in the year 2020, therefore data previous to this year was recorded and data beyond 2020 is predicted. Figure 1.1 illustrates the growing role wind energy will play in Europe's electricity production, reaching 50% of all electricity produced by 2050. It is also clear to see that fossil fuel sources of electricity production will diminish, and ultimately be phased out. It is predicted that wind energy will be the main source of electricity generation within Europe by 2025 and will provide 50% of the electricity requirement by 2050 [1].

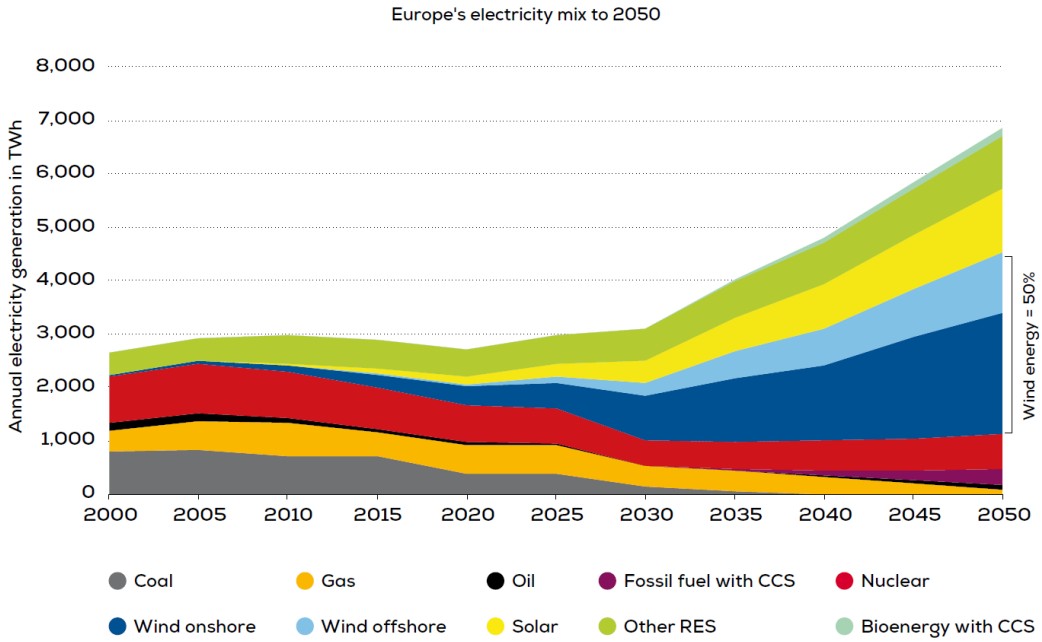

Figure 1.1: Europe's Electricity Mix, 2000-2050. [1]

The increased capacity of wind generation is achieved partially due to developments in wind turbine substructures which allow wind turbines to be located offshore. Offshore wind farms allow for larger turbines, reaching higher wind speeds, which will have to endure challenging environmental conditions. Typically, a wind turbine has a design life of around 20 to 25 years in operation. To achieve this, careful consideration has gone into the material selection of the wind turbine components to ensure that the wind turbine can function for the duration of the entire design life. Particular attention is paid to the turbine blades as they face large fluctuating loads as well as variable operating conditions during their lifetime.

Wind turbine blades are exposed to varying degrees of environmental conditions which have a detrimental effect on the surface of the blades. Conditions, such as ultraviolet light from the sun, thermal cycles and humidity fluctuations due to local climate, ice formation, lightning strikes, repeated impacts from rain and hail, abrasion due to solid particles within the wind and chemical attack due to substances interacting with the blades such as salts (sea), blood (insects) & excrement (birds), all must be considered and their effect quantified, where possible, to ensure the blade can survive and safely operated as expected

Wind turbine blade erosion is a research topic which is growing in prevalence and receiving much attention. Wind turbine manufacturers and operators are obtaining more operational information about their turbines and are realising that aggressive erosion is having an impact on turbine performance. Protective coatings are used to try and reduce the amount of erosion experienced on the blades however, these systems still experience erosion by rain impact and damage by other environmental factors. It is not yet known what contribution weathering effects make to the extent of the erosion. Nevertheless, erosion damage on blades is costly to repair and must be repaired to allow the turbine to operate at optimal performance.

1.1. Background to Research Challenge

The degradation mechanisms of wind turbine blade coatings are not fully understood. It is not fully known how stresses build up within the coating materials and whether on a molecular level, specific chemical bond types are attacked, if there is an order to the attacks and which bonds are most resistant to erosion. It is also not known what triggers the move from the incubation period, where no observable erosion damage is present to the naked eye, to erosion damage.

The mechanical aspect of the degradation mechanism has been established, as is discussed later. However, there is little understanding of the chemical degradation due to erosion. The chemistry of a coating plays a large part in the erosion process, arguably more so than the mechanical aspect. The mechanical response can only be changed so much by shape, geometry, thickness, lay-up etc. whereas chemical changes can alter the material properties significantly by implementing erosion resistant bonds allowing the coating system to remain intact.

In a real operational environment, erosion damage from rain impacts occurs concurrently with exposure to weathering from UV radiation, humidity, and thermal cycling. In an offshore environment, salts may be present which could have an impact on erosion. Weathering causing the degradation of coatings is well researched, however the influence of weathering on the rain droplet impact erosion process is not. This is constrained by the current standard requirements for laboratory testing for weathering and rain impact erosion occurring at different accelerated testing timescales. The standard practice for wind blade coatings is to pre-weather the rain erosion test samples and record the performance of a pre-degraded sample.

1.2. Research Objectives

The research challenge is addressed by two specific objectives to provide a comprehensive approach to assessing the combined effects of rain erosion testing and weathering degradation, and a suitable accelerated test method.

The first objective of this work is to investigate the degradation due to weathering and the combined effects of weathering and rain impact erosion on wind turbine blade coating materials. Furthermore, to examine the influence of weathering on the incubation period and erosion rate of the protective coating systems.

The second objective is to develop an accelerated test method for assessing the performance of wind turbine blade coatings which is representative of an offshore wind turbine environment. The test is developed using data from Offshore Renewable Energy Catapult's NOAH met mast, located offshore from Blyth, in conjunction with the current International Organisation for Standardisation testing standard ISO/TS 19392 [2]–[4].

The novelty of this work is highlighted in the approach to analyse the erosion process on a chemical level, in tandem with the mechanical response. It is noted that currently available research focuses primarily on quantifying and explaining how the mechanical behaviour of the erosion process occurs. The present work addresses the issue of why, at a molecular level, changes occur in the structure during erosion and how are these changes influenced by environmental factors.

1.3. Overall Project Plan

The wide-ranging scope of this work, to investigate the effects of rain droplet impacts as well as weathering effects on wind turbine blade coating systems, has meant that the work was split into three distinct sections. The first section, work package 1, considers the effects of rain droplet impacts on the coating systems. The second section, work package 2, looks at the effects of weathering on the coating systems. The third section, work package 3,

combines the effects of both rain droplet impacts and weathering on the coating systems.

The UK's Offshore Renewable Energy Catapult (OREC) played a vital part in the present work by creating a parallel project, Blade Leading Edge Erosion Research (BLEER). The BLEER project was led and managed by Dr Kirsten Dyer from OREC and was supported by two PhD students from Bristol University and one PhD from Strathclyde University, who is the present author. Within the BLEER project, two leading industrial coatings manufacturers collaborated with the three PhDs and supplied wind turbine blade coating systems to be investigated. The industrial coatings manufacturers also contributed time to aid understanding of the coating systems as well as access to their research facilities. In addition to the supplied coating systems, the industrial collaborators also provided a financial contribution to the BLEER project. This allowed for an experimental budget which was used to purchase consumables and gain access to specific testing apparatus. The BLEER project provided the wind turbine blade coating systems to be investigated throughout this piece of work. The work packages reported in this work are the sole work of the present author.

1.3.1. Work Package 1 – Rain Erosion

WP1 investigated the effects of repeated rain droplet impacts on each coating system. An accelerated rain erosion test rig was used to erode each coating system. The tested specimens were then assessed in the laboratory to characterise and quantify any erosion damage.

1.3.2. Work Package 2 – Weathering

WP2 involved various weathering tests of the coating systems. Accelerated weathering testing and real time, natural outdoor testing was used. Test specimens were regularly analysed in the laboratory to allow any material and chemical changes to be tracked.

1.3.3. Work Package 3 – Combined Rain Erosion and Weathering

WP3 was a combination of the previous two work packages. A novel experimental test plan was created and carried out, where test specimens would undergo several alternating stages of accelerated weathering exposure and accelerated rain exposure. Test specimens were analysed at regular intervals to track any material and chemical changes.

1.4. Summary

To summarise, this work aims to quantify the influence of weathering on wind turbine blade erosion. Firstly, by quantifying the effects of both rain erosion and weathering individually, then as a combined study. As part of each assessment, a thorough investigation measures changes in surface microstructure along with changes in material and chemical properties. Visual assessments and novel approaches are also used to provide detailed understanding and methodologies to combined rain erosion and weathering testing.

Chapter 2 - Literature Review

This chapter examines the available literature published on the wind turbine blade erosion problem and provides background theory and relevant industrial practice for blade erosion testing.

The power available in the wind, P_{wind}, is given by the expression in Equation 2.1 [5]. The terms within the expression are ρ, the density of the wind(air), u, the wind velocity, and A is the area of available wind potential. This is the general expression which governs the amount of power a wind turbine can capture.

$$P_{wind} = \frac{1}{2}\rho A u^3 \qquad \text{Equation 2.1}$$

If the goal is to utilise the maximum available wind potential energy, the main approach is to enlarge the area of wind that the turbine can access, which is achieved by increasing the length of the blades. Figure 2.1 shows the trend in wind turbine design to increase the rotor swept area to allow for greater power capture, which will, in turn, enable the turbine to produce an increased power output, from the A term in Equation 2.1.

Due to the trend of increasing the rotor swept area to allow for greater power capture, modern wind turbine blades require to be larger to facilitate this increase. The largest blade designed at the time of writing is the Mingyang Smart Energy 140m long blade, which provides a rotor swept area of over 66,050m^2 [6]. The limiting factor on the size of a blade is weight. Typically, as the length of a blade doubles, the weight increases by a factor of eight [7]. Consideration has then to be given to the supporting structure of the turbine, the tower and nacelle, to ensure that the turbine can withstand the weight of the blades as well as manage extreme loading conditions.

Figure 2.1: Growth in Wind Turbine Swept Area and Power Output. [8]

Larger turbine blades will lead to higher blade tip speeds as shown by Equation 2.2, where v_t is the tip speed of the blade, ω is the rotational velocity of the blade, and R is the blade length [5]. Typically, for larger offshore wind turbines tip speeds are in the region of 90 – 110m/s [9]. With the trend for newer turbines leaning towards an increase in rotor area and therefore blade length, the tip speed of the blade will inevitably increase. Any rise in tip speed will also cause the impact velocity of any rain or particles which strike the blade to increase, which will lead to a surge in the erosion rate. The impact velocity has a dominant role in determining the erosion rate of a blade.

$$v_t = \omega R \qquad \text{Equation 2.2}$$

2.1. Blade Structure

Wind turbine blades are required to be stiff and lightweight. Stiff so that they hold their shape with minimal deformation under wind loading, this should prevent a blade colliding with the wind turbine tower, and lightweight to reduce the total load on the turbine nacelle and tower structure. Wind turbine blades are subjected to varying loads during their lifetime. Typical loads include aerodynamic loading, due to the generation of lift and drag as a result of the blade's aerodynamic profile. Gravitational and centrifugal loading, dependant on the mass of the blade and the rotational speed for centrifugal loads &

operational. Other loads which occur from pitching, yawing, breaking and in an emergency stop situation.

Each blade has three distinct sections, the blade root, the midsection, and the blade tip, as illustrated in Figure 2.2. The blade root sacrifices aerodynamic properties for structural integrity and the ability to transfer the loading on the blade to the rotor. The root is heavier than the other blade sections as it houses components for the connection between the blade and the drivetrain, housed in the nacelle. The midsection is the key aerodynamic section of the blade with moderate structural demands. The midsection is made to be lightweight, but it must also be stiff to prevent a collision with the tower. The blade tip is designed to have excellent aerodynamic properties and to shape the airflow over the blade to reduce the noise of the blade whilst operating.

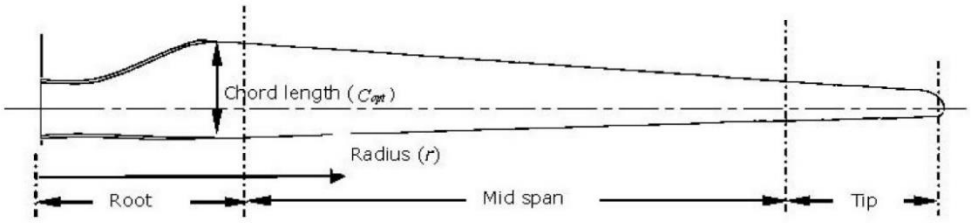

Figure 2.2: Blade Sections. [10]

Each blade is made of two surfaces, also known as shells, which have been designed to operate as an aerofoil, see Figure 2.3. The aerofoil shape of the blade allows for an upwind side (pressure) and a downwind side (suction), like an aircraft wing. This difference in pressure, due to the applied wind loading, is what drives the blades to move.

Blades are stiffened by using shear webs. Shear webs give structural support along the length of the blade allowing the blade to cope with compressive, tensile and shear loading forces. Figure 2.3 shows how shear webs are located along the length of the blade. Spar caps run perpendicular to the shear webs, both above and below. The spar caps are in place to strengthen and stiffen the blade and to allow loading forces to transfer through the shear webs. Figure

2.4 illustrates a typical cross section of a larger blade where the shear webs have been modified into a box spar design which can offer additional structural support [11].

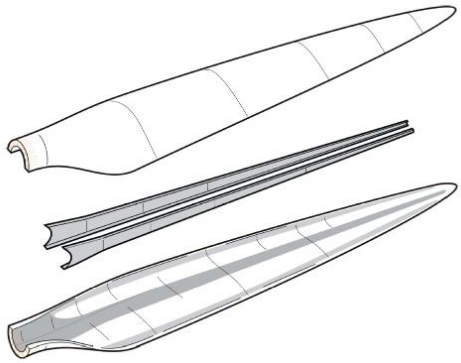

Figure 2.3: Blade Structure with Shear Webs. [12]

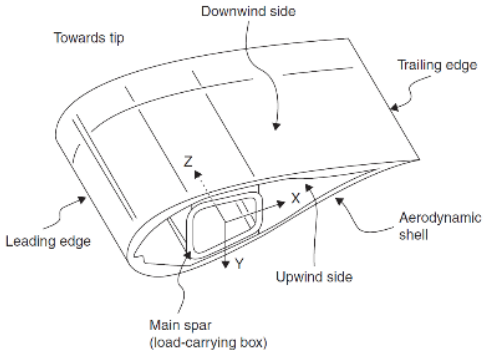

Figure 2.4: Typical Blade Cross-Section (Box Spar). [11]

The blade shells are joined together to form the aerodynamic profile with adhesive joints at the leading edge, trailing edge and at the web joints, where the shear webs meet the spar caps. The main types of adhesives used to create the bond are Epoxy, Polyurethane and Methacrylate [13]. Each adhesive type will have differing benefits depending on the materials used for the blade shells and webs.

Blades are then finished with a coating to give a smooth aerodynamic finish. The applied coating is also in place to resist effects from weathering, including water ingress and erosion damage. The coating is typically applied all over the blade's outer surface with particular attention paid to the leading edge where, usually, a tape, preformed softshell or a paint is applied to give extra erosion resistance. This is commonly referred to as the Leading Edge Protection (LEP).

2.2. Blade Materials

The materials used for wind turbine blades are required to perform for the design life of up to 25 years, during this time the blades will face challenging

operational environments, subjecting the blade materials to varying loads, temperatures, impacts and chemical attacks.

Wind turbine blades are constructed using composite materials. A composite material is made up of two or more constituent materials which when combined give properties superior to any of the individual constituent materials. Common composites include fibre reinforced polymers (FRP) where the combined properties of the composite are greater than that of each component - fibres and resin, see Figure 2.5.

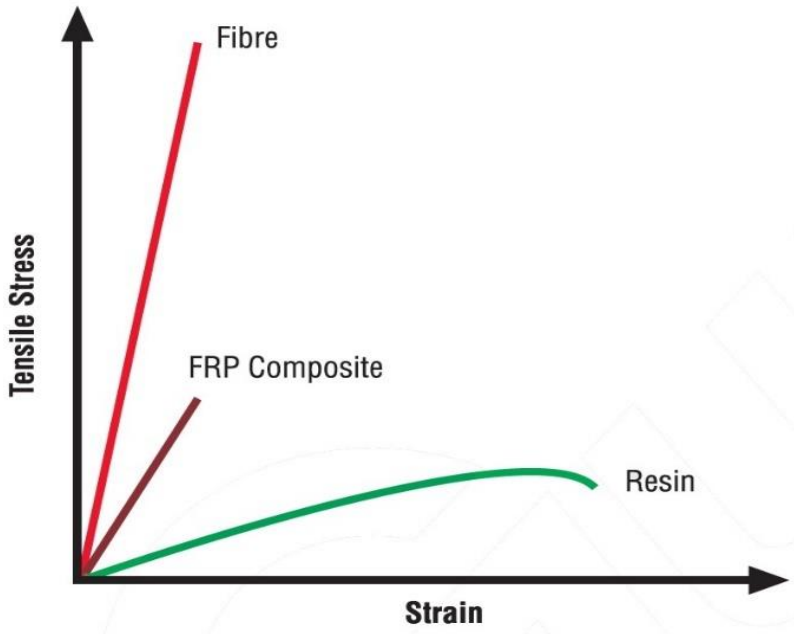

Figure 2.5: Plot of Individual and Combined Composite Properties. [14]

As illustrated in Figure 2.5, the fibre provides a high tensile strength which is useful for resisting deformation under loading, however this also renders the fibre brittle and is susceptible to fail under low strain. This is of no use for the application of a wind turbine blade as the blade will have an amount of flex under loading conditions. The opposite is true for the resin, the resin is able to flex. The resin is ductile and can withstand high strain, however, the resin cannot endure a high tensile stress [15]. Combining both the resin and fibres to create a composite gives desirable properties which can be used within a wind turbine blade.

Wind turbine blades use fibre reinforced polymer composite materials, specifically glass fibre reinforced polymers (GFRPs) or carbon fibre reinforced polymers (CFRPs). GFRPs tend to be more dominant in that they cost significantly less whilst having good performance characteristics however, slightly less than CFRP as demonstrated in Figure 2.6. The desirable characteristics for a wind turbine blade are strength, stiffness and to be lightweight. Costing information on fibres is difficult to obtain, as a rough estimate, glass fibres are priced at around 20 USD$/kg and carbon fibres are priced at around 140 USD$/kg [16].

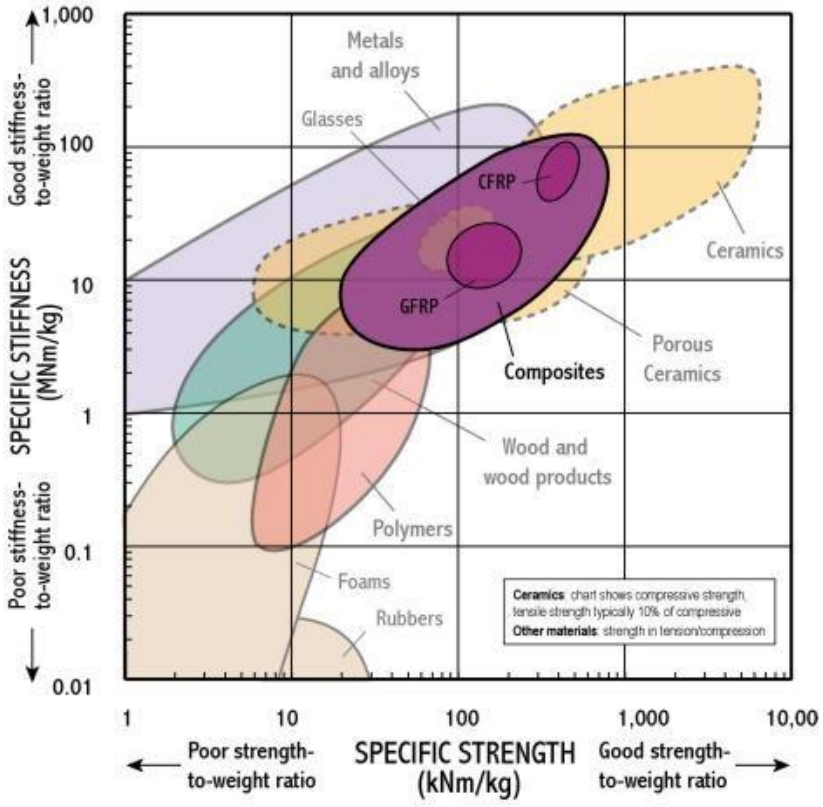

Figure 2.6: Specific Stiffness vs Specific Strength - Composite Materials. [17]

The fibres, glass or carbon, are usually orientated in a specific direction depending on the material demands of the section of blade where they are to be used. If the fibres are all orientated in the same direction, at 0° the layup is unidirectional (UD) as in Figure 2.7. Fibres can be orientated in other directions, common orientations are bi-axial (BX), where fibres are oriented at

0° and 90°, double bias (DB) where fibres are oriented at −45° and +45° and tri-axial (TX) where fibres are oriented at −45°, +45° and 90°. The fibres are then set into place using a thermosetting polymer resin material, also known as matrix material, which is most commonly an epoxy, vinyl ester or polyester [15]. Multiple fibre orientation types can be stacked and then set in matrix to create a laminate, Figure 2.8.

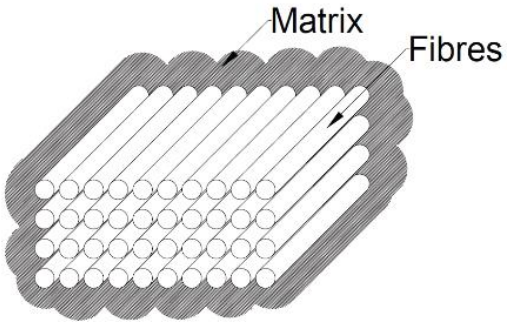

Figure 2.7: Fibre Orientation - Unidirectional (UD) Layup. [18]

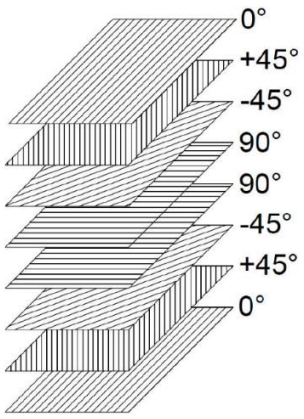

Figure 2.8: Fibre Orientation - Laminate Construction. [18]

Typically, the blade's surface, the skin, is moulded using a GFRP structured with a DB layup [19] . The core of the blade, the internal supporting structure, is usually made from a lightweight wood such as balsa wood, a foam such as polyvinyl chloride (PVC), polyethylene terephthalate (PET) or styrene acrylonitrile (SAN) [20] or a honeycomb structure can be used. The internal box spar and shear webs are usually reinforced with layers of UD GFRP to provide the blade with stiffness along its length, as illustrated by Detail AA of Figure 2.9. The outer sides of the box spar and both the pressure side and suction side of the blade, shown by Detail BB & Detail CC of Figure 2.9, require additional layers as they are necessary to be weather resistant. These extra layers are protective coatings which can be in the form of a gelcoat, a tape, a softshell or a paint.

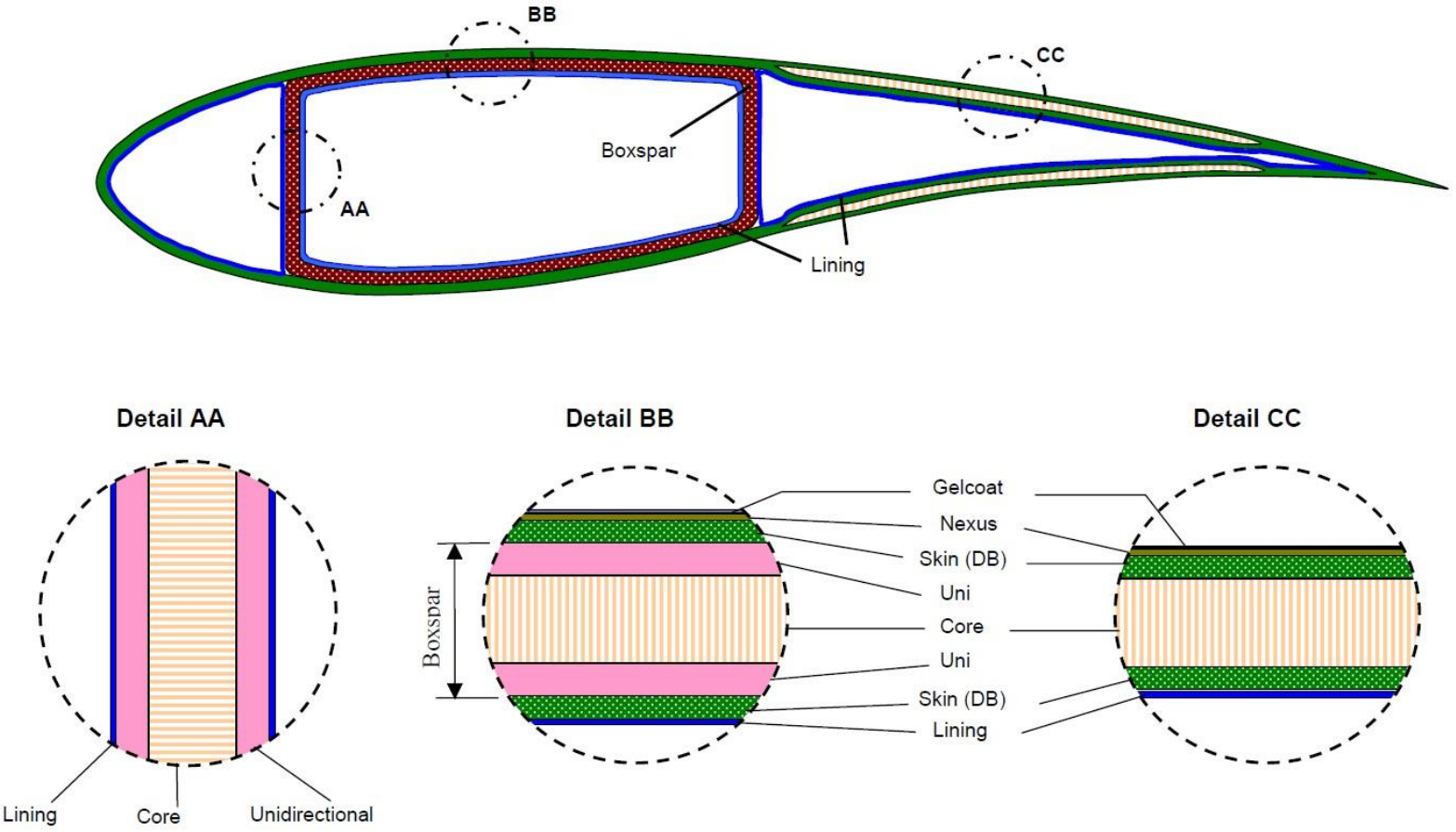

Figure 2.9: Generic Blade Material Layup Sections. [21]

There are several different types of glass fibres which are available to be used within a wind turbine blade. Figure 2.10 displays some of the mechanical properties for various types of glass fibre. E-glass is most commonly found in wind turbine blades due to its high strength and high stiffness features. Cost is also a factor to be considered when selecting a glass fibre type; E-glass ranges from 1-2 £/kg, where S-glass ranges from 12-20 £/kg [22]. However, cost increases with mechanical performance properties. Therefore, with regards to wind turbine blades the materials are expected to undergo severe loading conditions and require the good performance characteristics offered by E-glass, without being too expensive and costing much less than S-glass.

Fiber type	Density, (g/cm3)	Tensile Strength, MPa	Modulus, GPa	Percent Elongation
A-glass	2.44	3300	72	4.8
AR-glass	2.7	1700	72	2.3
C-glass	2.56	3300	69	4.8
D-glass	2.11	2500	55	4.5
E-glass	2.54	3400	72	4.7
ECR-glass	2.72	3400	80	4.3
R-glass	2.52	4400	86	5.1
S-glass (also S-2 glass)	2.53	4600	89	5.2

Figure 2.10: Mechanical Properties of Glass Fibres. [23]

The purpose of the glass fibres is to provide the blade with strength and stiffness, the resin is used to bind the fibres together and to distribute the applied blade load throughout the fibres. Resins are typically either an unsaturated polyester, a vinyl ester or an epoxy. Each have varying mechanical properties as shown in Figure 2.11. Epoxy is the most common resin type used within modern wind turbine blades however, resins are an area of development and new resin types such as a polyurethane resin may become

prominent in the near future [24]. The cost of the resin is also a factor in deciding which resin to use. Estimates of costs for the resins named are, Polyester - 1.80 £/kg, Vinyl Ester - 2.80 £/kg and Epoxy - 3.20 £/kg [25].

	Polyester	**Vinyl Ester**	**Epoxy**
Specific gravity	1.10-1.46	1.1-1.2	1.2-1.3
Flexural strength, MPa	60-160	120-140	110-215
Tensile strength, MPa	40-90	70-90	50-130
Compressive strength, MPa	90-200	-	110-210
Tensile elongation, %	<5	<6	<9
Modulus, GPa	2-4	3-4	3-4.5

Figure 2.11: Cast Resin Properties. [25]

2.2.1. Resin Infusion

A common process of binding the fibres with the resin to create one composite material is resin infusion. Resin infusion uses vacuum pressure to draw the resin throughout the fibre layup. The dry fibre sheets are laid in a mould in the desired layup before any resin is applied. The fibre layup is then ’bagged’ where a pressure seal is created around the layup to prevent any resin escaping and to allow a vacuum to be formed [22]. Once the vacuum is applied, the resin can be inserted. The resin will then penetrate and spread through the fibre layup. Depending on the resin, an increase in temperature may be required to allow the resin to cure, the vacuum is required to be held until the composite is fully cured [26], [27].

Resin infusion is used to form sections of the blade shell [12]. A specific low viscosity resin is used that can cure at room temperature; it would be impractical to use a resin that requires an elevated temperature to cure due to the size of oven needed to contain a wind turbine blade. Typically, heat would be applied through the mould.

2.2.2. Prepreg Materials

Another type of composite construction material is one that combines both the fibre and the resin system in one manufactured sheet which is ready to apply to a mould and undergo a curing stage. This is known as a pre-impregnated, prepreg, material. The fibres are woven into a sheet of a specific orientation which is then injected with the resin system, including the curing agent. The prepreg sheet can then be laid into the mould and a target layup created. The prepreg mould is then cured by elevated temperature and pressure, no additional material components are added to the prepreg to allow it to cure.

Prepreg materials give more consistent mechanical properties than resin infusion due to the evenly distributed injected resin. However, prepreg materials require an elevated temperature and pressure to cure, this adds to the difficulty of using prepreg materials in wind turbine blades due to their size. Cost is also factor in prepreg materials, they tend to cost more versus creating the same piece using resin infusion [28]. Gurit [29] have used unidirectional prepreg materials to create spar caps for wind turbine blades.

2.3. Blade Coatings

Blade coating research is the main area of interest within this Thesis. However, the publicly available literature is limited as each coating system will have a unique coating composition, and that manufacturers retain as commercial intellectual property. The main generic coating types comprise of polyurethane, polyurea and polyaspartate.

The main function of a coating is to act as a barrier between the blade shell and any outside factors which could cause damage to the shell. Blade shell

damage during turbine operation would primarily occur due to a deterioration of the resin used in the substrate of the composite shell by methods such as water ingress, long term UV exposure or direct impact. The coatings which are applied to the blade are required to resist against all environmental deterioration to protect the blade shell.

Environmental degradation factors, identified by Kjærside Storm [30], which the surfaces of wind turbine blades are exposed to consist of:

- temperature (-50°C to 70°C)
- UV radiation from sunlight
- chemical attack (from various chemicals)
- blood from insects
- faeces from birds
- lightning and other mechanical attack
- ice
- water attack
- hailstorms
- rain erosion
- salinity in the air
- wear from sand and other small particles

Some of the effects caused by the environmental degradation factors on the protective coatings include:

- Thermal changes due to local climate, cyclic temperature variations, both daily and seasonal cycles, can weaken the chemical structure of the coating due to the fatigue effect of heating and cooling.
- Ultraviolet (UV) light from the sun, this can cause a chemical change in the structure of the coating, possibly weakening it, UV exposure can also cause a yellowing effect of the coating colour.
- Chemical attack/blood/faeces, this could cause undesirable chemical reactions on the surface of the coating, leading to coating degradation.
- Lighting strike and mechanical impact, this could cause the coating to crack and break off along with reducing the adhesion of the coating to the substrate. Ice, the freeze thaw action of ice formation can cause the coating to crack, with additional freeze thaw action deepening the cracks leading to water ingress to the substrate.

- Moisture exposure from rain and humidity, water diffusion through and water ingress beneath the coating can cause blistering and coating failure, the coating cannot be water soluble.
- Impacts from rain and hail, repeated impacts can cause the surface to erode by creating pits which can deepen and coalesce.
- Salts, this could cause chemical reactions on the surface of the coating, also could dissolve within rain/moisture to create a more erosive medium.
- Wear by solids, small particles could erode the coating by abrasion, acting as a form of sandpaper on the blade surface.

It should be noted that blades can be exposed to multiple environmental degradation factors simultaneously, requiring increased durability from the protective coating. When selecting a coating, all the degradation factors must be considered.

There are four main forms of protective coatings: gelcoats, tapes, paints and softshells.

Gelcoats are applied in-mould during the construction of the blade. A layer of the gelcoat is applied as the first layer in the blade moulding process so that when the blade is fully constructed the gelcoat is the outermost surface of the blade. Gelcoats are typically thermosetting polymers, commonly an epoxy, polyurethane or polyester, which cure to form a hard brittle surface.

Tapes are applied after the blade is constructed. Tapes are focused on leading edge protection where they are applied over the length of the leading edge of a blade. Tapes are constructed of a highly flexible material, such as polyurethane, which provides great impact resistance and shape recovery because of the high elasticity and durability of the material.

Softshells are applied after blade construction. Softshells are pre-cast to fit over the leading edge and are bonded to the blade. Softshells are ductile and durable, and are commonly made of polyurethane.

Paints are applied after blade construction. Paints can be applied by brush, roller or by spraying. Paints are generally made of flexible, durable materials such as polyurethanes. With the same principle of the tape, the aim of the paint is to provide the flexibility and durability required by the blade surface to withstand the erosion degradation factors.

Gelcoats were once the most prominent coating type, however, operators as well as maintenance teams have found that the brittleness of the gelcoat doesn't deliver the durability required for the wind turbine blades. Therefore, the industry has seen a trend to move towards the more flexible coating systems such as polyurethanes. The flexible paint systems offer high impact resistance, shape memory due to high elasticity and a resistance to abrasion [15]. Some blade manufacturers may decide to combine a gelcoat/paint system with a tape over the leading edge with the aim of enhancing the erosion resistance of the blade [31]. It is commonplace for multiple layers of coatings to be used on a blade with the most durable layers applied to the leading edge.

2.3.1. Polymer Chemistry

All the coating chemistries which are used for wind turbine blades are polymeric, meaning that the chemistry of the coating consists single blocks which are linked together, via a reaction, to form a chain. The single blocks are known as monomers, the linked chain is a polymer, and the reaction is known as polymerisation, shown in Figure 2.12.

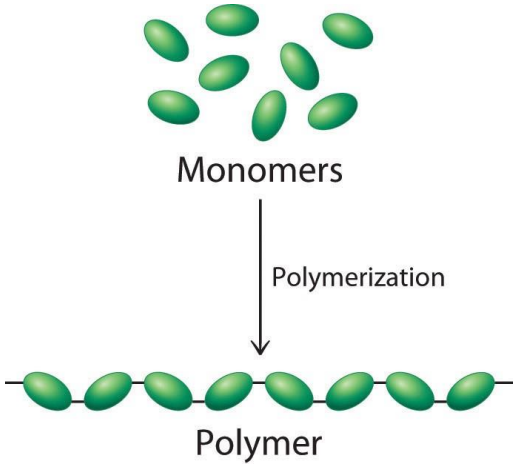

Figure 2.12: Depiction of Monomers and a Polymer. [32]

Polymer chains are able to interact with adjacent polymer chains by forming various types of bonds between each chain. The amount of bonding between each chain is dependent on the architecture of the polymer. The type of bonds formed between chains governs the material properties of the polymer [33].

Polymer architecture affects how polymer chains interact. The architecture depends on the arrangement of monomers within the polymer chain. Polymer architecture can be controlled through varying the polymerisation method. Some typical architectures are shown in Figure 2.13. The structure of homopolymers and alternating copolymers allow for multiple polymer chains to interact and bond together in a tight, dense, ordered structure, meaning they can crystallise [34]. Some other polymer architectures can partially crystallise such as block polymers and graft polymers. The amount of crystallisation will have an effect on the material properties, an increase in crystallinity, the percentage of crystallisation, will yield a denser material which would tend to become more brittle, but this is dependent on molecular weight. The Young's modulus of the material will increase linearly, along with the degree of crystallinity [34].

Figure 2.13: Common Polymer Architectures, Where A and B Are Two Distinct Monomers. 1 - Homopolymer, 2 - Alternating Copolymer, 3 - Statistical Copolymer, 4 - Block Copolymer, 5 - Graft Copolymer. [35]

Polymer-polymer interactions occur due to two categories of molecular bonding, primary bonding and secondary bonding [36]. Primary bonding involves the movement of electrons to form stable molecular structures, these are ionic bonding and covalent bonding. Secondary bonding is the interaction of intermolecular forces between polymers, such as Van der Waals forces and Hydrogen bonding.

Primary bonding of polymer chains allows individual chains to join together via cross-links and form one large complex chain, a simple illustration is shown in Figure 2.14. Primary bonds are much stronger than any secondary bonds. Primary bonding between polymer chains is known as cross-linking. Cross-linking of polymer chains allows the chains to be firmly held together, affecting the material properties of the polymer. Increasing the number of cross-links between chains will also increase the Young's modulus of the polymer [37].

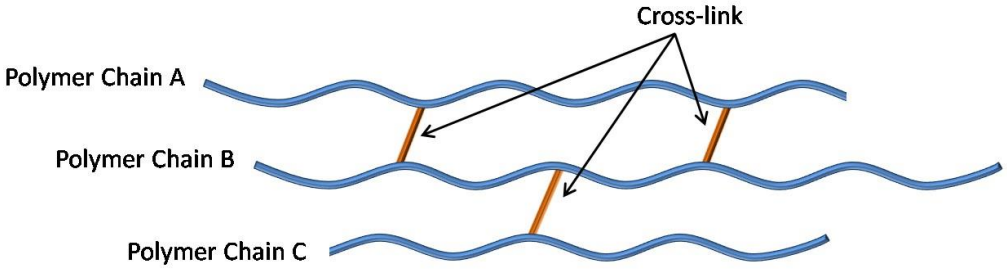

Figure 2.14: Polymer Cross-links. [38]

Cross-links are physical covalent or ionic bonds. Covalent bonds form due to unstable atoms sharing electrons in order to gain a full valence shell, a full valence shell will give the atom stability. Ionic bonds form due to the transfer of electrons from one atom to another, giving the receiving atom a negative polarity creating an anion, and the donating atom a positive polarity creating a cation, thus, the atoms become attracted to each other due to the difference in polarities [39]. Figure 2.15 and Figure 2.16 illustrate the formation of both covalent and ionic bond types.

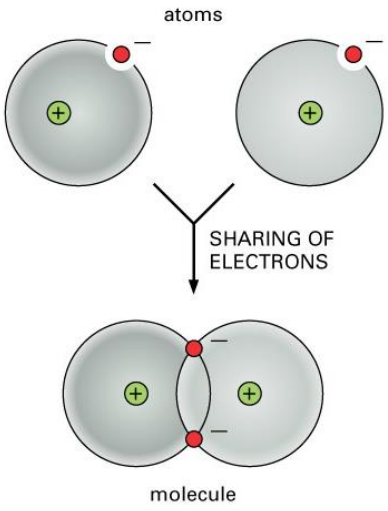

Figure 2.15: Primary Bonding – Covalent. [40]

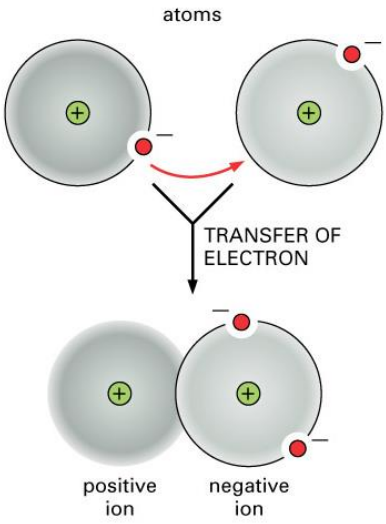

Figure 2.16: Primary Bonding – Ionic. [40]

Secondary bonding is the interaction of polar forces within molecules. Secondary bonds are weaker than primary bonds and occur in two main forms. Firstly, Van der Waals forces which are the interaction of polar forces between atoms, such as dipoles. Dipoles occur due to the tendency of polar molecules to order themselves so that the positive end of one molecule is near the negative end of another [39]. Secondly, Hydrogen bonding is the attractive force produced by a hydrogen atom which is covalently bonded to a highly electronegative atom, such as oxygen, fluorine, or nitrogen [39]. Hydrogen bonding is a particular kind of dipole-dipole bonding which has a slightly stronger attraction force and must involve hydrogen interacting with oxygen, fluorine, or nitrogen. Figure 2.17 shows an illustration of methanol where both dipole-dipole bonding and hydrogen bonding are present.

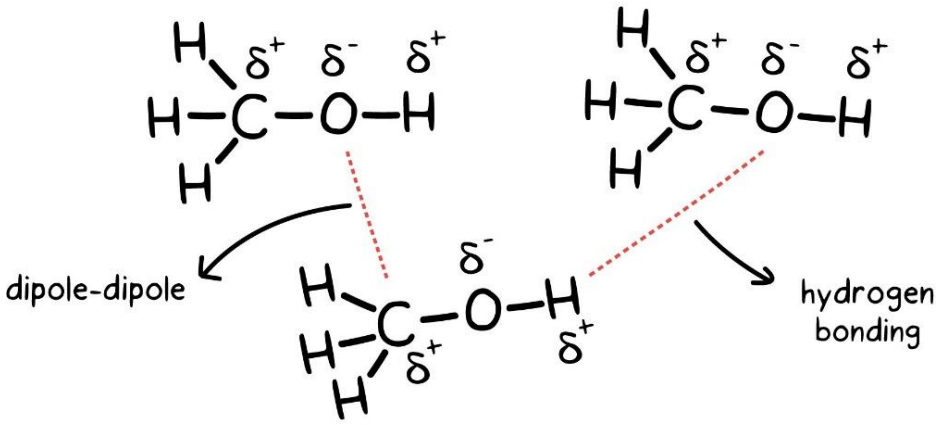

Figure 2.17: Dipole-Dipole Bonding and Hydrogen Bonding. [38]

Both primary and secondary bonding forces are involved with polymer chain interactions however, primary bonds in the form of cross-links will dominate.

2.3.2. Wind Blade Coatings

Several polymer coating types are used to coat wind turbine blades, these are polyurethane, polyurea and polyaspartate. Polyurethanes are becoming the most prominent coating type, applied as a paint or tape, as they exhibit the desirable characteristics of high flexibility along with durability whilst also yielding good UV resistance [30]. Figure 2.18 displays some of the advantages and disadvantages of commonly used materials for wind turbine blade coatings.

Material	Advantages	Disadvantages
Unsaturated polyester	Cheap. Can cure up at room temperature. Difficult to control the curing process.	Low chemical resistance, but this depends on the formulation. Long curing time to full curing.
Epoxy	Good chemical resistance. Hard surface can be obtained.	Curing has to be carried out at elevated temperature. Long curing time.
Acrylate	Short curing time. Cures up at room temperature. UV resistant.	Brittleness can be introduced in the surface. Low chemical resistance. Needs energy to cure, e.g. from IR or UV radiation.
Polyurethane	Short curing time. Can cure at room temperature. Tough surface, which can give good wear resistance because of uptake of sharp particles by the surface.	Tough surfaces. Low wear resistance.

Figure 2.18: Advantages and Disadvantages of Typical Coating Materials. [30]

2.3.2.1. Polyurethane

Modern coatings for wind turbine blades are most commonly made from a polyurethane material. Polyurethanes are slightly different to a typical polymer in that they can have additional chemical components added to their structure as well as the repeating monomer unit. The standard repeating monomer for polyurethane, the urethane link, is presented in Figure 2.19.

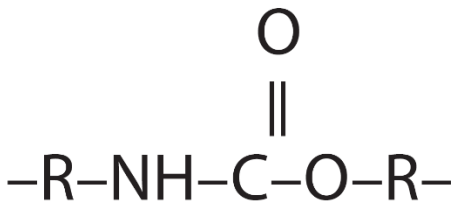

Figure 2.19: Typical Urethane Repeating Unit (Monomer). [41]

It is worth noting that polyurethanes are created in many different forms, such as foams, solids, and flexible moulded pieces. Each form varies by changes in their chemistry. Chain extenders can be used to create extra reaction sites

along the polymer chain, encouraging cross-links between polymer chains and increasing targeted material properties as a result.

According to Rosu & Visakh [42], the main factors which cause polymer degradation are heat, light, humidity, and mechanical action. Szycher [41] notes that polyurethanes which are aromatic tend to absorb more energy from ultraviolet light, leading to degradation and discolouration with a loss of mechanical properties. Therefore, polyurethanes used as coatings are typically aliphatic in nature.

Most coating manufacturers keep their coating compositions and material properties protected. Therefore, it is very difficult to obtain information on the chemistry and formulation of industrial products.

2.4. Wind Turbine Blade Erosion

Erosion is defined as the gradual destruction of a material. With regards to a wind turbine blade, erosion is the gradual destruction of the blade's surface, particularly the leading edge of the blade. In the UK, the predominant cause of blade erosion is rain which induces repeated liquid droplet impacts on the solid surface of the blade.

2.4.1. Liquid Droplet Impacts

The degradation process of surface coatings which are eroded by liquid droplet impacts is understood on a mechanical level. The widely accepted Springer Model [43], shown in Figure 2.20, displays a liquid droplet impacting a solid surface, the forces induced on the solid surface and how the droplet collapses. As the liquid droplet collides with the solid surface three distinct stress waves are generated within the solid. Firstly, a compressional wave in the longitudinal axis and a shear wave in the transverse axis is radiated from the point of impact. Next, a Rayleigh surface wave radiates in an annular shape along the surface of the solid from the point of impact.

Once the compressional wave has reached a material boundary layer, such as a coating/substrate layer, it can be reflected back on itself and cause additional stress waves within the solid.

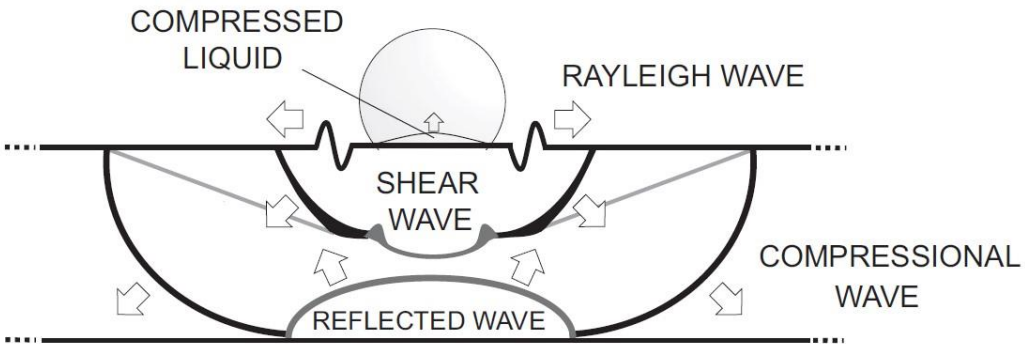

Figure 2.20: Springer Model of Liquid-Solid Impact Erosion. Modified from [44].

After the initial impact of the liquid droplet, the droplet compresses whilst still attached to the solid surface until the pressure within the droplet cannot increase any further. Once the droplet is fully compressed, the droplet collapses and is de-pressurised due to lateral jetting [45] as shown in Figure 2.21. The process of lateral jetting is detrimental to any surface with existing imperfections, the jetting shoots out from the main droplet tearing away any material which is obstructing the jetting path.

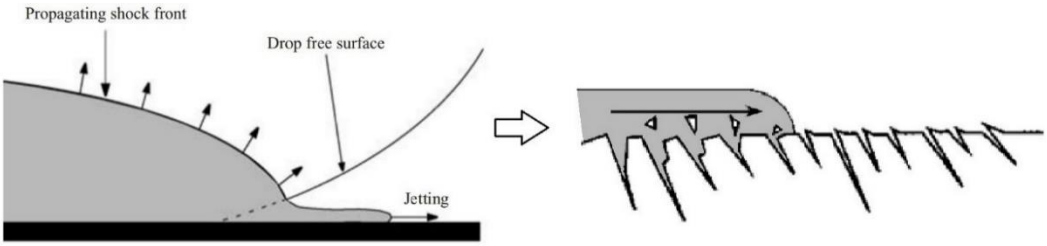

Figure 2.21: Droplet Lateral Jetting. Modified from [45].

The force of the impacting droplet can be modelled in two stages [44], [45]. Firstly, as the droplet compresses it can be modelled as a 'water-hammer pressure' P_{wh}, a pressure surge due to an abrupt stop or directional change of a fluid in motion. The water-hammer pressure is as shown in Equation 2.3 [44]. Where u_i is the impact velocity, ρ_l & ρ_s are the densities of the liquid droplet

and solid surface respectively and C_l & C_s are the speed of sound in the liquid droplet and solid surface respectively. Then, as the droplet becomes fully compressed it can be modelled as the dynamic pressure.

$$P_{wh} = \frac{u_i \rho_l C_l \rho_s C_s}{\rho_l C_l + \rho_s C_s} \quad \text{Equation 2.3}$$

The velocity component of each stress wave can also be calculated as demonstrated by Gohardani [44], here E is the Young's modulus, ν is the Poisson's ratio and ρ the density, all of the solid material. The calculations for the velocity of the compressional longitudinal wave c_L, the velocity of the shear transverse wave c_T and the velocity of the surface Rayleigh wave c_R are shown in Equation 2.4, Equation 2.5 & Equation 2.6 respectively.

$$c_L = \left(\frac{E}{\rho(1+\nu)} \left(\frac{\nu}{1-2\nu} + 1 \right) \right)^{\frac{1}{2}} \quad \text{Equation 2.4}$$

$$c_T = \left(\frac{E}{\rho(2+2\nu)} \right)^{\frac{1}{2}} \quad \text{Equation 2.5}$$

$$c_R = \left(\frac{0.862 + 1.14\nu}{1+\nu} \right) \left(\frac{E}{2\rho(1+\nu)} \right)^{\frac{1}{2}} \quad \text{Equation 2.6}$$

The damage threshold velocity (DTV), explained in detail by Gohardani [44], is a measure of the minimum impact velocity required for a defined liquid droplet/solid system before any erosion damage is observable. This implies that if the impact velocity is low there will no observable erosion damage. Within wind turbines, the impact velocity is dependent upon the velocity of the falling rain as well as the rotational velocity of the turbine blade, which increases along the length of the blade. The expression for DTV, v_{dt}, is shown in Equation 2.7 where K_{ic} is the fracture toughness of the solid, c_R is the Rayleigh wave velocity on the surface of the solid, ρ_l is the density of the liquid droplet, c_l is the compressional wave speed within the liquid droplet and d_l is

the diameter of the liquid droplet. The DTV considers material properties of the system and the size of the impacting droplet.

$$v_{dt} \approx 1.41\left(\frac{K_{ic}^2 c_R}{\rho_l^2 c_l^2 d_l}\right)^{\frac{1}{3}}$$ Equation 2.7

As mentioned previously, as the length of wind turbine blades increase typically so does the tip speed of the blade. This in turn increases the impact velocity of the colliding raid droplets, v. This will then cause a greater water hammer pressure, P_{wh}, which will induce greater stresses on the surface of the blade. Induced stresses of higher magnitude are likely to have a detrimental impact on erosion of the blade surface.

2.4.2. Repeated Impacts

Repeated rain droplet impacts can fatigue the surface of a blade. The repeated impacts can cause a depression in the coating surface, which creates stresses at the outer ring of the depression, as shown in Figure 2.22. Further impacts on the already stressed section of the material will lead to the tensile stress accumulating to a magnitude which is greater than that of the ultimate tensile stress for the material, the material will begin to crack. With continued impacts on a cracked surface, the crack will deepen and grow. If multiple cracks have formed in close proximity, they can combine and fracture resulting in material detaching from the surface of the blade. This follows the stages of fatigue failure: initiation, propagation, and fracture.

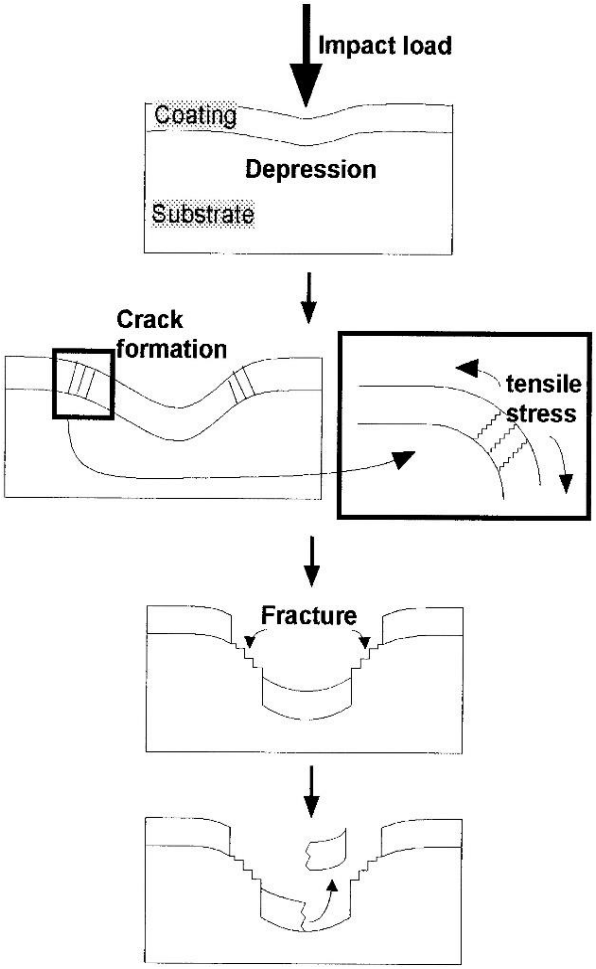

Figure 2.22: Fatigue Erosion Mechanism. [46]

2.4.3. Erosion Patterns

Erosion is a gradual process which develops over time. Over this period of time, several stages of the erosion process are identifiable. Figure 2.23, Figure 2.25 & Figure 2.24 show photographs of wind turbine blades which have suffered from erosion damage. Figure 2.23 displays the initiation of the erosion damage where small pits develop along the leading edge of the blade. These small pits then deepen and coalesce to form larger eroded patches as shown in Figure 2.24. The larger patches further erode until the protective coating has been completely removed from the blade's leading edge, the erosion damage then starts to attack the blade structural material as shown in Figure 2.25.

Figure 2.23: Small Pits Form [47]

Figure 2.24: Pits Join and Deepen [47]

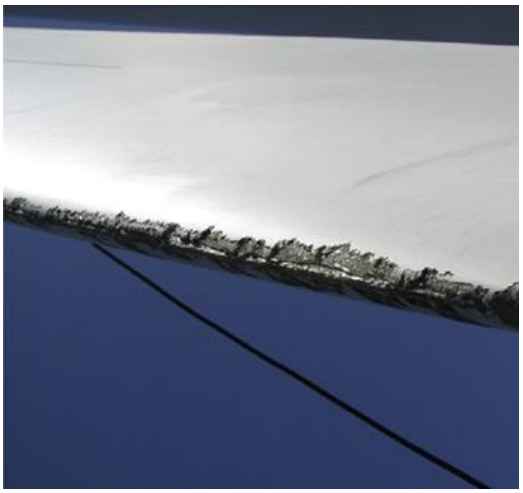

Figure 2.25: Exposure of the Blade Structure Material. [47]

In a study by Gaudern [48], blade inspection reports and blade photographs from operational wind turbines were investigated to search for any correlation in the patterns of wear on the leading edge of the blades. Five categories of

wear were identified and are shown in Figure 2.26, with Figure 2.27 displaying the average depth and size of each category.

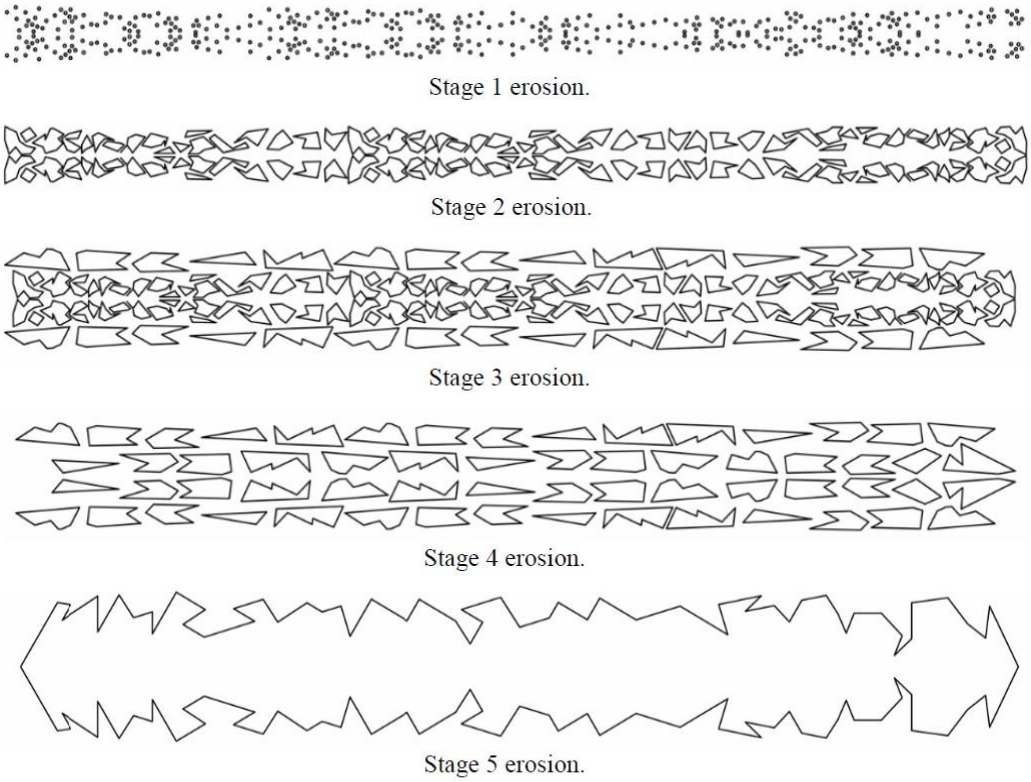

Figure 2.26: Erosion Stages Designed from Photographic Data of Erosion Progression. [48]

Erosion pattern	Erosion depth (mm)	Average feature diameter (mm)	Approx. % chord coverage
1	0.1-0.2	2	3
2	0.1-0.2	15	3
3	0.3-0.5	20/40	5
4	0.5-0.8	40	5
5	0.8-1.2	>500	8

Figure 2.27: Erosion Categories Average Feature Dimensions. [48]

Gaudern showed that as the erosion develops further, the depth and area of the eroded sections grow. Firstly small, scattered pinholes evolve which then develop into pinholes that have coalesced creating small, eroded patches. Then, the small patches coalesce generating a larger eroded patch with an

increase in depth. The larger patches then combine into a large area where the coating has been entirely removed. Figure 2.28 shows the typical erosion stages which were generated by this study. Figure 2.26 is a predicted erosion pattern at each stage and was developed using real-world wear and erosion data from Vestas's wind turbines that have been operating for up to five years.

As part of this study, tests were performed in a wind tunnel where a section of blade was placed within the wind flow path. Measurements of lift and drag were taken as the angle of attack of the blade section was varied. Firstly, measurements were taken where there was no erosion damage on the blade section. Then, the erosion patterns identified, as in Figure 2.26, were imprinted onto the blade section to mimic erosion damage. Measurements were taken at each erosion stage, and it was found that as erosion progresses a reduction in the coefficient of lift, by an average of 6%, and an increase in the coefficient of drag, by an average of 86%, was observed [48]. This erosion damage is reflected by a reduction in the annual energy production (AEP), as discussed by Herring et al. , where only a small amount of erosion can cause a reduction of 3-5% in the AEP.

Erosion category	Description
1	Small pin-holes of missing paint distributed across LE with some grouping
2	Pin-holes have coalesced in to larger eroded patches
3	Affected area has increased, with isolated larger patches with a greater depth
4	Patches have coalesced further and depth has increased
5	Large areas of LE laminate exposed

Figure 2.28: Erosion Categories Derived from Blade Reports and Photographs. [48]

2.4.4. Incubation Period

During erosive conditions, before any form of erosion damage occurs, there is a distinct period where no erosion damage is observable, to the naked eye the blade's surface remains practically unaltered. This is defined as the incubation period. O'Carroll et al. note that during the incubation period the impacting rain droplets create depressions on the blade's surface, gradually increasing the blade's surface roughness until the build-up of stress due to the depressions

begin to crack and fatigue the surface [49]. Figure 2.29 illustrates the incubation period on a plot of mass loss versus the number of impacting water droplets.

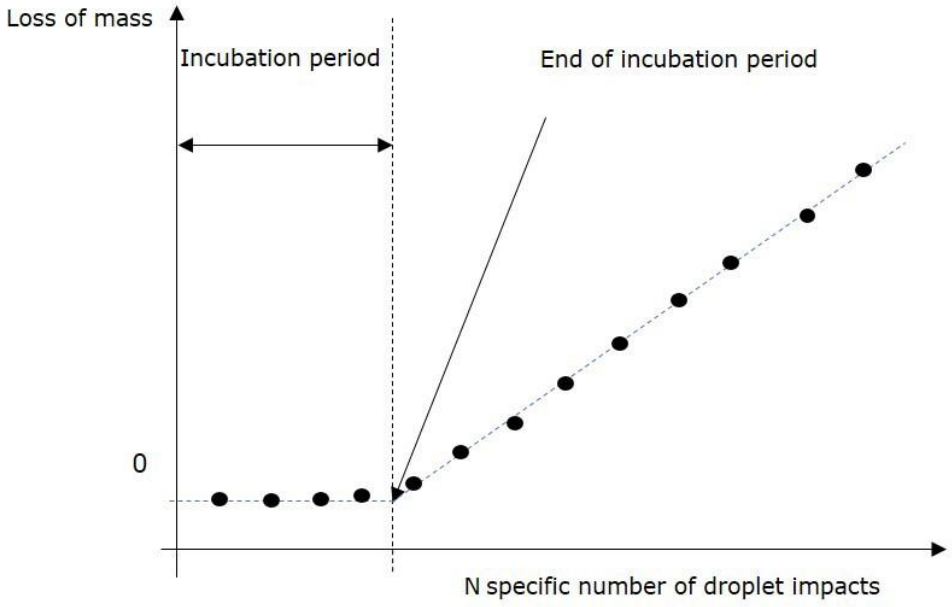

Figure 2.29: Erosion Test, Showing the Incubation Period. [50]

The incubation period is measured either visually, by looking for any pits which have formed on the surface, resulting in material loss, or by weighing the sample to identify any mass loss. During the incubation period the mass of the sample will remain constant. When the sample begins to lose mass, the incubation period has ended and an increase in mass loss will be detectable, as shown in Figure 2.29. The erosion rate can then be calculated as the amount of mass lost over time.

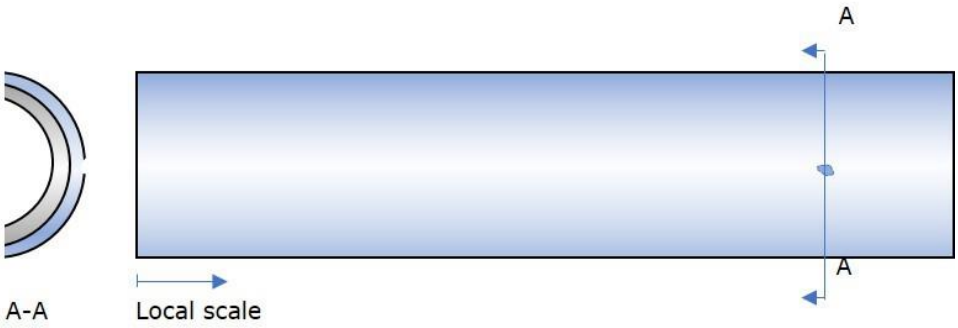

Figure 2.30: Test Sample - End of Incubation Period. [50]

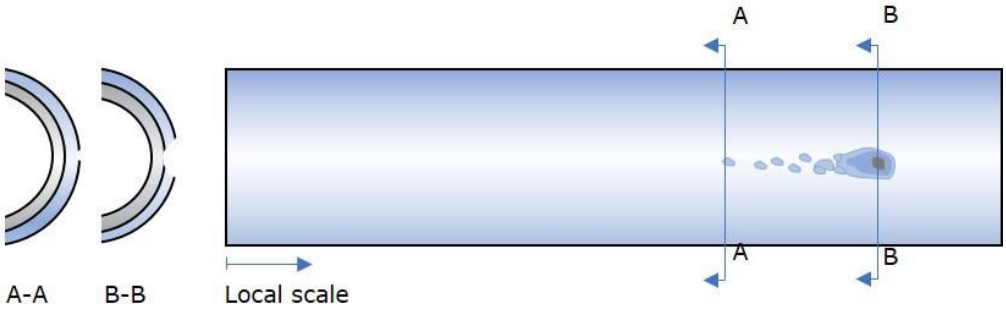

Figure 2.31: Test Sample - Breakthrough to Substrate. [50]

Figure 2.30 shows the initiation of erosion damage at A-A. Once this damage is observed or measured, the incubation period is over. The erosion damage will then progress, leading to further mass loss and deeper and wider pits until the coating has been entirely removed leaving the substrate exposed as shown in Figure 2.31 at B-B.

Figure 2.31 shows section A-A moving down the sample, initiating erosion damage towards the direction of the blade root. Erosion damage is first observed towards the blade tip, due to the higher rotational velocity, resulting in a higher impact velocity for the rain droplets. Blade sections which experience lower impact velocities from the rain droplets will still see erosion damage, but at a slower rate, provided the impact velocity is higher than the damage threshold velocity (DTV).

2.4.5. Erosion Assessment

Typically, wind turbine blade erosion is measured, in-situ, by visual methods. A team of technicians would climb a turbine and rappel down each blade, checking for visual signs of damage such as large pits, cracks and delaminations, recoding each by taking photographs. More recently, drones have been used to conduct a visual check on the blade, removing the requirement for climbing technicians. However, this method of inspection negates any damage which cannot be seen by the naked eye, in turn, vastly reducing the effectiveness of this inspection method. As previously mentioned, erosion begins as small pits and then develops into larger, collated pits which then become observable to the naked eye as the blade reaches active erosion. As discussed by Mishnaevsky et al. [51], these visual assessments only offer an observation, which is typically recorded at low resolution, where no direct link to the damage formation can be concluded. This visual assessment of erosion is qualitative in that there is no definitive measure, only an estimation of conditions.

At the laboratory scale, erosion is assessed by both a visual check and by measuring the mass of the test sample, allowing for mass loss to be calculated. Mass loss, over a period of rain erosion test time or per number of rain droplet impacts, is the main method of erosion assessment. However, mass loss is only an effective measure once the test sample has reached active erosion. During the incubation period, there is no observable mass loss and therefore any damage which is initiated during this phase goes undetected.

Furthermore, analytical techniques such as x-ray computed tomography (XCT) and dynamic mechanical thermal analysis (DMTA) are beginning to be used within research laboratories to investigate the effects of erosion. An XCT analysis study by Fæster et al. [52] has shown the effect of bubbles within the coating system layers. The study found that a greater presence of bubbles within the coating system aligns with a reduced RET performance during accelerated testing. The bubbles detected were shown to act as initiation sites for cracks to form within the coating layers, leading to erosion development.

The negative effect of bubbles or voids in the coating system layers is also found in an XCT study by Katsivalis et al. [53] where the voids are shown to act as stress concentrations, in turn increasing crack propagation. Katsivalis et al also conducted a DMTA study which showed that the polymeric coatings tested all followed a similar behaviour where at low temperatures in the glassy region the storage modulus was highest. Then, during the glass transition region at increased temperature, the highest loss modulus was recorded, as was the highest tan δ value. As the temperature further increased and entered the rubbery region, the values for storage modulus, loss modulus and tan δ all decreased. However, this DMTA study was only conducted on virgin materials, no eroded materials were used. Therefore, the effect of any erosion on storage and loss moduli remains unknown.

Additionally, nano-indentation has also been used to investigate changes in mechanical properties due to erosion. A study by O'Carroll et al. [49] showed that viscoelasticity can be assessed using the nano-indentation technique, by fitting of a spring and dashpot model. The authors suggest that nano-indentation can be used to evaluate rain erosion performance, by using the data for the creation of numerical models.

2.5. Accelerated Testing of Wind Blade Coating Systems

The testing and validation of wind turbine blade coating systems is an accelerated process conducted within a laboratory setting in accordance with an industrial code of practice or standard. The practicality of real world testing to validate every coating system would simply take too long, considering wind turbine blades are designed to last for 25 years. Therefore, several methods have been developed to speed up and mimic the natural environmental degradation of the coating systems which concentrate on erosion from rain droplet impacts and effects from weathering.

2.5.1. Rain Erosion Test Rig Types

Several accelerated rain erosion test rig designs have been developed over the years, all stemming from two main design types. The most common rig types are detailed below.

2.5.1.1. Water Jet

The water jet type erosion rig consists of a constant jet of high pressure water which is fired at a disk. The disk has pre-cut holes, to allow water to pass through, and the disk is rotated. The rotation of the disk allows only small segments of water to pass though the disk, which are then fired at the sample as shown in Figure 2.32.

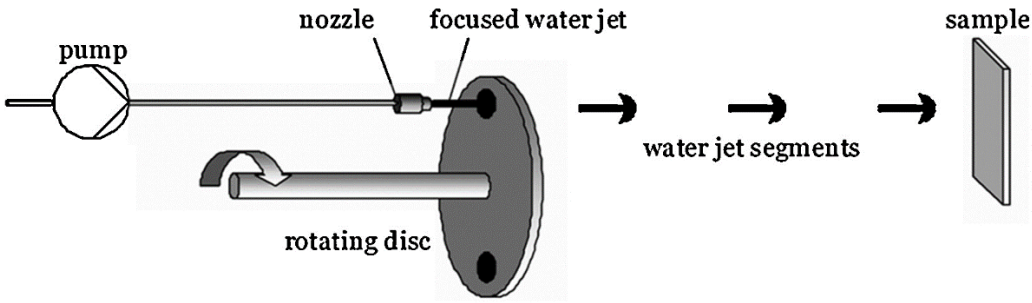

Figure 2.32: Water Jet Type Erosion Rig Schematic. Adapted from [54]

Within the water jet testing setup, the sample is fixed in location. The pressure of the water jet and the rotational speed of the disk can be altered to allow variations to be made on the water segments that strike the sample.

2.5.1.2. Whirling Arm

The whirling arm type erosion rig uses a radially distributed grid of needles which face downwards. These needles are used to create water droplets, as shown in Figure 2.33.

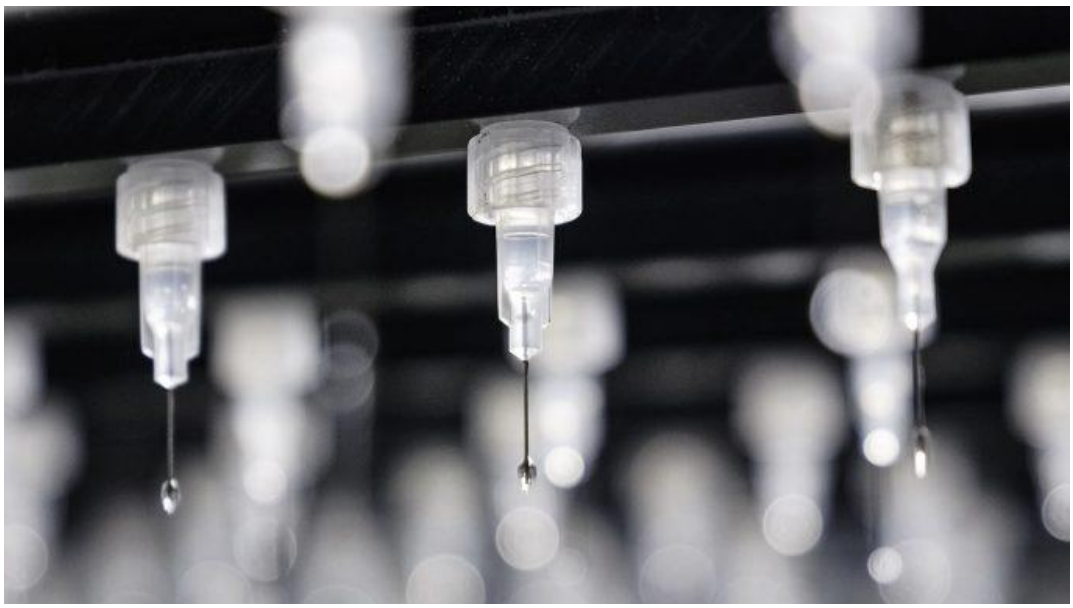

Figure 2.33: Close-Up Photograph of Droplet Formation on Needles on R&D A/S Rain Erosion Rig. [55]

Below the grid of droplet creating needles sits the rotating arms which the test samples are mounted to. The rotating arms and the grid of needles are shown in Figure 2.34. During testing, the rotating arms spin and strike the water droplets created by the needles, simulating leading edge strikes of a turbine blade. The rotating arms are controlled via a central motor, much like a helicopter blade, where the rotational speed of the arms is set. Additionally, the droplet flow rate from the needles can be adjusted via the water pressure and the water droplet size can be altered by changing the needle size.

Figure 2.34: Photograph of R&D A/S Whirling Arm Type Rain Erosion Rig. [55]

2.5.2. Weathering Test Rig Types

There are various methods of accelerated weathering, and therefore, various types of weathering testing equipment. Looking specifically at equipment used for the testing of coating systems used for wind turbine blades, several methods are detailed below.

2.5.2.1. Ultraviolet (UV)

Ultraviolet weathering is usually split into two sub categories depending what type of test is required, these are UVa and UVb. The UVa test uses a 340 nm UV lamp and the UVb test uses a 313 nm UV lamp, each focusing in on a different testing zone of the electromagnetic spectrum. The UVa band of the electromagnetic spectrum is at 315 nm to 400 nm and the UVa band is at 280 nm to 315 nm.

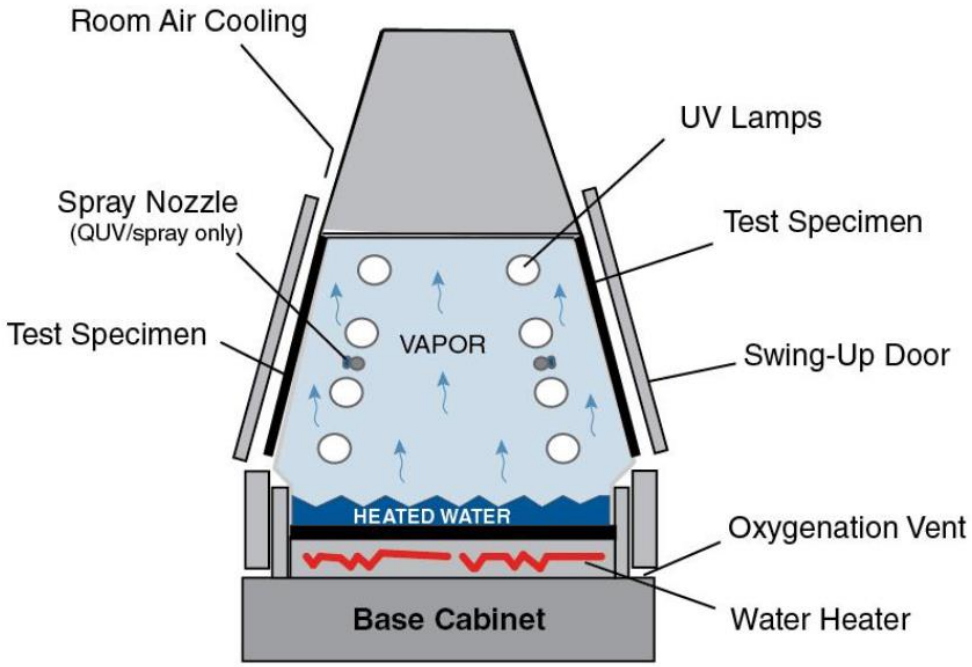

Figure 2.35: Schematic of an Accelerated Ultraviolet Weathering Cabinet, QUV. [56]

Shown in Figure 2.35 is the setup of a typical accelerated ultraviolet test. Specimens are placed in the angled holders at the sides of the cabinet, where they are exposed to ultraviolet light from the lamps as well as water, either from a direct spray or as condensation. The temperature of the cabinet is controlled using a water heater at the base.

The accelerated ultraviolet cabinets are relatively small in size, 0.5m wide, 1.4m high and 1.4m long, and can be stacked, allowing for multiple cabinets to be run at the same time in the same location.

2.5.2.2. Xenon-Arc

The Xenon-Arc testing chamber, also known as a weatherometer, is show in Figure 2.36.

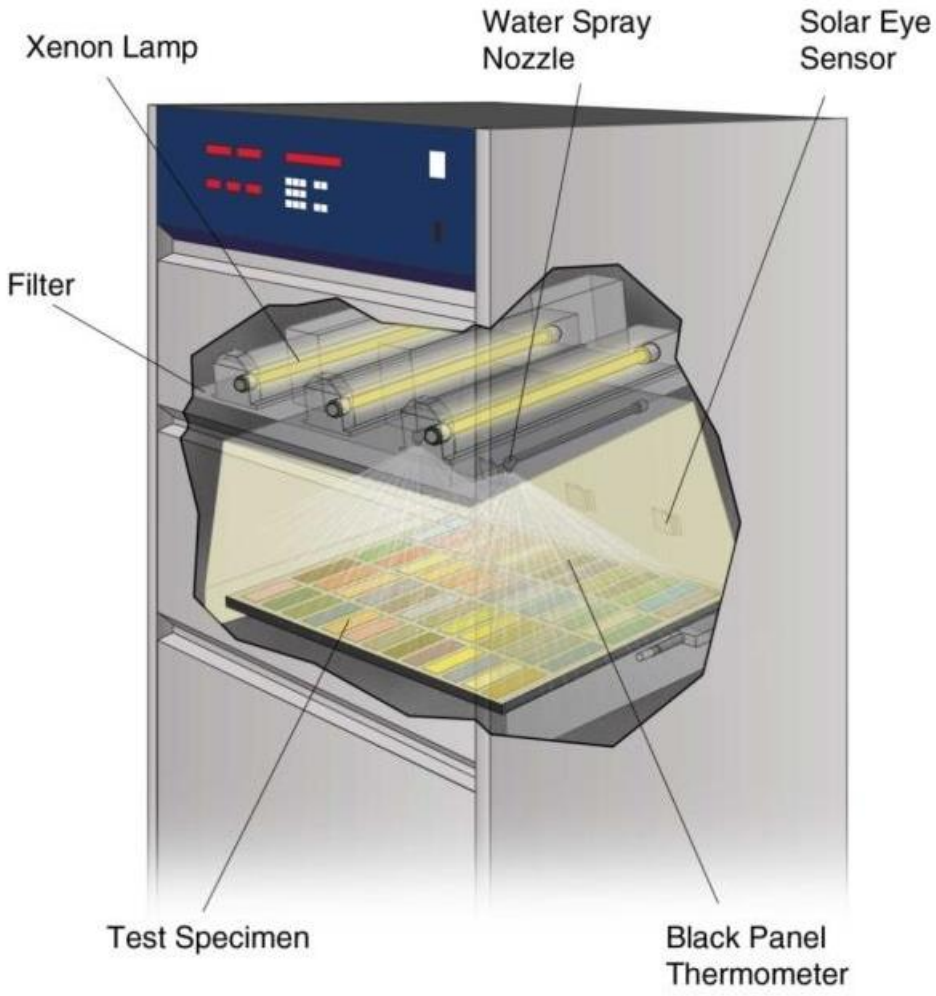

Figure 2.36: Schematic of a Xenon-Arc Weathering Chamber, Q-SUN. [56]

The Xenon-Arc chamber uses two regions of the electromagnetic spectrum for testing. A broadband at 300nm to 400 nm and a narrowband focusing at 340 nm. This allows the Xenon-Arc test to better reflect real world conditions, where sunlight would cause irradiance over a range of wavelengths.

The typical setup of a Xenon-Arc test chamber has the specimens laid flat underneath the lamps and water spray nozzles. There is no condensation functionality with the Xenon-Arc test. The weatherometers come in a range of sizes, though are typically larger than the ultraviolet testers.

2.6. Testing Standards for Wind Blade Coating Systems

There are several, industrially accepted, testing standards for wind turbine blade coating systems to be validated against, namely:

- International Organisation for Standardisation - IPD ISO/TS 19392 [2]–[4]
- DNV - DNVGL-RP-0171[50]
- ASTM International - ASTM G73-10 [57]

These standards, listed above, provide detailed guidance on the best practice associated with testing and validating the performance of wind turbine blade coating systems. They describe test methodology and apparatus used, specimen material type and specimen geometry, and other key factors such as test rig calibration, inspection and evaluation, and how to produce the resultant test report.

One of the key factors with the testing standards which is most relevant to this piece of work is that of weathering. In the International Organisation for Standardisation's technical specifications IPD ISO/TS 19392 [2]–[4], consideration has been given to the effect of weathering on a wind blade coating system. Similarly, weathering is included with a general LEP test program in DNV-RP-0573 [58]. However, the weathering testing and rain erosion testing are considered as two distinct, separate processes. There is one test to assess the weathering performance of the coating system, [2], and another to assess the rain erosion performance of the coating system, for rotating-arm type rigs [3], and for water-jet type rigs [4]. There is no overlap between the weathering and rain erosion tests, and minimal consideration given to the effect(s) that weathering could have on the rain erosion performance of a coating system.

In DNV's recommended practice DNVGL-RP-0171 [50], there is no detailed guidance on how to test for weathering of wind blade coating systems. The recommended practice mentions accelerated ageing, though it is considered

an optional additional test and not part of the core test programme for testing and validating wind blade coating systems.

The ASTM International test methodology ASTM G73-10 [57] does not mention weathering or accelerating ageing in any form. There is a separate ASTM International standard practice for Natural Weathering of materials [59], however, this a more generic standard practice and is not linked to wind turbine blade coating systems testing.

Current testing standards treat weathering and rain impact erosion as two separate processes that occur independently of each other. There is no consideration given to repeated phases of weathering and rain exposure. Whereas in the operational environment of a wind turbine, weathering and rain occur both simultaneously and individually and are interlinked.

2.7. Industrial Blade Erosion Research

There are several industry focused research groups who are looking at the problem of rain erosion on wind turbine blades at the time of writing. The key international efforts are noted as:

Fraunhofer IWES - Fraunhofer is a German research organisation which has multiple topic specific subdivisions, including the Institute for Wind Energy Systems (IWES). At IWES, the issue of blade erosion is a topic of interest, they have an ongoing project named BeLeB [60]. This project looks at methods for determining the service life of blade coatings [61] as well as investigating effective prevention of rain erosion on wind turbine blades. One of the aims for the BeLeB project is to contribute to the development of reliable forecasting models for erosion damage and to apply them to turbine operation.

EIROS - EIROS (Erosion and Ice Resistant Composites for Severe operating condition) is a Horizon 2020 funded project consisting of a multidisciplinary team, the project is led by TWI Ltd, Cambridge, UK. The EIROS project also considers cryogenic tanks, automotive components, aerospace wings as well as wind turbine blades. The project is looking at novel materials that can be

used to reduce the impact of ice and erosion on the performance of wind turbine blades [62].

EROSION - The EROSION project is led by the Technical University of Denmark, DTU, with partners from around Europe. The aim of this project is to implement a control strategy to combat rain erosion by reducing the tip speed of the blade during conditions that are deemed too likely to erode the blade. This is then expected to increase the lifetime of the blades along with reducing the operations and maintenance costs [63].

BLEEP - The BLEEP project is run by ORE Catapult and looks at erosion damage from an operator's point of view, aiming to quantify the impact of erosion damage on the annual energy production. The project also looks at inspection methods for wind turbine blades including the development of a classification system for erosion damage [64].

Sandia National Laboratories - Sandia National Laboratories are funded by the US Department of Energy and they work on a variety of energy technologies. They have a project looking at leading edge erosion and the effect of dirt and insects of the aerodynamic performance of wind turbines. The project aims to characterise roughness and roughness effects and the impact on annual energy production [65].

COBRA Project – The COBRA project, managed by DNVGL, is a joint industry project set up to investigate damage caused by rain and hail to the leading edge of wind turbine blades and to determine methods for blade protection. The aim of the project is to develop a recommended practice for erosion protection system design [66].

IEA Wind Task 46 – The International Energy Agency (IEA) host collaborative research projects across the whole energy sector. Task 46 specifically focuses on erosion of wind turbine blades. Contributors come from both academia and industry and consist of 25 organisations from 10 countries [67]. The main aim of Task 46 is to develop a better understanding of the technical challenges associated with wind blade erosion.

Current industrial research activity around the blade erosion problem considers the wider effect of erosion on the likes of annual energy production and control schemes to reduce erosive conditions. However, there are no industrial projects focusing on the understanding of how erosion initiates and develops, looking at the erosion mechanism, and considering the applications to erosion quantification and classification. Furthermore, no industrial projects are currently looking at the effects of weathering on wind turbine blade degradation, yet alone the combined effect of both rain erosion and weathering.

2.8. Industrial Coating Manufacturers

Some of the leading industrial coating manufacturers, who develop and create coatings for leading edge protection on wind turbine blades are listed in Table 1. Most manufacturers develop full blade coating systems which include base coats, primers, topcoats, and leading-edge protection coatings.

Manufacturer/Company	**Product**	**Description**
3M	W8750	Polyurethane Tape
Aerox	AROLEP	Polyurethane Paint
AkzoNobel	RELEST	Blade Protection System
Belzona	5721	Blade Protection System
Hempel	Hempablade Edge	Blade Protection System
Jotun	Jotatop	Polyurethane Paint

Mankiewicz	ALEXIT	Blade Protection System
Polytech	ELLE	Polyurethane Shield
Teknos	TEKNODUR	Blade Protection System

Table 1: Short Summary of Available Industrial Coatings and Coating Systems.

2.9. Summary

The literature review and background information study has identified a gap in knowledge regarding weathering testing as well as the combined rain erosion and weathering testing of wind turbine blade coating systems.

Additionally, current widely used methods of erosion assessment are qualitative, with laboratory techniques unable to be employed on an in-situ wind turbine blade, due to scale. There is a requirement for improved assessment and quantification of erosion on wind turbine blades, which will allow for greater certainty over maintenance and repairs. Additionally, the assessment of weathering on wind turbine blade coating systems is still in it's infancy, with no published work available at the time of writing. However, it is understood that research has been conducted within this area and not published due to commercial sensitivity. The combined effects of weathering and erosion, conducted as an integrated test campaign, as undertaken within this study, is the key novelty to this work.

Chapter 3 - Foundation for Rain Erosion and Weathering Experimentation

The rationale for undertaking research into the rain erosion and weathering problem is firstly outlined in this chapter. This chapter then outlines the analytical techniques used within the experimentation and evaluation of rain erosion and weathering testing within this work. The final section of this chapter goes on to detail how the test specimens used within this work were prepared and manufactured.

3.1. Research Requirement

As highlighted in the previous chapter, Literature Review, Chapter 2, there is a gap in knowledge with regards to firstly, quantitative assessment of rain erosion and then secondly, the effects of weathering and combined rain and weathering on wind turbine blade coating systems. This work goes some way to addressing these knowledge gaps by firstly applying a novel, quantitative methodology for erosion assessment and then combining this with a quantitative weathering degradation study. The initial studies provide baseline assessments for both rain erosion and weathering degradation. Then, the final study combines both rain erosion and weathering degradation to explore the influence of each on wind turbine blade coating systems.

3.2. Analysis Methodologies

Several methods of assessing rain erosion have been widely used within academia and industry and are well documented, as discussed in Chapter 2, Section 2.4.5. These include visual assessments, which offer a qualitative indication of erosion, though they cannot quantify erosion. Mass loss

measurements, which can quantify erosion on a laboratory scale, however, only after the test specimen has eroded beyond the incubation period.

Within this work, greater detail is required to understand the mechanisms of degradation and to allow quantification of damage throughout the work packages. The analysis methodologies used herein are detailed in the following subsections. In addition to the techniques detailed below, other more common methodologies were also used such as visual assessment using photographs, microstructure assessment using optical microscopy and mass loss measurement using a mass balance.

3.2.1. Dynamic Mechanical Analysis (DMA)

Dynamic mechanical analysis was used to provide an understanding of changes in the viscoelastic properties of the coating system as the test specimens progressed through rain erosion test stages.

DMA offers a variety of test clamp types, such as compression, tension, shear, 3-point bend and cantilever. Furthermore, DMA provides several test modes, such as constant strain (isostrain) in which the applied strain is held constant where the temperature can be controlled, multi-frequency which applies a controlled sinusoidal stress at various frequencies, creep stress which applies a stress for a fixed period of time and then measures the effects when the controlled stress is removed, multi-stress which varies the applied stress and holds temperature and frequency constant and controlled force which ramps the applied stress at a constant rate.

Within this work, a dual-cantilever clamp with a multi-frequency test mode was used. Initially, a 3-point bend clamp was used as this clamp type requires no clamping on the specimen, however, during testing specimens fell out of the clamp at the higher frequencies. Therefore, the dual-cantilever clamp was selected to secure the specimens in place. The dual-cantilever clamp held the specimen in place by a static clamp at either end, as shown in Figure 3.1, with the central clamp moving according to the test mode selected.

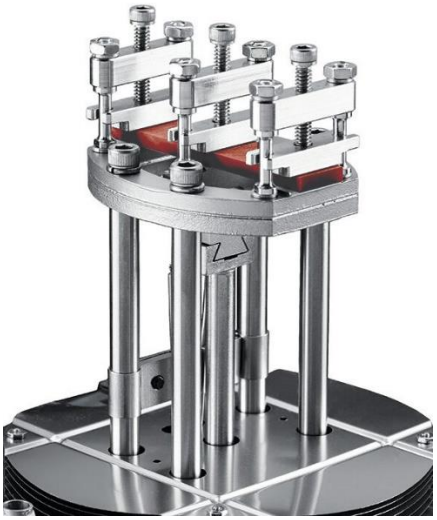

Figure 3.1: DMA Dual-Cantilever Clamp Type [68]

A multi-frequency test mode was selected as this offered multiple test frequencies to mimic the variation of impacting rain droplets on a wind turbine blade. The multi-frequency mode also allows the assessment of viscoelastic properties, such as the loss modulus, storage modulus and tangent of delta at the varying test frequencies. However, it is acknowledged that the test frequencies do not match that of rain droplet impacts on wind turbine blades, impacting rain droplets occur at much higher frequencies, which are limited by current testing equipment, as discussed by Ouachan et al. [69].

Within viscoelastic materials analysis, the storage modulus represents the materials ability to store energy, representing the elastic fraction and the loss modulus represents the materials ability to dissipate energy, usually as heat, representing the viscous fraction. The tangent of delta, tan δ, represents the phase lag between an impact force and the resultant force that reached the body of the material. tan δ is a good measure of a materials capability to absorb and disperse energy. tan δ is the relationship between the loss modulus, E'', and storage modulus, E', as shown in Equation 4.4.

$$\tan\delta = \frac{E''}{E'}$$ Equation 4.4

DMA testing allows for the viscoelastic effects of the coating systems to be analysed throughout various stages of erosion and combined erosion and weathering. The dual-cantilever clamp allows the specimens to be tested securely in the DMA whilst the multi-frequency test mode provides a range of test frequencies while holding temperature and stress constant.

The main drawback with using DMA within this work is that the coating system cannot be isolated from the composite substrate. This means that all the DMA results show a compound effect of the coating system and the substrate. As the substrate is a rigid polymer composite, this would tend to dominate any measurements and make any small changes due to erosion more difficult to detect.

3.2.2. Gloss Measurement

Gloss was used to measure changes in the coating system surface for both rain erosion and weathering. Gloss is measured using a glossmeter, which is a handheld device. The working principle of a glossmeter is based upon a beam of light which is cast on a surface, at a known angle from the normal. The specular reflection of the light beam is then captured by the glossmeter where the intensity and quantity of light at the detector are measured, shown in Figure 1. Gloss is quantified by Gloss Units (GU). Gloss Units range from a scale of 0GU—where the surface is fully matt, to 100GU—where the surface is a perfect mirror.

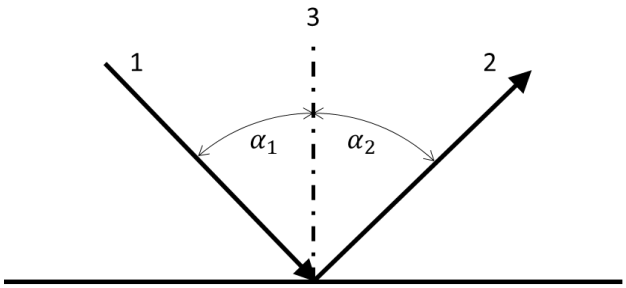

Figure 3.2: Gloss - Spectral Reflectance

The angle of measurement for gloss is also an important parameter to consider. Typically, for plastic materials, angles of 20°, 60°, and 85° are used as denoted by BS EN ISO 2813:2014 [70]. The angles refer to the incident angle of the beam of light, where in Figure 3.2, line 1 with angle α_1 is the incident angle and line 2 with angle α_2 is the specular reflection, which for a perfectly smooth surface is always the same as the incident angle, $\alpha_1 = \alpha_2$ for specular reflectance. Line 3 is the normal line, a perpendicular line to the measured surface.

The intensity of the specular reflection is dependent on the surface which the beam is reflected off. If the surface is smooth and uniform, a high quantity of the incident beam is reflected as the specular reflectance and has a low diffuse reflectance as shown in Figure 3.3(a). If the surface is uneven or has an irregular or unsmooth pattern, the amount of the incident beam reflected as specular reflection is low and there is a high diffuse reflectance as in Figure 3.3(b).

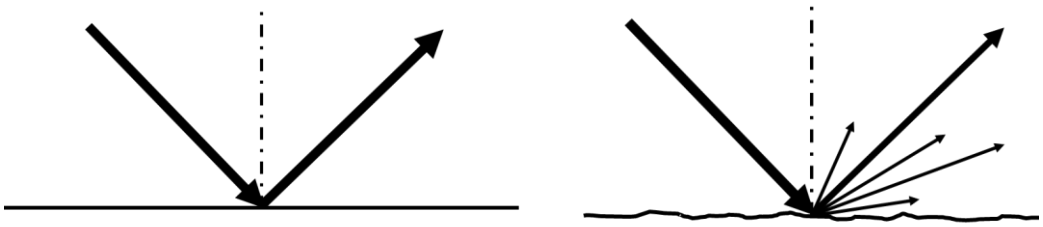

(a) (b)

Figure 3.3: Gloss - (a) Low Diffuse Reflectance; (b) High Diffuse Reflectance

The angle selected to measure gloss will influence the gloss measurement obtained. First, the perceived glossiness of the surface is obtained by a visual check. If the surface is matt, 85° is used. If the surface is mid gloss, 60° is used. If the surface is high gloss, 20° is used. Different angles give a larger usable range of gloss, as shown by the linear portions of Figure 3.4. Working within the linear region is particularly useful when measuring gloss over a range of time or conditions that will cause a change in the gloss value, as the linear region offers the greatest range of gloss units for the perceived surface glossiness. Similarly, the linear region allows for the greatest measurement accuracy due to the larger operational gloss unit range, the Y-axis on Figure 3.4, versus operating on the curved section. It is therefore important to select the appropriate angle when conducting a gloss analysis.

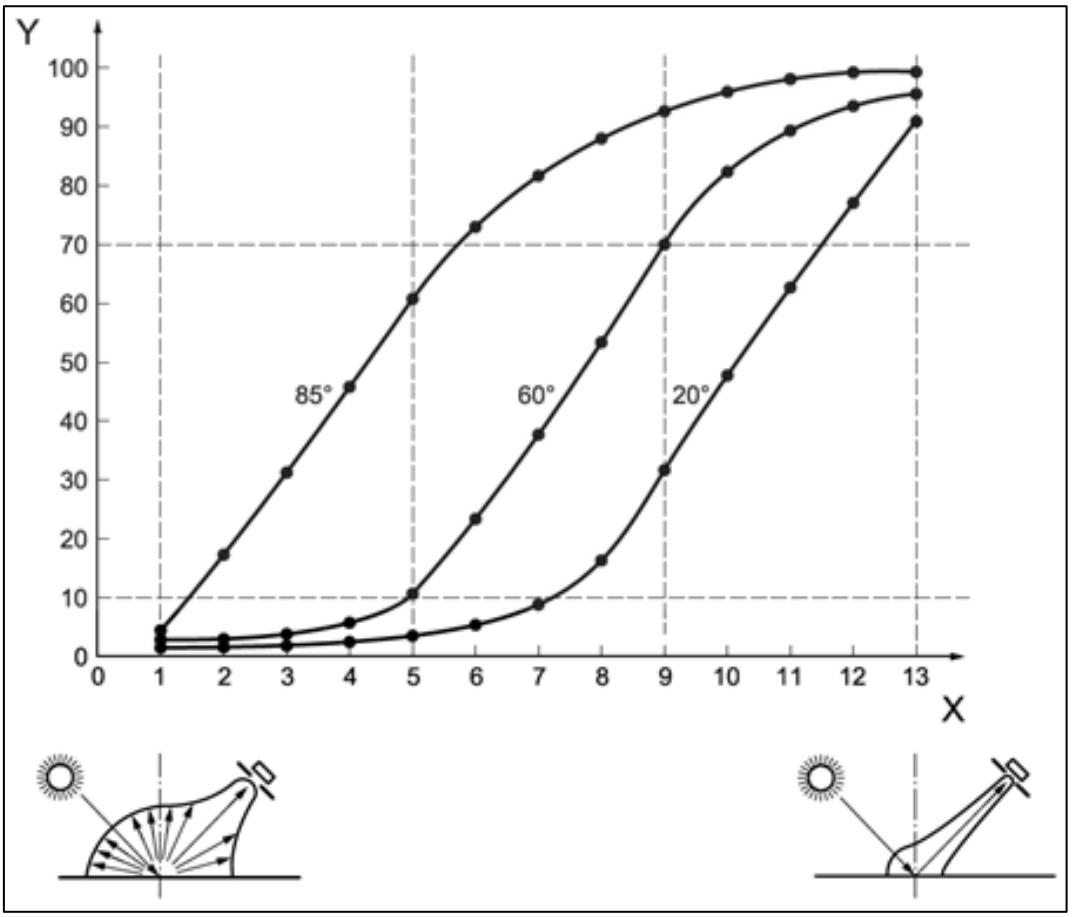

Figure 3.4: Gloss - Incident Angle for Gloss Measurement. Y-Axis Represents the Gloss Value. X-Axis Represents the Gloss Perception, From Matt to Glossy. [70]

For all gloss analysis within this work, 60° was selected as the measurement angle as this gives a wide range of values to be accurately measured. An angle of 20° would not be suitable to measure low gloss values and an angle of 85° would not be suitable to measure high gloss values. It is anticipated that a large range of gloss values will be detectable in both the rain erosion and weathering studies.

Gloss measurement is commonplace within weathering studies, however, no evidence within the literature was found for using gloss for erosion assessment.

3.2.3. Colour Measurement

Within this experimental assessment of a coatings' performance, the measurement of the coatings' surface colour plays an important role. Colour can indicate changes in the chemical structure of the coating, such as an increase in lightness could indicate a chalking effect. Colour measurement plays an important role in coating performance assessment is more than an aesthetic parameter. Several colour measurement methods and colour spaces exist, as therefore the methods and colour spaces used are described herein along with the impact of colour measurement on the overall coating performance.

3.2.3.1. CIELAB Colour Space

The CIELAB colour space is a three-dimensional measure of colour and is particularly useful to measure changes in colour. The CIELAB colour space compromises of three parameters, L^*, a^* & b^*, each representing a value of a particular colour. The L^* parameter represents the lightness of the measured sample, with $L^*=0$ representing black and $L^*=100$ representing pure white. The a^* parameter represents the position between red and green, where a negative a^* value indicates more green and a positive a^* value indicates more red. The b^* parameter represents the position between blue and yellow, where a negative b^* value indicates more blue and a positive b^* value indicates more yellow. The CIELAB colour space can be visualised, as shown in Figure 3.5.

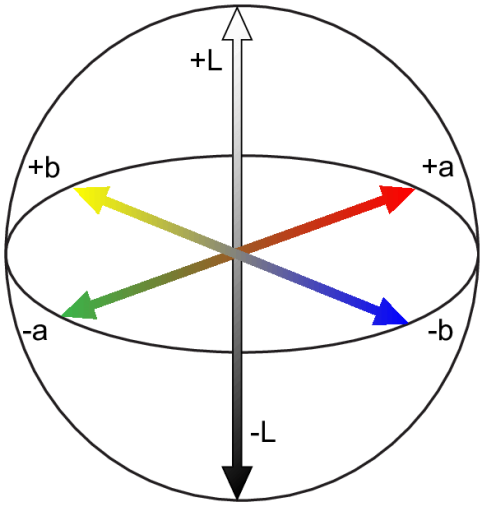

Figure 3.5: Visual 3D representation of CIELAB Colour Space. [71]

Each parameter can be used to provide an overall colour change value, ΔE^*, between two measured samples. The parameter, ΔE^*, can be calculated as in Equation 3.1, where the subscript 1, denotes the initial specimen measurement and subscript 2, denotes the specimen to be compared, as detailed in BS EN ISO/CIE 11664-4:2019 [72].

$$\Delta E^*_{ab} = \sqrt{(L^*_2 - L^*_1)^2 + (a^*_2 - a^*_1)^2 + (b^*_2 - b^*_1)^2} \quad \text{Equation 3.1}$$

3.2.3.2. Colour Spectrum Analysis

Another method of colour difference measurement is to directly compare the absorption spectra for each test specimen. Within the electromagnetic spectrum the visible light region exists between 400 nm and 700 nm. This region can be split into three broad colour subdivisions of red, green and blue. Red exists between 601 nm and 700nm, green between 501 nm and 600 nm and blue between 401 nm and 500 nm, as shown in Figure 3.6.

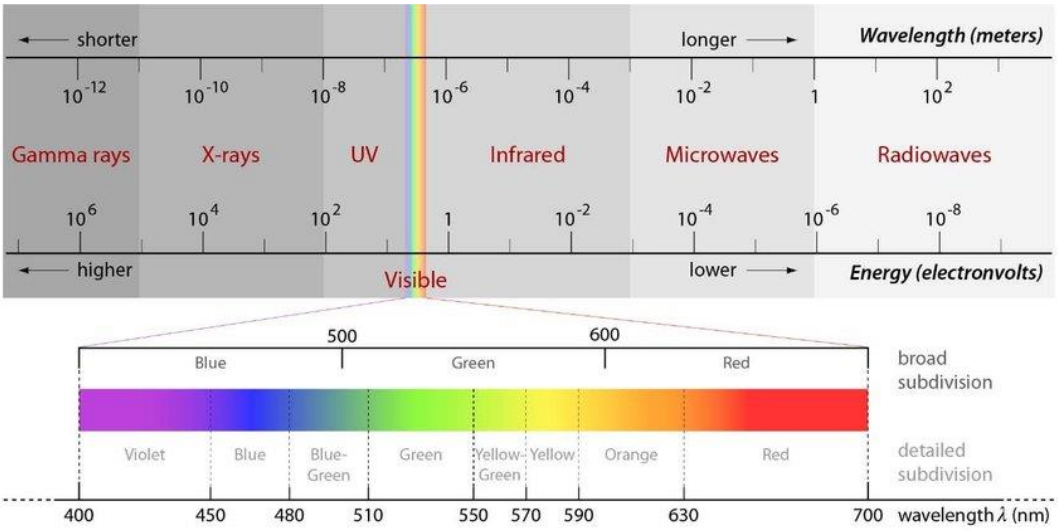

Figure 3.6: Visual Representation of the Electromagnetic Spectrum. [73]

Each subdivision can then be used as a colour parameter which then allows for a comparison between two, or more, test specimens. The colour difference, measured as the Euclidean distance, can be calculated as in Equation 3.2, where R, is the red subdivision, G, the green subdivision and B, the blue sub division, with subscripts 1 and 2 representing the initial and comparison specimens respectively.

$$Colour\ Difference = \sqrt{(R_2 - R_1)^2 + (G_2 - G_1))^2 + (B_2 - B_1))^2} \quad \text{Equation 3.2}$$

3.2.4. Fourier Transform Infrared Spectroscopy (FTIR)

Fourier transform infrared spectroscopy (FTIR) was used to gain an understanding of the chemical structure of the coating systems and how this changes due to accelerated weathering testing.

FTIR works by passing a beam of infra-red (IR) light through a sample, some of this light will be absorbed by the sample and some of the light will pass through the sample. The light which passes through the sample will reach a detector which measures the intensity of the transmitted light. A Fourier transform is then applied to the measured intensity signal which breaks the

signal down into its magnitude at individual wavenumbers. A wavenumber is the number of waves which occur over a unit distance, typically quantified in waves per centimetre, cm^{-1}. A typical infra-red spectrum displays the wavenumber on the x-axis and either transmittance or absorbance on the y-axis. Once you have obtained the spectrum of the sample, the spectrum can be analysed to identify the presence of particular chemical functional groups. Different chemical bonds will show on the spectrum at distinctive bands of wavenumber, for example a Carbon-Oxygen bond would show as a peak in the region of 1000 – 1300 cm^{-1} and an Oxygen-Hydrogen bond would show in the region of 2500 - 3300 cm^{-1}. Knowing the types of bonds which are present in a sample as well as their quantity, derived from the intensity, can allow for any changes in bond type and quantitatively to be investigated.

FTIR has four main operational modes, Transmission, Specular Reflection, Diffuse Reflection and Attenuated Total Reflection (ATR). For transmission, the IR beam must pass through the sample and as the coating system specimens are not transparent, this technique was not used. Diffuse Reflectance is typically used for powders and was therefore not used for this work. Specular reflectance is typically used for thin films and reflective surfaces and again was not used for this work. ATR can analyse solids and uses a crystal to pass the IR beam through to the sample. Different crystals can be used such as Germanium, Zinc Selenide and Diamond. For this work, ATR with a diamond crystal was selected as it has a wide spectral range, 100 to 25,000 cm^{-1}, and depth of penetration into the sample of up to 2µm. ATR requires contact with the sample to be analysed and can provide a quantitative analysis, providing the surface contact is repeatable.

3.2.5. Analysis summary

Several analytical methods have been identified for coating system investigation and quantification. The techniques selected allow parameters to be tracked throughout both the rain erosion and weathering degradation processes and offer a quantitative measurement at each stage. Past

techniques, such as visual observation alone, do not offer a quantitative measure of degradation. As such, the techniques selected can provide a greater understanding on the degradation process.

However, there are some limitations with the techniques selected. DMA cannot match the oscillating frequency to that of impacting rain droplets in a real world environment, without the aid of multiple DMA tests at various temperatures. Additionally, the test specimen size is heavily limited by DMA, the DMA can only accommodate a specimen up to 60mm long by 15mm wide and 7mm thick. For the glossmeter, the measurement zone is small, only a few millimetres square. Therefore, multiple measurements are required which are then averaged to provide an overall measurement. A single glossmeter measurement would not necessarily be representative of the specimen. Regarding FTIR, the diamond crystal used for ATR penetrates the surface up to 2µm, therefore, this will not provide a true surface measurement, rather a measurement of the top 2µm of specimen.

3.3. Specimen Manufacture and Preparation

This section details how test specimens were manufactured and prepared for testing. An in-depth material properties analysis at progressing stages of degradation due to erosion and weathering is crucial to this work, therefore it is imperative that the test specimens are made to the highest quality and there is uniformity across all test specimens.

Initially it was planned to use the composite sample form shown in Figure 3.7. The aerofoil shape of the sample, based on NACA 63_4-021, has been well characterised for droplet impact locations by previous research from Mackie [74], whilst using the rain erosion rig at the Energy Technology Centre, East Kilbride.

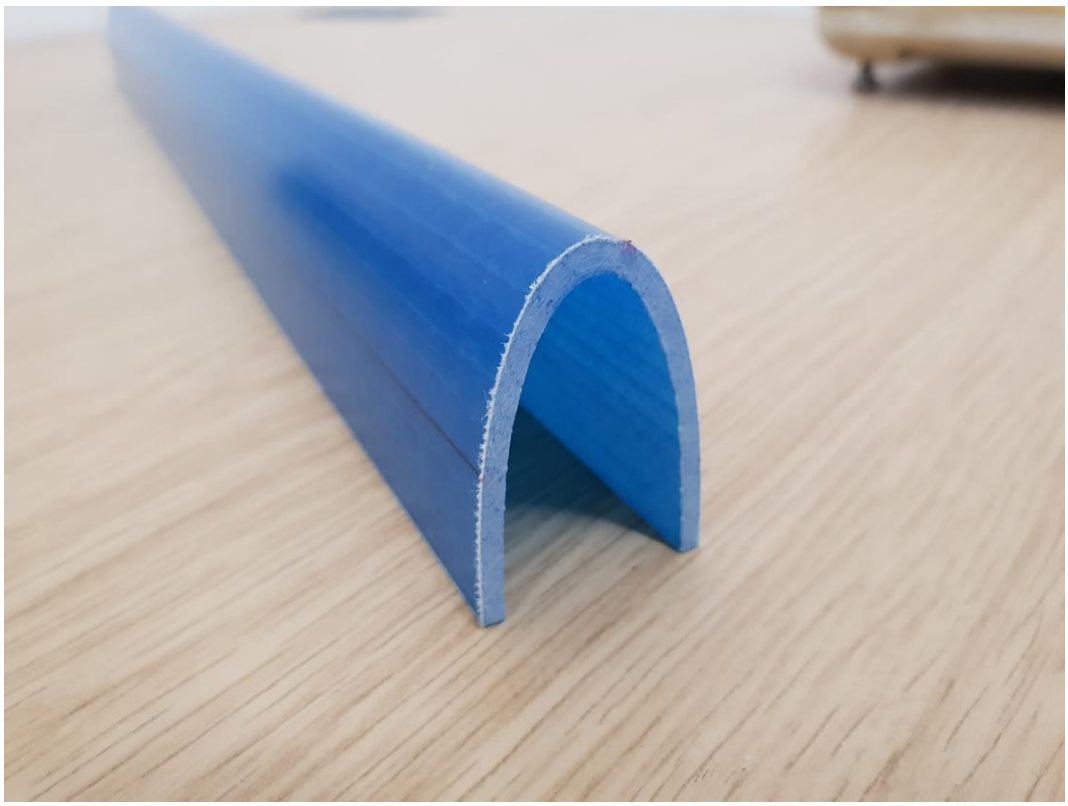

Figure 3.7: Aerofoil Section Used for Commercial Rain Erosion Testing

However, the curved nature of the aerofoil sample as well as the height of the sample pose restrictions when it came to laboratory analysis and material characterisation, particularly with Dynamic Mechanical Analysis technique as it requires a flat surface for the prepared sample. Therefore, the option of cutting the curved samples after the erosion exposure stages was considered, but discounted due to the induced heat and stresses that any cutting technique would have had on the sample which would render any results invalid due to external influences. A flat panel sample was adopted to eliminate any unnecessary manufacturing effects. Additionally, the combined weathering and RET tests required the test specimen to be compatible with both the accelerated rain erosion test rig and the accelerated weathering test rig. The accelerated weathering test rig types are only compatible with flat test specimens due to the geometry of the accelerated weathering chamber.

The flat panel was cut into sample pieces pre-degradation, see Figure 3.8 and Figure 3.9, and then fitted into a custom made flat sample holder at the accelerated rain erosion test house, see Figure 3.10.

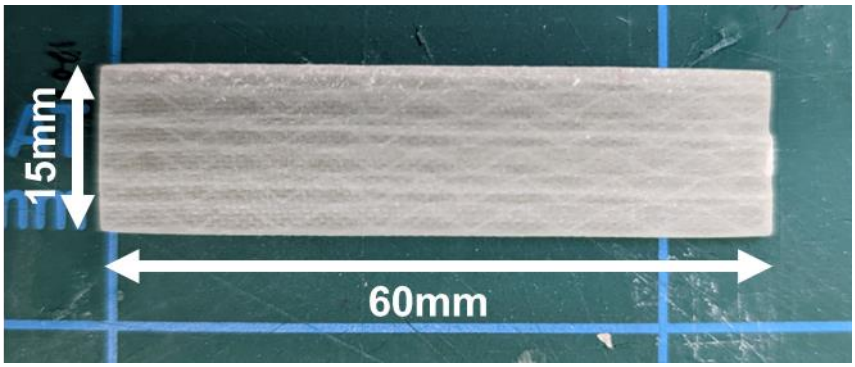

Figure 3.8: Plan View of Flat Specimen

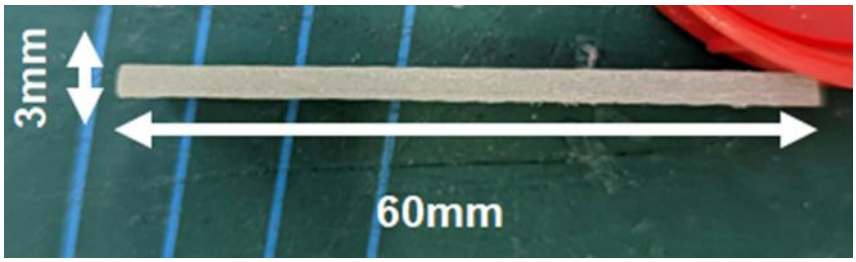

Figure 3.9: Front View of Flat Specimen

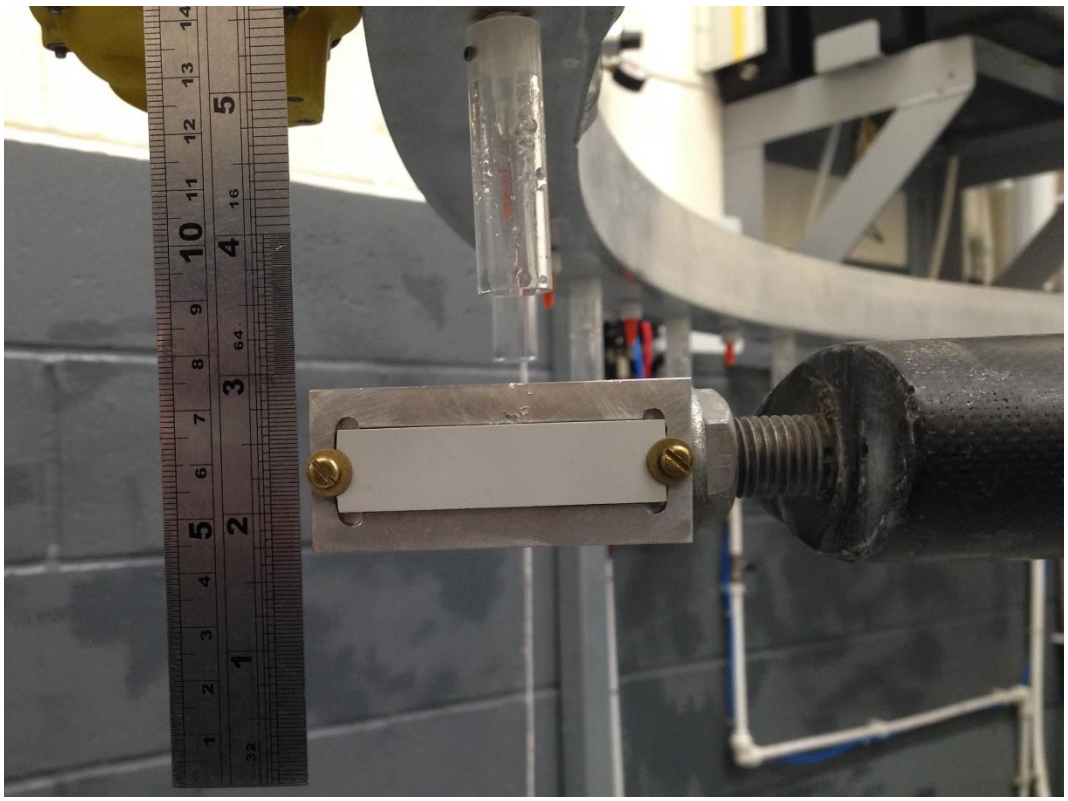

Figure 3.10: Flat Specimen Mounted in Test Rig

3.3.1. Specimen Substrate Manufacture

The composite panels were manufactured in the Composites Lab at the Offshore Renewable Energy Catapult, Blyth. Four images which give a general overview of the composite panel manufacturing process are displayed in Figure 3.11. All figures referred to in the specimen substrate manufacture section are located in Appendix A.

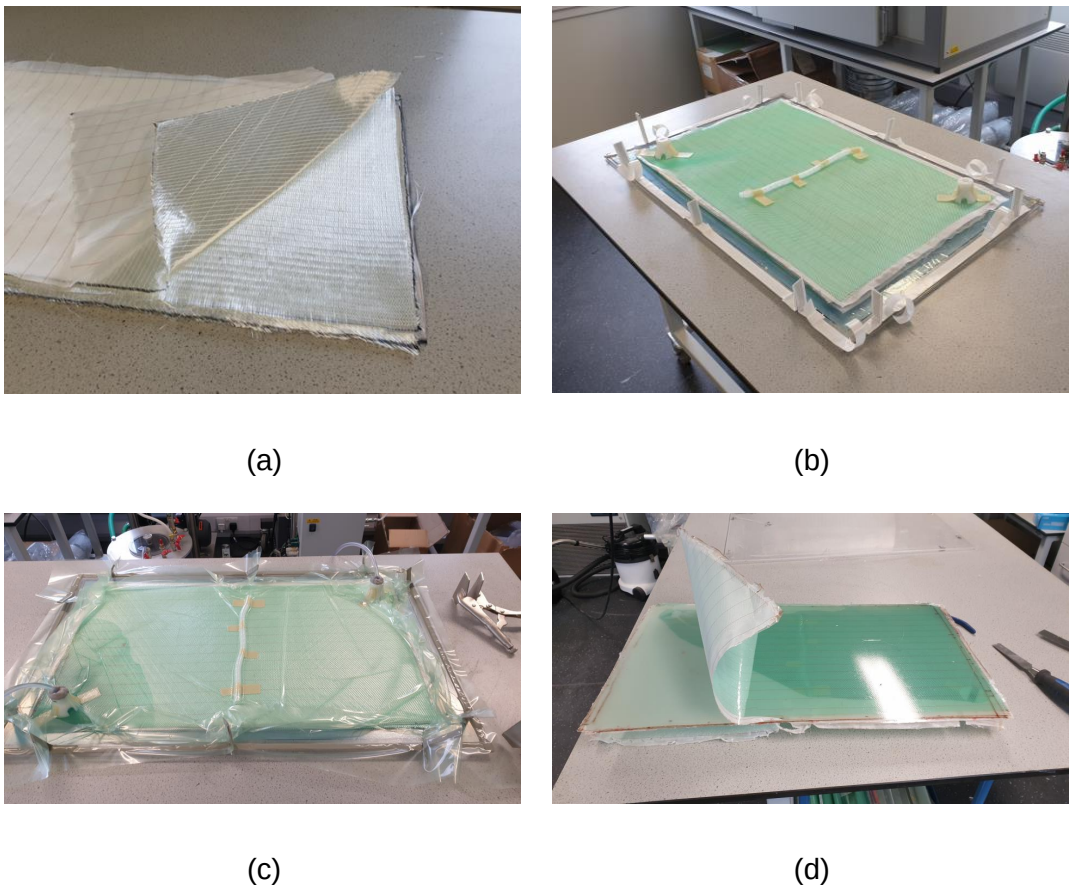

(a) (b)

(c) (d)

Figure 3.11: (a) Cut Glass Fibre Layup; (b) Layup on the Mound Before Bagging; (c) Vacuum Assisted Resin Injection; (d) Removal of Peel-Ply Layer Post-cure

The first stage of the composite manufacture was to clean and prepare the mould, as shown in Appendix A Figure 0.1, for resin infusion. The mould used was an 850mm by 535mm Perspex sheet. Firstly, the mould was cleaned using Zyvax Breez Granudan Surface Cleaner. After cleaning, the mould was sealed using Zyvax Breez Sealer BN201. The mould sealing process involves several applications of the sealing agent, four applications were used with a 15-minute waiting time between each application. The final application of the sealing agent required a cure time of 4 hours at 50°C. The last stage of the mould preparation is to apply a release agent. The release agent used was Zyvax Breez Granudan Watershield. The release agent was applied in two coats with a 15-minute wait time in between coats and a set time of 30 minutes after the

second coat. After the set time of the release agent, as detailed in the manufacturer's specification sheet, the mould was ready to use.

The next stage of the panel manufacturing process was to cut the glass fibre mats from the storing rolls, shown in Figure 0.2, down to the size required for the panel. Figure 0.3 and Figure 0.4 show the fibre mats cut down to the required size and how the mats are layered. The dimensions of the cut glass fibre mats were 550mm by 300mm and the layup of the composite starting from the bottom, on the mould, was as follows: PP/+45/-45/0/+45/-45/+45/-45/0/+45/-45/PP/RF/DM, where PP is peel-ply, RF is release film and DM is distribution mesh.

Once all the glass fibre mats, peel-ply, release film and distribution mesh had been cut to size, they were laid onto the mould ensuring that the correct layup was followed. The next stage of the process was to 'bag' the layup - to seal the layup in a bag to allow for a vacuum to be drawn within the bag. The first step of 'bagging' is to seal the edges of the mould with tacky tape, as shown in Figure 0.5. In addition, pleats were added along the outer edge of the tacky tape - this is to allow for room for the bag to compress and form a solid seal against the glass fibre layup during the vacuum drawing process. The resin injection site and extraction site were located at opposite corners of the layup, with a distribution aid between each site. The resin injection and extraction sites as well as the distribution aid can be seen in Figure 0.6. The bag was then placed over the layup and mould and then sealed along the tacky tape to allow a vacuum to be drawn between the mould and the bag, as shown in Figure 0.7.

The bagged mould and layup were then placed in the oven to make the next stage easier. If the mould is placed in the oven at this stage, it does not require to be moved again before it is infused with resin. Note, that the oven was switched off at this stage. After the mould was placed in the oven, the epoxy resin was created with a ratio of 10:3 of resin:hardener. Once the resin had been thoroughly mixed and degassed, it was then pulled through the layup.

Figure 0.8 shows the infusion process where the resin was drawn through the layup due to the applied vacuum.

When the resin had penetrated though the layup and had reached the outlet pipe - this is the pipe which is at the right side of the Figure 0.8 and is the source of the vacuum - the vacuum was turned off and then held within the bag. The oven was then switched on and the bagged mould and layup was left in the oven to cure. The layup was left to cure in the oven for 20 hours at 50˚C.

The cured layup, now composite material, was the taken out of the oven where the bag was then removed as shown in Figure 0.9, and the composite was removed from the mould. The distribution mesh and peel-ply layers on the top and bottom were removed to give the completed composite material, shown in Figure 0.10.

3.3.2. Coating System Application

Once the finished composite substrate was allowed to rest for two weeks, the blade coating systems could be applied. Firstly, the surface of the substrate was lightly sanded using P240 paper, to promote adhesion of the coating system, and then lightly cleaned with ethanol to remove any surface debris.

As multiple coating systems from different coating manufactures were used, specifics of each coating system application are detailed individually. Each coating system used was applied according to the manufacturers guidelines and specifications.

The coating systems used within this work are:

- Coating B
- Coating C1
- Coating C2

However, coating system C2 is only included from Chapter 5 -onwards, as coating system C2 was used for a weathering comparison between coatign systems from the same manufacturer.

3.3.2.1. Coating B

Once each substrate had been sanded and cleaned, the filler layer of the coating system was applied according to the manufacturers guidelines. The filler was mixed in a ratio, by weight, of 3:1 of A:B respectively. A thin layer of filler was applied to the substrate using a putty scraper/applicator tool. The applied filler layer on the substrate was then left to cure for 24 hours. The filler layer was then sanded back, using P180 grit sandpaper, until the substrate was exposed – only a very thin layer of filler remained, acting as a pore filler. The coated substrate was then cleaned using ethanol. Next, the topcoat layer was prepared accodring to manufactrers guidelines. A mix ratio, by weight, of 6:1 of A:B was used. In addition to parts A and B of the topcoat, a thinner was added at 5% weight of A+B. This allowed for easier application of the topcoat and increased the potlife to provide multiple applications (two coats) from one mix. The topcoat was applied to the filler coated substrate using a fine napped roller. Two coats were applied, each with a wet film thickness of 100µm, the second coat was applied 30 minutes after the first. The topcoat layer was then left to cure for 24 hours. After the cure period, the topcoat layer was lightly sanded using P240 grit sand paper and then cleaned with ethanol. The final layer, the LEP, could then be applied according to manufacturers guidelines. The LEP was prepared with a mix ratio, by weight, of 0.575:1 of components A:B. Two coats of LEP were applied using a fine napped roller. The second coat was applied 2 hours and 30 minutes after the first. Each coat had a wet film thickness of 200µm. After the LEP application, the whole coated substrate was left for 2 weeks to cure at ambient conditions.

3.3.2.2. Coating C1

Once the substrate had been sanded and cleaned, the filler layer of the supplied coating system was applied to the substrate using a putty spreader tool, according to the manufacturers guidelines. A thickness of 2mm was achieved, using a wet film thickness gauge to check. The filler layer was left to cure overnight at ambient conditions. The following morning, the filler layer was sanded, using P240 paper, to even out the surface and remove a thin layer of the filler. After sanding, the filler layer was lightly cleaned with ethanol to remove any surface debris. Next, the topcoat layer was prepared and mixed accoridng to the manufacturers guidelines. The topcoat was applied by a fine napped roller to a thickness of 150µm, checked by a wet film thickness gauge. The topcoat was allowed to cure, at ambient conditions, for 18 hours overnight. The following day, the LEP was prepared and mixed according to the manufacturers guidelines. The LEP was then applied by a fine napped roller to a thickness of 400µm, checked by a wet film thickness gauge. No sanding of the topcoat layer was required as the LEP was applied within the allowed overcoating interval. Once the LEP was applied, the coating system was complete. The coated substrate was then left to cure at ambient conditions for one week, see Figure 3.12.

Figure 3.12: Coated Substrate

Coating C2 was applied in exactly the same method as coating C1.

3.3.3. Panel Cutting to Specimen Dimensions

The cured, coated composite panels were then cut into specimen test pieces using a water-jet cutter in the Mechanical Engineering Workshop at the University of Strathclyde.

For RET, the dimensions of the test specimens were cut to 60mm x 15mm as shown in Figure 3.13. Figure 3.14 shows the test specimens used, where the multi-layer construction of the specimens can be observed. Figure 3.14 (a) shows a frontal view of a coating B specimen, where the very thin filler layer is present. Comparing coating B to coating C, Figure 3.14 (d) shows a frontal view of coating C1 where the filler layer is much thicker and more observable to the naked eye.

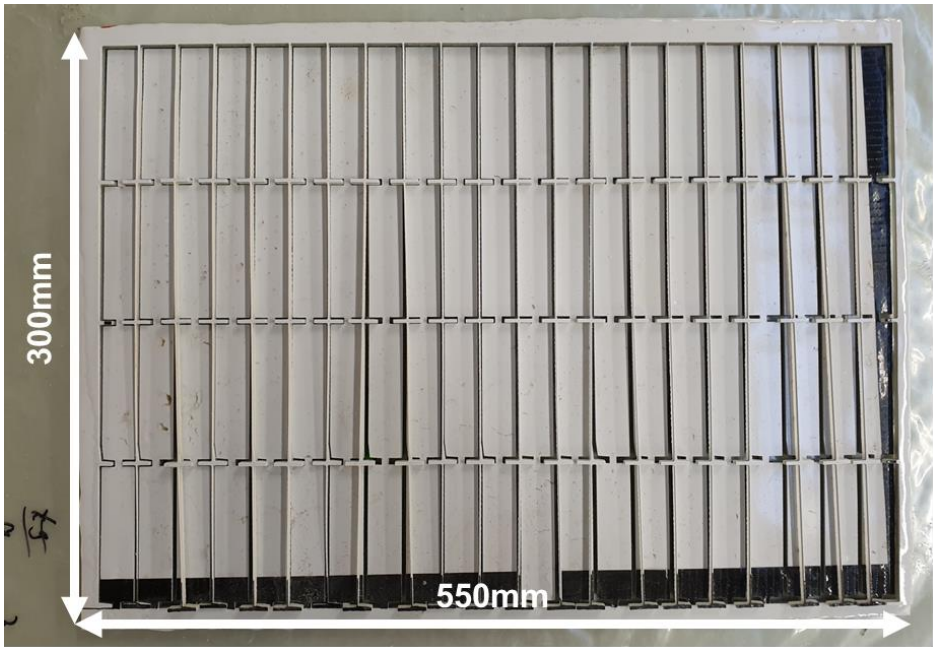

Figure 3.13: Water-Jet Cut Coated Substrate for RET

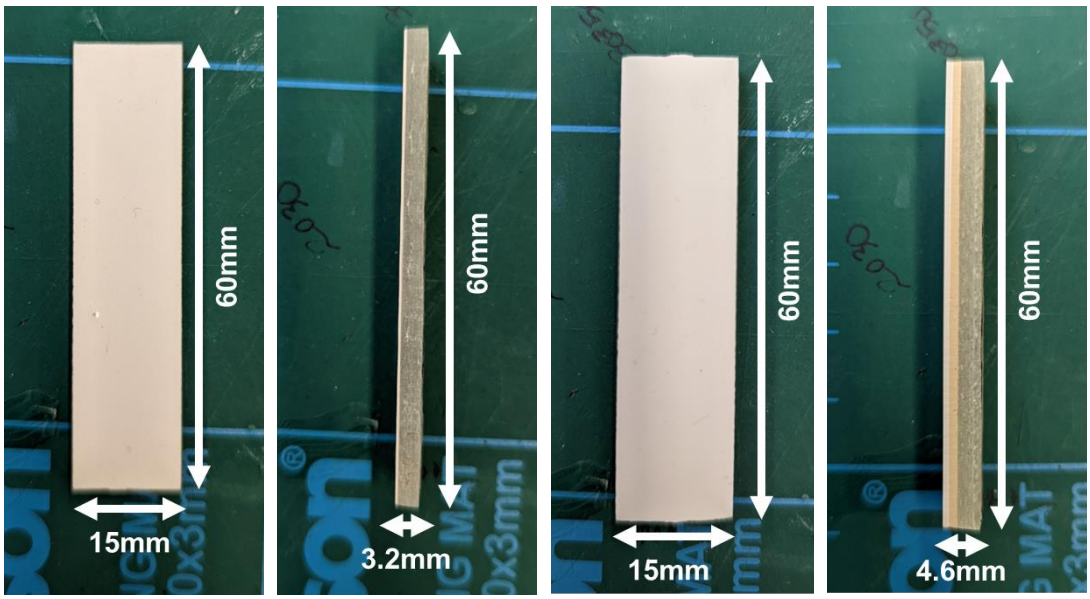

(a) (b) (c) (d)

Figure 3.14: (a) Coating B RET Specimen, Plan View; (b) Coating B RET Specimen, Front View; (c) Coating C1 RET Specimen, Plan View; (d) Coating C1 RET Specimen, Front View

For the weathering specimens, a larger specimen area was required due to the holding mount dimensions in the weathering chamber. The weathering specimens were each cut to 76mm x 152mm (3 by 6 inches) by the water-jet cutter.

3.3.4. Summary

To summarise, test specimens have been prepared with great attention to detail to ensure they are of the highest quality, uniform between specimens and are manufactured according to the material suppliers' guidelines.

The specimen type used differs from the typical aerofoil shape RET specimen in that the test specimens used within this work are flat in shape. The specimens are flat for multiple reasons; firstly, to eliminate any induced heat and stresses that may be caused by cutting the specimens post RET in order for the specimens to be analysed in the laboratory – the aerofoil shaped

sample was not compatible with select pieces of laboratory equipment. Secondly, the combined RET and weathering work required the test specimens to be exposed to both accelerated RET and accelerated weathering. The accelerated weathering chambers were only compatible with flat specimen types due to test chamber geometry limitations.

Some sources of variability within the samples could have been introduced due to the method of vacuum infusion used. Using the bagging method creates a slightly uneven surface on the top of the specimen panel, prior to coating application and cutting, versus another method such as using a resin transfer moulding (RTM) press. This in turn could create thickness variations within the applied coating systems. The bagging method was selected as there was no availability of an RTM press at the time of specimen manufacture.

Chapter 4 - Rain Droplet Impact Assessment

The work in this chapter quantifies and explains the mechanism of erosion on wind blade coating systems due to repeated rain droplet impacts. Several wind blade coating systems were used to offer a comparison between wind blade coating types and any variation in degradation mechanisms. This work also creates the baseline for rain erosion testing which is used to examine the effect of weathering during combined rain erosion and weathering testing. The combined rain erosion and weathering work is discussed in Chapter 6 -.

To facilitate this work, an accelerated rain erosion test (RET) rig is required and ideally one which is known and characterised. The RET facility at the Energy Technology Centre (ETC), located in East Kilbride, near Glasgow, was used for this study and has been used by researchers at Strathclyde [74]. Work, by Mackie [75] and the present author have led to a complete undertaking of the main variables and parameters which require to be controlled to establish meaningful results from the rig.

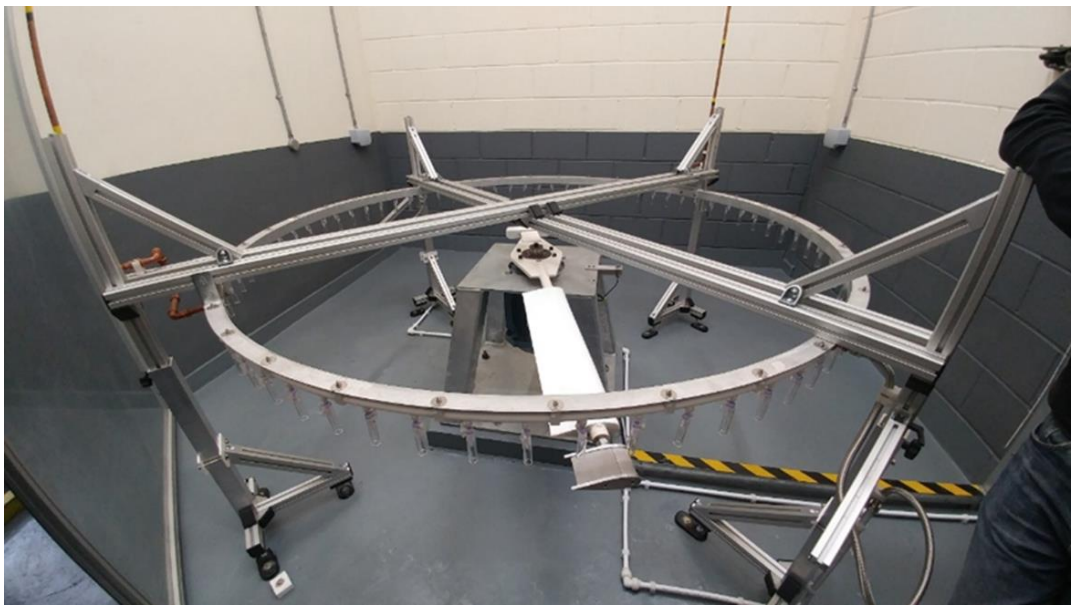

Figure 4.1: ETC Rain Erosion Test Rig

The ETC rig is of innovative design in that there is a single path of nozzles, which are equally distributed around the circumference of the rig at a fixed diameter, see Figure 4.1. There are 72 nozzles in total, each of which can be individually controlled. This allows for very specific test conditions to be achieved. The flow rate of water to the nozzles and the gauge of the needles which are attached to each nozzle can be controlled, therefore, offering control over the size of the water droplets created and the number of droplets which are produced over a given period of time.

Additionally, the height of which the droplets fall, before impacting the test specimen, is controllable by adjusting the height of the circumferential ring of nozzles. The last parameter which is controllable is the rotational velocity of the arm where the test specimen is mounted to. This determines the impact velocity of the water droplets.

Parallel work conducted by fellow researcher Dr Cameron Mackie [75] fully characterised the ETC rain erosion test rig. From this work, it was observed that the ETC rig displayed a resonance at 1050rpm. This was determined by using vibrational analysis of the rig at increasing rotational velocities. Running the rig at resonance would ultimately damage the motor, therefore, operating

at 1050rpm was avoided for any testing in the present work. Additionally, Mackie defined the droplet strike rate and location on the test specimen for multiple rotational velocities as well as the droplet diameter for multiple needle setups and water flow rates. Using this approach, the operational conditions for testing in the present study were determined.

Half of the available nozzles, 36 out of 72, were used as to slow the erosion rate and allow for easier erosion identification. The rotational speed of the test was set to 1100rpm, with a droplet fall height of 50mm. This test speed avoided the resonance of the motor whilst retaining a high droplet strike rate, which correlates to a blade tip speed of 120m/s. Additionally, the droplet fall height of 50mm was selected due to high percentage of droplets falling straight down, versus a high percentage of deflected droplets at a fall height of 100mm, again this was based on Mackie's approach. A needle size of 27 gauge (0.21mm inner diameter) was used for each of the 36 nozzles with a pressure head of 350mm, this gave a flow rate of 0.087 l/h from each nozzle. A measured droplet diameter of 2.34mm was recorded during the calibration tests.

4.1. Erosion Stages

A test methodology was developed to provide an in-depth view of the whole rain droplet erosion process on wind turbine blade coating systems. The test methodology was based upon industrial testing standards [3], [50] which were modified to provide distinct phases of erosion to analyse. Several key stages of the erosion process were identified to be of interest based upon work by Gaudern [48], during the incubation period, at the end of the incubation period, during active erosion and at failure of the coating system. Therefore, a staged approach to erosion analysis was created.

Five stages of erosion were identified to be of the greatest importance. Firstly, Stage 1 is defined as a new, fresh sample which has not been exposed to any rain droplets. Stage 2 occurs during the incubation period, the sample has been exposed to some rain droplets however, there is **no observable visual surface damage or mass loss**. Stage 3 follows where the incubation period

ends, and **surface damage begins to be visually observable and mass loss detectable**. Stage 4 appears during active erosion, there is **clearly observable surface damage and detectable mass loss**. Finally, Stage 5 occurs when **the coating system has failed**, and the substrate material that the coating system was applied to is observable due to erosion damage. Figure 4.2 shows where each of the identified five stages of erosion occur on a mass loss versus number of droplet impacts plot.

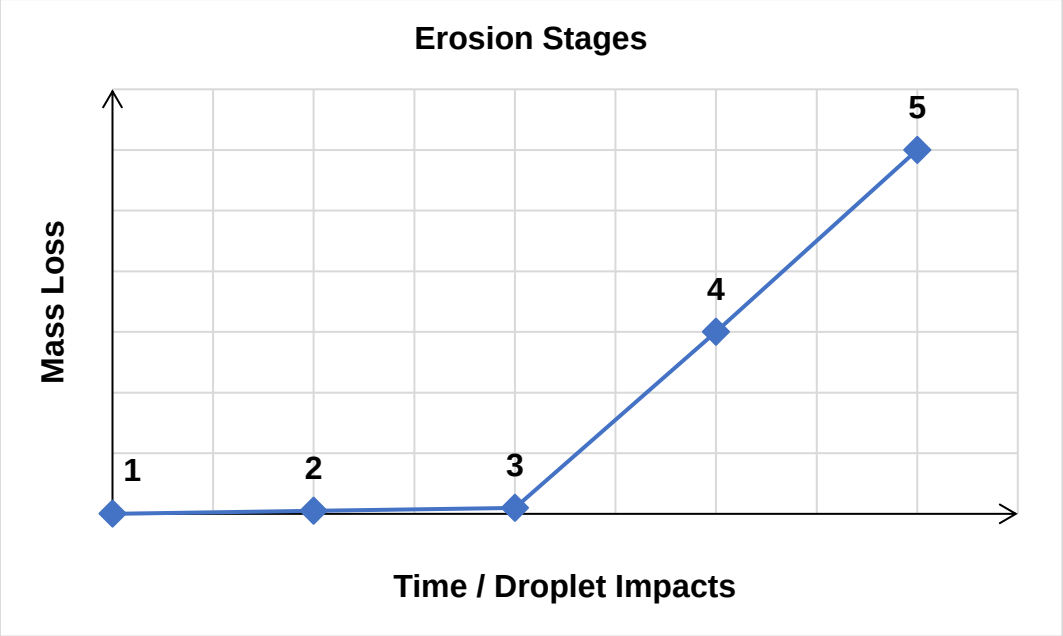

Figure 4.2: Erosion Stages

4.1.1. Droplet Energy

Due to the well characterized nature of the ETC rig, it is possible to calculate the amount of energy that each tested specimen has received due to droplet impacts. The total impact energy is a function of time spent on test, and so the impact energy was calculated as follows. For the impact energy calculation, it was assumed that the flat profile specimen type presents the same droplet impact strike rate on the specimen surface as the curved profile specimen type used within previous work by Mackie.

Firstly, the kinetic energy of each impacting droplet, E_k, was calculated. This is a function of the droplet's mass, m, and the impact velocity, u_i, see Equation 4.4.1. It was assumed that as the droplet struck the sample, the velocity due to falling under gravity was negligible and the rotational velocity of the test rig was dominant. Therefore, u, is the linear velocity of the test rig. The droplet mass was calculated as shown in Equation 4.4.2, where the density of the droplet was multiplied by the volume of the droplet. The testing was conducted at ambient conditions and the density of the water droplets was taken to be 997 kg/m^3. The droplets were assumed to be spherical and therefore the volume of each droplet, V, was calculated as shown in Equation 4.4.3 where r represents the radius of the droplet. The droplet radius was measured during calibration tests to be 1.17mm.

$$E_k = \frac{1}{2}mu^2 \qquad \text{Equation 4.4.1}$$

$$m = \rho V \qquad \text{Equation 4.4.2}$$

$$V = \frac{4}{3}\pi r^3 \qquad \text{Equation 4.4.3}$$

Next, the kinetic energy, E_k, was multiplied by the droplet strike rate to get the strike energy rate. The droplet strike rate was known from previous work on the ETC rig [75], where high speed camera footage was used to count and locate the number of droplets which struck the specimen during a test. The droplet strike rate for the described test conditions was given as 830 droplet strikes per minute.

Then finally, the impact energy for a specimen at a given erosion stage can be calculated by multiplying the strike energy rate by the test time to reach the erosion stage.

4.2. Rain Erosion Test Methodology

This section details the rain erosion testing approach used within this work and describes specifics of the testing process.

Firstly, specimens were manufactured as detailed in Specimen Manufacture and Preparation, Chapter 3, Section 3.2. Two coating systems were used, coating B and coating C. The test specimens each measured 60mm by 15mm.

Before any erosion testing was undertaken, a baseline assessment of the test specimens was performed. The baseline characterisation was carried out to allow for any changes in the coating materials, due to rain droplet erosion, to be detected. The baseline assessment consisted of measuring the mass, gloss and photographing each test specimen. Additionally, each test specimen was analysed using dynamic mechanical analysis (DMA) and magnified images were captured of the test specimen's surface using optical microscopy. The equipment used for each parameter is listed below. All the equipment used was located in the Advanced Composites Group Characterisation Laboratory, at the University of Strathclyde.

- Photography: The rear 12 MP camera on a Samsung Galaxy S9
- Microscopy: Leitz Ergolux Optical Microscope with a Leitz NPL FLUOTAR 10×/0.22 lens
- Mass: A&D Instruments GR-120-EC mass balance
- Gloss: Rhopoint IQ (Goniophotometer) 20°/60°/85°
- DMA: TA Instruments Q800 DMA with a dual-cantilever clamp

4.2.1. Rain Erosion Testing

The rain erosion test rig at ETC was used to investigate the conditions required to reach each of the previously identified erosion stages. The test rig conditions were: 36 active nozzles, 27-gauge needles, 50mm droplet fall height, pressure head of 350mm and rotational arm velocity of 1100rpm. To investigate the erosion stages, five test specimens were used as calibration samples. Each of the five calibration samples was run in the test rig, stopping the rig every 15 minutes to conduct a visual assessment and take a photograph of the sample. This progressed until the sample had failed, and the substrate material was clearly visible. The photographs of each 15-minute period, from all five

samples, were then compared and each erosion stage was identified. From this, the average time to reach each erosion stage was calculated. The erosion stage calibration process was the same for each coating system investigated.

This then provided an estimated time required in the test rig at ETC to reach each erosion stage. The estimated time allowed for more targeted testing, rather than having to stop the rig every 10 or 15 minutes to see what the state of the test specimen is. The rig could be run for a longer period, with fewer stoppages, and still achieve the desired output.

Once the average time to reach each erosion stage was known, the calibration stage was completed and testing of specimens could begin. Five specimens were used for each erosion stage, giving 25 test specimens in total. This testing was not cumulative, and as such, a new specimen sample was used each time.

Each specimen was mounted in the test rig to a custom manufactured flat sample holder. The sample holder was made from aluminium and had an indent cut to the size of the test specimens – 60mm by 15mm. The test specimen was secured, at either end, by a washer held in place by a slotted screw, shown by the expanded red box in Figure 4.3.

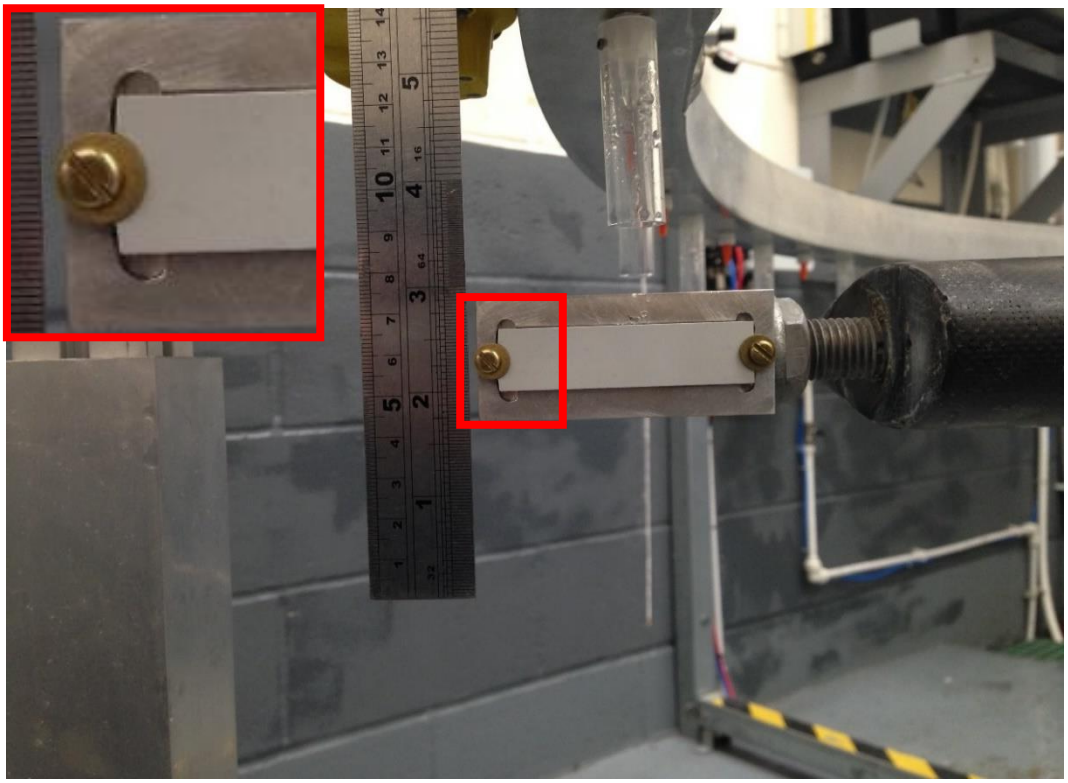

Figure 4.3: ETC RET Rig Flat Sample Holder

Once the test specimen was mounted in the rig, the water was then initiated, creating the droplets from the nozzles. Next, the motor of the rig was run up to the test speed of 1100rpm. The rig was then left operating for the average time to reach the targeted erosion stage minus 10 minutes, whilst being monitored from the control room. A period of 10 minutes was taken off the average time to allow for the targeted erosion stage to be captured and not bypassed. The rig was stopped, and the test specimen visually inspected and photographed every 5 minutes beyond the average time minus 10 minutes, until the specimen was deemed to have reached the targeted erosion stage. The specimen was then removed from the RET rig and taken to the laboratory for analysis.

4.2.2. Laboratory Analysis

All the materials characterisation analysis performed on the test specimens was non-destructive. However, the order in which the analysis was conducted is important. Firstly, the specimens were photographed to identify damage

visible to the naked eye, and then the optical microscope was used to investigate the surface microstructure of the specimen. Next, the specimens were weighed using the mass balance, then the glossmeter was used to record the surface gloss value. Finally, the specimens were analysed using DMA, and as the DMA requires physical contact with the sample, at slightly raised temperature, this was done last.

Photography – Photographs of test specimens were captured at ETC during testing, both before a test began and after each stoppage interval. Additionally, photographs were also captured in the laboratory before all other laboratory testing began. Before any photographs were taken, the specimen surface was wiped with a wet paper towel to remove any surface debris and left to dry for 1 hour.

Optical Microscopy – Both x10 and x20 magnification lenses were used to explore the surface of the coating. At each erosion stage, the eroded zone and surrounding area, where most of the water droplets struck the specimen, was focused in on. Images were then captured, showing any area of change versus the previous erosion stage.

Mass – Before any mass measurements were taken, the test specimens were left at ambient conditions to dry out for two weeks. This was to allow for any retained water from RET to evaporate. Each specimen was weighed both before any RET, Stage 1 erosion, and then after each erosion stage in turn.

Gloss – The 60° angle was used on the glossmeter to measure the surface gloss at each erosion stage. Gloss measurements were taken before and after each erosion stage.

DMA – DMA with a dual cantilever clamp was used to perform a frequency sweep of each sample both before and after a period of RET. The frequency sweep test is performed by holding the temperature of the test constant, and then only changing the frequency of the oscillating clamp, which the specimen is mounted to. This test allows for the variable of frequency to be examined, in

the case of rain droplet impacts, the frequency of the droplet impacts is not constant. DMA test conditions were as follows: Temperature 30°C (selected due to high laboratory temperature, DMA did not have cooling applied); Frequencies tested 1Hz, 20Hz, 40Hz, 60Hz, 80Hz, 100Hz; Poisson's Ratio 0.33; Initial force 1N; Amplitude 10µm.

4.3. Rain Erosion Test Results

The average time taken in the RET rig to reach the targeted erosion stage is detailed in Table 2.

Erosion Stage	Average Time in ETC RET Rig (minutes)	
	Coating B	**Coating C1**
Stage 1	0	0
Stage 2	25	25
Stage 3	40	48
Stage 4	60	100
Stage 5	64	124

Table 2: Average Time to Reach Erosion Stage

It is clear from Table 2 that both coating systems performed differently during RET. Coating B lasted approximately half the time of coating C1 to reach Stage 5 – total failure. Additionally, some coating B specimens began to prematurely fail, they progressed straight to Stage 5, whereas coating C1 specimens followed a predictable erosion pattern. This is discussed in the following sections.

4.3.1. Visual Inspection

Photographs of all samples put though RET, for coating B, are presented in Figure 4.4 to 4.8. Photographs of all samples put though RET, for coating C, are presented in Figure 4.9 to 4.13.

Looking at the coating B specimens, the first area to note is that some of the specimens are failing prematurely. For example, in Figure 4.5 the incubation stage is shown where there should be no visible surface damage, however, the second specimen in from the left is showing a large area of substrate exposure where the coating system has been removed. This is also observable, though on a smaller scale, in the first and last specimens shown in Figure 4.5. Again, this same behaviour of premature failure can be seen in Stage 3 erosion in Figure 4.6.

An interesting point to note is that all the coating B specimens have failed from the edge and present a delamination type failure, rather than an erosion type failure. After the testing was complete, the manufacturer of coating B disclosed that they were aware of issues with adhesion between the layers of coating B. Another point of note is that, in the ETC RET rig, coating B erodes very quickly compared to coating C. Looking at Table 2, coating B takes approximately 25 minutes to degrade from Stage 3 to Stage 5. Looking at the photographs of Stage 3 to Stage 5, Figure 4.6 to Figure 4.8, the erosion damage onset is very severe. It is clear from Figure 4.7 that at Stage 4 the coating system had already failed, and the composite substrate was showing damage.

Examining coating C1 specimens, the first area to note is that all the specimens degrade in a very similar way. In Figure 4.9 to Figure 4.13, all specimens, at each stage, show almost identical patterns of erosion. Additionally, there is a tendency for coating C1 specimens to begin to erode from the centre of the specimen and not the edge, unlike coating B. Another point to note is that coating C1 expressed more distinct stages of erosion as is determinable from Table 2, where there is some 75 minutes of active erosion testing between Stage 3 and Stage 5.

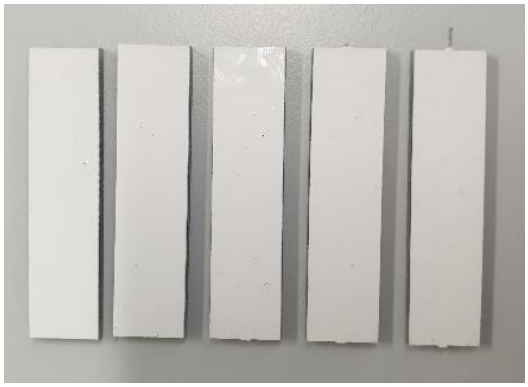

Figure 4.4: Photo, Stage 1, RET, Coating B

Figure 4.5: Photo, Stage 2, RET, Coating B

Figure 4.6: Photo, Stage 3, RET, Coating B

Figure 4.7: Photo, Stage 4, RET, Coating B

Figure 4.8: Photo, Stage 5, RET, Coating B

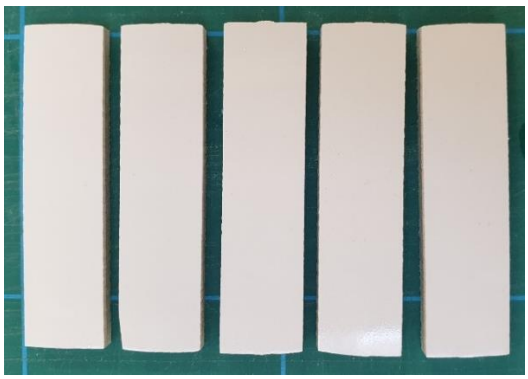

Figure 4.9: Photo, Stage 1, RET, Coating C1

Figure 4.10: Photo, Stage 2, RET, Coating C1

Figure 4.11: Photo, Stage 3, RET, Coating C1

Figure 4.12: Photo, Stage 4, RET, Coating C1

Figure 4.13: Photo, Stage 5, RET, Coating C1

4.3.2. Optical Microscopy Assessment

A representative optical microscopy image for each erosion stage, for coating B, is displayed in Figure 4.14 through Figure 4.18. A representative optical microscopy image for each erosion stage, for coating C1, is displayed in Figure 4.9 through Figure 4.13.

Firstly, looking at coating system B under the microscope, images for Stage 1 through to Stage 5 are displayed in Figure 4.14 through to Figure 4.18 respectively. To the naked eye, Stage 1 looks like the surface of the specimen is perfectly smooth and uniform, as shown in Figure 4.4. However, looking at Stage 1 under the microscope, Figure 4.14, this is not the case. The microstructure of the coating surface is textured, consisting of pinholes and small craters. This is due to air pockets, which were created in the coating during mixing and application, rising to the surface as the coating cures. As the specimen moves to erosion Stage 2, larger holes begin to develop. Figure 4.15 shows the newly formed holes after an average period of 25 minutes in RET. Moving to Stage 3, these holes deepen and collate, creating larger patches where pervious holes have merged. It is noted that these larger, collated holes are not visible to the naked eye, as can be observed in Figure 4.6. Stage 4 occurs during active erosion, where some coating removal occurs. Looking at the microscopy image Figure 4.7, a large crack can be seen. This crack is typical of what was observed towards the outer edges of the eroded zone, where the coating material was removed. The crack suggests a brittle mechanism of failure in the coating system, due to repeated impacts from rain droplets. Stage 5, shown in Figure 4.18, displays the eroded specimen, where the coating system has been entirely removed and the composite substrate has been exposed.

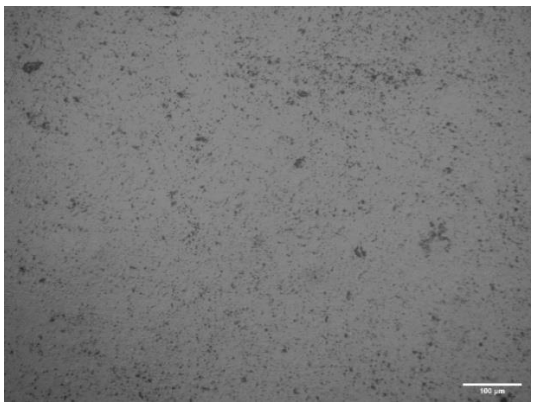

Figure 4.14: Microscopy, Stage 1, RET, Coating B

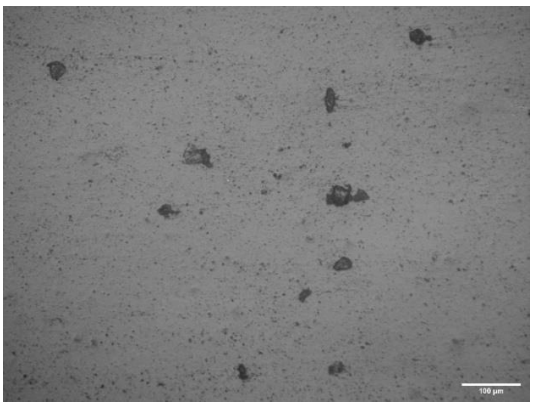

Figure 4.15: Microscopy, Stage 2, RET, Coating B

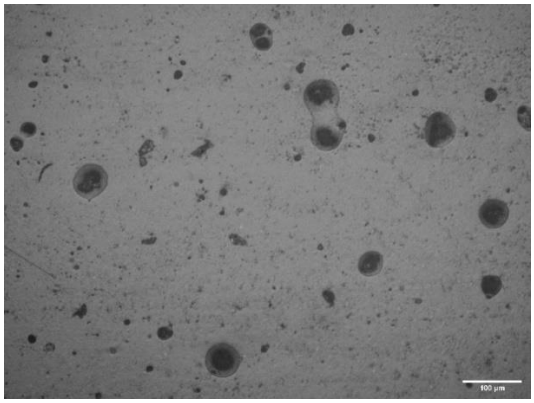

Figure 4.16: Microscopy, Stage 3, RET, Coating B

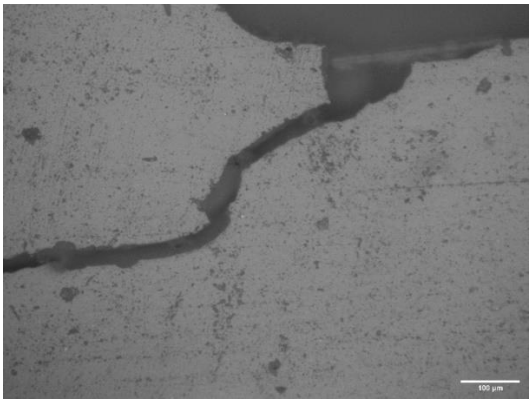

Figure 4.17: Microscopy, Stage 4, RET, Coating B

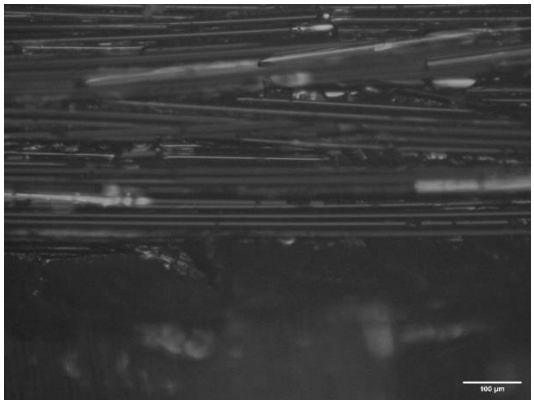

Figure 4.18: Microscopy, Stage 5, RET, Coating B

Next, looking at coating system C1 under the microscope, images for Stage 1 through to Stage 5 are presented in Figure 4.14 through to Figure 4.18

respectively. Stage 1 shows that the surface is not entirely smooth and uniform, as would be expected from looking at Figure 4.9. There are small pinholes and defects in the surface microstructure. Similar to coating B, this is due to the mixing and application of the coating system where air pockets have been trapped and rise to the surface during curing. Moving to Stage 2, Figure 4.10 shows that the pinholes have begun to grow and deepen, however, this damage is still not visible to the naked eye. Stage 3 is where the surface microstructure begins to heavily degrade. Figure 4.21 shows areas of coating removal, in the form of craters, at significant depth and size. In Stage 3, the smaller pinholes present at Stage 2 have collated and merged into much larger holes. Looking at Stage 4, large areas of coating have now been removed. This is also now easily detectable to the naked eye, Figure 4.12. Under the microscope, Figure 4.22 shows a cliff edge like erosion pattern where, once the LEP has been eroded, the remaining layers of the coating system fail and are removed quite quickly. Stage 5, Figure 4.23, shows that the coating system has failed entirely and there is no coating remaining on the specimen at the droplet impact area and the composite substrate is exposed.

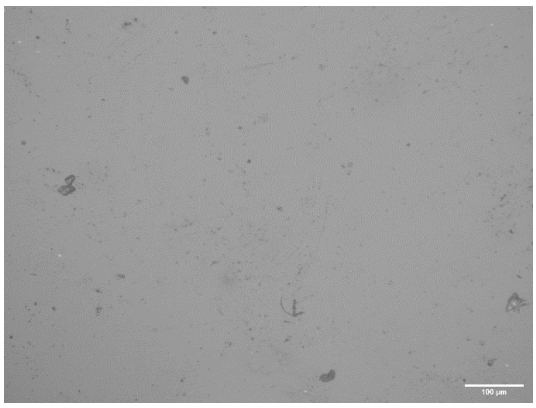

Figure 4.19: Microscopy, Stage 1, RET, Coating C1

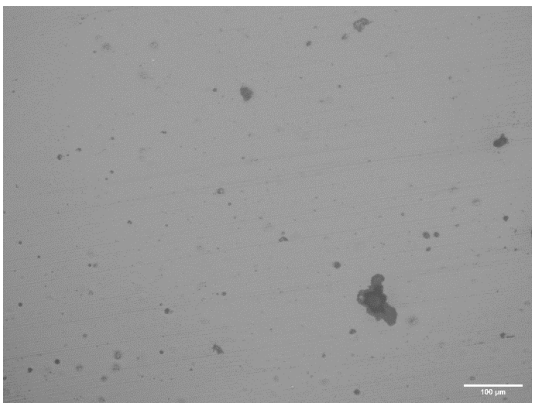

Figure 4.20: Microscopy, Stage 2, RET, Coating C1

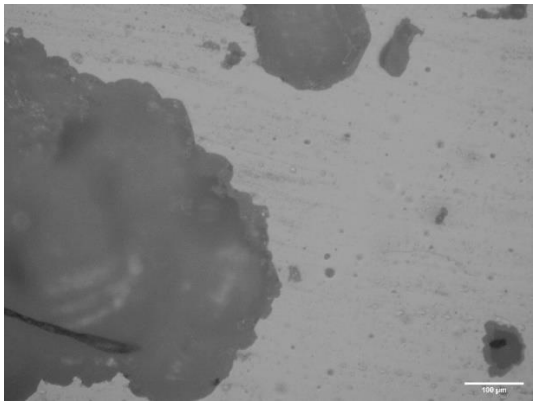

Figure 4.21: Microscopy, Stage 3, RET, Coating C1

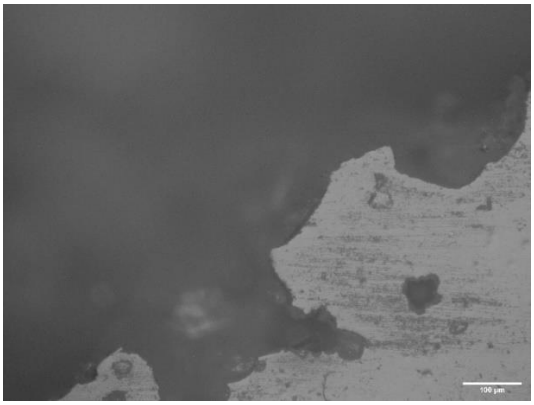

Figure 4.22: Microscopy, Stage 4, RET, Coating C1

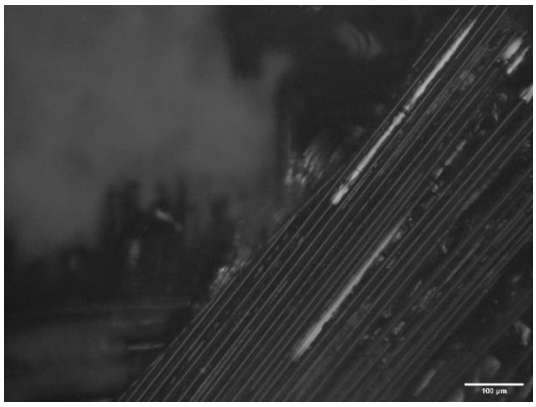

Figure 4.23: Microscopy, Stage 5, RET, Coating C1

4.3.3. Mass Loss Measurements

Mass measurements at each erosion stage, for both coatings systems, are presented in Figure 4.24. Mass measurements at impact energy are presented in Figure 4.25. The data is presented as a percentage of the initial mass measurement. Each data point represents the average measurement for the according erosion stage. The error bars attached to each data point represent a 95% confidence limit of the result.

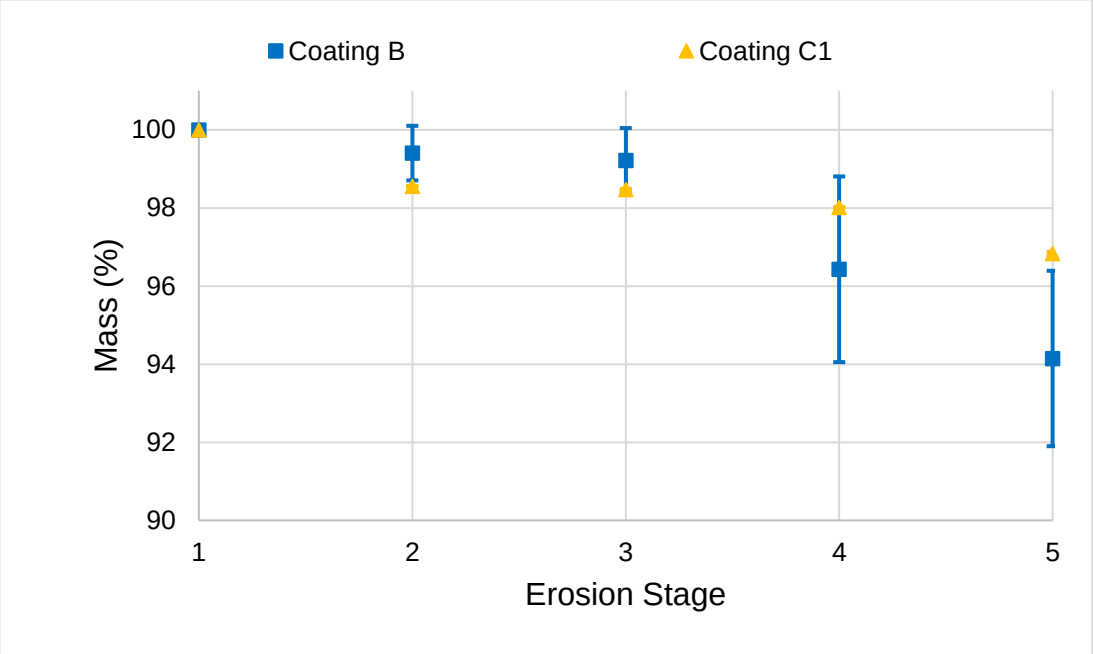

Figure 4.24: RET Mass loss, as percent, at Erosion Stage

The mass plot at each erosion stage for both coating systems, shown in Figure 4.24, shows that as the RET progresses, the specimens lose mass. This is due to the physical removal of the coating system from the specimen by the rain droplet impacts. For both coating systems, Stages 1 to 3 show minimal mass loss due to the incubation period. At Stage 4, both coating systems show an increased amount of mass lost, which is even more prominent at Stage 5.

There was a greater range of recorded mass measurements at each erosion stage for coating B compared to coating C1, this is reflected by the larger error bars attached to each data point.

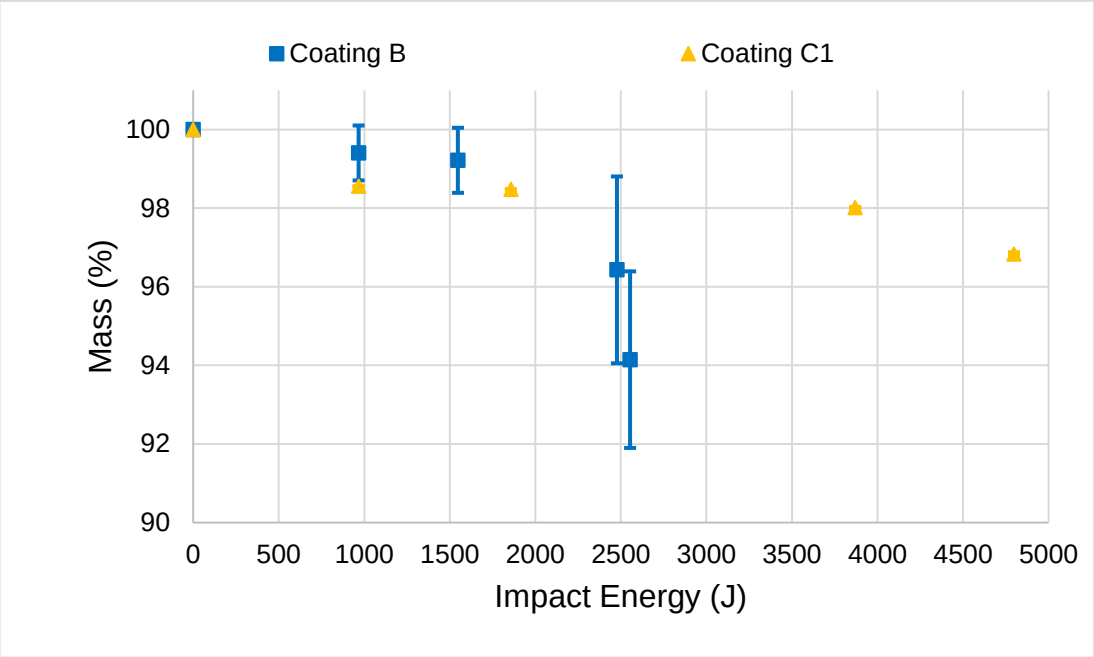

Figure 4.25: RET Mass loss, as percent, at Impact Energy

Looking at the amount of energy impacting each specimen to reach each erosion stage, Figure 4.25 shows that coating B failed after significantly less impact energy than coating C1. Coating B reached stage 5 (the 5th data point) at approximately half of the impact energy of coating C1.

It is noted that if the mass measurement was taken directly after a period of RET, the mass measurement would not be representative of the measure of material mass lost. During RET, the specimens absorb some of the water from the test, therefore increasing their mass. As such, specimens were left to sit for a minimum of two weeks to dry at ambient conditions before any measurements were taken.

4.3.4. Gloss Meter Measurement

Gloss measurements at each erosion stage, for both coatings systems, are presented in Figure 4.26. Gloss measurements at impact energy are presented in Figure 4.27. The data is presented as a percentage of the initial

gloss measurement. Each data point represents the average measurement for the according erosion stage. The error bars attached to each data point represent a 95% confidence limit of the result.

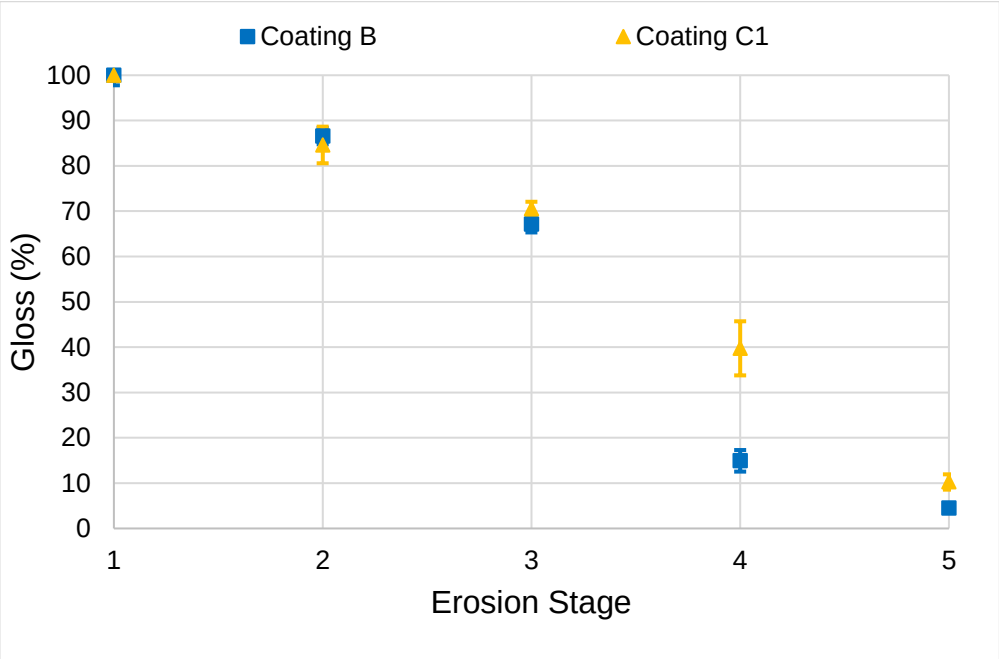

Figure 4.26: RET Gloss loss, as percent, at Erosion Stage

The plot of coating surface gloss at each erosion stage, presented in Figure 4.26, shows that as erosion progresses, the surface gloss decreases. The surface gloss value decreases due to the increase in surface texture and roughness as erosion progresses, as is also observable from the microscopy images. An important point to note is that there is a clear distinction in gloss value between all erosion stages, including the incubation period (Erosion Stages 1–3).

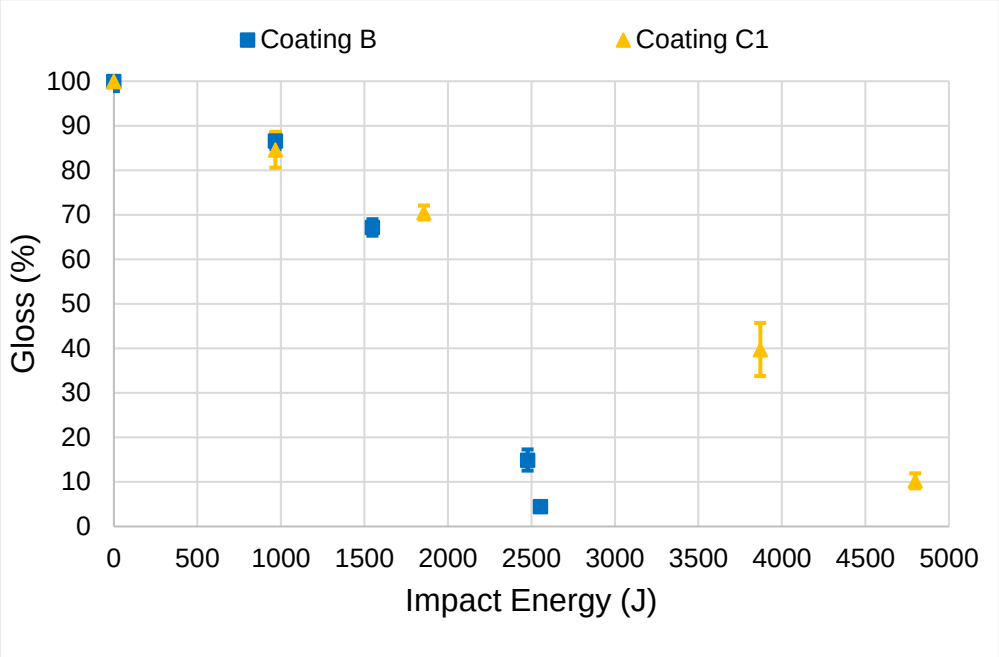

Figure 4.27: RET Gloss loss, as percent, at Impact Energy

From Figure 4.27, it can be observed that less impact energy is required to lower the gloss value of coating B compared to that of coating C1. This is due to coating B eroding faster than coating C1 and therefore requiring less droplet impacts to cause a similar change in the surface gloss value.

Similar to mass measurement, gloss measurements taken directly after RET exposure would be affected by water absorption. As a specimen absorbs water, the coating system swells, resulting in a slightly smoothened surface, which would be reflected in the gloss value measured. Therefore, all specimens were left for a minimum of two weeks to dry at ambient conditions before any measurements were taken.

4.3.5. Dynamic Mechanical Analysis (DMA)

Plots of storage modulus, loss modulus, and tangent of delta (tan δ), all versus erosion stage, for coating B and coating C1 are presented in Figure 4.28, Figure 4.29 & Figure 4.30 respectively. Data from two test frequencies, 1Hz and 20Hz, is presented. Each datapoint presented is an average of five individual specimen measurements.

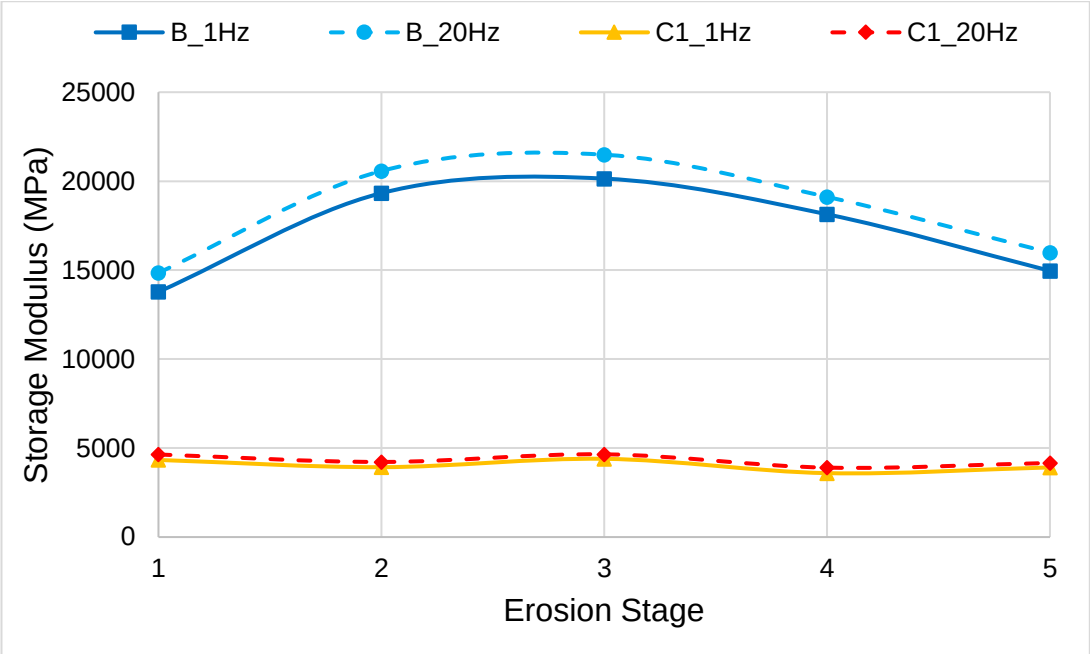

Figure 4.28: DMA Storage Modulus as Erosion Progresses for coatings B and C1.

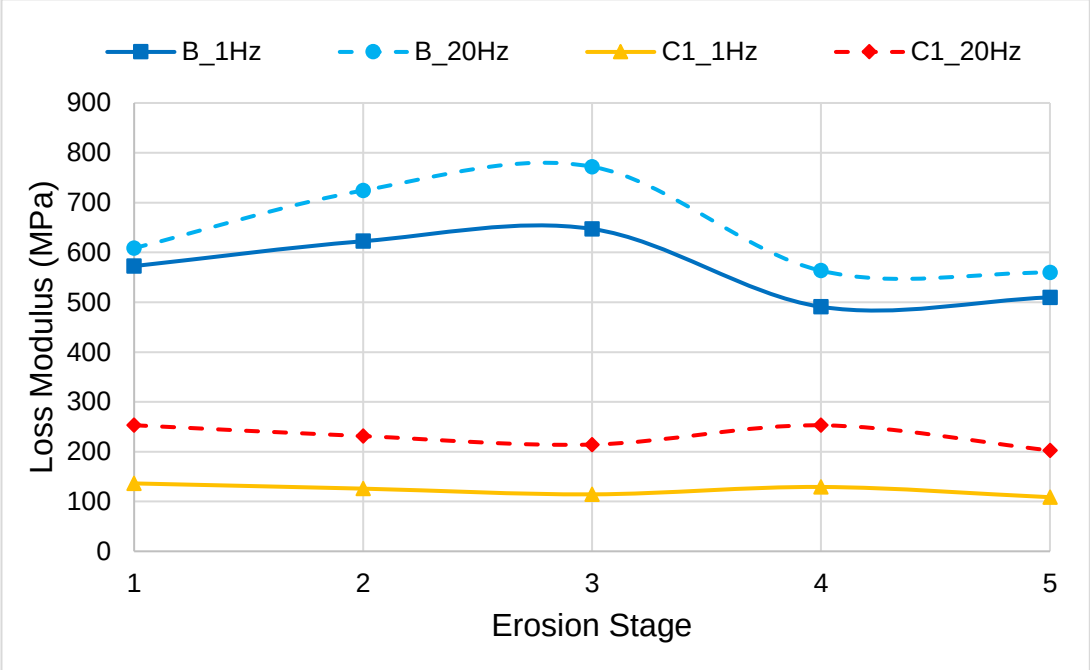

Figure 4.29: DMA Loss Modulus as Erosion Progresses for coatings B and C1.

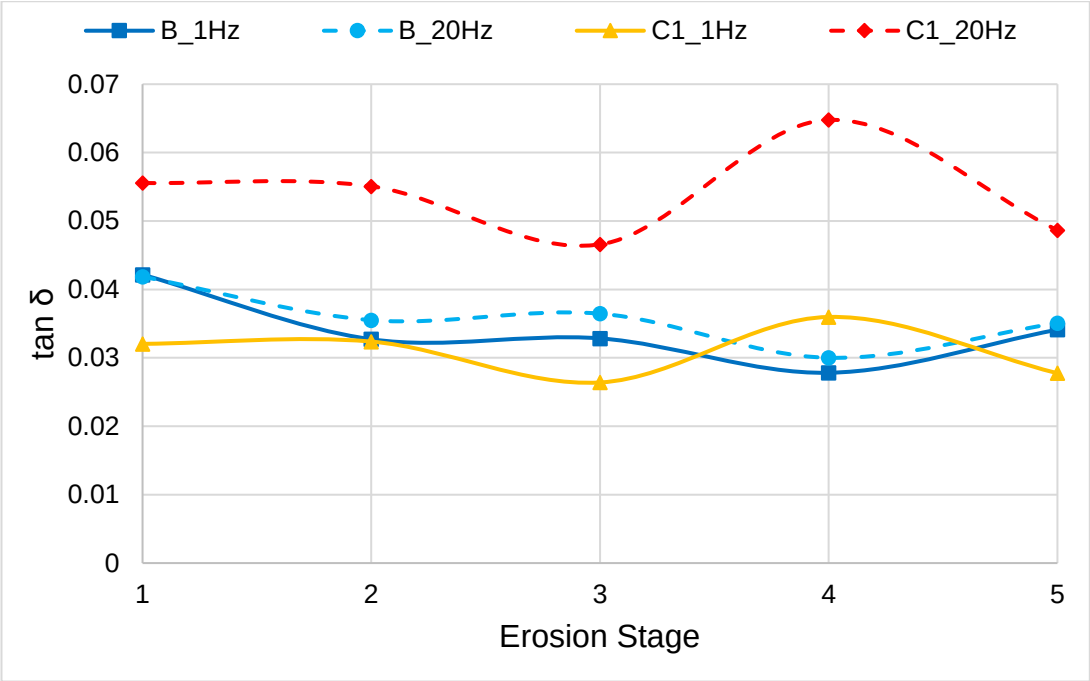

Figure 4.30: DMA tan δ as Erosion Progresses for coatings B and C1.

It can be seen from Figure 4.28 - Figure 4.30, increasing the frequency of the DMA test from 1Hz to 20Hz effectively shifts the datapoints upwards, but does not drastically alter the trend.

Looking at the storage modulus, Figure 4.28, it is clear that there is a difference between coating system B and coating system C1. Looking specifically at coating C1, it is clear that as erosion progresses, there is no major change in moduli. Across all erosion stages, the moduli, for a given test frequency, remains fairly constant with a total variation of 804MPa at 1Hz and 749MPa at 20Hz. Coating B shows a greater variation as the erosion stages progress, a total of variation of 6364MPa at 1Hz and 6636 MPa at 20Hz. However, between Stage 1 erosion and Stage 5 erosion, the difference is 1182MPa at 1Hz and 1135MPa at 20Hz, this shows that as the erosion has progressed there has been a recovery in the storage modulus, indicating an increase in energy storage potential within the material.

Considering the loss modulus, as shown in Figure 4.29, coating B displays a fluctuation in loss modulus measurement, 6364MPa for 1Hz and 6636MPa for

20Hz. However, as with the storage modulus, there is only a small change in the Stage 1 erosion and Stage 5 erosion. Looking at coating C1, again, the modulus measurements across all erosion stages are fairly constant. There is a total variation of 804MPa at 1Hz and 749MPa at 20Hz, with a difference of 27MPa at 1Hz and 50MPa at 20Hz between Stage 1 and Stage 5 erosion.

Next, the tan δ plot against the erosion stages is presented in Figure 4.30. From Figure 4.30, it is clear that as the erosion stages progress for coating B, the tan δ value remains fairly steady, with a total change in tan δ, from Stage 1 to Stage 5, of 0.007 at 1Hz and 0.006 at 20Hz. There is also only a very small difference in tan δ, an average of 0.06%, between the 1Hz and 20Hz plots. For coating C1, there is more variation and greater separation of the 1Hz and 20Hz plots, with an average of 0.43% increase at 20Hz. However, this is still at a very small scale with a total change in tan δ, from Stage 1 to Stage 5, of 0.004 at 1Hz and 0.007 at 20Hz.

4.4. Discussion

Firstly, comparing both coating systems tested, it is clear that coating C1 fails in a predictable manner, the erosion pattern and wear progresses as expected according to the mass loss plot, as shown in Figure 4.2. Coating B fails in a more irregular way, there is no clearly defined, repeated progression from one erosion stage to the next. Visual inspection assessment via surface photographs, as well as the error bars attached to the data points presented, show this to be the case. The error bars attached to the mass plots for coating B show an error range of up to ±2.35% at Stage 4, whereas for coating C1 the range is ±0.05%. This range represents a 95% confidence limit in mass measurements recorded, showing that there is a 95% certainty that all measurements made, at that particular stage, will fall between the error bars. Therefore, a smaller error bar range represents a greater certainty of the measurement.

The application of each coating system differed in that coating B required a thin layer of filler applied to the composite, which after curing, was sanded right

back to the composite surface before further coating system layer applications. The filler layer in coating B then acted as a pore filler for the composite substrate, rather than providing an additional layer for the coating system. This resulted in a much lower total specimen thickness, coating B averaged 3.15mm thick and coating C1 averaged 4.59mm thick. This presents a difference of 1.44mm in total coating system thickness, as the same composite substrate was used for all testing.

The rapid failure and progression of erosion on coating B is due to a combination of two factors. Firstly, the poor adhesion of the coating system itself. This has led to layers of the system separating and splitting, ultimately resulting in their removal from the specimen. Secondly, the nature of the ETC RET rig. The RET rig at ETC uses a single, radially distributed, circumference of needles to produce the rain droplets. This creates rain droplets which strike the specimen in almost the exact same location each time, resulting in a much-accelerated erosion process versus erosion rigs of other design, such as the R&D A/S type.

From observing the microscopy images, there is a pattern in which both coating systems erode. The erosion begins as small pinholes on the surface of the coating, this is likely a result of surface defects which are present during Stage 1. As the erosion progresses, due to further RET, these pinholes deepen and become enlarged in surface area. Stage 2 erosion presents a defined change in the surface micro-structure, a change which is not observable to the naked eye. The enlarged pits then collate and join together to create much larger pits with shear edges which often result in a fracture. As the newly created pits are rough and jagged in shape, this creates vulnerability within the coating system for further erosive attack. Once the filler layer of the coating system has been exposed, the system will fail and promptly reach Stage 5 erosion. The filler layer has very poor erosion resistance. Once Stage 5 erosion is reached on a wind turbine blade, this then poses a structural risk to the integrity of the blade.

With regards to quantifying erosion, mass loss measurement offers an insight into evaluating the change in the specimen due to erosion. Though, typically, mass loss measurement does not offer any value until the test specimen has reached beyond the incubation period. There is no way of assessing how far into the incubation period the specimen is, only when the specimen has gone through the incubation period and into active erosion. Additionally, the mass loss measurement methodology cannot be used on a real-world application of a wind turbine blade. It is not feasible to remove a wind turbine blade and measure its mass to track any erosion. However, the gloss measurement methodology, discovered and developed during this work, offers a quantification method for coating erosion on test specimens which can also be applied to a real-world wind turbine blade. Moreover, the gloss measurement methodology allows surface microstructure changes during the incubation period to be detected and quantified, giving valuable information on coating degradation rate. The difference in mass measurement versus gloss measurement is evident from Figure 4.31. Gloss offers a much wider range of detectability, which in turn increases the accuracy of the assessment of erosion.

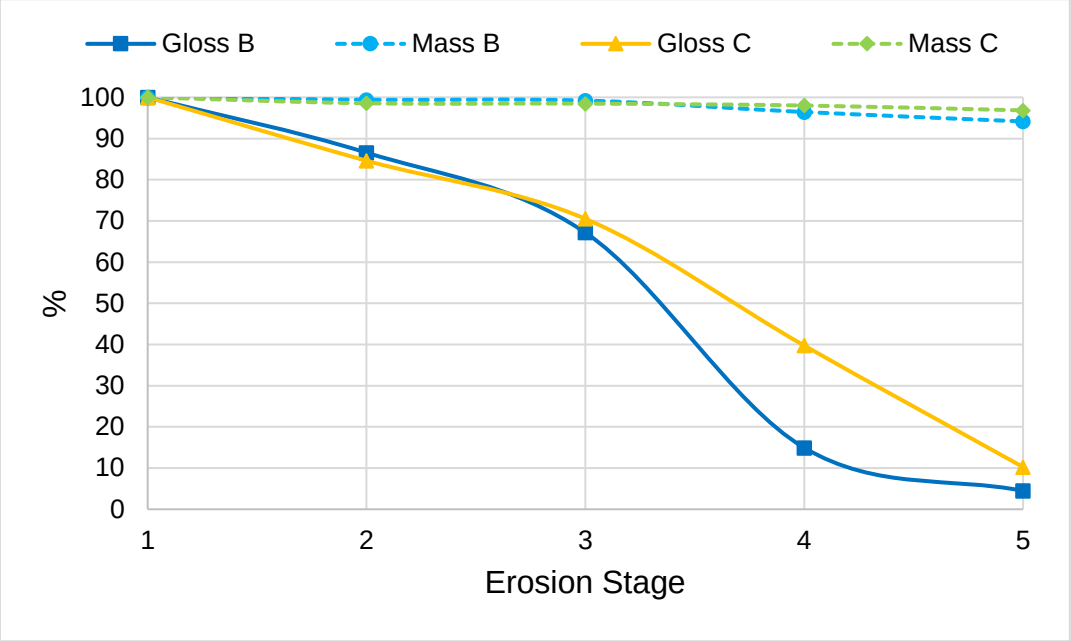

Figure 4.31: Gloss and Mass at Each Erosion Stage

Upon reflection, DMA testing does not offer any meaningful input to the understanding of the coating degradation. The specimens tested consisted of GFRP substrate, as to replicate a wind turbine blade as closely as possible. However, this led to the DMA results being dominated by the substrate and not showing much, if any, change in the coating system.

Due to the nature of the erosion testing, the geometry of the specimen was changed at each erosion stage. This change cannot be accounted for in the DMA as DMA assumes a perfect cuboid at each measurement. Additionally, the DMA also assumes a uniform, homogenous test specimen. As described in Chapter 3, the test specimens used were a multi-material, multi-layered, coated composite.

In order to better the DMA test, the coating system would need to be run in isolation, without the substrate, to each erosion stage. This then poses a problem and raises the question, how would the erosion stages be accurately replicated in RET without the substrate? If only the coating system was tested in RET, this would not reflect current testing best practice and real-world

application. Additionally, coating system testing in RET, solely in isolation, would likely reach erosion stage 5 very quickly.

4.5. Rain Erosion Summary

Wind turbine blade coating system erosion due to water droplet impacts has a detrimental impact on the structural integrity of a wind turbine blade. Erosion starts as small pinholes which then lead on to become larger holes resulting in sections of coating removal, exposing the blade substrate.

Rain erosion causes textural changes in the coating system surface microstructure before any changes are visible to the naked eye or are easily detectable using mass loss. However, gloss measurement allows for these textural changes to be detected, without the need for a microscope. Additionally, the glossmeter is an inexpensive, handheld device which can be used on a wind turbine blade to measure the state of erosion, as well as in the laboratory.

Future work in the area of RET for wind blade coating systems should include the creation of a catalogue of gloss measurements for various coating systems at all stages of erosion. This would allow wind turbine owners and operators to obtain an exact measurement of the state of erosion on an operational wind turbine, with the use of a glossmeter.

In the near future, it is likely that drones and climbing robots will become more prevalent in wind turbine inspection and maintenance. The glossmeter tool could be encompassed into these robots, allowing a fully remote, quantitative assessment of the blade’s condition.

Chapter 5 - Weathering Impact Assessment

Weathering is a key factor which affects the degradation of wind turbine blades. Wind turbines are exposed to large amounts of UV radiation, moisture and humidity, and temperature ranges, all due to their local operational environment.

This chapter focusses on work which quantifies the effects of weathering on wind turbine blade coating systems. Weathering refers here principally to ultraviolet (UV) radiation, which occurs due to sunlight exposure, and also covers other environmental effects such as temperature and humidity which can occur simultaneously.

Throughout this study, various weathering methods were used over differing timescales, and tests were undertaken in both accelerated and natural states at real time to fully understand the weathering response of the coating systems under consideration. Each coating system was exposed to an accelerated UV weathering cycle (UVa), a modified UV weathering cycle to better reflect conditions observed from the North Sea (NSM), and a predefined period of natural outdoor exposure in real time.

For this study, three coating systems were used and are designated coating B, coating C1 and coating C2. Coating B is the same composition as used in the Rain Droplet Impact Assessment, as detailed in Chapter 3, Section 3.2.1. Coating C1 is the same as in Rain Droplet Impact Assessment, as detailed in Chapter 3, Section 3.2.2, and Coating C2 is the same base coating system as Coating C1 however, the LEP layer has a slightly different composition, which is proprietary information. Both Coating C1 and Coating C2 are provided from the same industrial coatings manufacturer. Coating C2 was included to provide a comparison between the same coating system with a different LEP layer.

A limited number of tests was undertaken as part of the weathering test programme. Due to a finite budget, not all accelerated weathering methods were applied to the various coating systems. All tests were defined, specified and undertaken by the author with the exception of those for Coating B.

Coating B was tested at Element Materials Technology, a provider of materials testing services, in Edinburgh, UK.

Coating C1 & C2 was tested in-house by the author at the coating manufacturer. This gave much more flexibility in what was tested since there were no financial restrictions. Therefore, an additional weathering method was introduced and used on coating C1 & C2. The Xenon-Arc weathering, which is also known as a weatherometer, provides a wider bandwidth of wavelengths for the test, as outlined in Chapter 2, Section 2.5.2.2 and further detailed below. This can enhance the understanding of the coating system degradation by comparing the degradation mechanisms between the standard UV testing and the Xenon-Arc testing and linking the mechanisms back to specific individual test conditions. As access to this test capability was unrestricted, composite substrates, as well as the existing aluminium substrates, were used for coating system C1 testing. This allowed for the effect of substrate type on coating performance during accelerated weathering to be investigated.

The various weathering techniques and methodologies used in this work are detailed below:

UVa – This accelerated weathering cycle was taken from the technical standard BS EN ISO 16474-3, Method A, Cycle 1 [76]. The UVa cycle lasted for a total of 3000 hours, with repeating phases of 4 hours dry and 4 hours condensation. The lamp type used was a UVa-340nm, with irradiance set to 0.83 W/m^2/nm and was only active during the dry phase. During the dry phase, the black panel temperature in the test chamber was set to 60±3°C and during the condensation phase this was set to 50±3°C. The humidity was not controlled, as detailed by the test standard.

Xenon-Arc (Weatherometer) – This accelerated weathering cycle was taken from the technical standard BS EN ISO 16474-2, Method A, Cycle 1 [77]. The Xenon-Arc cycle lasted for a total of 1500 hours, with repeating phases of 102 minutes dry and 18 minutes of water spray. The Xenon-Arc test used a broadband exposure from 300nm to 400nm with an irradiance of 60±2 W/m^2 and a narrowband exposure at 340nm with and irradiance of 0.51±0.02 W/m^2/nm. Both the broadband and narrowband exposure were active during dry and water spray phases. During the dry phase, the black panel temperature was set to 65±3°C, the test chamber temperature was set at 38±3°C and the humidity was set to 50±10%. During the water spray phase, the black panel temperature, the chamber temperature and the humidity were not controlled.

Natural Outdoors – The natural outdoor test was conducted on two sites, roughly 20km apart, both in North East England near the North Sea. Coating B was tested at one site, in Blyth, and coating C1 & C2 tested at the other, located in Gateshead. Coating B was tested for 4400 hours and coating C1 & C2 for 13650 hours.

North Sea Method (NSM) – The North Sea Method, NSM, accelerated weathering cycle was based on a modified version of the technical standard BS EN ISO 16474-3, Method A, Cycle 1 [76]. The standard cycle was modified to include parameters measured in the North Sea. The NSM cycle lasted for a total of 1500 hours, with repeating phases of 4.4 hours dry and 3.6 hours condensation. The lamp type used was a UVa-340nm, with irradiance set to 0.5 W/m^2/nm and was only active during the dry phase. During the dry phase, the black panel temperature in the test chamber was set to 40±3°C and during the condensation phase this was also set to 40±3°C. The humidity was not controlled.

The NSM cycle was developed using 10-minute interval data from the NOAH offshore met mast, provided by Offshore Renewable Energy Catapult. Temperature (°C), humidity (%), rainfall (mm/hr), UVa (W/m^2) and UVb (W/m^2)

data from September 2018 to September 2019 was used in the cycle development.

Rainfall data on a 10 minute, hourly and daily basis was used to determine the amount of time, over the period of the year, where a rainfall event occurred. Similarly for humidity, the amount of time where the humidity was greater than 95% was determined. Both the amount of time per year when a rainfall event occurred and when the was humidity greater than 95% were used to ascertain when the surface would be wet. It was calculated that the surface would be wet 45% of the time, over the year. This was then used to adjust the wet and dry phases in the standard.

Next, the maximum and minimum temperatures from the data were found. The maximum recorded temperature was 24°C and the minimum was -1.5°C. Then, after discussions with the test house, it was found that the minimum operating temperature of the test chamber was 40°C. Therefore, 40°C was selected as the test temperature as to match the NOAH data as closely as practicable.

The lamp type of UVa-340nm was selected to remain the same, to ensure UVa exposure. The UVa data from NOAH was in the form of W/m^2 and was a band of wavelengths, not solely the 340nm for the accelerated test. An estimate of the irradiance at 340nm was determined by comparing the 10-minute UVa data across the year to the irradiance value of the standard BS EN ISO 16474-3, Method A, Cycle 1 test. After consultation with an expert in the field of accelerated weathering testing and the test house, it was then decided to run the NSM cycle with an irradiance of $0.5W/m^2/nm$ at 340nm. This value was selected as lower irradiance values are difficult to control in the test chamber and much higher irradiance values would accelerate the test too much, leading to the possibility of any changes and degradation mechanisms being missed.

5.1. Methodology

Firstly, specimens were prepared as described in Specimen Manufacture and Preparation, Chapter 3, Section 3.2, however, the dimensions of the specimens differed due to the dimension requirements of the accelerated testing equipment. Dimensions of all specimens tested in this work were 76mm by 152mm (3 by 6 inches). Coated specimens which were ready for testing can be seen in Figure 5.1.

Figure 5.1: Weathering Specimen Size

Table 3 outlines the test specimen ID, the coating system applied, the substrate type and the weathering method, all for coating B.

Specimen ID	Substrate Type	Coating System	Weathering Method
BW1	Aluminium	B	UVa
BW2	Aluminium	B	UVa
BW3	Aluminium	B	UVa
BW4	Aluminium	B	UVa
BW5	Aluminium	B	UVa
ODB1	Aluminium	B	Natural outdoors
ODB2	Aluminium	B	Natural outdoors
ODB3	Aluminium	B	Natural outdoors
ODB4	Aluminium	B	Natural outdoors
ODB5	Aluminium	B	Natural outdoors
NSMB1	Aluminium	B	NSM
NSMB2	Aluminium	B	NSM

NSMB3	Aluminium	B	NSM
NSMB4	Aluminium	B	NSM
NSMB5	Aluminium	B	NSM

Table 3: Weathering specimen ID for coating B

Table 4 outlines the test specimen ID, the coating system applied, the substrate type and the weathering method, all for coating type C.

Specimen ID	Substrate Type	Coating System	Weathering Method
A1	Aluminium	C1	UVa
A2	Aluminium	C1	UVa
A3	Aluminium	C1	UVa
A4	Aluminium	C2	UVa
A5	Aluminium	C2	UVa
A6	Aluminium	C2	UVa
A7	Composite	C1	UVa
A8	Composite	C1	UVa
A9	Composite	C2	UVa
B1	Aluminium	C1	Xenon-Arc
B2	Aluminium	C1	Xenon-Arc
B3	Aluminium	C1	Xenon-Arc
B4	Aluminium	C2	Xenon-Arc
B5	Aluminium	C2	Xenon-Arc
B6	Aluminium	C2	Xenon-Arc
B7	Composite	C1	Xenon-Arc
B8	Composite	C1	Xenon-Arc
B9	Composite	C2	Xenon-Arc
C1	Aluminium	C1	Natural outdoors
C2	Aluminium	C1	Natural outdoors
C3	Aluminium	C1	Natural outdoors
C4	Aluminium	C2	Natural outdoors
C5	Aluminium	C2	Natural outdoors
C6	Aluminium	C2	Natural outdoors
NSMC11	Aluminium	C1	NSM
NSMC12	Aluminium	C1	NSM
NSMC13	Aluminium	C1	NSM

NSMC14	Aluminium	C1	NSM
NSMC15	Aluminium	C1	NSM

Table 4: Weathering specimen ID for coating C

Throughout all experiments, several properties were tracked and recorded. These are detailed below.

Photography – Photographs of test specimens were captured using the rear camera on a Samsung Galaxy S9 for coating B and a Canon PowerShot SX620 was used for coating C. Before any photographs were taken, the specimen surface was wiped with a wet paper towel to remove any surface debris and left to dry for 1 hour.

Gloss – The 60° angle was used on the Rhopoint IQ (Goniophotometer) 20°/60°/85° to measure the surface gloss at each test interval. For each specimen five gloss measurements were made, which were the averaged to obtain a single specimen measurement.

Colour – Coating surface colour was measured using a Varian Cary 5000 UV-VIS-NIR Spectrophotometer for coating B and a Datacolour 600 Spectrophotometer for coating C. For each specimen, three colour measurements were made. The three measurements were then averaged to get a specimen colour change.

FTIR Spectroscopy – The chemical bonding was measured using an Agilent Technologies 4100 FTIR for coating B and a ThermoScientific Nicolet iS10 FTIR for coating C. Three scans were takes per specimen, these were then averaged to get a specimen result.

5.1.1. UVa Testing

The accelerated UVa test cycle was conducted in a Q-Lab QUV Accelerated Weathering Tester, shown in Figure 5.2. This test lasted for 3000 hours, and each sample was analysed every 500 hours. Coating B was tested at Element Materials Technology and coating C1 & C2 was tested in-house at the coating

manufacturer's facility. Additionally, coating C1 & C2 was further tested by continuing the cycle to a total of 7500 hours test duration, with 1000-hour analysis periods.

Figure 5.2: QUV Accelerated Weathering Chamber

5.1.2. Xenon-Arc Testing

The Xenon-Arc testing was performed solely on coating C1 & C2. The accelerated Xenon-Arc test cycle was conducted using a Q-Lab Q-Sun Xe-3 Xenon Test Chamber, onsite at the coating manufacturer's facility. This test lasted for 1500 hours, with analysis after every 500-hour period. The test was then extended and continued until 6000 hours, with analysis after every 1000-hour period.

5.1.3. Natural Outdoors Testing

Firstly, the natural outdoor samples were placed in a weathering rack, of Q-Rack type design, fixed at 45° to the ground and facing directly south to capture the greatest amount of sunlight. These samples were left outdoor, on-test, for as long as possible in order to capture any effects due to natural sunlight and local weather conditions.

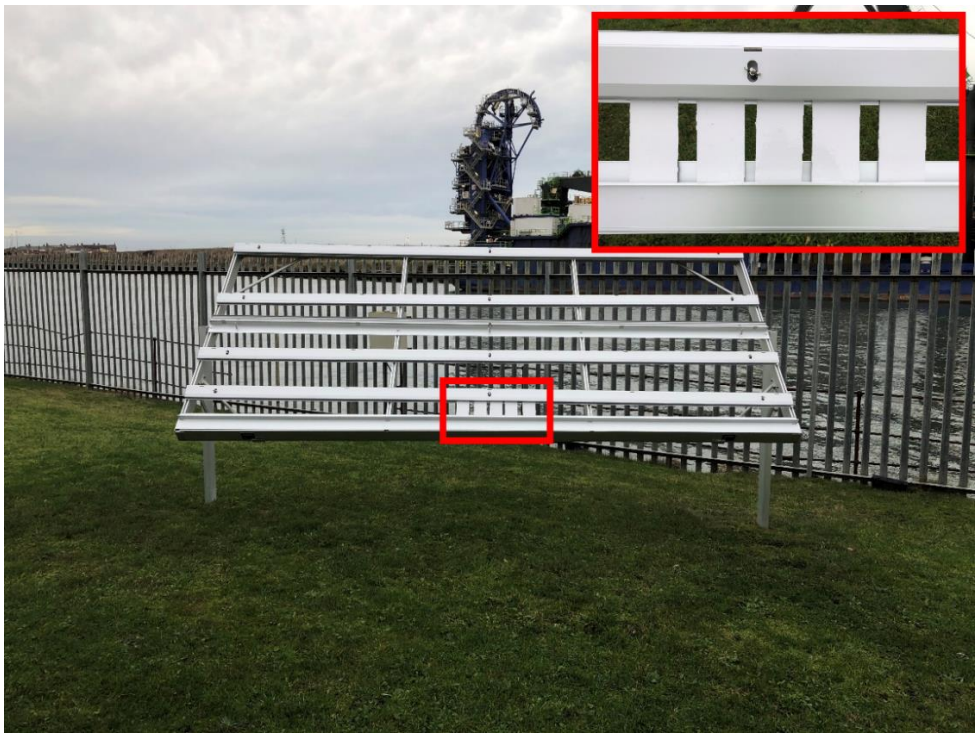

Figure 5.3: Natural Outdoors, Coating B, Blyth. Red box highlights sample location.

Figure 5.4: Natural Outdoors, Coating C, Gateshead. Red box highlights sample location.

Coating B, shown in Figure 5.3 was tested onsite at OREC, Blyth and coating C1 & C2, shown in Figure 5.4 was tested onsite at the coating manufacturer in Gateshead.

Testing of coating B commenced on 23rd November 2020 and ran until 8th July 2021, a period of approximately 4750 hours. Samples were analysed using photographs, gloss, colour and spectroscopy both before and after the test.

Testing of coating C1 & C2 commenced on 12th February 2020 and ran until 2nd September 2021, a period of approximately 13650 hours. Samples were analysed using photographs, gloss, colour, and spectroscopy before test began and then every 500 hours from then on until the test was complete. However, there was no analysis conducted between 10th March 2020 and 9th September 2020, a period of approximately 4400 hours, due to restricted site access during the COVID-19 pandemic.

5.1.4. North Sea Method Testing

The North Sea Method test cycle was conducted in a Q-Lab QUV Accelerated Weathering Tester, the same equipment at the standard UVa cycle. This test lasted for 1500 hours, and each sample was analysed every 500 hours. Both coating B and coating C1 were tested at Element Materials Technology.

5.2. Weathering Results

The results section is divided into subsections of each analysis technique used, as well as per each coating system tested. Firstly, photographs of each coating system are presented, followed by the gloss measurements. Then the colour change and spectroscopy plots are shown. Each subsection presents the data for Coating B, then Coating C1 and concludes with Coating C2.

5.2.1. Photographs

In this section, only photographs from the beginning and end of test, for each weathering method are presented. All data is presented for coating B. For coating C1 and C2, intermediate analysis photographs are located in Appendix B.

5.2.1.1. Photographs: Coating B

Figure 5.5: Photograph, Coating B, UVa, Start of Test (0hrs)

Figure 5.6: Photograph, Coating B, UVa, End of Test (3000hrs)

The comparison of photographs of coating B specimens taken before and after the UVa weathering cycle, Figure 5.5 and Figure 5.6 respectively, show that the accelerated UVa cycle causes a physical surface change in the coating system. After the period of UVa weathering, the surface begins to bruise where darker patches of surface coating develop.

Figure 5.7: Photograph, Coating B, Natural Outdoors, Start of Test (0hrs)

Figure 5.8: Photograph, Coating B, Natural Outdoors, End of Test (4750hrs)

Looking at the naturally weathered specimens, Figure 5.7 and Figure 5.8, there is not much change between the start of test specimens and the end of test specimens. Some surface staining is present along the top of the specimens, just below the hole, in a linear pattern. This is due to the mounting fixture of the test rack which holds the specimens in place. The mounting fixture would secure the samples along this line. Therefore, it can be reasonably assumed that the observed staining is due to dirt and grime collection along the mounting fixture.

Some other darker marks are present on a few of the specimens at the end of the test. Upon close inspection, these marks look like scuffs on the specimen.

Figure 5.9: Photograph, Coating B, NSM, Start of Test (0hrs)

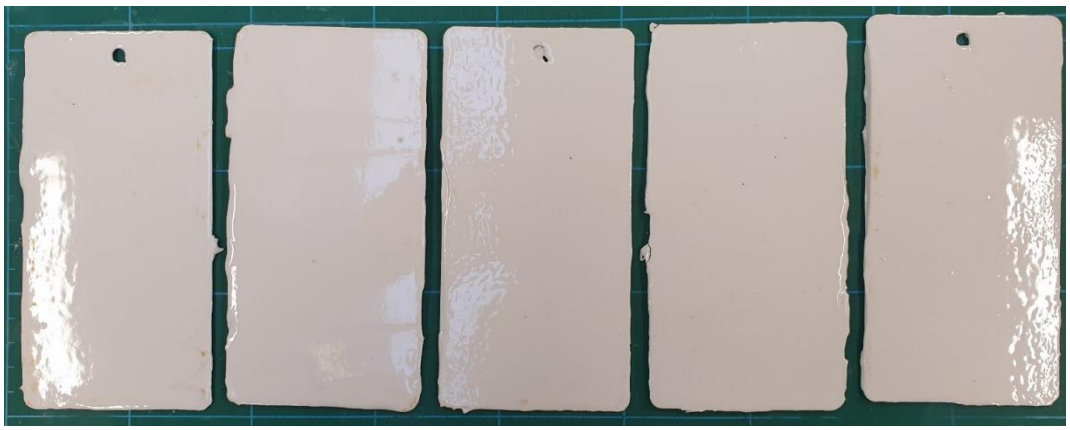

Figure 5.10: Photograph, Coating B, NSM, End of Test (1500hrs)

Next, the comparison of photographs for the North Sea Method of coating B. The start of test photographs are shown in Figure 5.9 and the end of test are shown in Figure 5.10. The specimens remain largely unchanged in their appearance, this is likely due to the shorter duration of the test at 1500 hours, versus the standard UVa cycle as well as the NSM cycle using lower irradiance and temperature values. Upon close inspection there are small dark marks which appear after on the specimen surface after the test, again, similar to the previous weathering tests.

The dark marks which appear on the specimen surface of coating B after each weathering test are likely a resultant factor of exposure to UV radiation and/or humidity.

5.2.1.2. Photographs: Coating C1

Figure 5.11: Photograph, Coating C1, UVa, Start of Test (0hrs)

Figure 5.12: Photograph, Coating C1, UVa, End of Test (7500hrs)

Figure 5.11 and Figure 5.12 show coating C1 under UVa weathering at the beginning and end of the test. Overall, there is no drastic change in the surface appearance of the specimens. Some small dark marks have appeared throughout the test.

Figure 5.13: Photograph, Coating C1, Xenon-Arc, Start of Test (0hrs)

Figure 5.14: Photograph, Coating C1, Xenon-Arc, End of Test (6000hrs)

Looking at the Xenon-Arc test of coating C1, Figure 5.13 and Figure 5.14Figure 5.15, it is clear that at the end of the test, there is a noticeable change in the surface appearance. Firstly, the surface is no longer shiny and glossy, it appears more matt. Also, a large crack had developed on one of the specimens on the left hand edge half way up.

Figure 5.15: Photograph, Coating C1, Natural Outdoors, Start of Test (0hrs)

Figure 5.16: Photograph, Coating C1, Natural Outdoors, End of Test (13650hrs)

Next, the naturally weathered samples, Figure 5.15 and Figure 5.16, show a distinct surface appearance change after weathering. The lines which are present on the sides of each specimen are due to the tape used to hold the specimens to the test rack, the middle area of the sample should be considered for analysis. Surface staining is apparent as well as surface debris. Both are likely due to the test location, near a wooded area. Leaves and branches are known to fall from the surrounding trees onto the specimens.

Figure 5.17: Photograph, Coating C1, NSM, Start of Test (0hrs)

Figure 5.18: Photograph, Coating C1, NSM, End of Test (1500hrs)

Then, looking at the North Sea Method test specimens for coating C1 shown in Figure 5.17 and Figure 5.18, there is very little visually observable difference between the start and end of test. However, there are a few small bruise marks which appear on some of the test specimens, but no significant observable change. This is primarily due to the reduced test duration of 1500 hours as well as the reduced irradiance intensity of the test.

5.2.1.3. Photographs: Coating C2

Figure 5.19: Photograph, Coating C2, UVa, Start of Test (0hrs)

Figure 5.20: Photograph, Coating C2, UVa, End of Test (7500hrs)

Looking at the UVa weathering of coating C2, Figure 5.19 and Figure 5.20 show the beginning and end of test. The most noticeable change is that of the formation of a crack at the top of one of the specimens as a result of the accelerated weathering. Aside from the crack, there is no obvious visual difference in the start and end of the test.

Figure 5.21: Photograph, Coating C2, Xenon-Arc, Start of Test (0hrs)

Figure 5.22: Photograph, Coating C2, Xenon-Arc, End of Test (6000hrs)

Next, the Xenon-Arc weathering of coating C2 shown in Figure 5.21 and Figure 5.22. The surface of the specimens after the weathering test appears to be more matt and less glossy. Additionally, there is a small crack developing at the top of one of the samples.

Figure 5.23: Photograph, Coating C2, Natural Outdoors, Start of Test (0hrs)

Figure 5.24: Photograph, Coating C2, Natural Outdoors, End of Test (13650hrs)

Now looking at the Natural Weathering of coating C2, shown in Figure 5.23 and Figure 5.24. Lines are present at the sides of the specimens, as well as

some residue tape, as a result of the tape used to fix the specimens to the test outdoor rack. Therefore, the middle area of the specimens should be used for analysis. Light surface staining as well as some surface debris is present on the specimens. This is a result of the test location near a wooded area where leaves and branches can fall on the specimens.

Figure 5.25: Photograph, Coating C2, NSM, Start of Test (0hrs)

Figure 5.26: Photograph, Coating C2, NSM, End of Test (1500hrs)

Then, looking at the North Sea Method test specimens for coating C2 Figure 5.25 and Figure 5.26, again, there is very little, if any, visually observable difference between the start and end of test. This is primarily due to the reduced test duration of 1500 hours as well as the reduced irradiance intensity of the test.

5.2.2. Gloss

This subsection presents the gloss data for each coating system tested and includes the results for each weathering method used. All gloss data presented uses the gloss measurement angle of 60°.

5.2.2.1. Gloss: Coating B

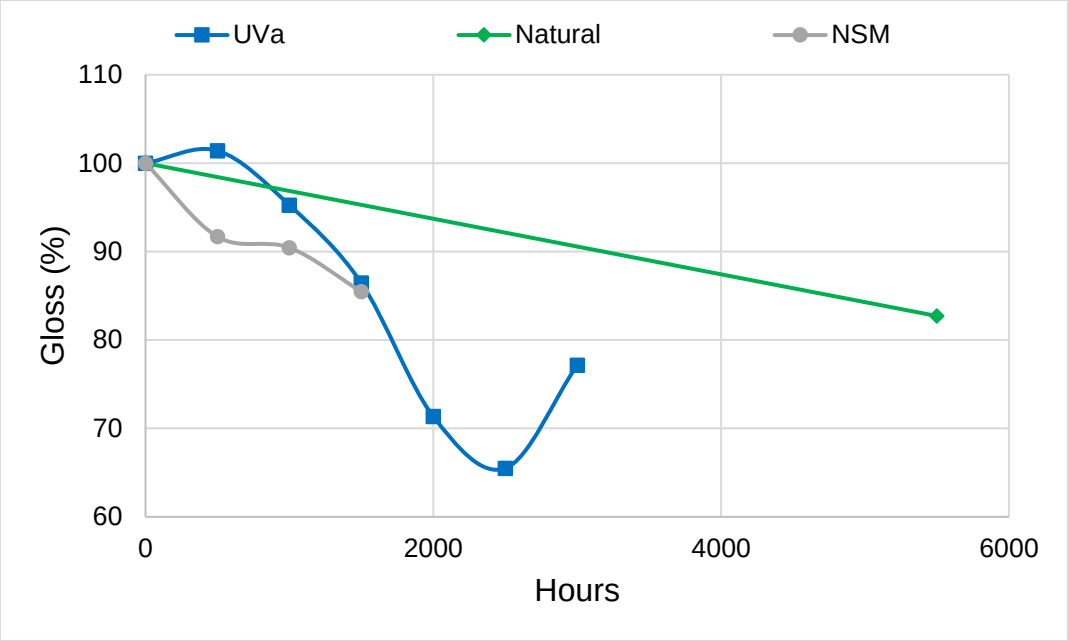

Figure 5.27: Gloss 60°, Coating B, All Weathering Methods

Considering the gloss measurements taken for coating B throughout all weathering methods used, Figure 5.27 presents these in the form of percentage change of gloss value against test duration in hours. Firstly, the accelerated UVa cycle has caused the gloss level to decrease by approximately 30% as the test progresses. However, there was a slight increase of 1.4% at the first assessment period and then, at the last assessment period of 3000 hours, the gloss value increased by 11.7%. Moving on to the NSM cycle, there was an overall decrease in the gloss measurement over the assessment periods, however only a small decrease of 1.2% was recorded between 500 hours and 1000 hours. Lastly, in the natural outdoor

cycle only two datapoints were captured which showed a decrease in gloss of 17.3% over the 5500 hours on test.

5.2.2.2. Gloss: Coating C1 & C2

Results presented in this section are subdivided by weathering method type, this to allow easier viewing of all data. Additionally, each coating system and substrate type is denoted as follows: Coating C1 with aluminium substrate – C1 Al, Coating C2 with aluminium substrate – C2 Al, Coating C1 with composite substrate – C1 Comp, and Coating C2 with composite substrate – C2 Comp.

All gloss measurements presented are displayed as a percentage of initial gloss values, the gloss measurement taken before any weathering occurred, against the duration of test in hours.

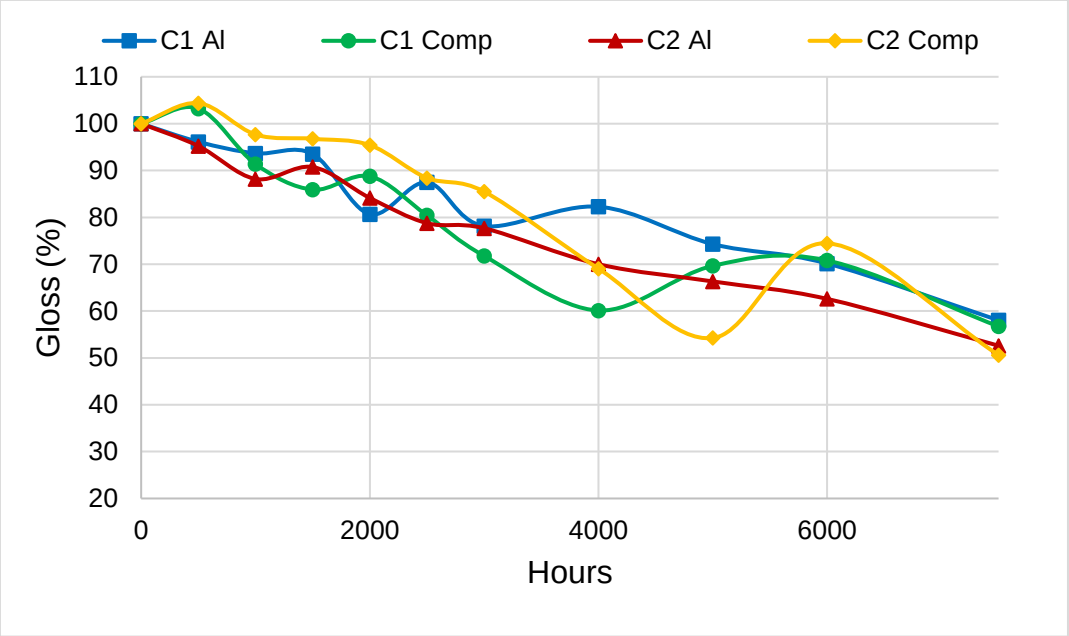

Figure 5.28: Gloss 60°, Coating C1 & C2, UVa Weathering

Considering Figure 5.28, the UVa weathering cycle gloss data for coating C1 and C2, on both composite and aluminium substrate, is illustrated. As a general overview, the gloss value decreases as the UVa weathering cycle progresses. Looking specifically at coating C1, on aluminium substrate there

is an overall decrease of 42.0% after 7500 hours on test, comparing this to the composite substrate, there is a 43.3% decrease. However, throughout the total duration of the test the differences in gloss between aluminium and composite substrate vary. Noting, that for the majority of analysis periods of coating C1, the gloss of the composite substrate is less than that of the aluminium substrate. The reverse is true of coating C2, where the gloss of the composite substrate is greater than that of the aluminium substrate for the majority of analysis periods. Upon test completion at 7500 hours, coating C2 on aluminium substrate has loss 47.4% of the initial gloss and coating C2 on composite substrate has lost 49.4%.

Comparing coating C1 and C2, on aluminium substrate they showed similar gloss loss until around 3000 hours on test, then coating C2 displayed a difference of 5.4% less than coating C1 by the end of the test. Looking at the composite substrate comparison of coatings C1 and C2, there is a clear difference throughout the majority of analysis periods, where coating C1 has shown a greater gloss loss than coating C2.

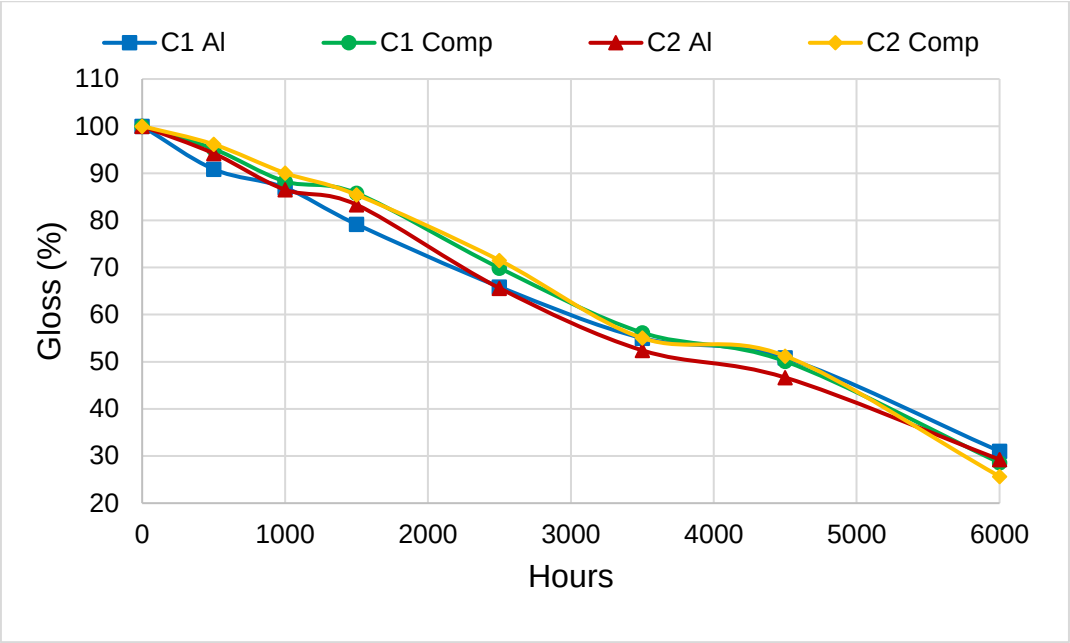

Figure 5.29: Gloss 60°, Coating C1 & C2, Xenon-Arc Weathering

Looking at the gloss results for the Xenon-Arc accelerated weathering test, which are shown in Figure 5.29, it can be seen that all specimens lose gloss with a similar trend. Throughout the majority of the test, the aluminium substrate specimens present a lower gloss measurement than the composite substrate specimens. At 2500 hours, there is a difference of 4.0% in coating C1 and a difference of 5.9% in coating C2 between composite and aluminium substrates. At the end of the test at 6000 hours, the aluminium substrate shows a small increase in gloss than that of the composite substrate. The gloss measurement for the aluminium substrate for coating C1 is 1.7% more than the composite substrate, and for coating C2, the aluminium substrate is 3.5% more.

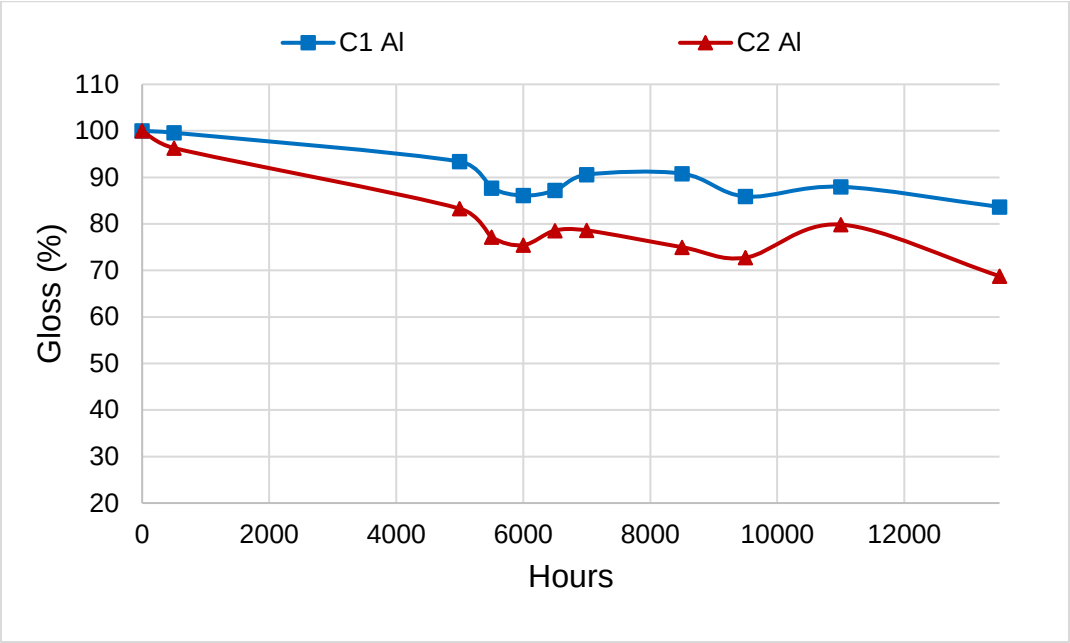

Figure 5.30: Gloss 60°, Coating C1 & C2, Natural Weathering

Now, looking at the gloss for natural outdoor weathering, which is shown in Figure 5.30, it is observable that there is a difference in gloss measurement between coating C1 and C2 throughout the test, with coating C2 recording a lower gloss value than C1 at every analysis period. The average difference throughout the test is 8.3%, with the end of test difference of 11.8% at 13500 hours.

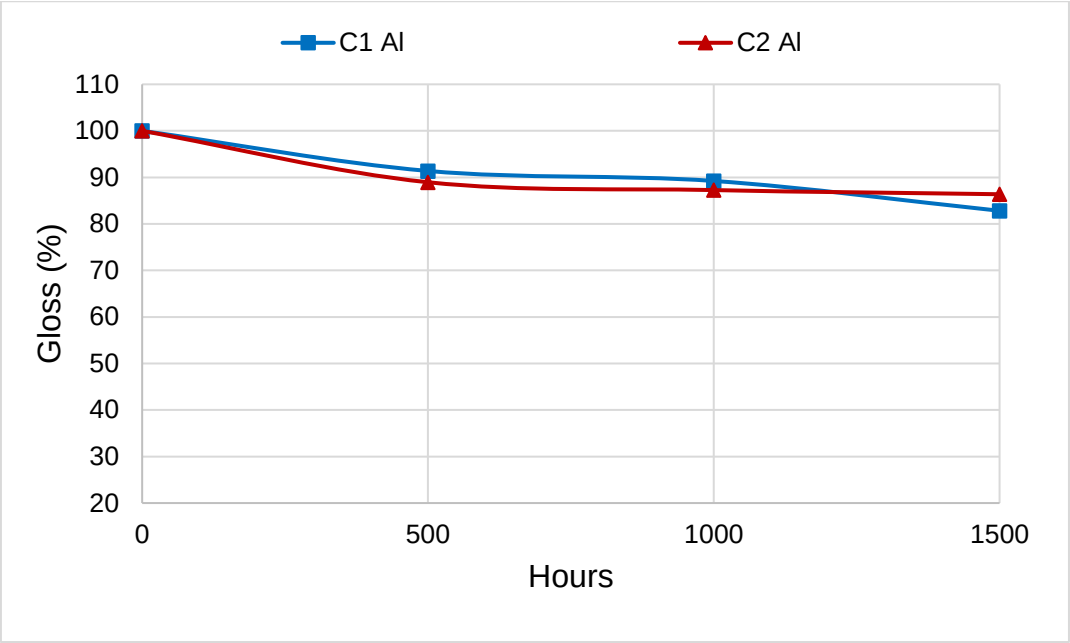

Figure 5.31: Gloss 60°, Coating C1 & C2, NSM Weathering

Then finally, looking at the gloss measurements for the North Sea Method weathering cycle, which is displayed in Figure 5.31, the gloss values recorded are similar for both coating C1 and C2 throughout the test, with coating C1 recording an increase of 2.4% and 1.9% at 500 hours and 1000 hours respectively over coating C2. At the end of the test at 1500 hours, there is a total difference of 3.6% between coating C1 and C2, where the gloss measurement of coating C2 is greater than coating C1.

5.2.3. Colour

Two different types of colour analysis were used, this dependent on the availability of equipment at the analysis location. UVa testing of coating B was performed externally, where the CIELAB colour space analysis was used. Additionally, the colour analysis of coating C1 and C2 under UVa, Xenon-Arc and Natural Weathering testing was also analysed using the CIELAB colour space, at the manufacturers on site laboratory. The remaining analysis, coating B natural and NSM, as well as coating C1 and C2 NSM were performed using absorbance spectra at the University of Strathclyde. Within the CIELAB colour space, the ΔE^* parameter is a measure of total colour

change, according to Equation 3.1, as discussed in Colour Measurement, Chapter 5, Section 5.1.

Tables showing all colour change values, including ∆*E**, *L*, a** & *b** parameters, for all colour measurements obtained are located in Appendix C - .

5.2.3.1. Colour: Coating B

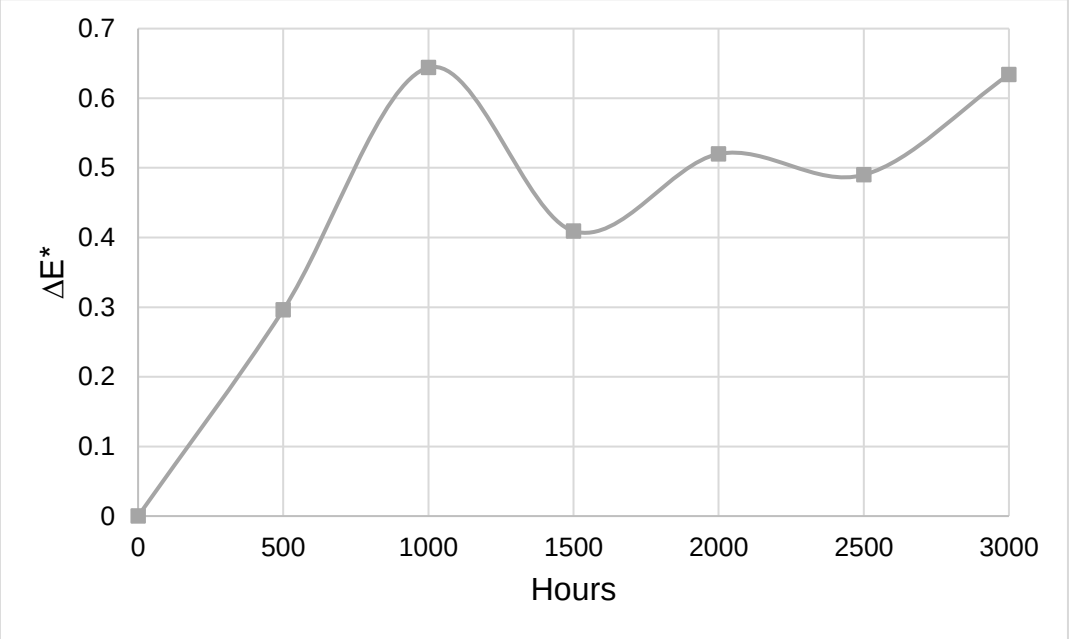

Figure 5.32: Colour in CIELAB, Coating B, UVa Weathering

Firstly, the colour differences measured during the UVa weathering cycle of coating B are shown in Figure 5.32. Initially, during the first 1000 hours on test there is a sharp increase in colour change up to a maximum ∆E* value of 0.64. The colour change then decreases at 1500 hours, meaning that the colour change has a lesser magnitude between 0 and 1500 hours than there was between 0 and 1000 hours. The colour change then slowly increases towards the end of test at 3000 hours where the overall colour change was recorded at an ∆E* value of 0.63.

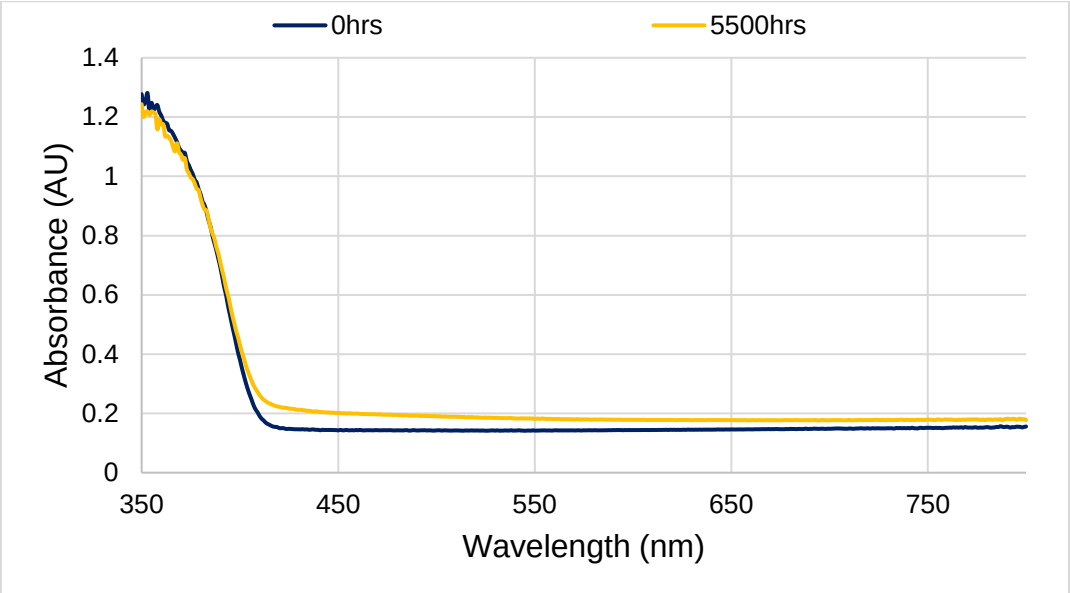

Figure 5.33: Colour as spectra, Coating B, Natural Weathering

Next, looking at the colour change due to natural outdoor weathering of coating B, as shown in Figure 5.33. First point to note is that only two measurements were made during this test, one before the test began and one after the test was complete. There is a noticeable difference in the spectra presented, indicating that a colour change has occurred, particularly between 410nm and 500nm. This difference in the 400-500nm region indicates an increase in the blue/violate region of the spectra, which in turn demonstrates that the coating has shown an increase in blue/violate colour as a result of the test. The resultant colour difference is calculated at 0.078, according to Equation 3.2.

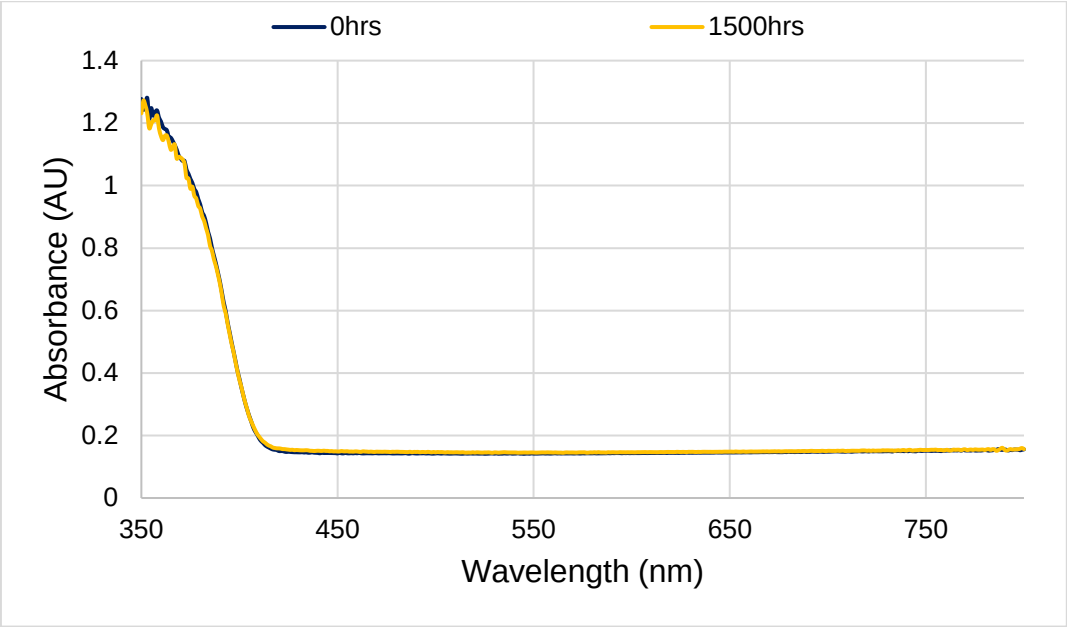

Figure 5.34: Colour as spectra, Coating B, NSM Weathering

Then, looking at Figure 5.34 which illustrates the colour change due to the North Sea Method weathering cycle of coating B. Again, a point to note is that only two measurements were made during this test, one before the test began and one after the test was complete. The spectra measured stack on top of each other, indicating that there is very little to no change in colour due to the North Sea Method cycle. This is reflected in the very small colour difference measurement of 0.007, calculated as in Equation 3.2.

5.2.3.2. Colour: Coating C1 & C2

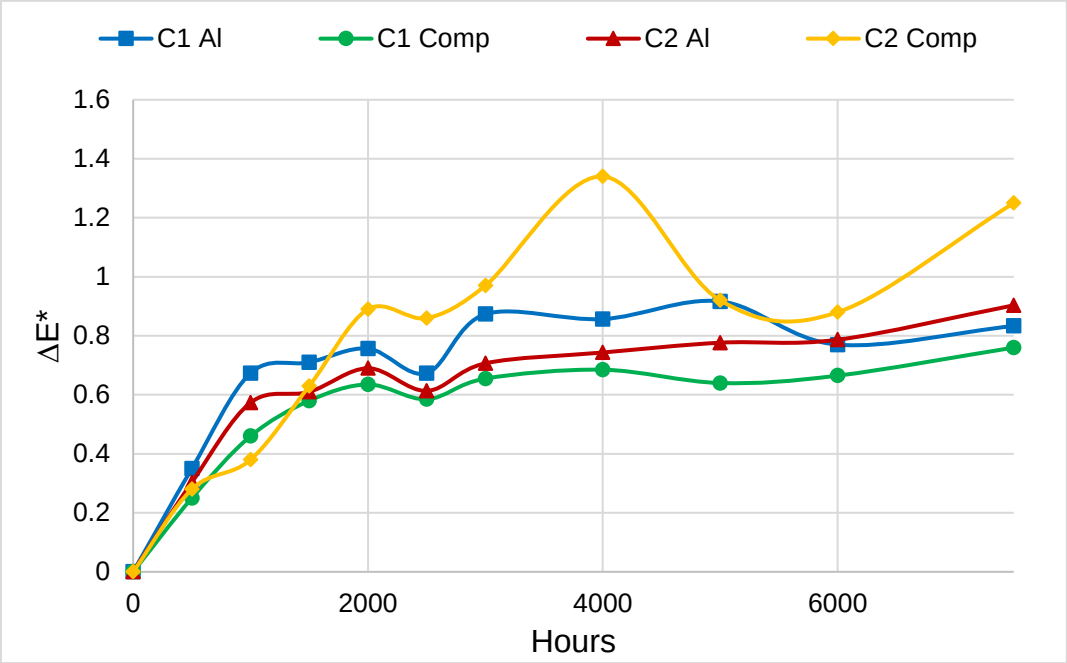

Figure 5.35: Colour in CIELAB, Coating C1 & C2, UVa Weathering

Figure 5.35 presents the colour data for the UVa weathering cycle for coatings C1 and C2, on both aluminium and composite substrates. Firstly, looking at coating C1, the aluminium substrate shows a greater colour difference than the composite substrate with a maximum difference in ΔE* of 0.28 at 5000 hours. Beyond the initial 1500 hours of test, the total colour change value ΔE*, for coating C1 on both the aluminium and composite substrate, begins to level off. There is a difference of 0.12 in ΔE* for the aluminium substrate and 0.18 in the composite substrate between 1500 hours and the end of test at 7500 hours.

Next looking at coating C2, the first observation is a large variation in colour difference between the aluminium and composite substrate, which was greatest at 4000 hours where the difference measured of 0.56. Coating C2 on aluminium substrate followed a similar trend to coating C1, where after 1500 hours the colour difference levelled out with a difference of 0.31 between 1500 hours and the end of test. Coating C2 on composite substrate showed high

variation in colour difference throughout the test, presenting a difference of 0.62 between 1500 hours and the end of test.

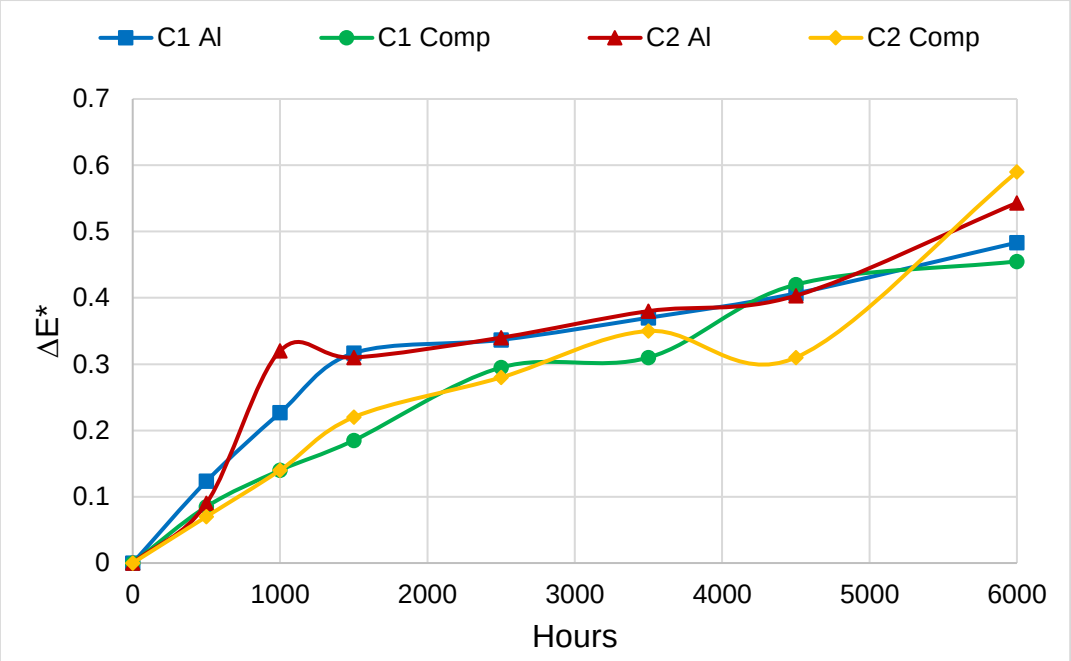

Figure 5.36: Colour in CIELAB, Coating C1 & C2, Xenon-Arc Weathering

Moving on to the colour change due to Xenon-Arc weathering of coating C1 and C2 which is shown in Figure 5.36. For all specimens measured, there is a gradual increasing trend in colour change throughout the test. Comparing coating C1 on the aluminium substrate and composite substrate, there is a greater colour difference shown on the aluminium substrate throughout the test. The difference is largest at 1500 hours where coating C1 with the aluminium substrate shows a colour difference value, ΔE*, of 0.13 more than the composite substrate. Similarly, coating C2 shows a distinction between the aluminium and composite substrate, with the aluminium substrate displaying a greater colour change until the last analysis period where the composite substrate showed a greater colour change than the aluminium.

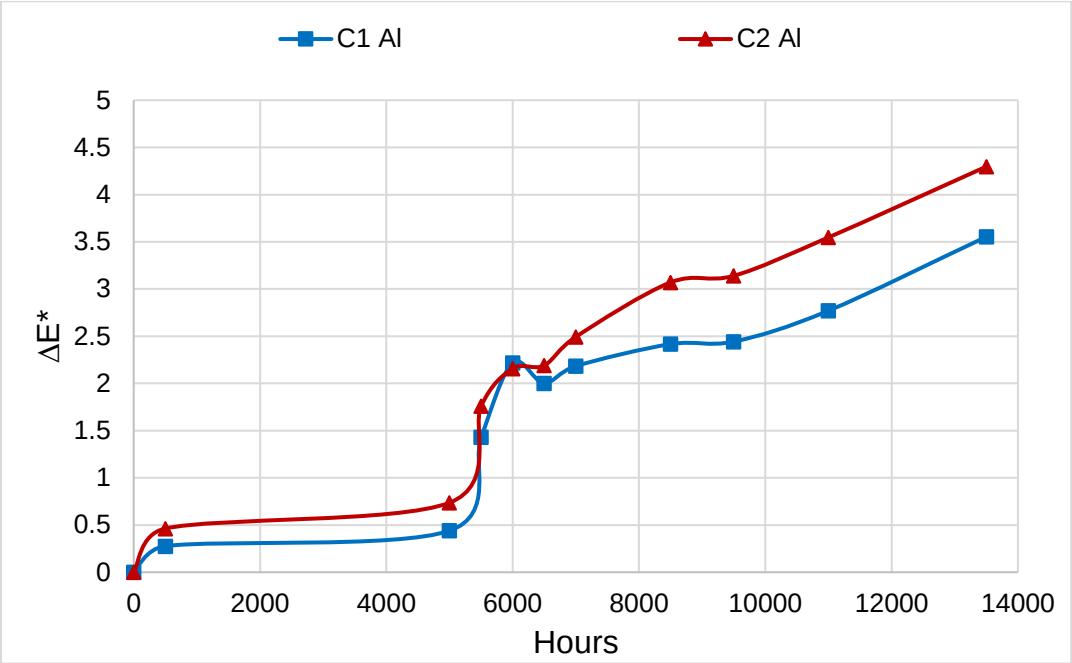

Figure 5.37: Colour in CIELAB, Coating C1 & C2, Natural Weathering

Then, looking at the colour change due to Natural Weathering of coatings C1 and C2 on aluminium substrate, as presented in Figure 5.37. For both coatings, there is a large colour change value, ΔE*, which increases as the test progresses. This is due to the location of the test specimens as well as the nature of the test. The test was located near a wooded area, where leaves and debris were prone to falling on to the specimens, resulting in surface staining and a large colour change value. Additionally, the outdoor nature of the test location exposed the specimens to any amount of interference from animals, birds and insects, which could result in surface staining, residue or debris.

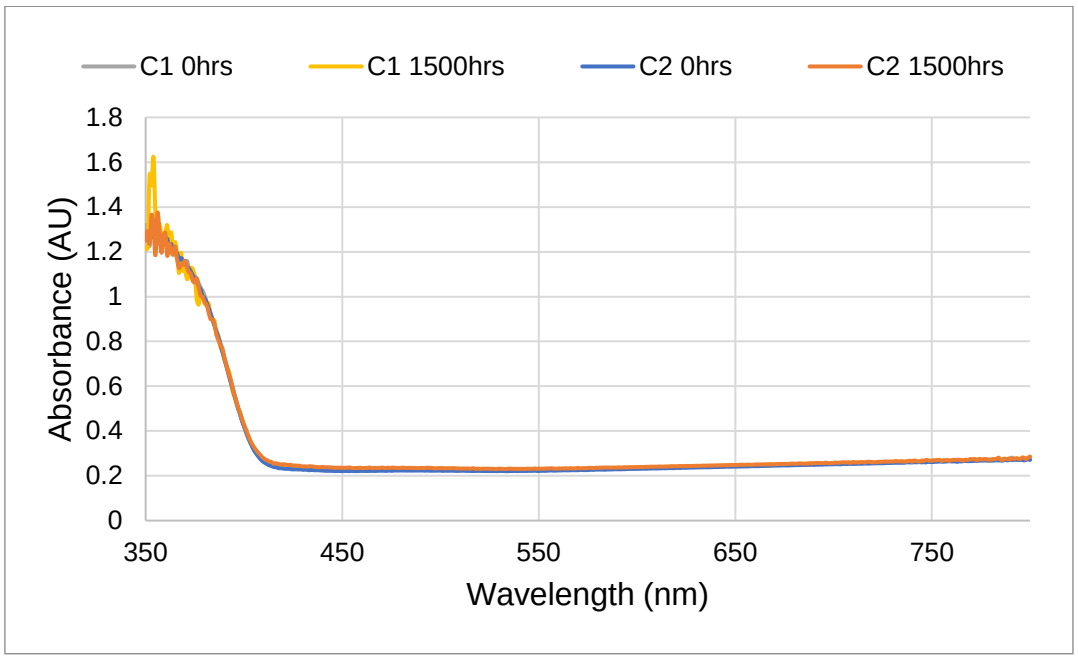

Figure 5.38: Colour as spectra, Coating C1 & C2, NSM Weathering

Finally, looking at the colour change due to the North Sea Method accelerated weathering, where Figure 5.38 presents the results of the test. One point to note is that only two measurements were made per specimen, one at the start of the test at 0 hours and one at the end of the test at 1500 hours. As is observable from Figure 5.38, there is no major change in the spectra from the start and end of the test, only a very small increase in absorbance from 400nm to 500nm, indicating a slight increase of violate and blue colour due to the test. The calculated coloured difference, according to Equation 3.2, for coating C1 is 0.005 and for coating C2 is 0.008.

5.2.4. Spectroscopy

Data obtained through FTIR analysis was processed using Spectragryph software, version 1.2.15 [78]. The spectroscopy figures presented were also produced using Spectragryph software.

In all spectra presented, only a section of 1000 cm^{-1} to 1800 cm^{-1} is shown on each figure. Above 1800 cm^{-1} no changes in spectra were observed and below 1000 cm^{-1} lies the “fingerprint region” where lots of absorptions occur, which

causes a large amount of noise in the signal detected, rendering this section of the signal not useful for interpretation. Full spectra, wavenumbers 500 cm^{-1} to 4000 cm^{-1}, for all specimens are presented in Appendix D -.

5.2.4.1. Spectroscopy: Coating B

The spectra for coating B were all normalised about the highest peak present in the spectra, 1249 cm^{-1}, to allow direct comparison between analysis periods.

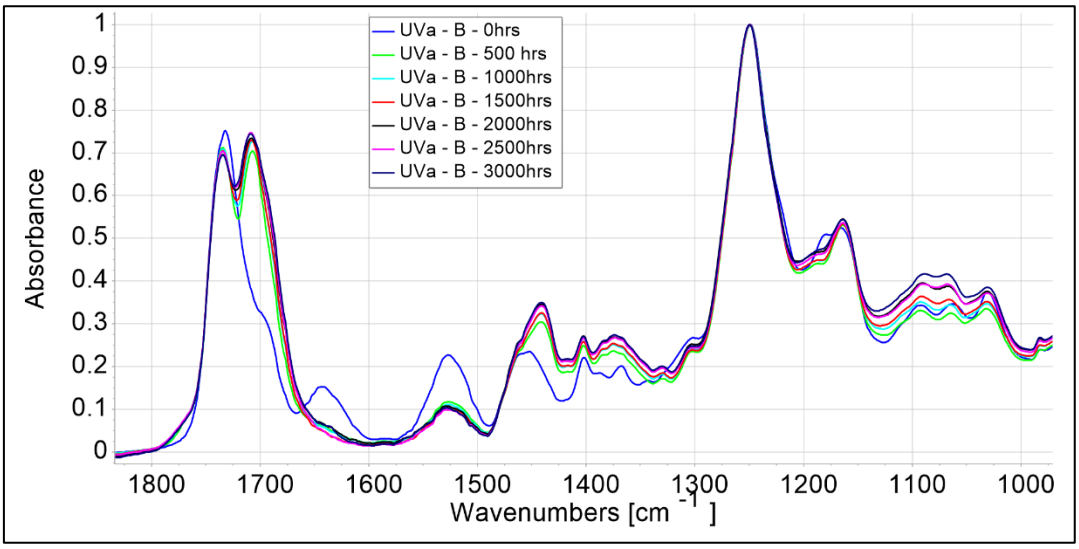

Figure 5.39: FTIR, Coating B, UVa Weathering

Figure 5.39 presents the FTIR spectra for UVa weathering of coating B. It is immediately identifiable that as the specimen is exposed to the weathering cycle, and goes through each analysis period, a change in the coating surface chemistry occurs. This change occurs in several regions of the spectra, firstly, at 1708 cm^{-1} a new peak has formed, next at 1644 cm^{-1} a peak is absent, then at 1526 cm^{-1} the magnitude of the peak has significantly reduced, and at 1454 cm^{-1} the peak has become wider and shifted to 1442 cm^{-1}. Also, the small shoulder type peak at 1180 cm^{-1} is absent. The identified changes occur after the first analysis period of 500 hours and are present for the remainder of the test.

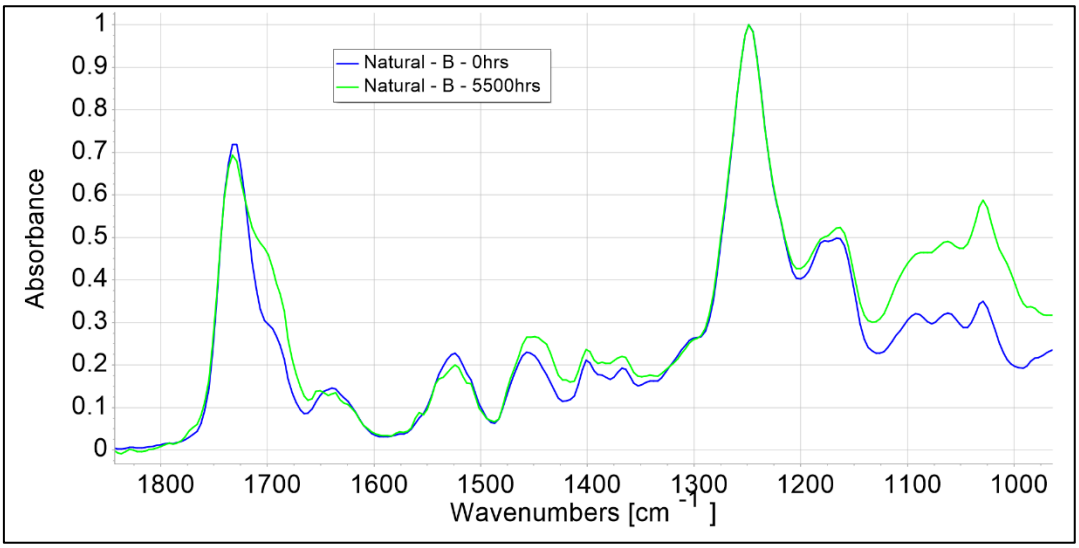

Figure 5.40: FTIR, Coating B, Natural Weathering

The FTIR spectra for the Natural Weathering of coating B is shown in Figure 5.40. There is a noticeable change which is linked to the period of Natural Weathering. Namely, at 1700 cm^{-1} a peak has begun to develop, resulting in a shoulder from the previous peak at 1732 cm^{-1}. Additionally, the region from 1125 cm^{-1} to 1000 cm^{-1} has increased in amplitude, though no new peaks have formed.

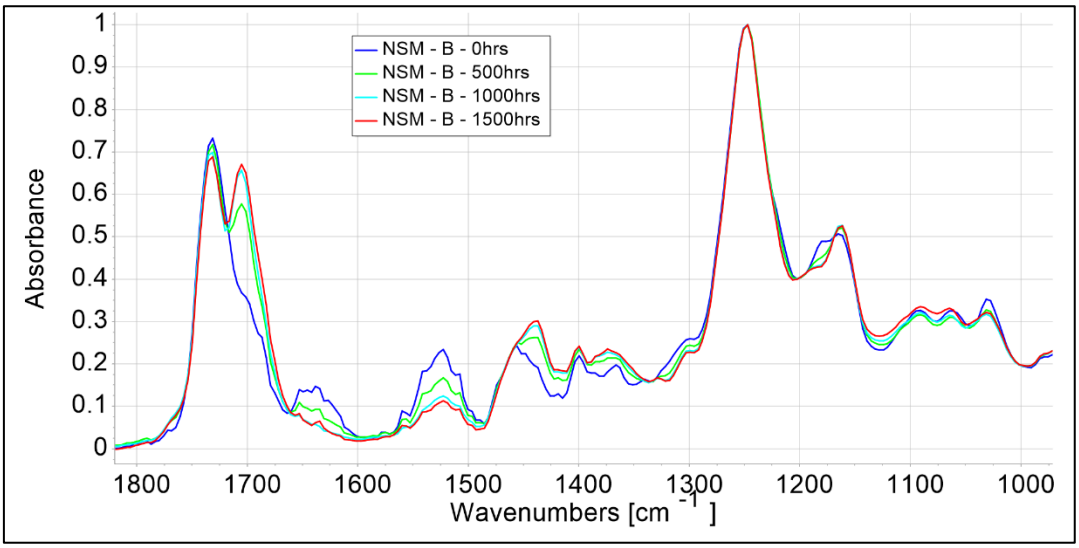

Figure 5.41: FTIR, Coating B, NSM Weathering

Next, considering Figure 5.41, which presents the FTIR spectra for the NSM weathering of coating B. Similarly, to the UVa weathering, a new peak has formed at 1708 cm^{-1} and the peaks at 1644 cm^{-1} and 1526 cm^{-1} have begun to decrease. Also, as in the UVa weathering, the peak at 1454 cm^{-1} has begun to widen and shift towards 1442 cm^{-1} and the small shoulder type peak at 1180 cm^{-1} has begun to decrease. The identified changes occur after the first analysis period of 500 hours and remain for the duration of the test.

5.2.4.2. Spectroscopy: Coating C1 & C2

The spectra for both coating C1 and coating C2 were all normalised about the highest peak present in the spectra, 1244 cm^{-1}, to allow direct comparison between analysis periods.

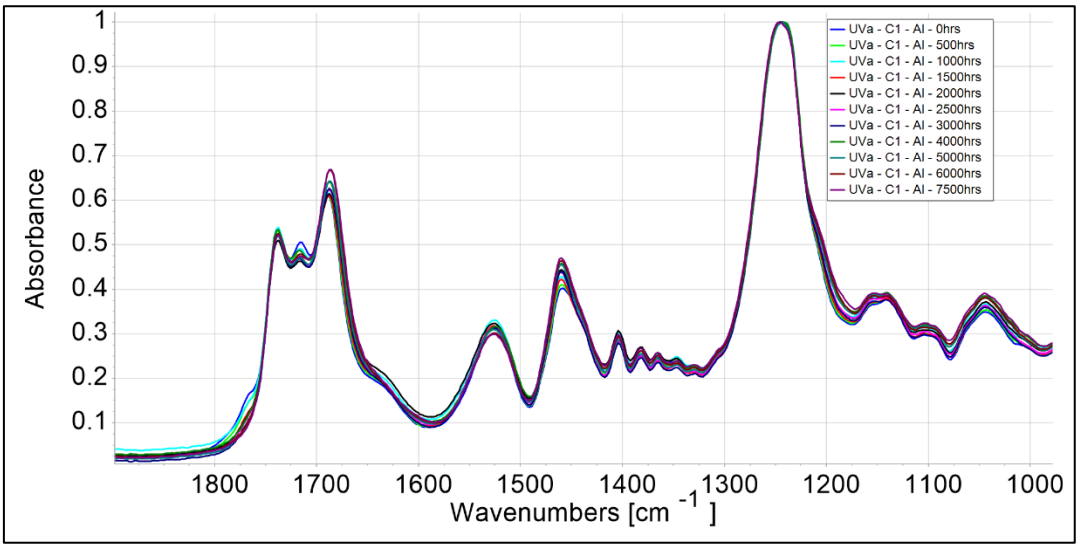

Figure 5.42: FTIR, Coating C1, Aluminium Substrate, UVa Weathering

The FTIR spectra for the UVa weathering of coating C1 on aluminium substrate is presented in Figure 5.42. There are no obvious changes in the spectra as the test progresses, apart from the removal of the short shoulder type peak at 1768 cm^{-1}. The remainder of the spectra continues unchanged throughout the test.

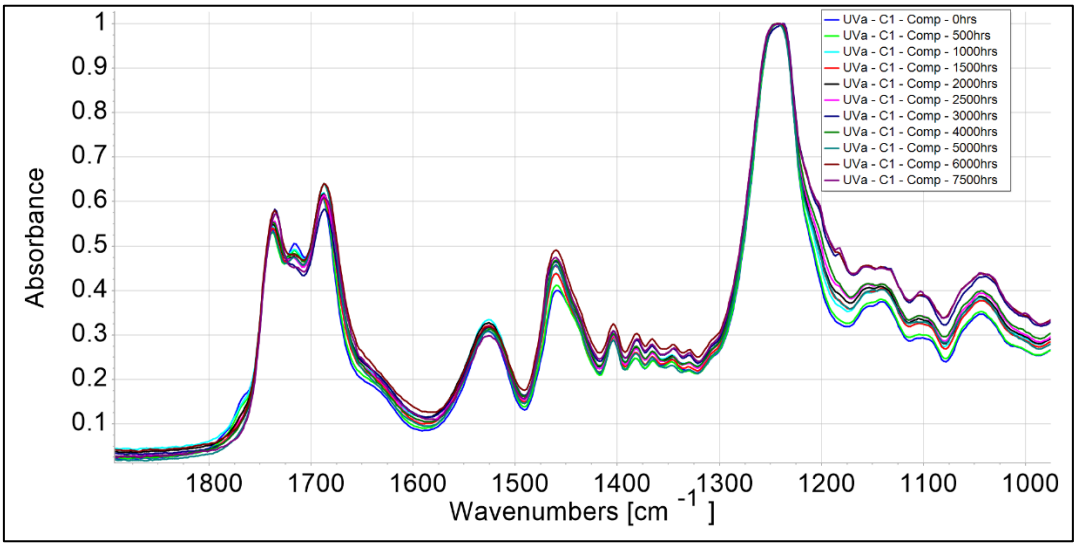

Figure 5.43: FTIR, Coating C1, Composite Substrate, UVa Weathering

Figure 5.43 shows the FTIR spectra for the UVa weathering of coating C1 on composite substrate. Again, there are no immediate obvious changes as the

test progresses, however, the short shoulder type peak at 1768 cm^{-1} is removed and the peak at 1716 cm^{-1} has begun to decrease as the test progresses. Additionally, towards the later stages of the test a small peak has begun to form at 1182 cm^{-1}. The remainder of the spectra continues unchanged throughout the test.

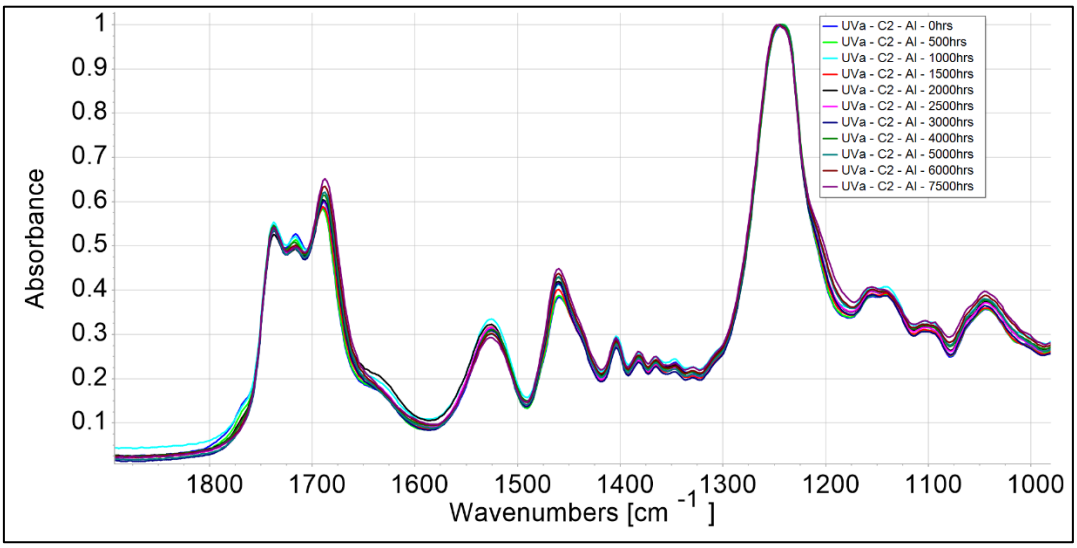

Figure 5.44: FTIR, Coating C2, Aluminium Substrate, UVa Weathering

Figure 5.44 presents the FTIR spectra of coating C2 on aluminium substrate as a result of UVa weathering. The only observable change is small, at 1768 cm^{-1} the short shoulder type peak begins to soften as the test progresses and is removed by the end of the test. The remainder of the spectra continues unchanged throughout the test.

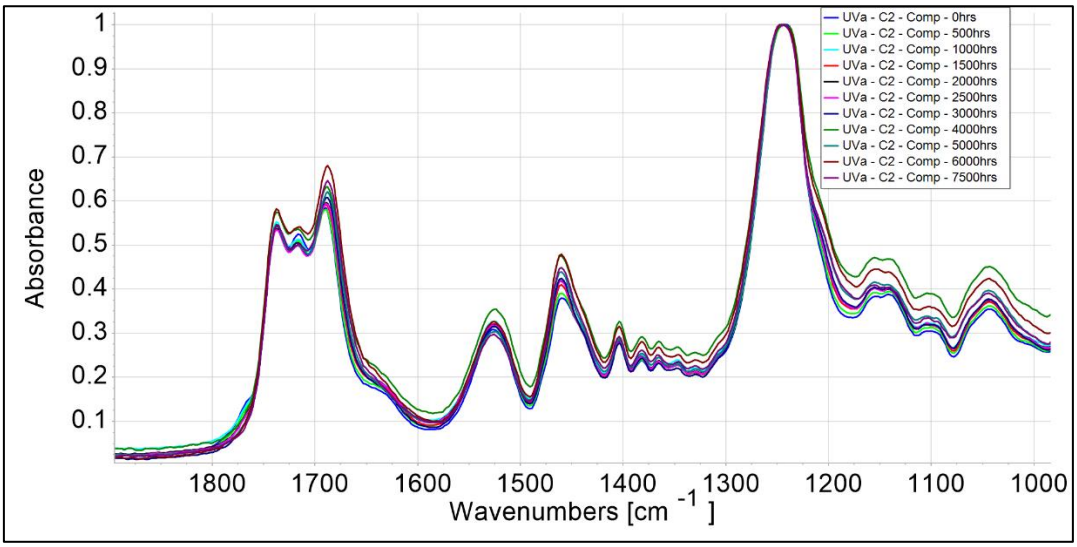

Figure 5.45: FTIR, Coating C2, Composite Substrate, UVa Weathering

Looking at Figure 5.45 which shows the FTIR spectra of coating C2 on composite substrate, there are no large changes occurring. Only a small shoulder type peak at 1768 cm^{-1} shows a change by reducing as the test progresses. The remainder of the spectra continues unchanged, with a slight upward shift in the 1000 cm^{-1} to 1200 cm^{-1} region, throughout the test.

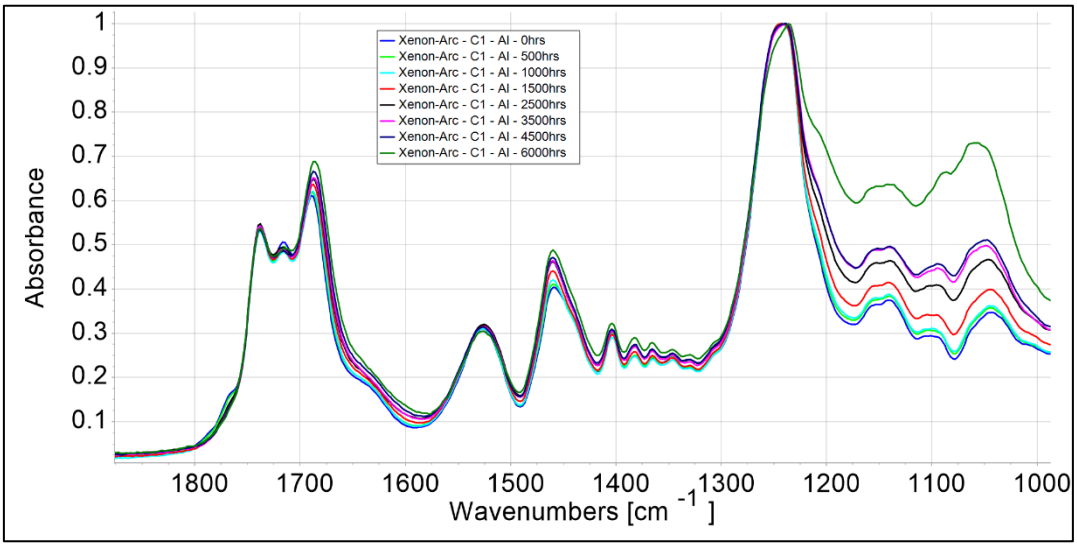

Figure 5.46: FTIR, Coating C1, Aluminium Substrate, Xenon-Arc Weathering

The FTIR spectra for Xenon-Arc weathering of coating C1 on aluminium substrate is shown in Figure 5.46. The small shoulder type peak at 1768 cm^{-1}

is absent after the initial analysis period at 0 hours. Also, as the test progresses there is an increasing upward shift in the 1000 cm^{-1} to 1200 cm^{-1} region with a shoulder type peak beginning to form at 1208 cm^{-1}. The remainder of the spectra continues unchanged throughout the test.

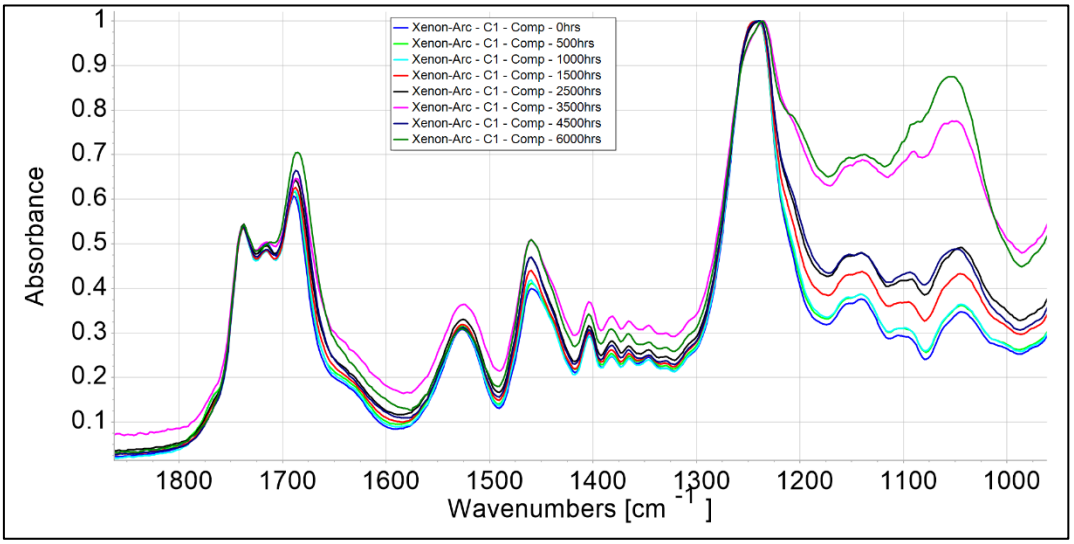

Figure 5.47: FTIR, Coating C1, Composite Substrate, Xenon-Arc Weathering

Figure 5.47 presents the FTIR spectra for Xenon-Arc weathering of coating C1 on composite substrate. Again, the small shoulder type peak at 1768 cm^{-1} is absent as the test progresses beyond 0 hours. Additionally, there is an upward shift throughout the spectra, particularly at 1000 cm^{-1} to 1200 cm^{-1}, as the test progresses and the formation of a new shoulder type peak at 1208 cm^{-1} can be observed.

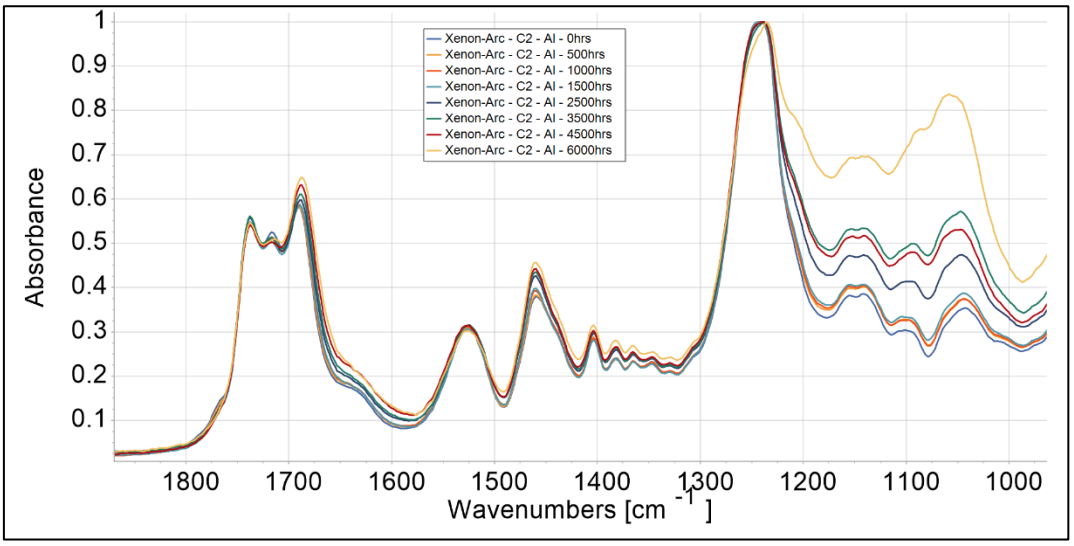

Figure 5.48: FTIR, Coating C2, Aluminium Substrate, Xenon-Arc Weathering

Next, looking at Figure 5.48 which shows the FTIR spectra for Xenon-Arc weathering of coating C2 on aluminium substrate. Similar to the previous analysis, the short shoulder type peak at 1768 cm^{-1} is not present as the test progresses. Furthermore, there is a large upward shift in the 1000 cm^{-1} to 1200 cm^{-1} region as the test progresses, with the start of a new shoulder type peak showing at 1208 cm^{-1}.

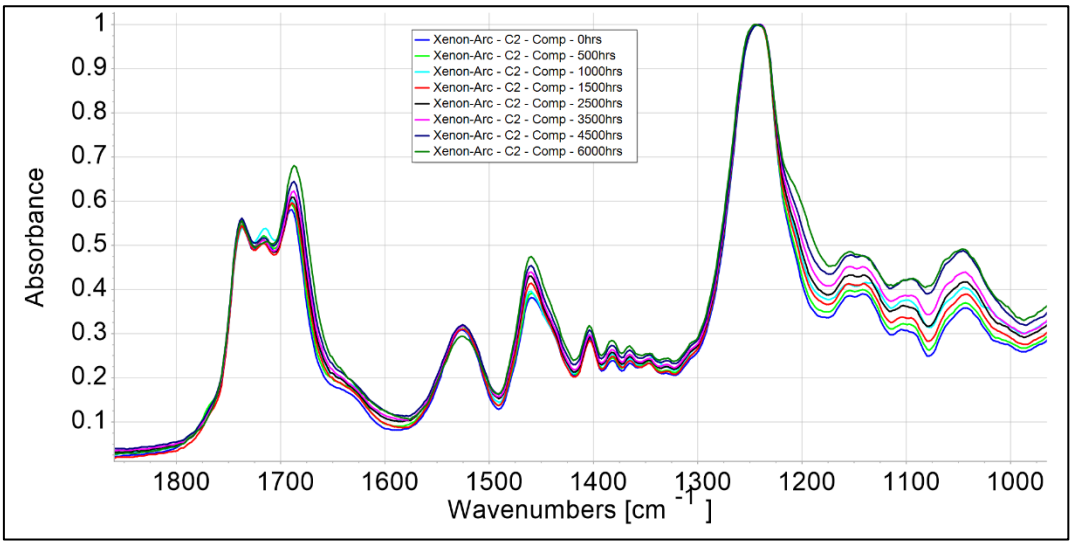

Figure 5.49: FTIR, Coating C2, Composite Substrate, Xenon-Arc Weathering

Figure 5.49 presents the FTIR spectra for the Xenon-Arc weathering of coating C2 on composite substrate. The short shoulder type peak at 1768 cm^{-1} is absent as the test progresses, though not as easily observably as in previous analysis. Additionally, a new shoulder type peak has begun to form at 1208 cm^{-1}.

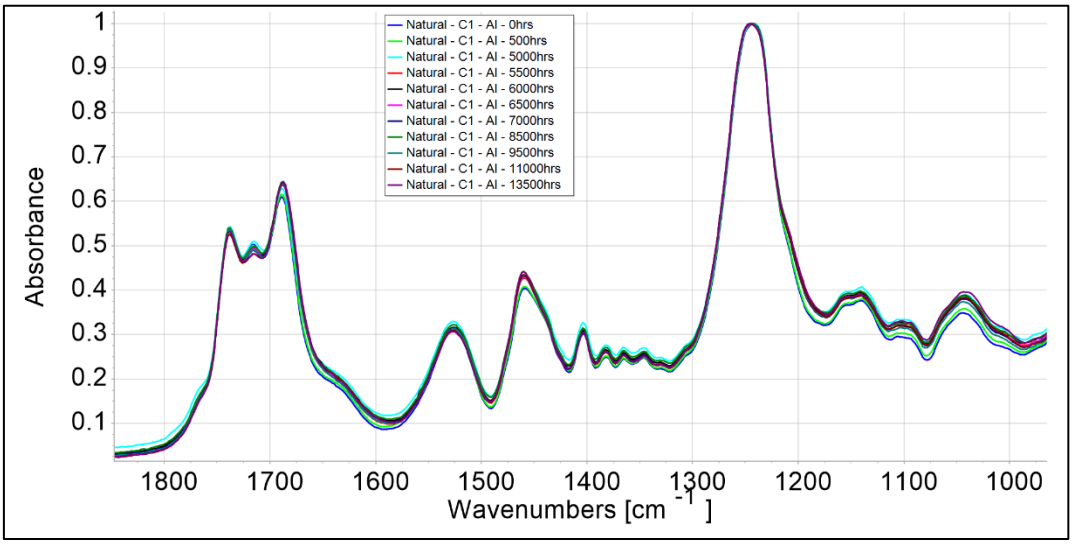

Figure 5.50: FTIR, Coating C1, Aluminium Substrate, Natural Weathering

The FTIR spectra for Natural Weathering of coating C1 on aluminium substrate is presented in Figure 5.50. As is observable, there are no major changes

within the spectra as the test progresses. The short shoulder type peak at 1768 cm^{-1}, which was the first detectable change, is present throughout the test.

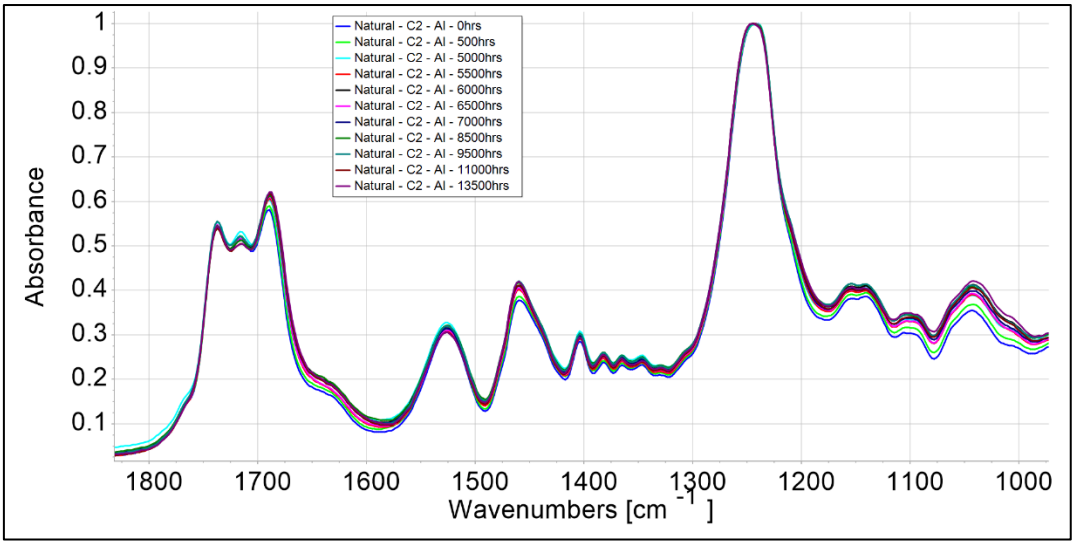

Figure 5.51: FTIR, Coating C2, Aluminium Substrate, Natural Weathering

Next, the FTIR spectra for Natural Weathering of coating C2 on aluminium substrate is presented in Figure 5.51. Similarly, to Natural Weathering of coating C1, there is no observable changes as the test progresses, with the short shoulder type peak at 1768 cm^{-1} remaining throughout.

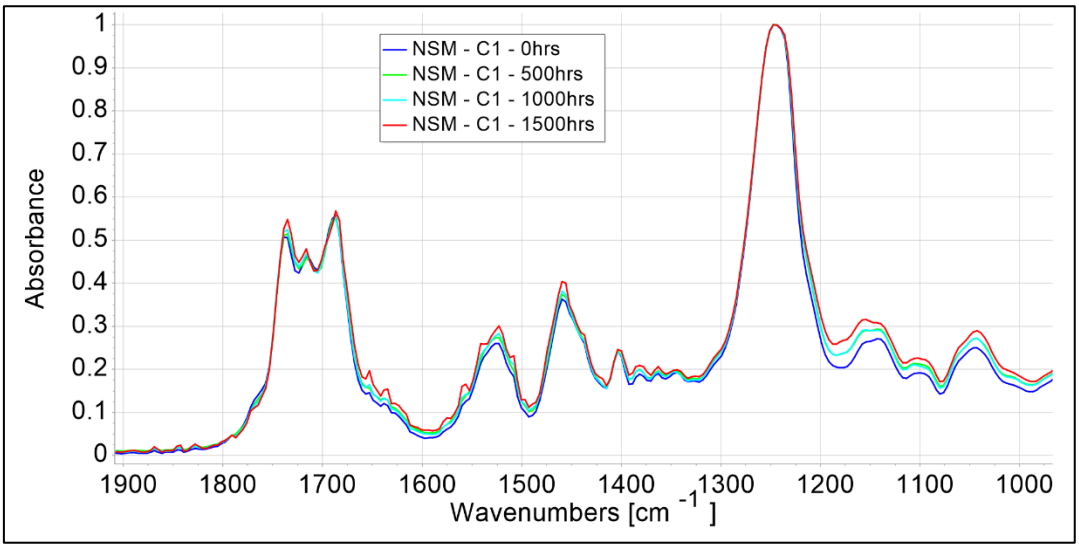

Figure 5.52: FTIR, Coating C1, Aluminium Substrate, NSM Weathering

Moving on to the NSM weathering, Figure 5.52 shows the FTIR spectra for coating C1 on aluminium. Here, there are no major changes as the test progresses. The short shoulder type peak at 1768 cm^{-1} remains in place throughout. However, there is some noise present in the signal for 1500 hours which presents as small spikes along the signal.

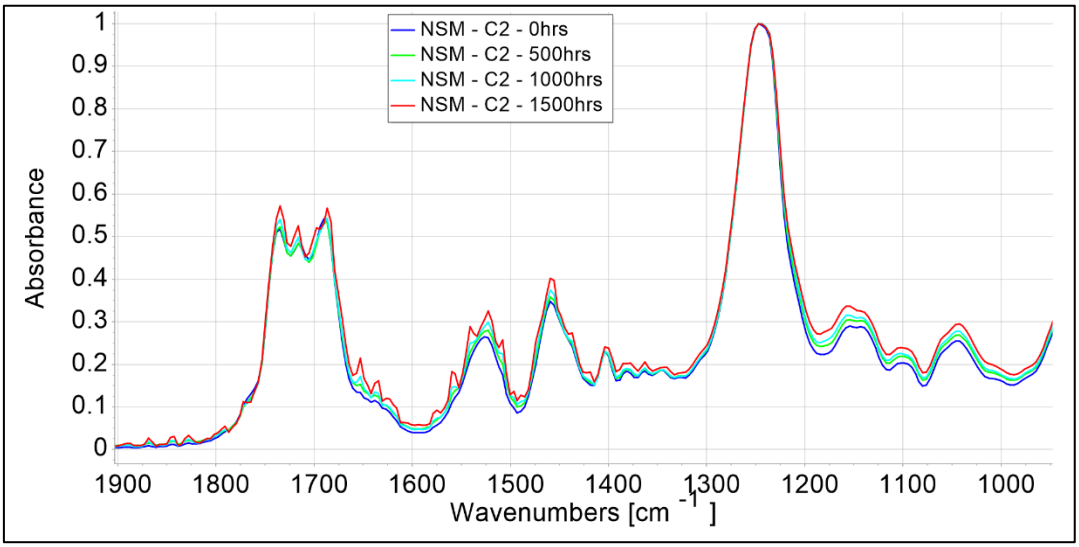

Figure 5.53: FTIR, Coating C2, Aluminium Substrate, NSM Weathering

Finally, the FTIR spectra for NSM weathering of coating C2 on aluminium is presented in Figure 5.53. Similar to the NSM weathering of coating C1, there

is no major change as the test progresses, though there is some signal noise present at 1500 hours which looks like small spikes on the signal.

5.3. Discussion

As an overall observation, it is clear from the results presented that weathering, in general, has a direct effect on the chemical structure of wind turbine blade coating systems. This weathering effect is immediately noticeable as a difference in colour between the before and after weathering analyses, as well as some surface marking due to weathering. Additionally, the measured surface gloss decreases as the weathering progresses, and is therefore a good indication of the amount of weathering that the coating system was exposed to.

5.3.1. Coating B

Photographs

Looking at each analysis parameter in greater detail, starting with the photographs, the following conclusions can be drawn. All of the weathering testing conducted has caused a visual change in the specimen surface, some more noticeable than others. With coating B, the UVa weathering cycle caused the surface of the specimen to bruise in areas where dark colourations appear after testing. The bruising appears to be at random on the coating surface, with no observable pattern. Considering only very small sections display bruising, it is likely that the bruising is related to patches of the coating system which have not been thoroughly mixed, or the application layer thickness differs to the remainder of the specimen. The accelerated UVa weathering cycle has caused these imperfections on the coating system to develop, as a combination of the effects from the heat, humidity and UVa exposure, and produce dark patches. The bruising could also be linked to a post-cure effect of the weathering cycle, where the high temperature and humidity of the cycle cause a chemical reaction on the coating system surface. This post-cure effect is observable in the FTIR data and is discussed further in the following section.

Similarly, the NSM cycle specimens also show small amounts of surface dark patches, though there are noticeably fewer than the UVa cycle and they are much smaller in size. This ties in to the results from the UVa cycle in that the NSM cycle is half of the total test duration with a lower irradiance intensity and test temperature. The NSM could be showing the initial development stages of the bruises.

Now, considering the Natural outdoor test photographs, again, some surface dark patches are present. However, during this test there was no increase of temperature or humidity, other than seasonal effects, as the specimens were located outdoors. Due to the outdoor nature of this test, the specimens were open to contamination from wildlife, birds, insects, and combustion products from engines which cannot be ruled out as the cause of visual surface changes. Given that both the UVa cycle and the NSM cycle have shown the development of dark patches on the surface, it is more likely that the dark patches are due to exposure to natural sunlight and water due to rain.

One possible explanation for the dark patches could be linked to the method in which the test specimens were stored and transported. Typically, specimens would be wrapped in paper towel and stored one on top of the other. This would provide the opportunity for the test specimens to rub against each other and in turn, damage the specimen surface. However, given that the dark patches and bruising appears mostly in the centre of the test specimens, with no obvious scratches or scrapes present, this could be unlikely. The FTIR data will offer a greater insight to any chemical changes that have occurred as a result of weathering testing.

Gloss

Looking at the surface gloss of coating B, starting with the UVa cycle, the gloss initially shows a slight increase of 1.4% at the first measurement period of 500 hours then steadily decreases to a value of 65.5% at 2500 hours before then increasing to 77.2% at the end of test at 3000 hours.

The decrease in gloss value indicates that the coating surface is dispersing and/or absorbing more light than the baseline assessment at 0 hours. Any light absorbed by the coating system will be transferred to heat. The light that is scattered or dispersed is linked to the surface texture and microstructure. An increase in roughness or non-uniformity would cause the gloss to decrease.

The decrease in gloss can be linked back to changes in the polymeric structure of the coating system surface. It is likely that the high amount of energy associated with the UVa weathering cycle has caused polymer chains to break and amorphous regions to develop within the top coating layer thus yielding a greater deviation in surface uniformity, which is reflected by the gloss measurement.

However, there is also a significant increase in gloss between 2500 hours and 3000 hours of the UVa test. It is known that humidity and water retention play a role in gloss measurement. As a specimen is exposed to a wet environment, the specimen will typically absorb some of the water, causing the specimen to swell. This swelling effect pushes on the polymer chains, causing the coating to expand and the coating surface to even out and level off slightly, resulting in an increase in the surface gloss measured. This could be the reason why there are increases in the surface gloss measured. The specimen could have been removed from the accelerated test chamber during, or just shortly after, a wet phase. This would cause the sample to swell, increasing the measurable surface gloss.

Looking at the NSM cycle, there is a decrease in gloss throughout all analysis periods. There is an 8.3% reduction after the first 500-hour period, leading to a 14.5% reduction at the end of test at 1500 hours. There is a 1% difference in gloss between the NSM cycle and the UVa cycle at 1500 hours, with the UVa cycle retaining more of the original gloss value. Again, the loss of surface gloss can be linked back to changes in the polymer structure. It is likely that surface polymer chains are breaking, causing an increase in surface roughness, in turn increasing the amount of incoming light that is dispersed.

Then, looking at the Natural outdoor weathering test, there is a loss in surface gloss. Only two measurements were made for this test, which was not ideal. However, there was a 17.3% reduction in measured gloss after 5500 hours on test. Due to the outdoor nature of this test, the specimens were exposed to various sources of contamination and pollution which could be reflected by a gloss measurement.

Colour

Considering the colour measurements for coating B, firstly looking at the UVa weathering cycle. There is a sharp increase in colour difference up to the second analysis period at 1000 hours, with the overall colour change parameter, ΔE^*, reaching 0.64. It should be noted that the colour change measurement is always made against the initial specimen colour measurement, which is the baseline measurement. Within the overall colour change parameter, several other parameters exist, as discussed in Colour Measurement, Chapter 5, Section 5.1. At the 1000-hour analysis period, the lightness parameter, L^*, decreased by 0.31, indicating that the specimen had become darker. Additionally, the a^* parameter reduced by 0.04 and the b^* parameter increased by 0.55, indicating that the specimen had become slightly more green (a^* parameter) and more yellow (b^* parameter) respectively. After the second analysis period, the colour change drops with the specimens showing a lightness change of $L^* = -0.17$ and smaller changes in green and yellow with $a^*=-0.02$ and $b^*=0.37$ with an overall colour change of $\Delta E^*=0.41$. Then, towards the end of the test at 3000 hours, the overall colour change parameter climbs to $\Delta E^*=0.63$, with small increases in green colour, $a^*=-0.04$, and a larger increase in yellowing, $b^*=0.53$.

When considering the Natural Weathering colour change of coating B, which was measured using absorbance spectra from wavelengths of 350nm to 800nm to include the visible light region, there is a clear difference in spectra, indicating that a significant colour change has occurred. The greatest difference occurs between 415nm and 500nm, indicating that more light is

absorbed within this region. The 400nm to 500nm range encompasses violate and blue colours within the electromagnetic spectrum. Therefore, the spectrum shows that as a result of the Natural Weathering test, the specimens have become more violate/blue in colour. There is also a generic upward shift of the end of test spectrum at 5500 hours compared to the baseline assessment, indicating that within all regions of the visible colour spectrum, after the test there is a greater amount of light absorbed. This then illustrates an overall darkening effect of the specimens as a result of the Natural Weathering test.

Now, looking at the colour change due to the NSM weathering cycle of coating B. There is very little difference in spectra, only a very slight increase in the blue/violet region at 500nm-400nm, indicating a small change in blue/violate colour as a result of the NSM test. The NSM test was short in duration compared to the standard UVa weathering test, this could be the reason that hardly any change in colour was observable.

Spectroscopy

Firstly, looking at the FTIR plots for the UVa weathering cycle for coating B, there is a clear change in the spectra from the first analysis period at 500 hours which remains as the test progresses. A peak has formed at 1708 cm^{-1} which is indicative of a Carbon-Oxygen double bond, the FTIR data shows that this bond has formed as a result of the UVa weathering cycle and is present at the first analysis period of 500 hours. Next, the peak at 1644 cm^{-1} has disappeared at, and beyond, the first 500 hours analysis period. This peak is representative of a Carbon-Carbon double bond and shows that the UVa cycle has caused this bond type to break and no longer be detectable. It is likely that the weathering cycle has induced an oxidation reaction involving the Carbon-Carbon double bond, which has led to the formation of the Carbon-Oxygen double bond. Then, the magnitude of the peak at 1526 cm^{-1} has been reduced as a result of the weathering cycle, even after the first 500 hour period. This peak relates to a Nitrogen-Oxygen single bond. Additionally, the peak at 1454 cm^{-1}, representing a Carbon-Hydrogen bond, has become much wider and the

shifted to 1442 cm^{-1}. The new peak at 1442 cm^{-1} represents an Oxygen-Hydrogen bond associated with a Carboxylic acid, indicating that a Carboxyl group has formed because of the UVa weathering cycle. Then, the small peak at 1180 cm^{-1} has vanished, this peak represents a Carbon-Oxygen single bond, suggesting the removal of this bond type as a result of weathering exposure.

Given that such changes are detectable after a short test period of 500 hours, it is likely that the FTIR is detecting a further curing step of the coating system. It is considered that an Aldehyde functional group is reacting with the water during the weathering cycle and the elevated cycle temperature is acting as a catalyst for the oxidation reaction. Thus results in the formation of a Carboxyl functional group. However, as the chemical formulae of the coatings is not known, this cannot be said for certain.

Moving on to look at the FTIR plots for the NSM weathering cycle of coating B, again there are immediate noticeable changes. All of the changes occurring are the same as in the UVa weathering cycle, however, they are occurring at a lower rate. The gradual change in peaks of the spectra show a much slower chemical change in the coating system surface. As the NSM cycle progresses, the peaks begin to fully form or are fully removed, as in the UVa cycle. This slower rate can be linked to the lower intensity and energy levels of the NSM cycle versus the UVa cycle. This suggests that the higher the temperature and irradiance values are, the faster the detected reaction will take place.

Then, looking at the Natural outdoor FTIR plots for coating B, only two FTIR measurements were taken. One measurement as a baseline before the test began and one at the end of test at 5500 hours. The FTIR plots show the initial development of the reaction which is taking place, at 1700 cm^{-1} a shoulder type peak has begun to form, with the removal of the lower shoulder type peak at 0 hours. It is in this region where a Carbon-Oxygen double bond is detectable, therefore it is assumed that the development of this bond type is occurring.

The difference in peak formation and removal rate throughout all of the spectra from coating B further highlights the importance of elevated temperature and irradiance as a catalyst to the reactions occurring.

5.3.2. Coating C1

Photographs

Starting with the UVa cycle of coating C1, the photographs show that some surface marking is present at the end of test at 7500 hours compared to the baseline assessment. Most of the marks present look to be the result of a scratch or scrape, likely during specimen transportation. The scratches and scrapes can be identified by the long, flat nature of the mark with sharp edges. The other visual difference on the specimens is around the edges where the sample holder would sit. Here there is surface staining, likely as a result of the sample holder for the weathering cabinet beginning to corrode and in turn, staining the specimen surface.

Moving on to the Xenon-Arc weathering cycle for coating C1, there is a very noticeable change in specimen condition after the 6000-hour test. The specimens look very matt and have lost the surface shininess. Additionally, on one of the test specimens, a large crack has appeared. The crack has formed as a result of the high energy nature of the test, the Xenon-Arc test is the most energy intensive weathering cycle used within this work. The temperature of 65±3°C and humidity of 50±10% during the dry phases combined with the uncontrolled temperature and humidity of the wet phases, along with the bombardment of light, has led to repeated cyclic stresses on the coating system resulting in a fracture, which is identifiable in photographs at 3000 hours on test, which has developed into a crack and then propagated inwards toward the centre of the specimen. However, there is only one specimen which has shown a crack form. The crack could also have formed due to an imperfection in the coating application or in the substrate.

Then, looking at the Natural outdoor weathering cycle photographs of coating C1. The end of test photographs at 13500 hours appears heavily contaminated compared to the baseline assessment photographs. The lines on the edges of each specimen are due to the tapes used to hold each specimen in place during the test and can be neglected from any analysis. There is an observable change in colour as well as lots of marks, stains and surface debris present, most of which are due to the outdoor test location. Again, the outdoor location of testing allows for contamination and pollution of the test specimens from various sources, such as branches and leaves, wildlife, birds, insects and engine combustion products. Additionally, leaves are likely to fall onto the specimens and begin to decompose, resulting in surface staining of the specimens.

Finally, the NSM cycle photographs of coating C1. There is very little difference in the photographs from the end of test at 1500 hours and the baseline assessment. There are a few surface blemishes as a result of the test, but no major, easily observable differences. This is primarily due to the short nature of this test, combined with the lower intensity and test temperatures compared to the UVa cycle.

Gloss

Now, looking at gloss measurements for coating C1, beginning with the UVa weathering cycle, the first point to note is that there is a difference in gloss measurements between substrate type. Both substrate types show a decrease in gloss as the test progresses, with coating C1 on the aluminium substrate presenting a 42% decrease and on the composite substrate presenting a 43.3% decrease, all at the end of test at 7500 hours. However, the majority, indeed all but one, of the aluminium substrate gloss measurements show a higher gloss value than the equivalent composite substrate. It is noted that the composite substrate reacts differently to the heat and humidity of the test chamber than the aluminium substrate. The lower gloss measurement for the composite substrate indicates that the coating surface is rougher and more

uneven than that of the aluminium substrate, meaning that the polymer chains have broken down faster on the composite substrate, likely due to the composite absorbing more heat and water throughout the test than the aluminium substrate, thus, allowing the polymer chains break down quicker.

Looking at the Xenon-Arc test gloss measurements for coating C1, again the general trend is a decrease in gloss value. There are similar results for the composite and aluminium substrates, with the composite showing slightly higher gloss values than the aluminium. The composite substrate will absorb more water throughout the test than the aluminium substrate, causing the composite specimen to swell, and in turn increasing the gloss value due to the levelling out of the surface polymer chains.

The Natural outdoor weathering of coating C1 causes the surface gloss to slowly decline throughout the test. However, with this test, the specimens were exposed to surface dirt and grime which would have an effect the gloss measurement. Even though the specimens were lightly cleaned before any gloss measurements were made, surface staining remained. At the end of test at 13500 hours, the specimens lost 16.4% of the initial gloss value, a low amount compared to that of the UVa and Xenon-Arc weathering cycles.

Finally, the NSM weathering cycle of coating C1 shown the gloss value slowly decline over the 1500-hour test. The short 1500-hour test duration yields a 17.2% decrease in gloss value, indicating some polymer chain breaking and restructuring on the coating surface, increasing the surface roughness and changing the surface topography.

Colour

Firstly, looking at the colour change of coating C1 due to UVa weathering, when comparing the aluminium and composite substrates, they both follow the same trend throughout the UVa test. The composite specimens show a lesser overall colour change throughout all analysis periods, resulting in an overall colour difference of ΔE^*=0.07 between substrate types at the end of test at

7500 hours. Looking at the aluminium substrate, there is a sharp initial increase in overall colour change, up to ΔE^*=0.67 at 1000 hours. Within the total colour change at 1000 hours, the lightness parameter L^*=-0.34, and parameters a=0.02 and b=0.57. This indicates that the coating surface is darker in colour, due to the negative L^* parameter, as well as becoming more red, due to the positive a parameter, and much more yellow, due to the large value positive b parameter. After the first 1000 hours, the total colour change settles out with only a slight increase, and then decrease as the test progresses. This results in an end of test colour change of ΔE^*=0.83 with L^*=-0.52, a=0.01 & b=0.65, indicating that the coating surface is darker, more red and much more yellow than the starting colour measurement.

Moving on to look at the colour change of coating C1 due to the Xenon-Arc weathering test. Looking at both substrate types, again they follow a similar trend to each other, with the composite showing less overall colour change than the aluminium substrate. The largest difference in substrate type comes at 1500 hours, where a difference of ΔE^*=0.13 can be observed. With the Xenon-Arc test, the initial colour change, up to 1500 hours, is large reaching ΔE^*=0.32. Within the 1500-hour measurement, L^*=-0.22, a=0.05 & b=0.23, this indicates that the coating surface is becoming darker, more red and more yellow. Progressing through the remainder of the test, the total colour change increases steadily to a maximum of ΔE^*=0.48 at the end of test at 6000 hours.

Thereafter, looking at the colour change of the Natural outdoor weathering of coating C1, very large changes are observable. As previously discussed, the surface was prone to staining from leaves and debris from nearby wooded areas, along with other pollutants and contaminants associated with the outdoor test environment. The surface staining has been reflected in the colour measurements made. Initially, after the first 500-hour period, a total colour change of ΔE^*=0.27 was measured, with L^*=-0.16, a=0.02 & b=0.22 indicating that the coating surface is darker, more red and more yellow, all after only 500 hours on test. As the test progresses, large jumps in total colour change are observed, climbing to ΔE^*=2.22 after 6000 hours on test. The end of test at

13500 sees ΔE^*=3.55, with L^*=-2.77, a=0.57 & b=2.21 showing a large darkening of the surface colour as well as a moderate increase in red colour with a huge increase in yellow colour, as is easily detectable by the naked eye.

Finally, considering the colour change due to the NSM weathering cycle for coating C1. At first observations, there is not much change in colour for coating C1 due to the NSM weathering test. There is a very small increase in absorbance of the end of test spectra at 1500 hours in the region of 415nm to 500 nm, indicating that the specimens have become very slightly more blue/violate in colour.

Spectroscopy

Looking at the spectroscopy for coating C1 due to UVa weathering, there are no immediate changes as a result of the cycle. The only observable change, for the aluminium substrate type, is the removal of the small, short shoulder type peak at 1768 cm^{-1} which represents a Carbon-Oxygen double bond. The same change is observable on the composite substrate, along with the peak at 1716 cm^{-1} beginning to decrease. The 1716 cm^{-1} peak also relates to a Carbon-Oxygen double bond, however, it is included within a different functional group. Only speculations of functional groups and group changes can be made as the original coating formulation is not known. Additionally, for the composite substrate, a small peak has begun to form at 1182 cm^{-1} which relates to a Carbon-Oxygen single bond.

Moving on to consider the Xenon-Arc weathering of coating C1, the FTIR plots show the removal of the small shoulder type peak at 1786 cm^{-1}, a Carbon-Oxygen bond. This change is visible from the first 500-hour analysis period on both the composite and aluminium substrates. There is also a formation of a shoulder at 1208 cm^{-1} which is representative of a Carbon-Nitrogen single bond. Additionally, on both substrate types, there is a progressing upward shift in the 1000 cm^{-1} to 1200 cm^{-1} region as the test advances, indicative of an increased amount of bonds, which absorb within this region, are present. Furthermore, the trough at 1080 cm^{-1} on both the composite and aluminium

substrate, representative of a Carbon-Oxygen single bond linked to a primary alcohol, begins to increase and is barely present at the end of test. This suggests that the Carbon-Oxygen single bond is reacting and being consumed due to the Xenon-Arc weathering cycle. Alcohols can react with Oxygen, though an oxidation reaction, to produce a Carboxylic acid. The Carboxyl group Carbon-Oxygen double bond is present and increasing at in magnitude at 1668 cm^{-1} on the FTIR plots. As the absorption value of the Carbon-Oxygen bond decreases, the value of the Carbon-Oxygen double bond increases, showing that this is a likely scenario.

For the Natural Weathering of coating C1, the spectroscopy results show no change throughout the test. There are no peak formations or peak removals as a result of the Natural weathering test. The small shoulder type peak at 1768 cm^{-1} remains present throughout the test, unlike the other accelerated weathering methods, indicating that no chemical bond changes have occurred.

Then, looking at the NSM cycle for coating C1, the FTIR plots show no chemical bond changes. Again, the short shoulder type peak at 1768 cm^{-1} remains in place. This is likely due to the lower energy associated with the NSM cycle versus the UVa cycle. Prolonged exposure to the NSM cycle could cause the bond changes that are observed after 500 hours in the UVa cycle.

5.3.3. Coating C2

Photographs

Looking at the photographs for the UVa weathering cycle for coating C2, the end of test at 7500 hours shows some observable changes. Most noticeably, a large crack has appeared at the top of one of the specimens. Additionally, some surface marking and darker spots are present after the UVa weathering test. Similar to previous assessment, the majority of the dark marks are likely due to scratches and scrapes as a result of transport and storage of the test specimens. The marks are mostly thin and linear in shape with sharp edges. Considering the crack which has developed, again this could have initiated

from a flaw in the substrate or the coating system application. Given that the UVa test is less severe than the Xenon-Arc test, where previously a crack on coating system C1 was identified, an application flaw is likely as the root cause. However, the UVa weathering cycle is repeating wet and dry phases, at elevated temperature, which would exacerbate and flaw or fracture and cause propagation into a crack due to the cyclic stresses induced on the coating system.

Now, moving on to look at the photographs of Xenon-Arc weathering of coating C2, it is evident that a drastic change has occurred. Visually, the specimens have become very matt and lost the glossiness on the surface. Additionally, one of the specimens has cracked towards the top, which has led to a small delamination of the coating system from the aluminium substrate. As previously discussed, the high energy associated with the Xenon-Arc test, along with the repeating wet and dry phases, induces high cyclic loading on the specimens. In turn, the cyclic loading causes crack propagation of any flaws or defects present, resulting in loss of adhesion between the coating system and the substrate.

Then, observing the Natural outdoor weathering photographs of coating C2, there are clear differences after the 13500-hour test. Specimens appear dirty and stained in places, with areas of dark marks. The lines on the edges of each specimen are due to the tapes used to hold each specimen in place during the test and can be neglected from any analysis. Similarly with coating C1, coating C2 was testing at the same location, therefore the surface staining and dirt is likely a result of nearby trees and shrubs casting their leaves onto the specimens. The dark marks could be a result of specimen transportation and storage, or a reaction from the test. The FTIR study will highlight any chemical reactions that have taken place.

Finally, looking at the NSM weathering cycle photographs of coating C2, there appears to be very little change. There are a few surface marks and dark spots which don’t look like a scratch or scrape, more aligned to a bruise or blemish.

Again, the short nature of this test combines with the lower amount of energy involved has not shown much visual change of the specimens.

Gloss

Next, looking at the gloss measurements for coating C2, starting with the UVa weathering cycle, similar to coating C1, there is an observable difference in gloss between the composite and aluminium substrates. However, unlike coating C1, the composite substrate for coating C2 shows an increase in gloss versus the aluminium substrate. It should be noted that only one specimen was used for coating C2 on composite substrate. The majority of assessment periods recorded a higher value of gloss for the composite substrate than the aluminium substrate, though at the end of test at 7500 hours, the measurements are similar. At the end of test, the aluminium substrate lost 47.4% of gloss and the composite 49.4%. The composite substrate would typically absorb more water throughout the test, resulting in a smoother specimen surface due to the polymer chains levelling out, whin in turn would yield a higher gloss measurement.

The Xenon-Arc weathering of coating C2 shows that the gloss measurements are fairly similar between substrates and that the gloss decreases at every analysis period. At the end of test at 6000 hours, the aluminium substrate has lost 70.7% of gloss value and the composite has lost 74.3%, indicating that significant restructuring of the polymer chains has taken place with a vast increase in surface roughness and change in topography. Again, this is due to the high amount of energy within the Xenon-Arc test, from the various light intensities, heat and humidity.

Then, examining the Natural outdoor weathering of coating C2, the gloss shows a slow, steady decline in value. At the end of test at 13500 hours, 31.2% in gloss has been lost. Similarly to coating C1, coating C2 was tested in a location where leaves and airborne dirt could land on the specimens and cause surface staining, which would alter the gloss value measured.

Finally, considering the NSM weathering cycle for coating C2, the gloss measurements decline by 11% after the first analysis period, then remain almost constant for the remainder of the test, declining by only 2.6% between the first analysis period and the end of test. The initial decrease shows an immediate polymer chain restructuring on the coating surface where the surface roughness has increased, and surface topography changed.

Colour

Firstly, looking at the colour change of coating C2 due to the UVa weathering cycle. Comparing both substrate types, there is a vast difference in total colour change. Both show a sharp initial increase in overall colour change where at 1000 hours the aluminium ΔE^*= 0.57 and the composite ΔE^*=0.38. From 1000 hours onwards, the aluminium substrate slowly increases in total colour change to a maximum of ΔE^*=0.90 at 7500 hours. However, the composite substrate shows further large increases in total colour change after 1000 hours. At 2000 hours the composite shows E^*=0.89 and then further increases to ΔE^*=1.34 at 4000 hours, where L^*=-0.59, a=-0.03 & b=1.21, presenting a large yellowing and moderate darkening of the coating surface. The composite specimen colour then fluctuates to ΔE^*=0.88 at 6000 hours then to ΔE^*=1.25 at the end of test at 7500 hours. The large variations of colour in coating C2 on the composite substrate should be considered with some caution, as only one specimen of this type was used during the work.

Now, moving on to look at the colour change due to Xenon-Arc weathering of coating C2. Here, the composite substrate shows a lower total colour change than the aluminium throughout the test, except for the final analysis period. At the early stages of the test, the aluminium substrate shows large increases in colour change where ΔE^*=0.32 at 1000 hours, from there the colour change increases slowly at the test progresses to a maximum of ΔE^*=0.54 at the end of test at 6000 hours. The composite substrate shows a steady increase in total colour change, with the exception of 4500 hours, ending the test at 6000 hours with a total colour change of ΔE^*=0.59 where L^*=-0.48, a^*=0.07 &

*b**=0.34 showing a darkening in colour with a moderate increase in yellow and very slight increase in red colour.

Looking at the colour change in Natural outdoor weathering of coating C2, again very large changes are observed. This is due to the test location with specimens affected by leaves and debris falling on the surface, leading to surface staining. Similarly to coating C1, after 5000 hours ΔE^*=0.73, then after a further 1000 hours, the total colour change has drastically increased to ΔE^*=2.16, where *L**=-1.63, *a**=0.06 & *b**=1.41 showing a large darkening and yellowing of the coating surface colour. Throughout the remainder of the test, the total colour change continues to dramatically increase to a maximum of ΔE^*=4.30 at 13500 hours, showing a huge difference in colour between the end of test and beginning of test.

Then, looking at the colour change due to the NSM weathering cycle for coating C2. There is a small increase in absorbance of the end of test spectra at 1500 hours in the region of 415nm to 500 nm, indicating that the specimens have become more blue/violate in colour. Additionally, there is a slight upward shift in the end of test spectra, indication and overall absorbance increase would you mean that the specimens have become darker as a result of the NSM weathering cycle.

Spectroscopy

Firstly, the UVa weathering cycle of coating C2 has shown small changes in the FTIR plots. Firstly, for both the composite and aluminium substrate, the short shoulder type peak at 1768 cm^{-1} is removed after the first 500 period, this peak represents a Carbon-Oxygen double bond, indicating that this particular functional group involving a Carbon-Oxygen double bond has been removed. Then, with the composite substrate, there is a slight upward shift in the plot from 1000 cm^{-1} to 1200 cm^{-1} as the UVa test progresses, indicating a greater number of bonds present within this region.

Now, considering the Xenon-Arc weathering of coating C2, the FTIR plots show few changes as the test progresses. The small shoulder type peak at 1768 cm^{-1}, a Carbon-Oxygen double bond, is removed after the test begins on both substrate types. Additionally, the development of a small shoulder at 1208 cm^{-1} can be observed, this is representative of a Carbon-Nitrogen single bond. On the aluminium substrate, the trough at 1080 cm^{-1} begins to reduce as the test progresses. This indicates a decrease in Carbon-Oxygen single bonds, within a primary alcohol functional group, as the test progresses. This peak change is not detectable on the composite substrate. Then, on both substrate types, though it is more prevalent on the aluminium, an upwards shift in FTIR plots shows an increase in bond types withing the 1000 cm^{-1} to 1200 cm^{-1} region.

Looking at the spectroscopy for the Natural outdoor weathering cycle of coating C2, no changes in the chemical bond groups were observed throughout the 13500 hour test. There was no elevated temperature or irradiance, as in the accelerated weathering cycles, would act as a catalyst for any chemical reactions occurring.

Finally, considering the NSM cycle for coating C2, the FTIR plots show that no chemical bond changes have occurred as a result of the test. Similarly to coating C1, this is likely due to the lower energy associated with the NSM cycle versus the UVa cycle. It is expected that prolonged exposure to the NSM cycle would cause the bond changes that are observed after 500 hours in the UVa cycle.

5.3.4. Overall Weathering Comparison

Overall, the Xenon-Arc weathering cycle has shown the greatest visual difference in test specimens. The harsh nature of this test, with high energy levels due to irradiance, heat and humidity, has caused a distinct change in the coating system and led to a washed-out effect on the coating surface. Comparing the Xenon-Arc gloss measurements to the UVa gloss measurements, at 3000 hours the Xenon-Arc shows a gloss value of 55% for

coating C1 on aluminium, and UVa shows 78%. For the equivalent test duration, the Xenon-Arc has caused an additional 23% loss in gloss over UVa. For coating C2 on aluminium at 3000 hours, Xenon-Arc caused an additional 25.3% loss in gloss compared to UVa. Further confirming that the Xenon-Arc test is more damaging than the other testing used within this work.

Coating System	**Weathering Type**			
	UVa	**Xenon-Arc**	**NSM**	**Natural**
B	3.81 %	-	4.84 %	1.57 %
C1 Al	4.61 %	9.98 %	5.73 %	1.66 %
C1 Comp	3.16 %	11.10 %	-	-
C2 Al	4.74 %	10.11 %	4.54 %	3.12 %
C2 Comp	4.94 %	10.62 %	-	-

Table 5: Average Gloss Loss Rate per 500 Hours of Testing.

Considering the gloss loss rate, Table 5 presents the average percentage of gloss loss per 500 hours. This table shows the average decrease in gloss, as a percent if the initial baseline gloss value, for every 500-hour period on test. It is immediately noticeable that the Xenon-Arc cycle is approximately double that of the UVa and NSM cycles and the Natural cycle is a lot less. Again, this links back to the high amount of energy associated with the Xenon-Arc cycle with the elevated temperature and high irradiance across multiple wavelengths. For the Natural test, there was no elevated temperature, only seasonal variations. The UVa cycle and the NSM cycle show similar values, with the NSM rate slightly higher than the UVa. This could be due to the short test duration of the NSM cycle, where the fluctuations in gloss at later test periods are not captured. The UVa cycle shows increases and decreases in gloss throughout the test, particularly after 1500 hours, where the NSM cycle ends. Given that the NSM cycle has a lower overall energy associated with the

test, compared to the UVa cycle, it is expected that the gloss loss rate for the NSM cycle would be less than the UVa cycle.

It should be noted that gloss values can show an increase, where a decrease is expected, depending on what phase in the test cycle the specimen has been removed for analysis. If the specimen is removed during the wet phase, the specimen will typically be wet and have absorbed a proportion of water, causing the specimen to swell. This swelling of the coating causes the surface layer to level out, thus increasing the surface gloss. This could be a reason as to why some of the measured gloss values have shown an increase where a decrease was expected.

Now looking at the colour change in specimens due to weathering, the UVa cycle presents the greatest difference, even more so than the Xenon-Arc cycle. At 3000 hours on UVa test, coating C1 on aluminium shows ΔE^*=0.87 and coating C2 on aluminium shows ΔE^*=0.71. At 3000 hours on Xenon-Arc test, coating C1 on aluminium shows ΔE^*=0.35 and coating C2 on aluminium shows ΔE^*=0.36. This shows that the UVa cycle is cause more than double the amount of colour change than the Xenon-Arc cycle. This could be due to the greater intensity of the lamp during the UVa test. Through the UVa cycle, the lamp used focuses on 340nm with an intensity of 0.83 W/m^2/nm. During the Xenon-Arc cycle, there is a broadband exposure of 300nm to 400nm with intensity of 60 W/m^2 and a narrowband exposure, also at 340nm, with an intensity of 0.51 W/m^2/nm. The higher value of intensity for the UVa cycle at the 340nm wavelength has caused a greater change in overall colour, ΔE^*, than the combined broadband and narrow band exposure of the Xenon-Arc cycle.

Then, the chemical bond changes due to weathering can be observed with FTIR spectroscopy. For coating B, considering all figures presented, the mechanism of chemical change is shown. The Natural Weathering cycle gives a slowed down view, where the changes in spectra are gradual. The UVa cycle gives a highly accelerated view, where the changes in spectra are immediate

after the first 500-hour analysis period. Then the NSM cycle is a weaker version of the UVa cycle and shows how the peaks have formed and disappeared. Ultimately, leading to the removal of a Carbon-Oxygen bond and the formation of a Carboxyl bond group. Similar results are shown for the Xenon-Arc cycle for coating C1, where a Carbon-Oxygen bond is depleted and removed as the test progresses with the formation of a Carboxyl bond group. However, as the chemical composition is not known for any of the coating systems tested, these chemical bond changes are speculated. With the chemical formulation of the baseline assessments known, greater confidence would be given for the speculated bond group changes.

Considering the difference in results obtained due to substrate type, coating C1 and coating C2 show variations in gloss and colour between the composite and aluminium substrate. The composite substrate has shown an increase in gloss measurement at the first analysis period during UVa weathering for both coating C1 and C2. During the same test period, the aluminium substrate showed a decrease in gloss for both coating C1 and C2. The composite substrate is much more absorbent of water versus an aluminium substrate, therefore, after the initial exposure to the wet phase of testing, the composite substrate is likely to absorb water and swell, levelling out the coating surface and, in turn, increasing the gloss measured. For coating C2, the composite substrate type records higher gloss than the aluminium in all but one analysis periods, showing greater water absorption. For coating C1, the gloss values fluctuate for each substrate type between the higher value throughout the test. Throughout most of the Xenon-Arc test, the gloss for the composite substrate, for both coating C1 and C2, was higher than the aluminium substrate, again indicating surface swelling due to water absorption.

5.4. Weathering Summary

To summarise, weathering has a measurable effect on coating systems designed for use on wind turbine blades. The overall effect of weathering, regardless of cycle used, is a reduction in the gloss value of the coating

system, along with a change in colour, typically an increase in yellow colour measured. A 74% decrease in gloss was measured after 6000 hours of Xenon-Arc testing and a total colour change of ΔE^*=1.25 was measured after 7500 hours of UVa weathering. Additionally, chemical changes occur due to weathering, however, the cycle type used does influence these chemical changes. All weathering cycles used have shown a depletion of Carbon-Oxygen bond groups, however, the rate of depletion is heavily influenced by the weathering test used.

The approached used within this work was rigorous and identified changes due to weathering. However, for a total understanding of weathering on blade costing systems, a long-term study is required.

5.4.1. Suggestions for Future Work

A long-term study would provide the greatest benefit to understanding and allow the correct accelerated weathering cycle type to be used. Natural Weathering cycles lasting the expected lifetime of the coating system should be used to define the changes induced by weathering in the operation wind turbine environment. An accelerated weathering cycle can then be used to match these changes, targeting specific chemical bond changes along with gloss loss rate and colour change parameters. This will allow for a correlation to be developed between accelerated lab based weathering and weathering in an external environment.

Multiple test parameters, such as heat, humidity, and irradiance exposure, have been shown to affect the coating systems tested. All the test parameters are working together, simultaneously, during the accelerated weathering test cycles. To develop a greater understanding of exactly how each test parameter effects the coating system, each parameter should be run individually, and have the results compared to the accelerated weathering tests.

Additionally, the NSM cycle should be continued beyond 1500 hours to see if, and how, any dark spots or bruises develop on the coating surface. A

continuation of the NSM cycle would also allow further gloss measurement and comparison and to see if the gloss value for the NSM remains above that of the UVa cycle. If so, this would then tie in with the total amount of energy associated with each test cycle, with the NSM cycle having less energy.

Chapter 6 - Combined Rain Erosion and Weathering Impact Assessment

The work contained within this chapter incorporates both the effects of rain droplet impacts and weathering on wind turbine blade coating systems. To the author's best knowledge, this is the first treatment which addresses the combined interaction of rain droplet erosion with degradation effects from weathering.

The two previous chapters Rain Droplet Impact Assessment, Chapter 4 and Weathering Impact Assessment, Chapter 5, looked at the individual and independent effects of both rain droplet impact erosion and a variety of industrial weathering approaches. The work in this chapter looks at the compound effect and interaction of running both rain droplet impacts and weathering together.

The rain erosion testing (RET) was conducted at Energy Technology Centre (ETC), located in East Kilbride, near Glasgow. The accelerated weathering was conducted at Element Materials Technology, located in Edinburgh. The author designed and fully specified the requirements of the test programme and developed the test protocol.

The test parameters for the accelerated rain erosion rig at ETC remained the same as in the Rain Droplet Impact Assessment, to ensure comparability. In that, 36 nozzles were active with a droplet fall height of 50mm. 27-gauge needles were used from the droplet creation, which provided a droplet diameter of 2.34mm and the rotational speed of the arm was set to 1100r/min.

Accelerated UVa, BS EN ISO 16474-3, Method A, Cycle 1, was selected as the weathering cycle as both coatings B and C1 had went through this cycle as part of the Weathering Impact Assessment, Chapter 5.

The cycle lasted for a total of 3000 hours with repeating phases of 4 hours dry and 4 hours of condensation. A UVa-340nm lamp was used with irradiance set to 0.83 W/m^2/nm, which was only active during the dry phases. During the dry phase, the black panel temperature in the test chamber was set to 60±3°C and during the condensation phase this was set to 50±3°C. The humidity was not controlled, as detailed by the test standard [76].

It was not practical to run the accelerated rain erosion test and the accelerated weathering test concurrently, a staged approach to combined testing was developed. Periods of UVa weathering were interjected with periods of RET. As shown in Table 6, 1000-hour periods of UVa weathering were split by 20 periods of RET until a total of 3000 hours of weathering and 60 minutes of RET was reached. 20-minute periods of RET were selected based upon results obtained in Rain Droplet Impact Assessment, 20-minute RET intervals displayed detectable change from one erosion stage to the next between test stages. The first 20-minute RET phase was expected to be within the incubation period, with the second RET phase expected to be at the end of incubation and the start of erosion and the third RET phase was expected to be within active erosion.

Test Stage	**Amount of RET & Weathering**
Stage 1	0 hours UVa, 0 mins RET (baseline)
Stage 2	1000 hours UVa, 0 mins RET
Stage 3	1000 hours UVa, 20 mins RET
Stage 4	2000 hours UVa, 20 mins RET
Stage 5	2000 hours UVa, 40 mins RET
Stage 6	3000 hours UVa, 40 mins RET
Stage 7	3000 hours UVa, 60 mins RET

Table 6: Combined Erosion and Weathering Test Stage Description

6.1. Methodology

Within this work, two coating systems were used, Coating B and Coating C1. Both coating systems were applied to composite substrate, as described in Specimen Manufacture and Preparation, Chapter 3, Section 3.3. All specimens measured 15mm by 60mm.

To allow specimens to fit in both the accelerated rain erosion test rig and the accelerated UVa weathering test rig, specimens were mounted to a standard aluminium weathering panel using Velcro backed sticky tape, as shown in Figure 6.1. This allowed for the specimens to fit in the weathering rig and to be removed for testing within the rain erosion rig.

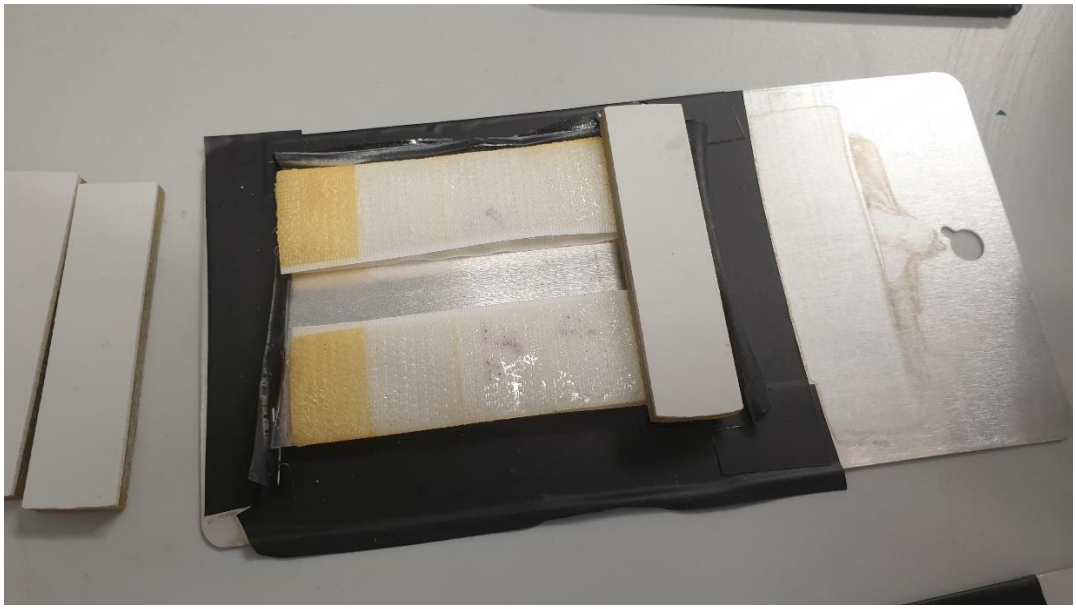

Figure 6.1: Specimen Mounting for Weathering

Five specimens per coating system were used, with an additional three specimens per coating system which were only used for RET. This was to allow a direct comparison between accelerated weathering interjected with RET and RET alone. Each specimen used is listed in Table 7.

Specimen ID	Coating System	Test Type
B1	Coating B	Combined
B2	Coating B	Combined
B3	Coating B	Combined
B4	Coating B	Combined
B5	Coating B	Combined
B13	Coating B	RET only
B14	Coating B	RET only
B18	Coating B	RET only
C16	Coating C1	Combined
C23	Coating C1	Combined
C28	Coating C1	Combined
C29	Coating C1	Combined
C48	Coating C1	Combined
C5	Coating C1	RET only
C12	Coating C1	RET only
C44	Coating C1	RET only

Table 7: Combined Test Specimen ID

Firstly, two standard aluminium weathering panels were prepared with the sticky backed Velcro as shown in Figure 6.1. Then, on one panel, specimens B1, B2, B3, B4 & B5 were mounted, and on the other panel, specimens C16, C23, C28, C29 & C48 were mounted. Before any testing began, all specimens

were analysed in the Advanced Composites Group (ACG) characterisation lab at the University of Strathclyde to provide a baseline assessment of the specimens. The specimens were then taken to Element Materials Technology where they began the accelerated UVa weathering cycle. After 1000 hours of the UVa cycle, the test was paused, and specimens were removed. The specimens were then taken to the ACG lab, where a range of analyses was performed. The next step involved taking the specimens to the Energy Technology Centre where they underwent the first phase of RET, lasting 20 minutes per sample. After the first phase of RET, the samples were then reanalysed in the ACG lab. After the analysis, the samples were returned to Element Materials Technology to resume with the UVa weathering cycle. This process of analysing, then weathering for 1000 hours, then analysing, then RET for 20 minutes, was repeated until all of the test stages were complete, as outlined in Table 6.

In addition to the combined test specimens, three specimens per coating system were used for RET alone. The same RET timings were used for these additional specimens and the additional specimens were tested alongside the combined specimens.

After each test stage, a laboratory analysis was performed. Several analysis methods were used, these are listed below:

Photography – Photographs of test specimens were captured at ETC during rain erosion testing. Additionally, photographs were also captured in the laboratory, using the rear 12 MP camera on a Samsung Galaxy S9, at each test stage. Before any photographs were taken, the specimen surface was wiped with a wet paper towel to remove any surface debris and left to dry for 1 hour.

Optical Microscopy – A Leitz Ergolux Optical Microscope with a Leitz NPL FLUOTAR 10×/0.22 lens was used to explore the surface of the coatings. At each test stage, the eroded zone and surrounding area where the majority of the water droplets struck the specimen was focused in on. Images were then

captured, showing any area of change versus the previous combined test stage.

Mass – An A&D Instruments GR-120-EC mass balance was used to weigh the specimens. Before any mass measurements were taken, the test specimens were left at ambient conditions to dry out for two days. This was to allow for any retained water from weathering or RET to evaporate.

Gloss – The 60° angle was used on the Rhopoint IQ (Goniophotometer) 20°/60°/85° to measure the surface gloss at each test interval. For each specimen five gloss measurements were made, which were the averaged to get a specimen measurement.

FTIR Spectroscopy – The chemical bonding was measured using an Agilent Technologies 4100 FTIR. Three scans were takes per specimen which were then averaged to get a specimen result.

DMA – TA Instruments Q800 DMA with a dual cantilever clamp was used to perform a frequency sweep of each sample after each combined test stage. The frequency sweep test is performed by holding the temperature of the test constant, and then only changing the frequency of the oscillating clamp, which the specimen is mounted to. DMA test conditions were as follows: Temperature – 30°C; Frequencies tested – 1Hz, 20Hz, 40Hz, 60Hz, 80Hz, 100Hz; Poisson's Ratio – 0.33; Initial force – 1N; Amplitude 10µm.

6.2. Combined RET & Weathering Results

6.2.1. Photography

Photographs from the start of the test, Stage 1, and the end of test, Stage 7 are presented herein. Additionally, photographs of the additional specimens which were exposed to RET only are also presented. Photographs from the intermediate analysis, Stages 2-6, are presented in Appendix E -.

Figure 6.2: Photograph, Stage 1, Coating B

Figure 6.3: Photograph, Stage 7, Coating B

Figure 6.2 shows the combined test specimens for coating B at Stage 1, a new sample with no exposure to RET or weathering. The specimen surface is

smooth and uniform to the naked eye, with no major defects. However, at the end of the combined test at Stage 7, shown in Figure 6.3, the specimen surface has visibly changed. Pinholes are present on each specimen along with small patches displaying a corrosion like surface staining.

Figure 6.4: Photograph, Stage 1, Coating C1

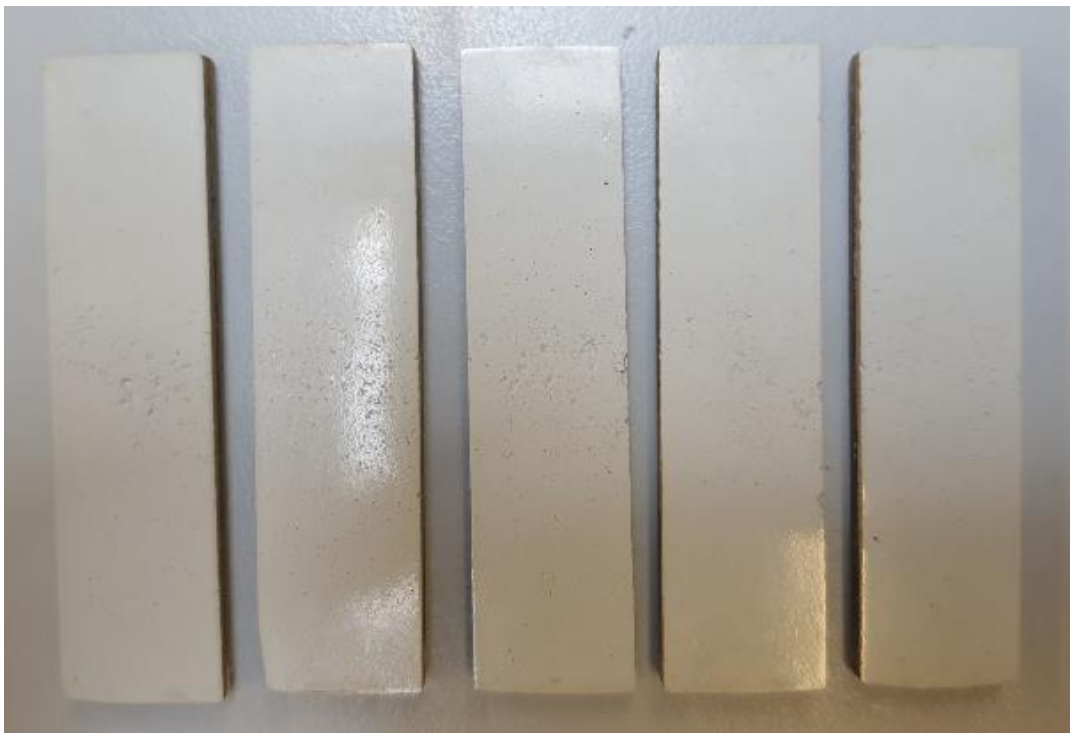

Figure 6.5: Photographs, Stage 7, Coating C1

Next, looking at Figure 6.4 which displays the coating C1 specimens at Stage 1. Again, the specimen surface looks smooth and uniform, with no major defects, as is expected of a new specimen. Then, at the end of the combined test at Stage 7, the specimens show signs of erosion which appear as pinholes on the surface with some areas of progressed erosion where larger holes have begun to develop.

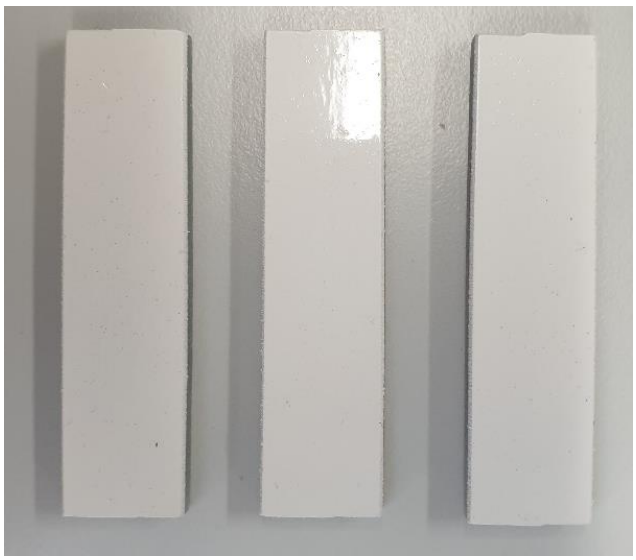

Figure 6.6: Photograph, RET only, 0 minutes, Coating B

Figure 6.7: Photographs, RET only, 60 mins, Coating B

Figure 6.6 displays the RET only specimens for coating B at the start of the test. These specimens are in the same condition as in Figure 6.2. After 60 minutes of RET, as shown in Figure 6.7, the surface of the specimens has changed. The surface has begun to show pinholes as a result of the RET exposure.

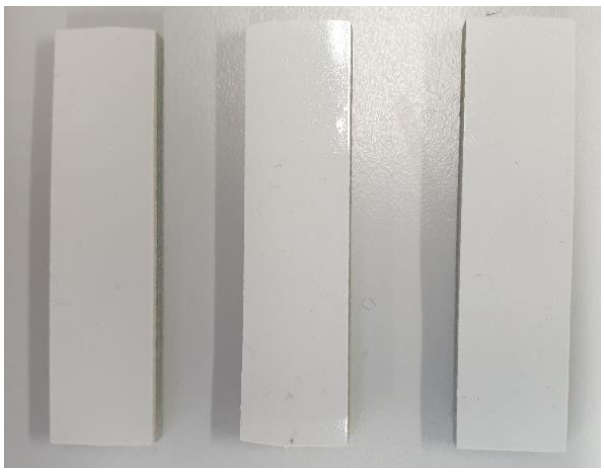

Figure 6.8: Photograph, RET only, 0 minutes, Coating C1

Figure 6.9: Photograph, RET only, 60 mins, Coating C1

Then, looking at Figure 6.8 which shows the start of test for the RET only specimens for coating C1. The same as Stage 1 of the combined test, as in Figure 6.4. Then, Figure 6.9 presents the RET only specimens after 60 minutes on test. The specimen surface has changed in that there are large sections where the top layer of LEP has been removed and other sections which show surface pinhole damage.

6.2.2. Microscopy

The microscopy images presented were captured at each of the individual test stages. The images are displayed in ascending order from Stage 1 through Stage 7 for both coating B and coating C1, with additional images of the RET only samples also presented.

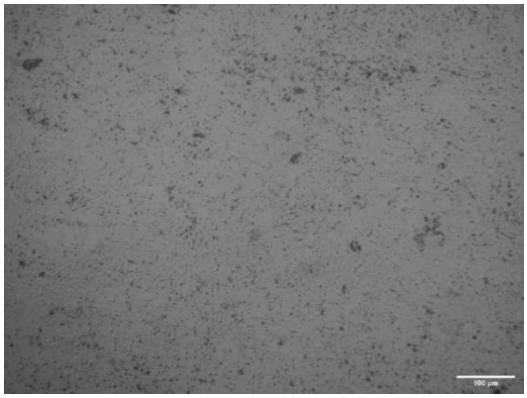

Figure 6.10: Microscopy, Stage 1, Coating B

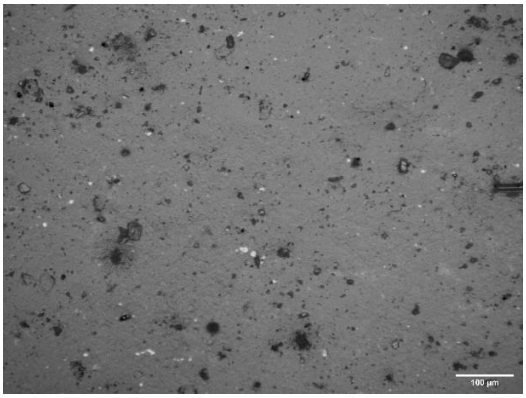

Figure 6.11: Microscopy, Stage 2, Coating B

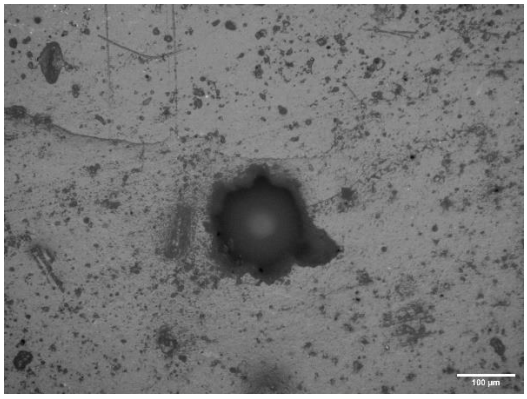

Figure 6.12: Microscopy, Stage 3, Coating B

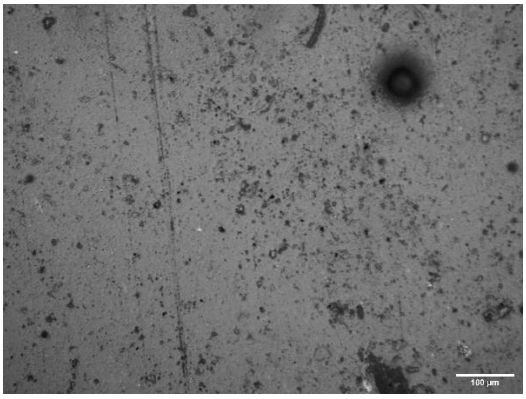

Figure 6.13: Microscopy, Stage 4, Coating B

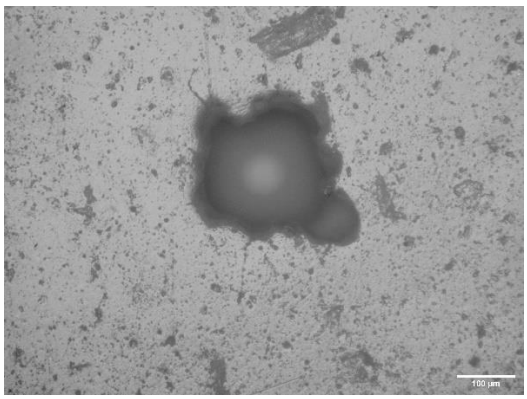

Figure 6.14: Microscopy, Stage 5, Coating B

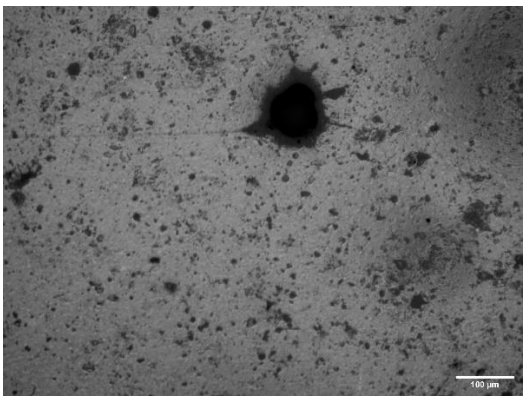

Figure 6.15: Microscopy, Stage 6, Coating B

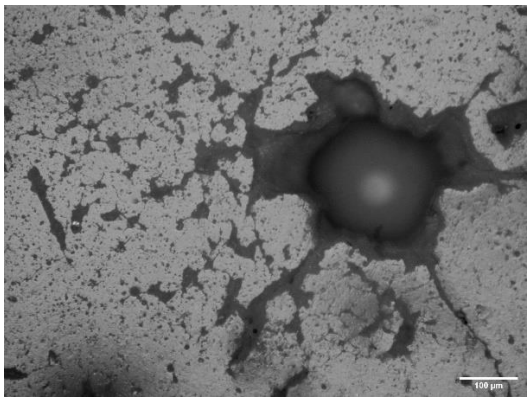

Figure 6.16: Microscopy, Stage 7, Coating B

Figure 6.10 through Figure 6.16 present the microscopy images for the combined test of coating B, for Stages 1 through 7 respectively. Initially, at Stage 1, the surface is shown to have an uneven texture with some small pinholes/bubbles present. Then, after the first period of weathering at Stage 2, there is an observable change in the surface texture. Larger pinholes appear on the surface along with small white flecks. Next, the first period of RET at Stage 3 causes much larger holes, along with cracks, to develop on the surface. Stage 4 is the second weathering period which induces further surface roughening and changes the surface texture. Further RET at Stage 5 increases the number of larger holes present on the surface. Stage 6 is the final weathering period which exacerbates the decline in surface texture, causing further roughening and an increase in the “orange peel” effect. The

final stage, Stage 7, shows a drastic change in surface texture with an increase in surface cracking and amount of surface holes.

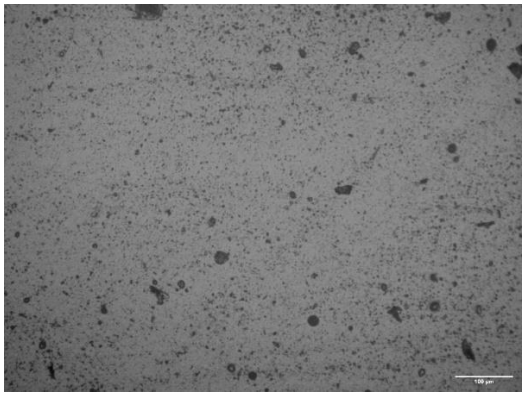

Figure 6.17: Microscopy, RET only, 0 minutes, Coating B

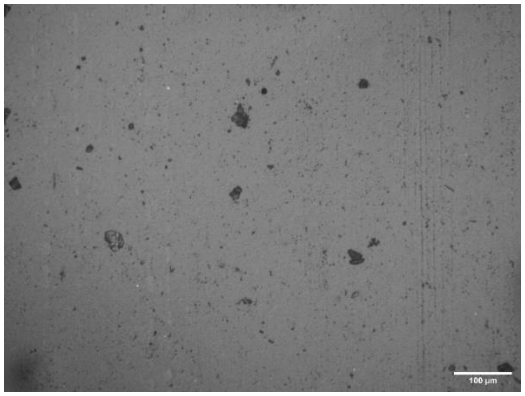

Figure 6.18: Microscopy, RET only, 20 minutes, Coating B

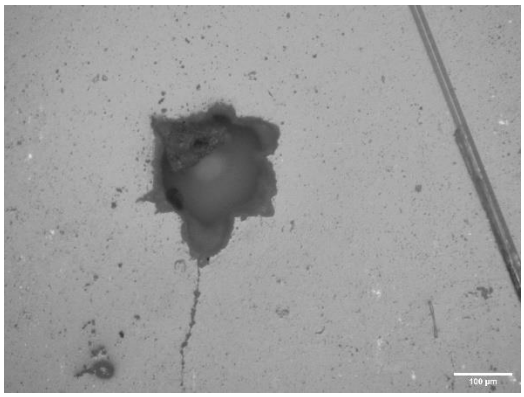

Figure 6.19: Microscopy, RET only, 40 minutes, Coating B

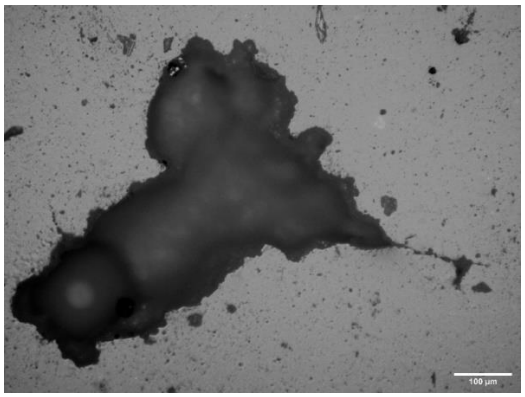

Figure 6.20: Microscopy, RET only, 60 minutes, Coating B

Microscopy images from the RET only test for coating B are shown in Figure 6.17 to Figure 6.20. Again, the undamaged specimens show an uneven surface texture with small pinholes/bubbles present. As the RET progresses, the surface damage begins to be observable. Initially with the increase in hole size, then with the formation of surface cracks which then lead to larger sections of LEP removal.

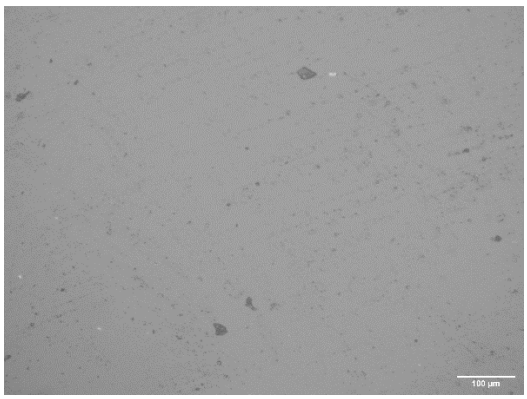

Figure 6.21: Microscopy, Stage 1, Coating C1

Figure 6.22: Microscopy, Stage 2, Coating C1

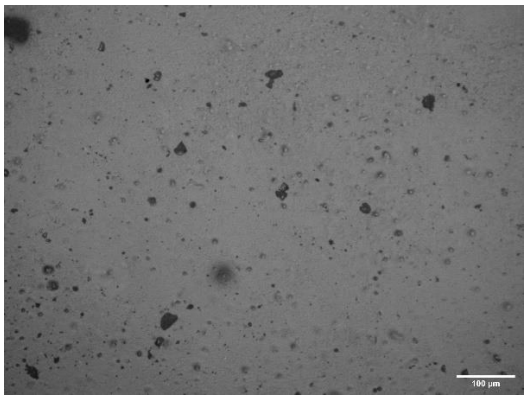

Figure 6.23: Microscopy, Stage 3, Coating C1

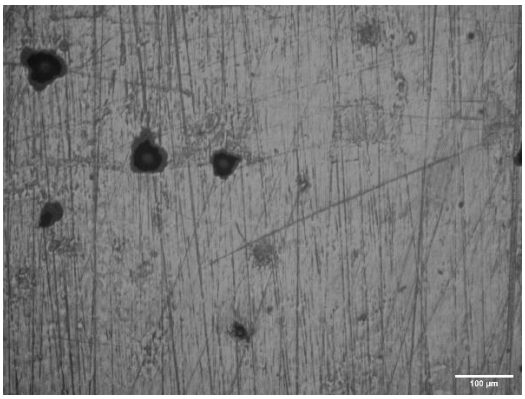

Figure 6.24: Microscopy, Stage 4, Coating C1

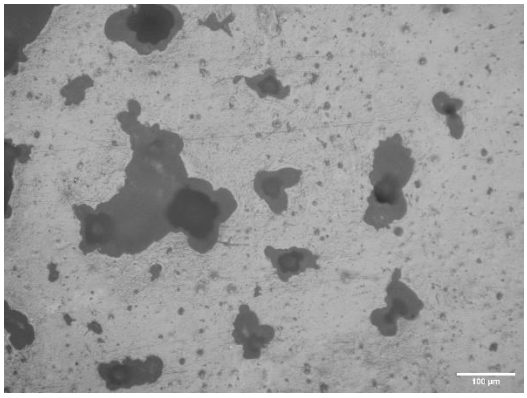

Figure 6.25: Microscopy, Stage 5, Coating C1

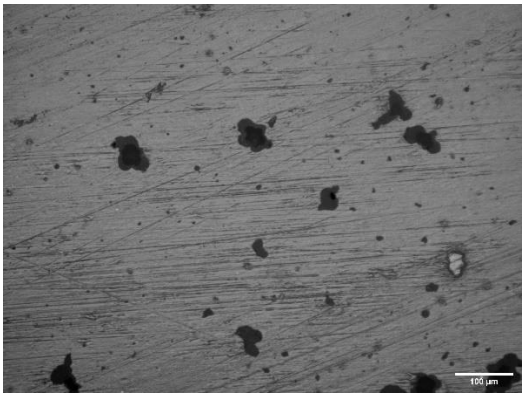

Figure 6.26: Microscopy, Stage 6, Coating C1

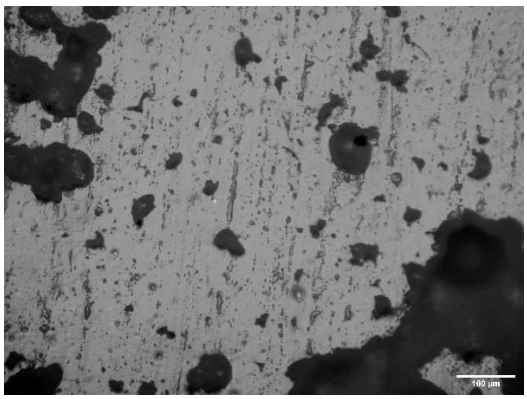

Figure 6.27: Microscopy, Stage 7, Coating C1

For coating C, the microscopy images for the combined test are presented in Figure 6.21 through Figure 6.27. Stage 1 shows a mostly smooth surface with some small pinholes/bubbles. However, after the first weathering period at Stage 2, lines are easily observable on the specimen surface. Moving to the next RET period at Stage 3, the lines have disappeared and the amount of pinholing has increased, with some larger holes beginning to emerge. Then, at Stage 4 the lines reappear after the second weathering period. Stage 5 brings the second RET period and a drastic change in surface texture with the removal of the lines which were present after weathering and an increase in the number and size of surface holes. The final weathering period at Stage 6 produces the lines on the surface of the specimens. The last RET period at Stage 7 causes large amounts of LEP loss with deepening surface pits and holes.

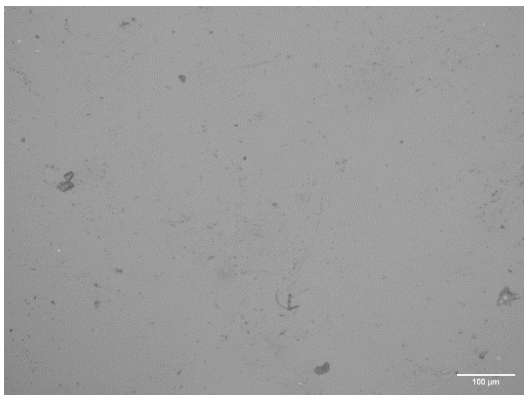

Figure 6.28: Microscopy, RET only, 0 minutes, Coating C1

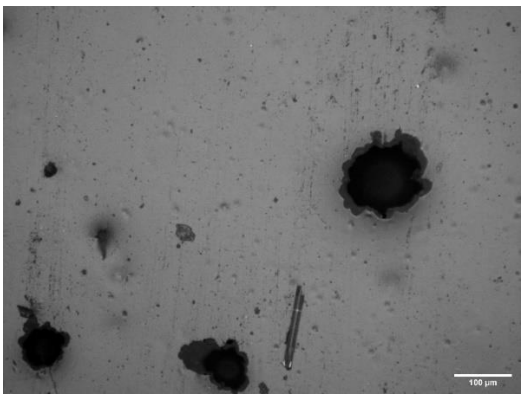

Figure 6.29: Microscopy, RET only, 20 minutes, Coating C1

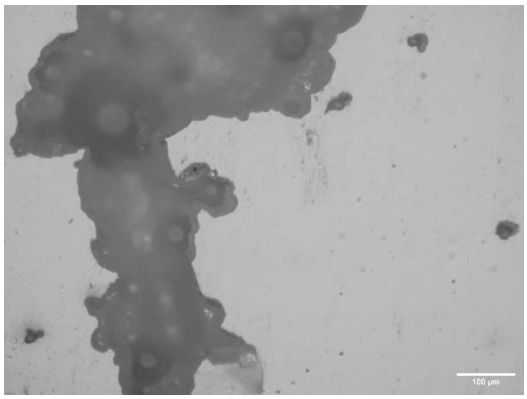

Figure 6.30: Microscopy, RET only, 40 minutes, Coating C1

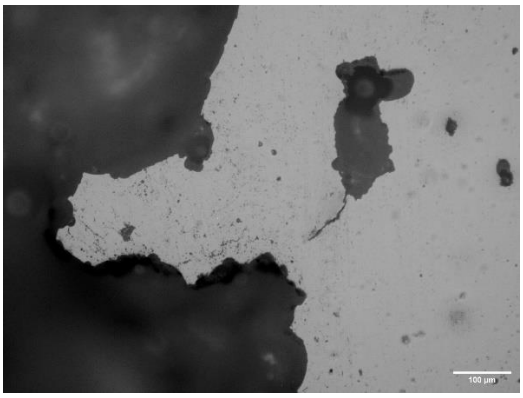

Figure 6.31: Microscopy, RET only, 60 minutes, Coating C1

The RET only test for coating C1 is presented in Figure 6.28 to Figure 6.31. Similarly to the combined test, the initial surface is mostly smooth with small amounts of pinholing/bubbles. As the RET progresses, holes become larger and increase in quantity. The holes then collate, creating larger sections of LEP removal, resulting in cliff edge like topography, as shown in Figure 6.31.

6.2.3. Mass

The data presented in this subsection shows the mass loss measurements, as a percentage of the initial mass, for each test stage for the combined test. Additionally, the mass loss data for the RET only samples is shown. The RET only samples are plotted against the corresponding combined test stage, even though they have experienced no weathering. This is to allow easy visual

comparison between the combined test and RET only. Error bars represent a 95% confidence limit on the results.

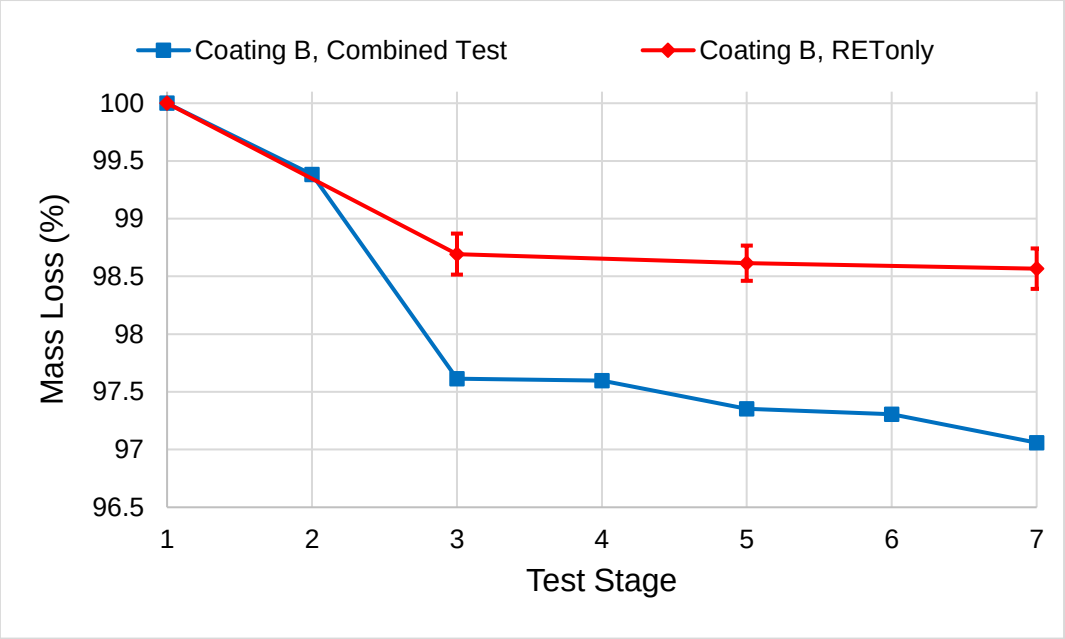

Figure 6.32: Mass Loss, Combined Test, Coating B

Mass loss for coating B for both the combined test and the RET only test is shown in Figure 6.32. Initially, there is a sharp decline in mass after the first RET period with both tests. The combined test causes a greater mass loss, likely as a result of elevated temperature due to weathering, with a difference of 1.1% after the first RET period. The difference extends to 1.5% at the end of test. Additionally, during the combined test, the mass loss is greater after a RET period than after a weathering period. Between Stages 3 and 4, a weathering period, the mass loss is 0.02% and between Stages 4 and 5, a RET period, the mass loss is 0.24%. This is similar between Stages 5 and 6, where the mass loss is 0.05% and between Stages 6 and 7, where the mass loss is 0.25%.

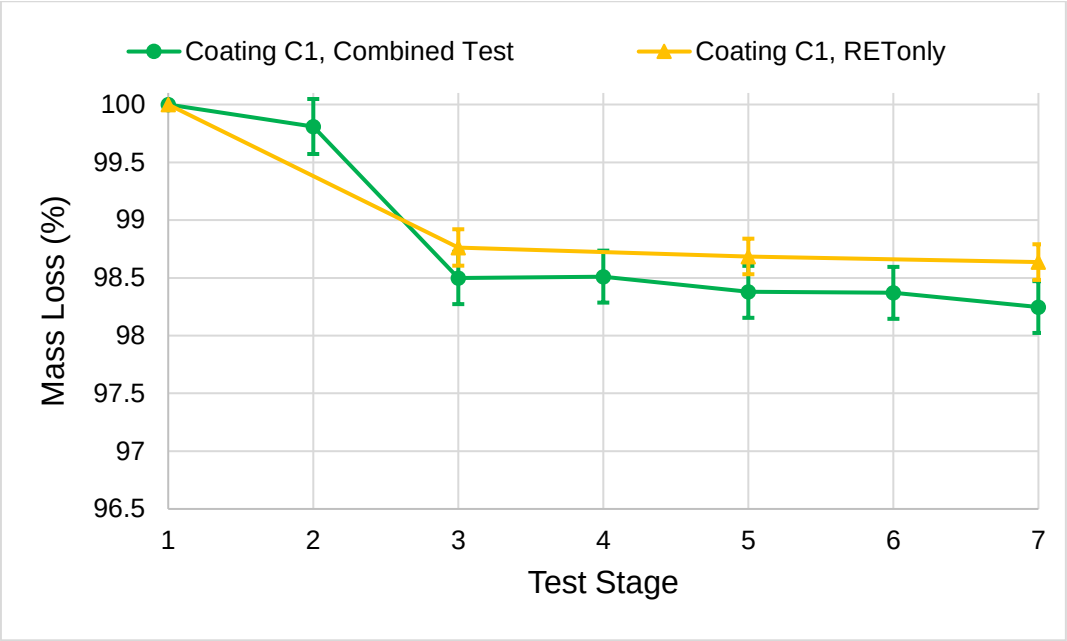

Figure 6.33: Mass Loss, Combined Test, Coating C1

Looking at the mass loss for coating C1 for the combined test and RET only test, Figure 6.33 presents both results. For both tests, there is a sharp decrease in mass after the first RET period, with the combined test losing 1.5% and the RET only just losing 1.2%. After which, the decrease in mass for both tests is much shallower, resulting in a difference of 0.4% at the end of test. Similarly with coating B, the mass loss after the second and third weathering periods is negligible and the mass loss after the second and this RET periods is much smaller than that of the first.

6.2.4. Gloss

The data presented in this subsection shows the gloss loss measurements, as a percentage of the initial gloss, for each test stage for the combined test. Additionally, the gloss loss data for the RET only samples is shown. The RET only samples are plotted against the corresponding combined test stage, even though they have experienced no weathering. This is to allow easy visual comparison between the combined test and RET only. Error bars represent a 95% confidence limit on the results.

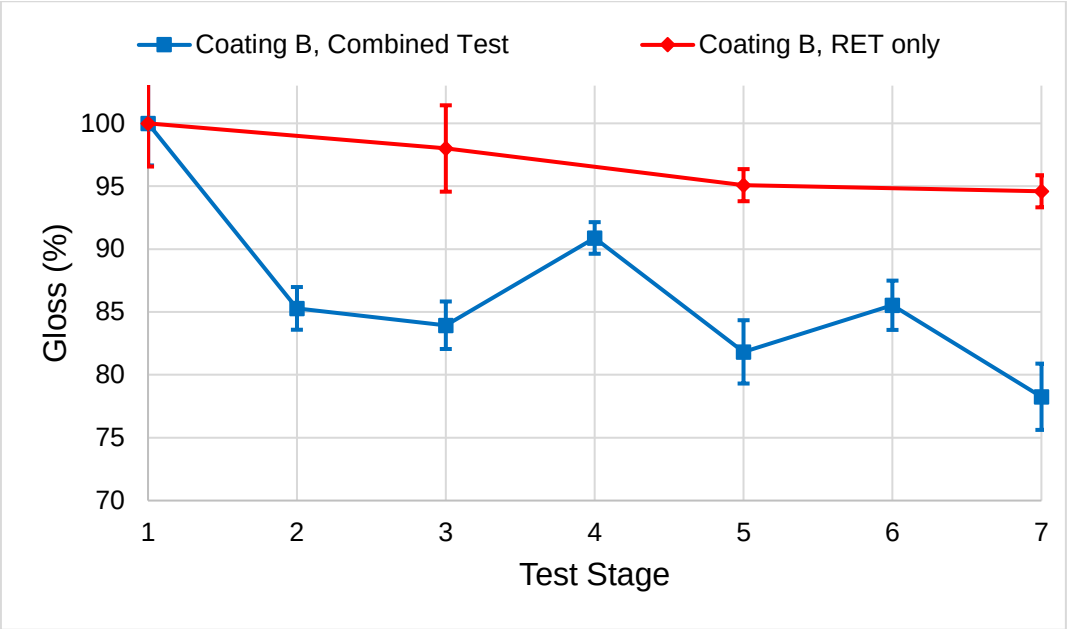

Figure 6.34: Gloss Loss, Combined Test, Coating B

Figure 6.34 presents the gloss results for coating B for both the combined and RET only tests. The RET only test shows a slow decrease in gloss as the test progresses, resulting in a 5.4% reduction. The combined test shows a sharp initial decrease after the first weathering period with a 14.7% reduction in gloss. The gloss measurement then reduces slightly after the first RET period, before then increasing by 7% after the second weathering period. This increase in gloss is repeated after the third weathering period where an increase in 3.7% was measured. After each RET period, there was a noticeable decrease in gloss with 9.1% after Stage 5 and 7.3% after Stage 7.

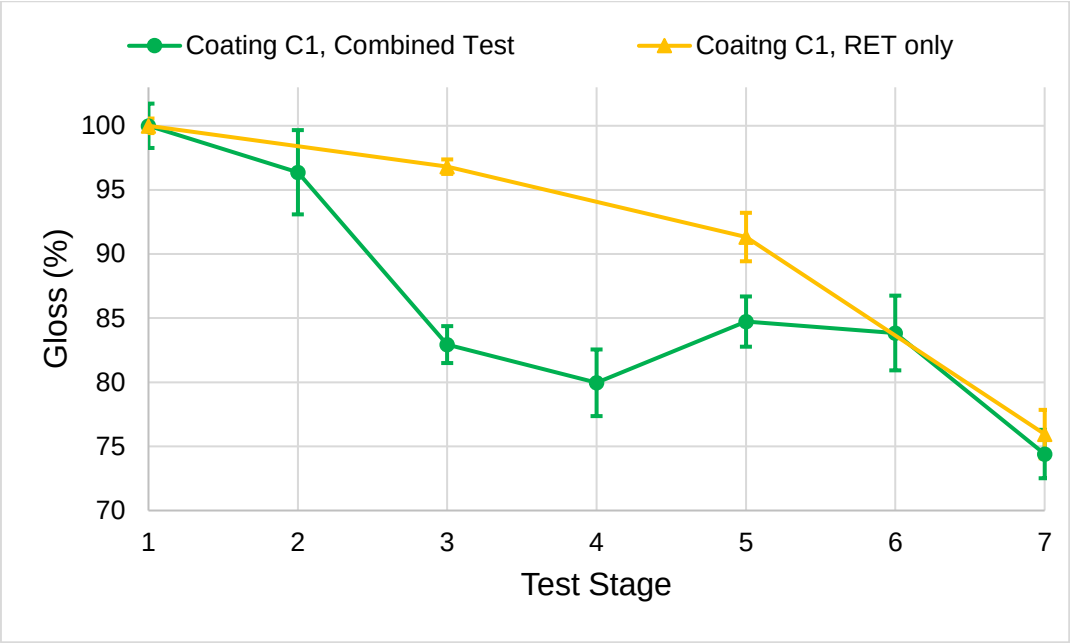

Figure 6.35: Gloss Loss, Combined Test, Coating C1

The gloss results for coating C1 during the combined test and the RET only test are shown in Figure 6.35. The RET only test shows a decrease after each RET period, with the largest decrease, of 15.4%, occurring between the 40-minute and 60-minute RET period. The combined test starts with a small decrease after the first weather period followed by a sharp decrease after the first RET period, resulting in a 17.1% loss in gloss. The weathering period at Stage 4 further decreases the gloss, though only by 3%. After the second RET period at Stage 5, the gloss then increases by 4.8%, before slightly decreasing after the last weathering period. After the final RET period, the gloss has further reduced by a total of 25.6%, 1.5% more that the RET only test.

6.2.5. Spectroscopy

The data presented in this subsection shows the spectroscopy analysis, using FTIR, after each UVa weathering period for both coating B and coating C1.

The data for coating B was normalised around 1249 cm^{-1} and the data for coating C1 was normalised about 1240 cm^{-1}.

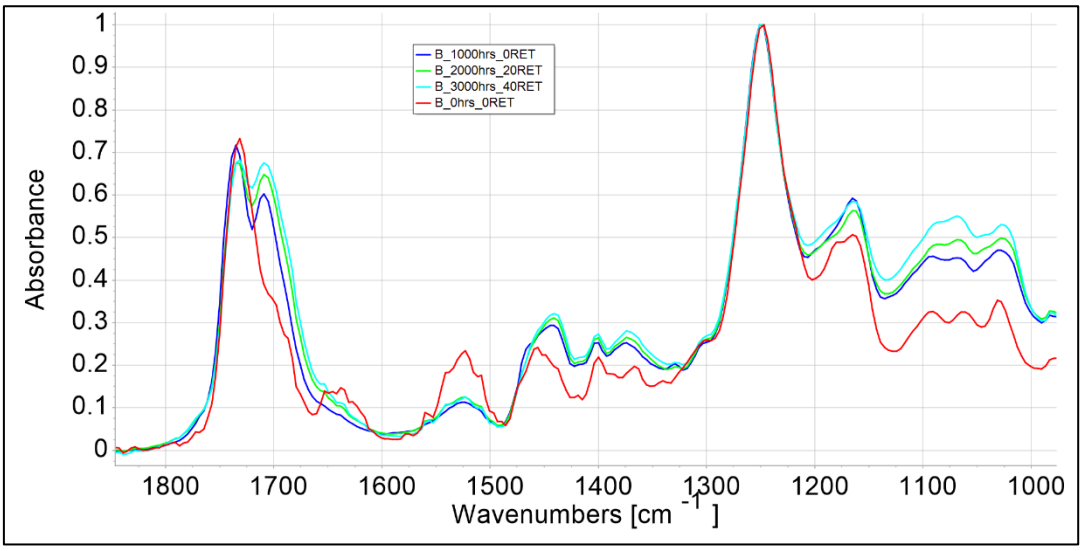

Figure 6.36: FTIR, Combined Test, Coating B

Figure 6.36 presents the FTIR plot for coating B after each weathering period during the combined test. Firstly, as the test progresses a new peak is formed at 1708 cm^{-1}, with the small peak at 1644 cm^{-1} disappearing. Next, the amplitude of the peak at 1526 cm^{-1} is reduced and there is an upwards shift and widening in the peak at 1454 cm^{-1}, all observable after the first weathering period. Additionally, the trough at 1077 cm^{-1} flattens out as well as a progressing upward shift in the 1200 cm^{-1} to 1000 cm^{-1} region as the test progresses.

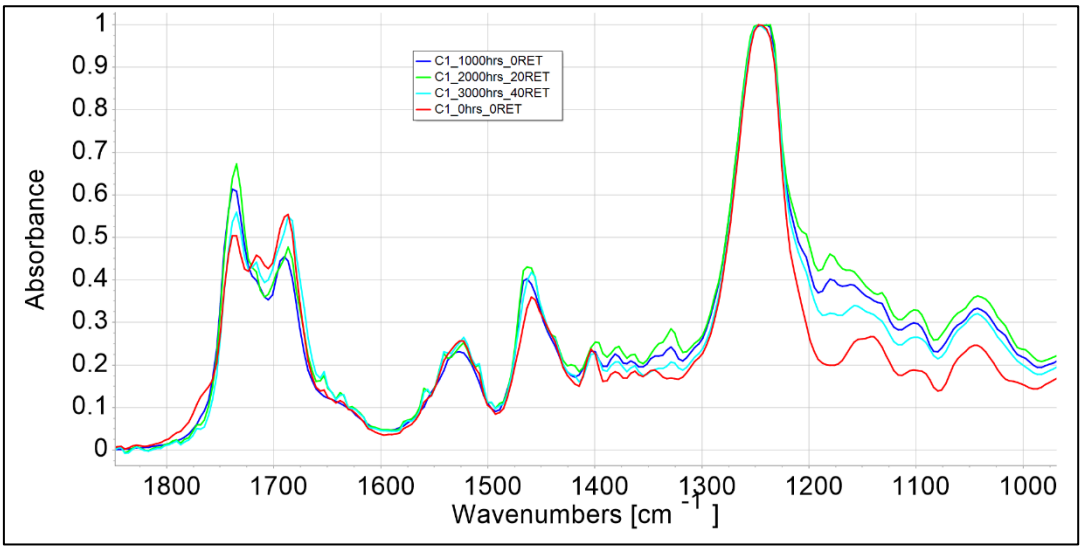

Figure 6.37: FTIR, Combined Test, Coating C1

The FTIR plot for coating C1 after each of the weathering periods of the combined test is shown in Figure 6.37. Firstly, the short shoulder type peak at 1768 cm^{-1} is removed after the first weathering period. Additionally, the peak at 1716 cm^{-1} is reduced as the test progresses and is then eliminated after the third weathering period. Next, a short peak is formed at 1330 cm^{-1} as well as another at 1182 cm^{-1} and as the test progresses, there is an increasing upwards shift in the 1200 cm^{-1} to 1000 cm^{-1} region.

6.2.6. Dynamic Mechanical Analysis

Presented within this subsection is the data from the dynamic mechanical analysis of the combined test specimens for both coating B and C1.

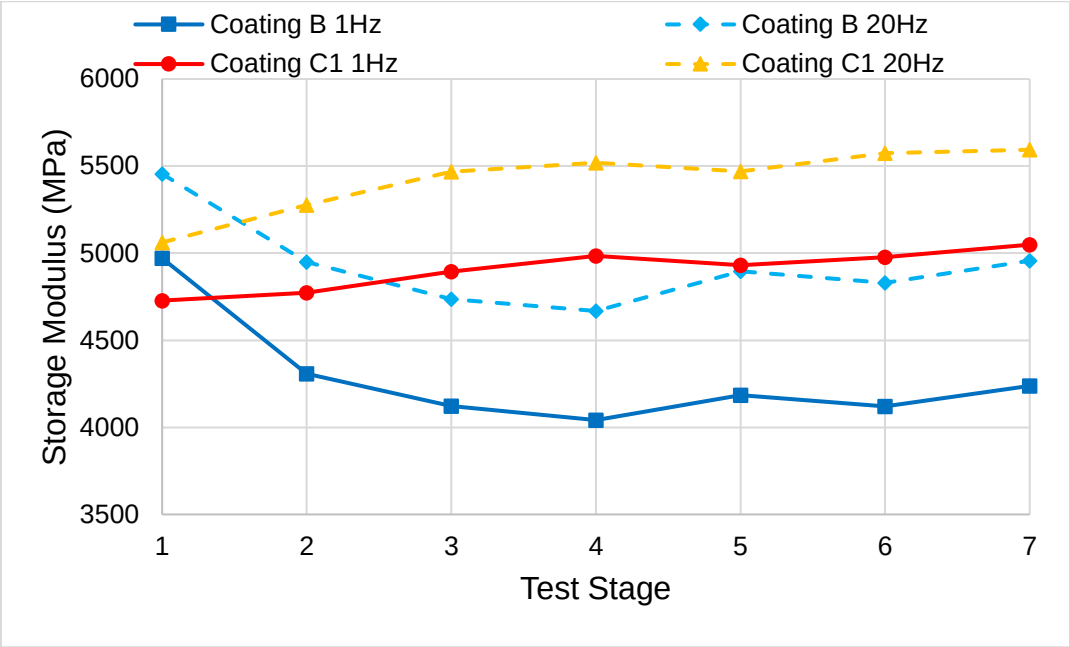

Figure 6.38: DMA, Storage Modulus, Combined Test, Coatings B & C1

Figure 6.38 displays the storage modulus measurements for both coating B and C1, at two test frequencies, 1 Hz and 20 Hz, at all stages of the combined test. The first observation is that increasing the test frequency from 1 Hz to 20 Hz shifts the plot upwards, this is the case for both coating systems.

For coating B, there is an overall decrease in storage modulus as a result of the combined test. An initial sharp decrease of 663 MPa at 1 Hz and 506 MPa at 20 Hz, both after the first weathering phase, can be observed. Then, for both test frequencies, there is a further decrease after the first RET and second weathering phases reaching 4041 MPa at 1 Hz and 4668 MPa at 20 Hz at Stage 4 of the combined test. After the second RET phase, there is a slight increase of 143 MPa in the storage modulus at 1 Hz and 228 MPa at 20 Hz. Continuing with the combined test stages, the final weathering phase, Stage 6 shows a slight decrease of 64 MPa at 1 Hz and 66 MPa at 20 Hz. The test ends with an increase after the third RET phase where the storage modulus at 1 Hz increases by 118 MPa and 127 MPa at 20 Hz.

Coating C1 shows an overall increase in storage modulus, for both frequencies, as a result of the combined test. The baseline assessment of

4728 MPa at 1 Hz and 5062 MPa at 20 Hz increases until Stage 4, where the storage modulus for 1 Hz is 4984 MPa and for 20 Hz is 5519 MPa. There is then a slight decrease of 53 MPa at 1 Hz and 50 MPa at 20 Hz after the second RET phase. The final weathering phase yields a small increase followed by a further minor increase due to the final RET phase. The combined test ends with a storage modulus of 5049 MPa at 1 Hz and 5594 MPa at 20 Hz.

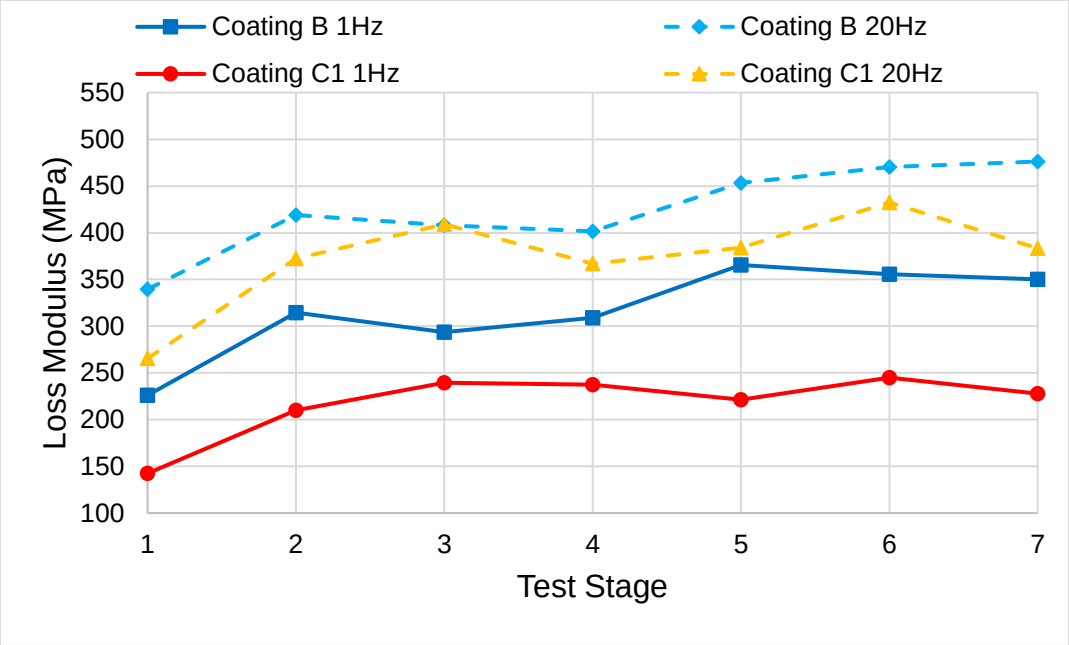

Figure 6.39: DMA, Loss Modulus, Combined Test, Coatings B & C1

The loss modulus measurements for both coating B and coating C1 are presented in Figure 6.39. Firstly, looking at coating B, after the first weathering phase at Stage 2, there is an increase in the loss modulus of 89 MPa at 1 Hz and 79 MPa at 20 Hz, both from the baseline assessment at Stage 1. The first RET phase brings a decrease of 21 MPa at 1 Hz and 10 MPa at 20 Hz at Stage 3. Beyond Stage 3, the 1Hz test increases by 15 MPa and then by a further 57 MPa after the second weathering and RET phases respectively. Whereas at 20 Hz, decrease by 7 MPa after Stage 4, then increases by 51 MPa after Stage 5. Then, at 1 Hz, there is a decrease after the final weathering and RET phases, resulting in an end of test loos modulus value of 350 MPa at 1Hz. At

20 Hz, an increase of 18 MPa after the final weathering phase and a further increase of 5 MPa after the final RET phase is observed.

Coating C1 presents a similar overall increase in loss modulus as the combined test progresses. The initial value of 142 MPa at 1 Hz increases by 68 MPa and the initial 20 Hz value of 265 MPa increases by 107 MPa as a result of the weathering phase. At 1 Hz, from Stage 2 onwards, there are only small changes in the measured loss modulus values with a difference of 18 MPa between Stage 2 and the end of test. At 20 Hz, beyond Stage 2, there are slightly larger variations in loss modulus through the combined test than at 1 Hz, though at the end of test there is a difference of 11 MPa between Stage 2 and Stage 7.

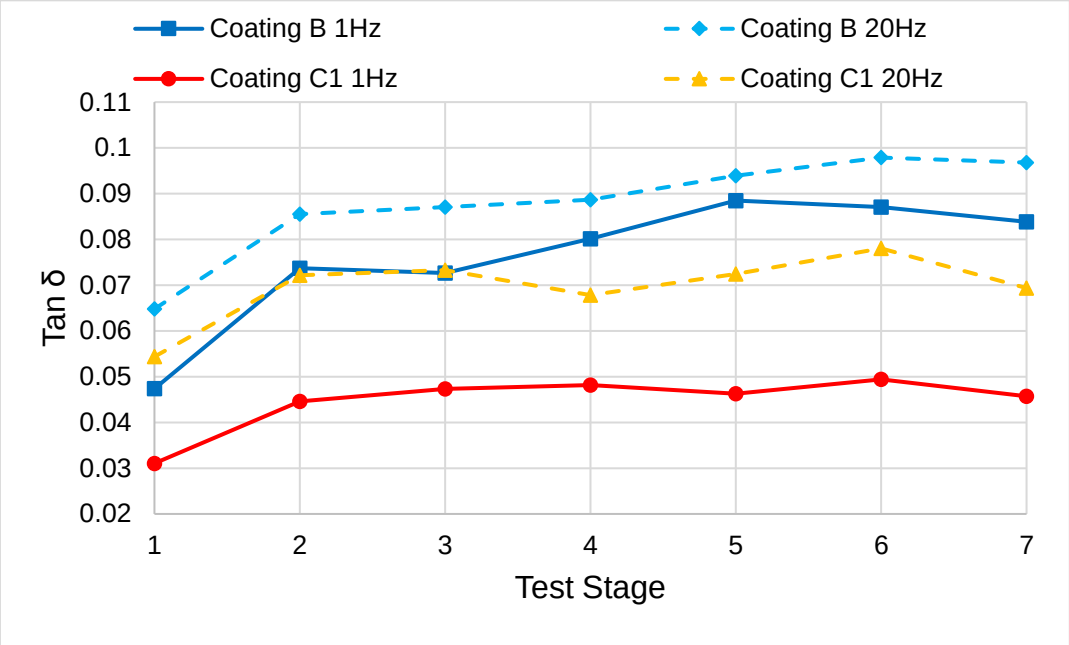

Figure 6.40: DMA, Tan δ, Combined Test, Coatings B & C1

Finally, the tan δ measurements for both coating B and coating C1 are shown in Figure 6.40. Looking at coating B, there is an initial sharp increase to 0.074 at 1 Hz after the first weathering phase at Stage 2, similarly at 20 Hz, the tan δ increases to 0.086. There is then a miniscule decrease at 1 Hz after the first RET phase at Stage 3, before a gradual increase to 0.088 at Stage 5, after the second RET phase. The 1 Hz combined test ends with a reduction in tan δ to

0.084 at Stage 7. At 20 Hz on coating B, the tan δ continues to climb, slowly, after each test phase until Stage 6. As the test progresses, reaching a maximum value of 0.098 at Stage 6, before then reducing slightly at the end of test to 0.097 at Stage 7.

Coating C1 shows a similar sharp increase in tan δ after the first weathering phase, where the 1 Hz plot increases by 0.014 and 20 Hz increases by 0.018 at Stage 2. At 1 Hz, from Stage 2 to the end of test at Stage 7 there are only very small changes in tan δ measured, an increase of 0.001 between Stage 2 and Stage 7 at the end of test. At 20 Hz, there is slightly more variation, after Stage 3, a decrease to 0.068 is measured as a result of the second weathering phase. The tan δ then increases after the second RET phase and third weathering phase to reach 0.078 at Stage 6. Then, after the final RET phase at Stage 7, tan δ decreases by 0.009 at the end of the combined test.

6.3. Discussion

Considering the overall effect of the combined test, there are measurable differences versus RET alone. The weathering phases of the combined test induce chemical transformations on the coating systems, leading to a distinct change in surface micro-structure, in turn, lowering the surface gloss value and reducing the mass of the specimen. This ultimately leads to a restructuring of the polymer chains in the top layers of the coating systems. Within coating C1, a rougher coating surface was developed due to weathering phases, as highlighted by the gloss and microscopy measurements. A rougher coating surface will provide a greater surface area and non-uniform surface topography, which may lead to an increase in erosion. A surface smoothing effect, as seen in Figure 6.10 through to Figure 6.16, however, can prolong the life of the coating system by increasing erosion performance, as observed in coating B.

6.3.1. Coating B

Photographs

As a result of the combined test, the surface of coating B specimens visually changes with increased weathering and rain erosion. Some surface pitting is observable at the end of the test, which was not visible at the start of the test. However, no large areas of material have been removed and the specimens haven't begun to erode, only displaying surface pitting. Additionally, there is a noticeable colour change with the specimens appearing more yellow. Furthermore, what appears to be corrosion has formed as spots on the specimen surface. The corrosion is likely as a result of contamination during one of the test stages, as there are no metal elements present in the specimen substrate nor coating system, or due to contamination of the coating system components as a result of storage in metal containers. The coating storage containers were visually inspected, and no signs of corrosion were found, the storage containers appeared to be in good working order.

The RET only specimens display similar surface pitting to the combined test, though there is no observable change on colour as there is in the combined test.

Microscopy

The microscopy images show, in detail, how the surface micro-structure changes as a result of the combined test. Initially, at Stage 1, the surface is not perfect. There are small pinholes/bubbles present with an uneven surface texture. As the first weathering period is over, at Stage 2, the pinholes/bubbles have slightly deepened and widened, further exaggerating the uneven surface texture. At Stage 2, the micro-structure can be likened to the orange peel effect, where the specimen surface looks like the skin of an orange. The elevated temperature and humidity of the weathering phase are likely to cause a restructuring of the polymer chains on the coating surface. Additionally, the elevated conditions could induce a post-curing effect where any remaining

volatile components of the coating system are evaporated, causing the orange peel effect. Then, after the first RET period at Stage 3, much larger surface holes and pits develop along with some light surface cracks. Moving to the next weathering phase, Stage 4, the orange peel effect worsens and becomes more prevalent, likely as a result of further chemical reactions and polymer restructuring. Stage 5 sees further RET where previous holes identified at Stage 3 deepen and widen further, and small cracks begin to emerge from the holes. Stage 6 is the final weathering phase and shows a deepening of the small surface pits and overall smoothening of the edges of pits, holes and cracks. The final RET phase, Stage 7, presents a large textural difference in the coating surface with larger cracks developing at the holes and sections of orange peel effect are removed, causing further cracks and pits.

It is also noticeable that the orange peel effect is not present on the RET only samples. Therefore, the orange peel effect is a result of the weathering cycle, likely a chemical reaction involving volatile components. The post-cure effect is further investigated with FTIR spectroscopy.

Additionally, small white flecks are visible after the weathering phases. These flecks are likely a metal and ties in with the visible corrosion which can be seen in the photographs. As previously mentioned, the metal is likely a result of contamination, most likely from the water used within the weathering cycle.

Mass

The mass loss for the combined test was greater than the mass loss of the RET only test at all analysis stages. At the end of test, difference of 1.5% and 0.4% was measured for coating B and coating C1 respectively. The differences measured are small, however, scaling these differences to a full blade could result in an aerodynamic inefficiency or blade imbalance. The increased mass loss of the combined test further reinforces that a chemical reaction is occurring, where volatile materials are removed from the specimen as a result of elevated temperature during the weathering phase.

Gloss

The gloss measurement for coating B throughout the combined test shows a general decrease in gloss value. After the initial weathering phase at Stage 2, the gloss value decreases by 14.7%, a considerable gloss loss given that previous weathering testing in Chapter 5 presented an average of 10% gloss loss per 1000 hours of test. This is likely a result of the initial high temperature and humidity exposure causing a surface chemical reaction, in which volatile components are removed from the coating surface, yielding a more uneven surface texture which can be observed in the microscopy. However, after weathering phases at Stage 4 and Stage 6, the gloss value has increased. The weathering phases cause the specimens to swell and take on water. This leads to the coating surface levelling off, ultimately rendering the surface as more uniform and smoother, which will be reflected in the gloss measurement as an increased value. Comparing the gloss results with the microscopy images, Stages 4 and 6 show an increase in orange peel effect along with a smoothening of the edges of the pits and holes which were a result of previous RET phases. There are no obvious sharp edges in the surface topography after a weathering phase. This would increase the gloss value as more light would be returned as a specular reflection, whereas with sharp, uneven topography, a higher diffuse reflection is expected, lowering the gloss value measured.

A possible solution as to why the gloss value both increases and decreases during the combined test could be due to what weathering cycle phase, wet or dry, the specimens were removed from the test cabinet. If the specimens were removed during a wet phase, they are likely to have retained a water causing specimen swelling which would increase the gloss value. If they were removed during a dry phase, they specimens would have had time to dry off and present a more realistic gloss value.

Comparing the combined test to the RET only test, the RET only test losses much less gloss than the combined test, resulting in a 16.3% difference at the

end of test. However, the weathering phases induce a surface topography change which is reflected in the gloss measurement. Combining the increase in gloss values after a weathering phase with the microscopy images, the change is an overall smoothening of surface texture after a weathering phase.

Spectroscopy

Now, considering the FTIR spectroscopy results for the combined test of coating B, a distinct change in spectra is observed, as with the same spectra changes which occurred during the UVa weathering cycle within the Weathering Impact Assessment, Chapter 5. After the first weathering phase, a peak is formed at 1708 cm^{-1} which is representative of a Carbon-Oxygen double bond. The peak at 1644 cm^{-1}, representing a Carbon-Carbon double bond, is removed and the amplitude of the peak at 1526 cm^{-1}, a Nitrogen-Oxygen single bond, is vastly reduced. Additionally, the baseline peak at 1454 cm^{-1} has shifted to a wider peak at 1442 cm^{-1} representing a change from a Carbon-Hydrogen bond to an Oxygen-Hydrogen bond associated with a Carboxyl functional group. Furthermore, the trough at 1077 cm^{-1} begins to flatten out as the test progresses, indicating an increasing presence of Carbon-Oxygen single bonds.

Looking at the wider spectrum, shown in Appendix F -, peaks at 2920 cm^{-1} and 2852 cm^{-1} have become more prominent and greater in amplitude. This region is associated with Oxygen-Hydrogen single bonds and each peak is likely linked to the formation of a Carboxyl group or intramolecularly bonded alcohol groups.

All of the FTIR data indicates a chemical reaction is taking place with the removal and formations various of bond types. As the detailed formulation of the coating is proprietary information and retained by the company, without the initial chemical formulae, the exact changes cannot be confirmed with FTIR alone. However, FTIR can provide insight as to what changes are occurring. In this case, it is likely that a Carboxyl functional group has formed with the removal of an Aldehyde functional group. This ties in which what was observed

from the microscopy images and the gloss measurement. A surface restructuring of the polymer chains is occurring as a direct result of the accelerated weathering test. This surface restructuring leads to a smoother coating surface, as is observable from both the microscopy and gloss loss measurements, prolonging the life of the coating system.

Dynamic Mechanical Analysis

Firstly, as shown in Figure 6.38, the storage modulus for Coating B presents an initial sharp decrease, followed by a slight increase and levelling out after the second RET phase at Stage 5. The initial decrease shows a loss in elasticity, the ability to store energy, of the specimens, indicating a change in polymeric structure and a reduction of polymer interlinking. Towards the end of the test, the storage modulus begins to slowly increase indicating a greater prevalence of polymer interlinking. The loss modulus shows an overall increase throughout the combined test, with an initial sharp increase observed. The initial increase in loss modulus ties in with the polymer restructuring and loss of interlinking seen in the storage modulus, which has increased the ability to dissipate energy. The tan δ data shows an initial sharp increase followed by an overall slower increase as the combined test progresses. The increase in tan δ represents an increase of damping within the specimens, meaning that during and after the combined test, the specimens convert more of the input mechanical energy to heat.

However, from the measured data, there is no conclusive evidence that suggests that either weathering or RET cause a specific change in the moduli of the specimens. It should be noted that the specimens include the composite substrate as well as the coating system. Additionally, as the specimens progress through the combined test, their geometry changes, whether due to swelling as a result of water absorption or a removal of surface material due to erosion. The input geometry parameters remained the same throughout all of the DMA testing.

6.3.2. Coating C1

Photographs

There is a distinct visual difference in the specimens before and after the combined test. After the test, there is severe surface pitting with some areas of erosion present. Additionally, there is an observable colour change with a yellowing of the specimens. Comparing the combined test to the RET only specimens, the RET only specimens appear to show more surface erosion. There are larger patches of erosion along with areas on pitting and surface coating removal, though there is no yellowing effect. This visual observation suggests that adding weathering stages, as in the combined test, could increase the lifetime of coating system C1.

Microscopy

Again, the initial surface texture at Stage 1 is not perfect. There are a few pinholes/bubbles present with a mostly smooth coating surface. The first weathering phase, at Stage 2, brings prominent lines to the surface micro-structure. The lines appear to be application lines from using a brush to apply the coating system to the substrate. Similar to coating B, the elevated test temperature and humidity could cause a restructuring of the polymer chains and a possible chemical reaction involving volatiles, therefore disturbing the surface topography. Stage 3 brings the first RET phase, where the previously formed lines have been removed and surface pits have begun to develop. The removal of the surface lines could be due to the RET removing a very thin layer of the coating surface material and causing a smoothening effect on the majority of the coating surface, except where pits and pinholes are present as these are exacerbated by the RET. The next weathering phase, Stage 4, causes the re-emergence of the application lines. A likely result of further surface chemical reactions and polymer restructuring due to the weathering cycle’s elevated test conditions. Stage 5 bring further surface pitting and holes begin to develop as pits collate as a result of RET. The final weathering phase,

Stage 6, causes the surface lines to reappear with Stage 7, the final RET phase, bringing further pits as well as the deepening and widening of holes.

The RET only specimens show a different surface textural change, where the weathering cycle is not present. The RET only specimens display an increased amount of surface holes, which are wider and deeper than the equivalent combined cycle specimens with the same amount of RET. This suggests that the weathering phases have a beneficial effect on the coating visually to the naked eye, yielding fewer surface holes and pits which are less severe.

Mass

The mass loss for the combined test is less than the RET only test at all analysis stages, like coating B. Again, this further strengthens the suggestion that a surface chemical reaction is occurring where volatile components are evaporated due to elevated temperature during the weathering cycle test conditions, thus, lowering the mass of the specimen for the combined test.

Gloss

The gloss measurements for the combined test of coating C1 show a general decrease as the test progresses. The first weathering phase at Stage 2 causes a decrease of 3.6% in gloss and comparing this to the microscopy image of Stage 2, the lines which are present are the source of the gloss loss and surface topography change. Then, after the first RET phase at Stage 3, pinholes and pits appear more obvious and defined which would increase the amount of diffuse reflectance, lowering the gloss value. An anomaly lies at Stage 5, where after the second RET phase, the gloss has increased. Looking at the surface micro-structure in the microscopy image, the majority of the surface is smooth with small pits, however there are larger areas of holes and materials removal. One possibility could be that the RET has removed a very thin layer of the coating surface, evening out the surface topography and removing the application lines. This smoother, more even surface would yield a higher gloss measurement. Then, the surface gloss decreases with further

weathering which causes the lines to appear, again increasing the diffuse reflectance. The final RET phase at Stage 7 presents the lowest gloss value of the test, looking at the microscopy, it is evident that the surface has begun to erode with large areas of material removal creating a very uneven and steep surface topography. The large differences in surface topography would cause the gloss value to drop by increasing the amount of diffuse reflectance.

Comparing the RET only test to the combined test, the RET only test presents a higher gloss value at all test Stages, thought by the end of test they are similar with a difference of 1.6% reported. Throughout the combined test, the weathering phases change the surface texture and topography, as is evident from the microscopy images. This change is reflected in the gloss measurements and is not observed from the RET only test. At the end of test, the gloss values are similar as both tests have begun to show signs of active erosion, with observable areas of coating removal.

Spectroscopy

Looking at the FTIR spectroscopy for the combined test of coating C1, some small changes have occurred, much like that in the Weathering Impact Assessment, Chapter 5. Firstly, the short shoulder peak at 1769 cm^{-1} representing a Carbon-Oxygen double bond has been removed along with the peak at 1716 cm^{-1} which also represents a Carbon-Oxygen double bond, though of a different functional group, and is reduced throughout the test. A peak has formed at 1330 cm^{-1} which relates to an Oxygen-Hydrogen single bond and another peak has formed at 1182 cm^{-1} which relates to a Carbon-Oxygen single bond.

Again, looking at the wider spectrum, shown in Appendix F -, two peaks, at 2918 cm^{-1} and 2848 $cm^{-}1$, have become more prominent and increased in amplitude as a result of the combined test. This region represents Oxygen-Hydrogen single bonds, and the peaks likely represent and increase in Carboxyl groups and intramolecularly bonded alcohol groups.

Given all of the FTIR data, it is clear that a chemical reaction is taking place. This reaction causes surface restructuring of polymer chains and in turn an increase in surface roughening, as is identifiable by gloss and microscopy measurements. This is likely a formation of Carboxyl groups with the removal of Carbon-Oxygen double bonds due to the increased presence of Carbon-Oxygen and Oxygen-Hydrogen bonds.

Dynamic Mechanical Analysis

Considering the storage modulus results, there is a gradual increase as the combined test progresses. This indicates an increase in elasticity, meaning that the specimens can store more energy as a result of the test. Likely as a result of polymer restructuring with an increased prevalence of polymer interlinking. For the loss modulus, there is a similar trend in that there is a gradual increase as the test progresses. This indicates that the specimens can also dissipate more energy as a result of the combined test, likely as a result of polymer restructuring. The tan δ shows a sharp initial increase followed by a mostly steady level throughout the remainder of the combined test. The initial increase shows a gain in material damping, meaning that more of the mechanical input energy is lost and converted to heat.

Again, as with coating B, there is no evidence that suggests that either a weathering phase or RET phase cause a specific moduli change. Also, as specimens go through the combined test, their geometry changes as a result of the test. The input geometry parameters remained the same throughout all of the DMA testing.

6.3.3. Overall Combined Weathering and RET Comparison

Overall, clear changes between the combined test and RET alone test are easily identifiable. Visually, for coating C1 the RET alone test showed a greater amount of erosion versus the combined test, shown in Figure 6.5 and Figure 6.9. This suggests that the weathering cycles have had a positive effect of the coating in terms of rain erosion performance. Under the microscope, distinct

surface topography changes are evident on each coating system as a result of both weathering and RET phases. Coating B presented an increase in orange peel effect, which was reflected in the gloss measurements where there was a large difference between the combined test and RET alone. Both coatings presented a greater mass loss value for the combined test versus the RET only test, indicating that a chemical reaction could be occurring. This was confirmed by the FTIR spectroscopy where several bond group changes were detected for each coating system as a result of the weathering phases of the combined test.

The difference in measured mass between the combined test and the RET only, both after a rain erosion phase is presented in Table 8, additionally, the difference in measured gloss is presented in Table 9.

Mass Difference	**Coating B**	**Coating C1**
Stage 3	1.08 %	0.26 %
Stage 5	1.26 %	0.31 %
Stage 7	1.51 %	0.39 %

Table 8: Mass Difference Between the Combined Test and RET Only Test.

Table 8 shows, for both coating systems tested, that as specimens were subjected to increasing amounts of rain erosion testing the difference in mass loss between the combined test and RET only specimens increases. This is likely due to the weathering phases of the combined test causing surface chemical reactions and altering the polymeric structure of the coating surface. The RET then washes away any lose or rough surface polymers, resulting in a lower mass measurement.

Gloss Difference	**Coating B**	**Coating C1**
Stage 3	14.06 %	13.87 %

Stage 5	13.26 %	6.59 %
Stage 7	16.34 %	1.55 %

Table 9: Gloss Difference Between the Combined Test and RET Only Test.

The gloss difference between the combined test and RET alone is considerable for coating B and remains sizeable throughout the tests. However, for coating C1, the difference starts off large after the first RET phase, then lessons after each further RET phase until there is a small difference after the last RET phase at Stage 7, as shown in Table 9. The considerably lower gloss values for the combined test show what the effect of weathering is having on the coating surface. Polymer restructuring, both chemical and physical, increases the surface roughness and alters the surface texture, thus reducing gloss measured.

The gloss difference decrease during the combined test and RET only of coating C1 suggests that rain droplet impacts are the dominant from of surface topography change. Whereas in coating B, the weathering has a greater effect on surface topography change, with RET showing only a small change in gloss measurements.

6.4. Combined RET & Weathering Summary

To summarise, weathering has been shown to affect the rain erosion performance of the coating systems tested. The coating systems are affected by increased mass loss as well as a large reduction in surface gloss values. Furthermore, the coating surface micro-structure is altered as a result of weathering. However, each coating system tested reacted in a different manor, coating B showed little to no visual change between the combined test and RET only, apart from some corrosion due to contamination. Whereas coating C1 showed a greater amount of erosion damage after the RET only, by visual inspection as shown in Figure 6.8 and Figure 6.9, indicating that weathering has had a positive effect on the coating system in terms of rain erosion performance. Coating B presented a surface smoothening effect after

weathering phases and coating C1 presented a slight roughening effect, all detected by a combination of FTIR, microscopy and gloss measurements. This suggests that the coating surface polymers are reacting due to different chemical mechanisms induced by the combination of weathering and RET exposure. For coating B, this restructuring shows a positive effect in that it prolongs the life of the coating top surface, by smoothening the top surface as shown in Figure 6.13. Coating C1 also presents a positive effect due to the combined test, where the erosion performance in terms of visual assessment by the naked eye is slightly improved by the combination of weathering exposure and RET versus RET alone. However, coating C1 presents a slight surface roughening after a weathering phase.

Chapter 7 - Summary Discussion

Within this section, work from the previous three sections, Rain Droplet Impact Assessment, Weathering Impact Assessment, and Combined Rain Erosion and Weathering Impact is discussed and contrasted.

Comparing the rain erosion testing from the Rain Droplet Impact Assessment and the Combined Rain Erosion and Weathering Impact, for the RET only test, there is a difference in observable erosion after the same amount of testing.

Figure 7.1: Coating B, RET, 60mins (1)

Figure 7.2: Coating B, RET, 60mins (2)

Figure 7.3: Coating C1, RET, 48mins (1)

Figure 7.4: Coating C1, RET, 60mins (2)

Figure 7.1 and Figure 7.2 both have been exposed to 60 minutes of RET. However, Figure 7.1 has experienced 60 mins of RET in one continuous test

and Figure 7.2 has experienced three periods of 20 minutes each separated by a period of six weeks. There is a clear visual difference in specimens after each test, the continuous 60-minute test has caused massive damage to the coating with large areas of coating removal. The three 20-minute RET exposures show very little signs of erosion, with only small surface pinholes observable. This difference in survival time highlights the importance and effect of stoppage intervals and specimen recovery time during RET. However, the difference is more likely due to batch-to-batch variation in specimen manufacture. The batch variation explanation is more likely as the failure mechanism changes between both tests, the initial test shows an edge type delamination failure and the second test shown a surface erosion type failure.

Figure 7.3 shows coating C1 after 48 minutes of continuous RET and Figure 7.4 shows coating C1 after three periods of 20 minute RET, totalling 60 minutes RET, each separated by a rest period of six weeks. Figure 7.3 presents slightly less surface damage than Figure 7.4, it also has 12 minutes less RET time in total. However, it was expected that both test specimens, with continuous and long rest periods, would show similar amounts of erosion at 60 minutes of RET. This highlights the differences in coating systems and their individuality to testing. Coating B displayed a clear reaction to RET stoppage intervals, whereas coating C1 does not show significant variation.

The response of the coating systems to weathering testing has shown that chemical changes in the coatings do occur. These changes are likely a result of an oxidation reaction, most likely a photooxidation due to light, catalysed by high heat and humidity, particularly in the accelerated tests. The photolysis mechanism of the urethane link is shown in Figure 7.5, where the polyurethane monomer unit is degraded by light, with several possible resultant products. From here, two bonds are susceptible to attack, the Carbon-Oxygen bond and the Carbon-Nitrogen bond. Each reaction produces free radicals which are highly reactive and likely to go on to further react.

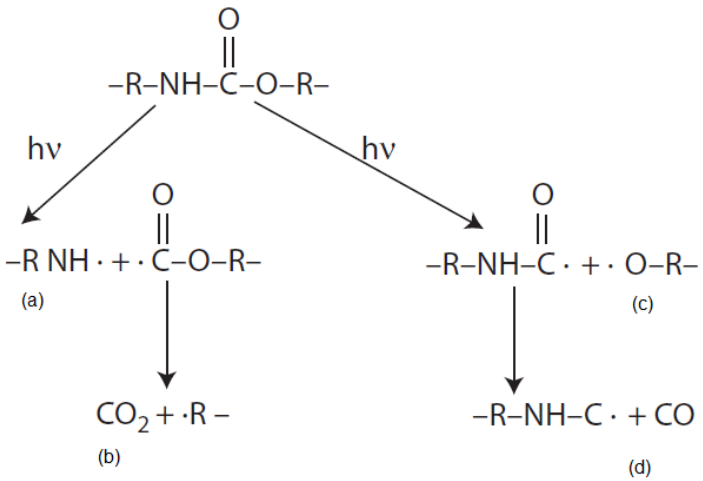

Figure 7.5: Urethane Link Photolysis. Adapted from [41]

The spectroscopy studies within this work have shown a decrease in Carbon-Oxygen single bonding for coating C2 after weathering, along with a retention of Carbon-Oxygen double bonding, indicating a possible degradation mechanism as in Figure 7.5 route (c). However, coating C1 has shown an increase in Carbon-Oxygen double bonds, an increase in Carbon-Oxygen single bonds and an increase in Oxygen-Hydrogen bonds, with no reduction in Carbon-Oxygen bonding. Similarly with Coating B, a reduction in Carbon-Carbon double bonds and an increase in Carbon-Oxygen double bonds are a result of weathering. This indicates that reactions are occurring outwith the urethane link and are occurring elsewhere on the polymer chain, where additives and chain extenders are located, the chemistry of which is only known by the coating manufacturer.

The more physically representative combined test reflects what wind turbines in-situ would experience, with dry periods, wet periods, periods of heavy rain and periods of intense sunlight. Considering the combined test results, between the beginning and end of test, the inclusion of weathering phases during RET caused an additional 1.5% loss in mass for coating B and an additional 0.4% loss in mass for coating C1. Furthermore, the inclusion of weathering caused an additional 16.3% loss in gloss for coating B and 1.6%

for coating C1. Therefore, weathering has been shown to affect the rain erosion performance of the coating systems and has affected each coating system somewhat differently. The difference is likely due to chemical reactions taking place as a result of the weathering phases, where for both coating systems, weathering has shown a beneficial effect to rain erosion performance. Coating B showed that weathering phases caused a surface smoothing effect, greatly increasing erosion performance by changes in microstructure, shown in Figure 6.15, and surface gloss increases, shown in Figure 6.34, whereas coating C1 showed a slight surface roughening after a weathering phase, Figure 6.24. Overall, both coating systems presented a reduction in erosion due to interjected weathering phases versus RET alone.

Coating B presents as a less rigid coating system than coating C1. The physical surface of coating B was able to be depressed and marked, whereas coating C1 showed no signs of marking after a depression. The link between coating hardness and surface restructuring due to weathering could be drawn to say that a less rigid coating recovers from a weathering phase with better surface microstructure than a more rigid coating system. The less rigid coating system develops a smoothened surface whereas the more rigid coating systems has shown a slight increase in surface roughness. However, both coating systems presented an increase in erosion performance, both visually and by gloss and microstructure measurement, when weathering was involved.

Linking all of the observed changes back to an in-situ wind turbine blade, there is a positive outcome in that the combined action of weathering along with erosion has been shown to have a beneficial effect in terms of erosion performance, for coating C1 this is visually by the naked eye by comparing Figure 6.5 and Figure 6.9, and for coating B by gloss and microstructure changes, and coating lifetime. However, only two coating systems were tested as part of this work therefore, a universal conclusion for all polyurethane type coating systems cannot be made.

Chapter 8 - Summary and Conclusions

For weathering testing, there is no ‘one size fits all’ approach, and as such several accelerated weathering cycles as used in industry to prove the efficacy of a particular coating system. These cycles have been developed to reflect a hot, humid environment. However, the majority of offshore wind in Europe is not located in a hot, humid environment. Therefore, specific and realistic environmental conditions should be considered when testing a coating system and thereafter employ an appropriate accelerated weathering test reflect these conditions.

In the present work, each coating system tested has shown individuality in test results, indicating, although all of the coating systems used were polyurethane based, they each show a different response. The difference is due to particular additives used withing the coating systems, such as UV blockers and antioxidants. This poses an additional complication when studying these systems as the exact chemical composition and formulation is closely guarded, and as such, the manufacturers are reluctant to share this information. As within this work, this ambiguity of chemical formulation leaves some uncertainty over the nature of chemical degradation mechanisms observed.

To truly tackle the issue of wind turbine blade erosion, industrial relationships with academia are vital. Within these relationships, the sharing of information and data, particularly focusing on chemical compositions of coating systems, will provide the greatest benefit to understanding and also the fastest route for future solutions to be developed.

The current work has shown that weathering can have a beneficial effect, in terms of surface microstructure and gloss, on the coating systems tested within this work. Surface chemical reactions, as well as changes in gloss and surface microstructure, have shown that the polymer chains of the coating system top layer have restructured as a result of weathering. In coating B, this

restructuring led to a smoothening effect of the coating surface whereas in coating C1, a slight surface roughening was observed. Both effects presented an increase in coating lifetime, however, the smoothened surface of coating B showed very little observable erosion damage at the end of test, whereas signs of erosion were present on the slightly roughened surface of coating C1. Coating B presented as a less rigid coating and coating C1 more rigid. Therefore, within this work, the less rigid coating system has shown a great benefit from weathering exposure with regards to rain surface gloss and surface microstructure. It is noted that the main focus of this work addressed the surface finish, chemistry and overall system response due to RET and weathering and in combination. However, no hardness testing was undertaken as it was outwith the scope of the research programme.

To conclude, this work has shown how weathering and rain erosion testing can be combined to provide a more representative accelerated environmental test for wind turbine blade coating systems. This work has also shown how several commonly used weathering tests differ and that a bespoke weathering cycle, the North Sea Method, was developed to specifically reflect weather conditions measured from the North Sea. Furthermore, this work has demonstrated the importance of including weathering within the assessment of wind turbine blade coating systems and that weathering has a measurable effect on erosion performance.

8.1. Future Work

Further work in this area should examine the independent effects of the accelerated weathering cycles. This will allow the chemical, and physical, changes observed throughout this work to be isolated and directly linked to an effect from temperature, humidity or light, and if the compound effect exacerbates these changes. Additionally, a study looking at stoppage interval duration and frequency during RET and the impact on erosion performance is required.

The continuation of the combined cycle until sample failure, where the composite substrate is exposed, would allow for the active erosion rate to be explored. Additionally, the fully tested specimens could be compared to RET alone specimens as well as a further test involving pre-weathered specimens which are then exposed to RET. The effect of an initial exposure to weathering versus a repeated weathering exposure could then be explored.

The amount of coating systems tested should be increased to allow comparison between various coating chemistries, formulations, and hardness.

In addition, a temperature sensitivity study, using DMA, on each coating system without the substrate would allow for the degree of polymer crosslinking to be explored as a function of temperature. This would provide clarity on the state of crosslinking between polymer chains as a result of accelerated weathering exposures.

Furthermore, gloss has been shown to provide a quantifiable measure of erosion. For gloss to be used as a measure of erosion on an operational wind turbine, a data bank of gloss values at all stages of erosion, for all coating systems used within the wind turbine blades, is required. The gloss data from the accelerated testing can be directly related to the operational wind turbine, allowing for any repairs to be justified.

Bibliography

[1] D. Fraile *et al.*, “Getting fit for 55 and set for 2050 Electrifying Europe with wind energy,” 2021.

[2] *PD ISO/TS 19392-1:2018. Paints and varnishes -- Coating systems for wind-turbine rotor blades -- Part 1: Minimum requirements and weathering*. BSI Standards Limited, 2018.

[3] *PD ISO/TS 19392-2:2018. Paints and varnishes -- Coating systems for wind-turbine rotor blades -- Part 2: Determination and evaluation of resistance to rain erosion using rotating arm*. BSI Standards Limited, 2018.

[4] *PD ISO/TS 19392-3:2018. Paints and varnishes - Coating systems for wind-turbine rotor blades Part 3: Determination and evaluation of resistance to rain erosion using water jet*. BSI Standards Limited, 2018.

[5] T. Burton, D. Sharpe, N. Jenkins, and E. Bossanyi, *Wind Energy Handbook*. John Wiley & Sons, Ltd, 2001.

[6] Adnan Durakovic, “Mingyang Goes Beyond 18 MW with New Offshore Wind Turbine,” *offshorewind.biz*, Jan. 13, 2023. https://www.offshorewind.biz/2023/01/13/mingyang-goes-beyond-18-mw-with-new-offshore-wind-turbine/ (accessed Feb. 01, 2023).

[7] J. M. Thomsen, “Here is the world’s largest wind turbine blade,” *Technical University of Denmark, News*, 2018. http://www.dtu.dk/english/news/2018/03/dynamo-the-worlds-largest?id=00d429c3-eb5b-4e1a-8102-8016d0f15699 (accessed Aug. 13, 2018).

[8] DNV, “Offshore wind power expands globally,” Feb. 2020. https://www.dnv.com/expert-story/maritime-impact/Offshore-wind-power-expands-globally.html (accessed Apr. 08, 2022).

[9] R. Herring, K. Dyer, F. Martin, and C. Ward, “The increasing importance of leading edge erosion and a review of existing protection solutions,” *Renewable and Sustainable Energy Reviews*, vol. 115, p. 109382, 2019, doi: 10.1016/j.rser.2019.109382.

[10] P. J. Schubel and R. J. Crossley, “Wind turbine blade design,” *Energies (Basel)*, vol. 5, no. 9, pp. 3425–3449, 2012, doi: 10.3390/en5093425.

[11] F. M. Jensen and K. Branner, “1 - Introduction to wind turbine blade design,” in *Advances in Wind Turbine Blade Design and Materials*, P. Brøndsted and R. P. L. Nijssen, Eds., in Woodhead Publishing Series in Energy. Woodhead Publishing, 2013, pp. 3–28. doi: https://doi.org/10.1533/9780857097286.1.3.

[12] L. Mishnaevsky, K. Branner, H. N. Petersen, J. Beauson, M. McGugan, and B. F. Sørensen, “Materials for wind turbine blades: An overview,” *Materials*, vol. 10, no. 11, pp. 1–24, 2017, doi: 10.3390/ma10111285.

[13] K. P. Subrahmanian and F. Dubouloz, “Adhesives for bonding wind turbine blades,” *Reinforced Plastics*, vol. 53, no. 1, pp. 26–29, Feb. 2009, doi: 10.1016/S0034-3617(09)70044-X.

[14] Gurit Holding AG, “Guide to Composites,” *Available in URL: http://www. netcomposites. com/ …*, p. 74, 2000, doi: GTC-3-0509.

[15] M. H. Keegan, “Wind Turbine Blade Leading Edge Erosion: An investigation of rain droplet and hailstone impact induced damage mechanisms,” *PhD thesis*, p. 360, 2014.

[16] Reuters, “Cheaper carbon fibre will slash auto making costs-manufacturer,” 2014. https://www.reuters.com/article/sgl-

fibres/cheaper-carbon-fibre-will-slash-auto-making-costs-manufacturer-idUSL5N0MP2RP20140328 (accessed Jul. 12, 2018).

[17] University of Cambridge - Materials Group, “Specific stiffness - Specific strength.” http://www-materials.eng.cam.ac.uk/mpsite/interactive_charts/spec-spec/basic.html (accessed Oct. 08, 2018).

[18] H. Macdonald, “The Influence of Hail on Wind Turbine Blade Leading Edge Erosion and Damage,” *PhD thesis*, 2017.

[19] D. S. Cairns, T. Riddle, and J. Nelson, “Wind Turbine Composite Blade Manufacturing: The Need for Understanding Defect Origins, Prevalence, Implications and Reliability ,” Albuquerque, Feb. 2011.

[20] Gurit, “New Core Materials for Weight, Cost Reduction and Sustainability,” in *Wind Blade Materials Development Forum*, Hamburg, 2018. [Online]. Available: https://tbmgroup.eu/product/wind-blade-materials-development-forum/

[21] P. Bir, GS; Migliore, “Computerized method for preliminary structural design of composite wind turbine blades,” *Journal of Solar Energy Engineering-Transactions of the Asme*, vol. 123, no. 4, pp. 372–381, 2001, doi: Doi 10.1115/1.1413217.

[22] D. Cripps, “Glass Fibre.” https://netcomposites.com/guide-tools/guide/reinforcements/glass-fibrefiber/ (accessed Sep. 19, 2018).

[23] Prince Engineering, “Glass Fiber Differences and Properties.” https://www.build-on-prince.com/glass-fiber.html (accessed Sep. 16, 2018).

[24] Covestro, “Alternative Chemistries: First PUR Based Infusion Resin Ever Commercialized,” in *Wind Blade Materials Development Forum*, 2018.

[25] National Research Council, *Assessment of Research Needs for Wind Turbine Rotor Materials Technology*. Washington, DC: The National Academies Press, 1991. doi: https://doi.org/10.17226/1824.

[26] Vacmobiles.com, “What is resin infusion (or vacuum infusion)?” https://www.vacmobiles.com/resin_infusion.html (accessed Sep. 22, 2010).

[27] Fibreglast, “Vacuum Infusion Complete Guide.” https://www.fibreglast.com/product/vacuum-infusion-Guide/Learning_Center (accessed Sep. 22, 2018).

[28] Fibre Glast, “What Are Prepregs?” https://www.fibreglast.com/product/about-prepregs/Learning_Center (accessed Sep. 19, 2018).

[29] Gurit, “SparPreg : UD Prepreg Spar Solution,” 2012.

[30] B. Kjærside Storm, “Surface protection and coatings for wind turbine rotor blades,” *Advances in Wind Turbine Blade Design and Materials*, pp. 387–412, 2013, doi: 10.1533/9780857097286.3.387.

[31] M. H. Keegan, D. H. Nash, and M. M. Stack, “On erosion issues associated with the leading edge of wind turbine blades,” *J Phys D Appl Phys*, vol. 46, no. 38, 2013, doi: 10.1088/0022-3727/46/38/383001.

[32] Saraaloren, “CLASSIFICATION OF POLYMERS AND MONOMERS,” 2015. https://galaxact.wordpress.com/2015/03/17/classification-of-polymers-and-monomers/ (accessed Sep. 08, 2018).

[33] J. D. Robert and M. Caserio, “Forces Between Polymer Chains,” 2017. https://chem.libretexts.org/Textbook_Maps/Organic_Chemistry/Book%3A_Basic_Principles_of_Organic_Chemistry_(Roberts_and_Caserio)/29%3A_Polymers/29.3%3A_Forces_Between_Polymer_Chains (accessed Oct. 15, 2018).

[34] L. Yang, “ME523 Polymer & Polymer Composites.” University of Strathclyde, p. Lecture 1, 2018.

[35] Mankash, “File: Copolymers,” 2008. https://en.wikipedia.org/wiki/File:Copolymers.svg (accessed Sep. 23, 2018).

[36] Particle Sciences, “Glossary of Polymer Terms,” *Technical Brief*, 2011. https://www.particlesciences.com/news/technical-briefs/2011/glossary-of-polymer-terms.html (accessed Jun. 06, 2018).

[37] K. Davoudi, “Mechanical Properties of Polymers,” *Materials Science Seminar, Harvard University*, 2013. https://scholar.harvard.edu/files/kamyar/files/2013-10-17_deformation_of_polymers.pdf (accessed Oct. 03, 2018).

[38] SEAS Soft Matter. Harvard University, “Cross-linking.” http://soft-matter.seas.harvard.edu/index.php/File:Cross-link1.png (accessed Sep. 07, 2018).

[39] D. Ebbing and S. Gammon, *General Chemistry*, 9th ed. Belmont: Brooks/Cole, 2009.

[40] V. Jones, “Covalent Bonds.” https://people.seas.harvard.edu/~jones/es154/lectures/lecture_2/covalent_bond/covalent_bond.html (accessed Oct. 26, 2018).

[41] M. Szycher, Ed., *Szycher’s Handbook of Polyurethanes, Second Edition*, 2nd ed. CRC Press, 2013.

[42] D. Rosu and P. M. Visakh, Eds., *Photochemical Behavior of Multicomponent Polymeric-based Materials*, vol. 26. Springer International Publishing, 2016. doi: 10.1007/978-3-319-25196-7.

[43] G. S. Springer, *Erosion by Liquid Impact*. Scripta, 1976.

[44] O. Gohardani, “Impact of erosion testing aspects on current and future flight conditions,” *Progress in Aerospace Sciences*, vol. 47, no. 4, pp. 280–303, 2011, doi: 10.1016/j.paerosci.2011.04.001.

[45] E. A. Valaker, S. Armada, and S. Wilson, *Droplet erosion protection coatings for offshore wind turbine blades*, vol. 80, no. 1876. Elsevier B.V., 2015. doi: 10.1016/j.egypro.2015.11.430.

[46] M. K. Lee, W. W. Kim, C. K. Rhee, and W. J. Lee, “Liquid impact erosion mechanism and theoretical impact stress analysis in TiN-coated steam turbine blade materials,” *Metall Mater Trans A Phys Metall Mater Sci*, vol. 30, no. 4, pp. 961–968, 1999, doi: 10.1007/s11661-999-0149-y.

[47] H. M. Slot, E. R. M. Gelinck, C. Rentrop, and E. van der Heide, “Leading edge erosion of coated wind turbine blades: Review of coating life models,” *Renew Energy*, vol. 80, pp. 837–848, 2015, doi: 10.1016/j.renene.2015.02.036.

[48] N. Gaudern, “A practical study of the aerodynamic impact of wind turbine blade leading edge erosion,” *J Phys Conf Ser*, vol. 524, no. 1, 2014, doi: 10.1088/1742-6596/524/1/012031.

[49] A. O’Carroll, M. Hardiman, E. F. Tobin, and T. M. Young, “Correlation of the rain erosion performance of polymers to mechanical and surface properties measured using nanoindentation,” *Wear*, vol. 412–413, no. June, pp. 38–48, 2018, doi: 10.1016/j.wear.2018.07.008.

[50] DNV, *DNVGL-RP-0171. Testing of rotor blade erosion protection systems*, no. February. DNV GL AS, 2018.

[51] L. Mishnaevsky *et al.*, “Leading edge erosion of wind turbine blades: Understanding, prevention and protection,” *Renewable Energy*, vol. 169. Elsevier Ltd, pp. 953–969, May 01, 2021. doi: 10.1016/j.renene.2021.01.044.

[52] S. Fæster, N. F. J. Johansen, L. Mishnaevsky, Y. Kusano, J. I. Bech, and M. B. Madsen, “Rain erosion of wind turbine blades and the effect of air bubbles in the coatings,” *Wind Energy*, vol. 24, no. 10, pp. 1071–1082, Oct. 2021, doi: 10.1002/we.2617.

[53] I. Katsivalis, A. Chanteli, W. Finnegan, and T. M. Young, “Mechanical and interfacial characterisation of leading-edge protection materials for wind turbine blade applications,” *Wind Energy*, Oct. 2022, doi: 10.1002/we.2767.

[54] E. F. Tobin, T. M. Young, D. Raps, and O. Rohr, “Comparison of liquid impingement results from whirling arm and water-jet rain erosion test facilities,” *Wear*, vol. 271, no. 9–10, pp. 2625–2631, Jul. 2011, doi: 10.1016/j.wear.2011.02.023.

[55] “AeroNordic Rain Erosion Testing.” https://www.aero-nordic.com/lep-rain-erosion-testing/ (accessed May 17, 2022).

[56] A. Francis, S. Fowler, B. Tobin, and D. Duecker, “Color Change in Accelerated Weathering Testing of PVC Plastics.”

[57] *ASTM G71-10 (Reapproved 2021) Standard Test Method for Liquid Impingement Erosion Using Rotating Apparatus*. ASTM International, 2021.

[58] DNV, *DNV-RP-0573 Evaluation of erosion and delamination for leading edge protection systems of rotor blades*. 2021.

[59] *ASTM G7/G7M-21 Standard Practice for Natural Weathering of Materials*. 2021. doi: 10.1520/G0007_G0007M-21.

[60] Fraunhofer IWES, “BeLeb.” https://www.iwes.fraunhofer.de/en/research-projects/current-projects/beleb.html (accessed Mar. 05, 2018).

[61] Fraunhofer IWES, “Effective Prevention of Rain Erosion on Rotor Blades.” https://www.iwes.fraunhofer.de/en/press---media/archiv_2017/effective-prevention-of-rain-erosion-on-rotor-blades.html (accessed Mar. 05, 2018).

[62] TWI Ltd, “EIROS Project.” http://www.eirosproject.com/ (accessed Mar. 05, 2018).

[63] C. B. Hasager, “EROSION.” http://www.rain-erosion.dk/ (accessed Mar. 05, 2018).

[64] ORE Catapult, “BLEEP: Reducing The Cost Impacts of Wind Turbine Blade Erosion.” https://ore.catapult.org.uk/stories/blade-leading-edge-erosion/ (accessed Mar. 05, 2018).

[65] D. Maniaci, “Leading Edge Erosion.” http://energy.sandia.gov/energy/renewable-energy/wind-power/blade-reliability/leading-edge-erosion/%0A (accessed Mar. 05, 2018).

[66] DNVGL, “DNVGL COBRA Project.” https://www.dnv.com/news/wind-turbine-blade-erosion-to-be-tackled-in-new-joint-industry-project-141486 (accessed Jul. 19, 2020).

[67] “IEA Wind Task 46.” https://iea-wind.org/task46/t46-participation/ (accessed Jan. 07, 2021).

[68] “TA Instruments DMA 850.” https://www.tainstruments.com/dma-850/ (accessed Nov. 12, 2022).

[69] I. Ouachan, K. Dyer, I. Hamerton, and C. Ward, “ENGINEERING VISCOELASTIC PROPERTIES IN POLYURETHANE COATINGS TO REDUCE EROSION RISKS IN WIND TURBINE BLADES,” Oct. 2021.

[70] “BS EN ISO 2813 : 2014 BSI Standards Publication Paints and varnishes — Determination of gloss value at 20 degrees , 60 degrees and 85 degrees,” 2014.

[71] C. Bisulca, P. C. Nascimbene, L. Elkin, and D. A. Grimaldi, “Variation in the Deterioration of Fossil Resins and Implications for the Conservation of Fossils in Amber,” *Am Mus Novit*, vol. 3734, no. 3734, pp. 1–19, Feb. 2012, doi: 10.1206/3734.2.

[72] “BS EN ISO-CIE 11664-4-2019,” 2019.

[73] G. Verhoeven, “The reflection of two fields – Electromagnetic radiation and its role in (aerial) imaging,” *AARGnews*, vol. 55, pp. 13–18, Sep. 2017.

[74] Cameron Mackie, David Nash, Dean Boyce, Matthew Wright, and Kirsten Dyer, “Characterisation of a Whirling Arm Erosion Test Rig,” in *IEEE 2018 Asian Conference on Energy, Power and Transportation Electrification*, 2018.

[75] Cameron Mackie, “ESTABLISHING THE OPTIMAL CONDITIONS FOR ROTATING ARM EROSION TESTING, MATERIALS CHARACTERISATION AND COMPUTATIONAL MODELLING OF WIND TURBINE BLADE RAIN EROSION,” 2020.

[76] “ISO 16474-3:2013. Paints and varnishes — Methods of exposure to laboratory light sources Part 3 : Fluorescent UV lamps,” 2013.

[77] “ISO 16474-2:2013. Paints and varnishes — Methods of exposure to laboratory light sources Part 2 : Xenon-arc lamps,” 2013.

[78] F. Menges, “Spectragryph - optical spectroscopy software.” 2022. [Online]. Available: http://www.effemm2.de/spectragryph/

Appendix A - Sample Preparation Photographs

Figure 0.1: Flat Mould for Composite Forming

Figure 0.2: Rolls of Glass Fibres Used for Composite Manufacture

Figure 0.3: Glass Fibre Sheets Cut to Size

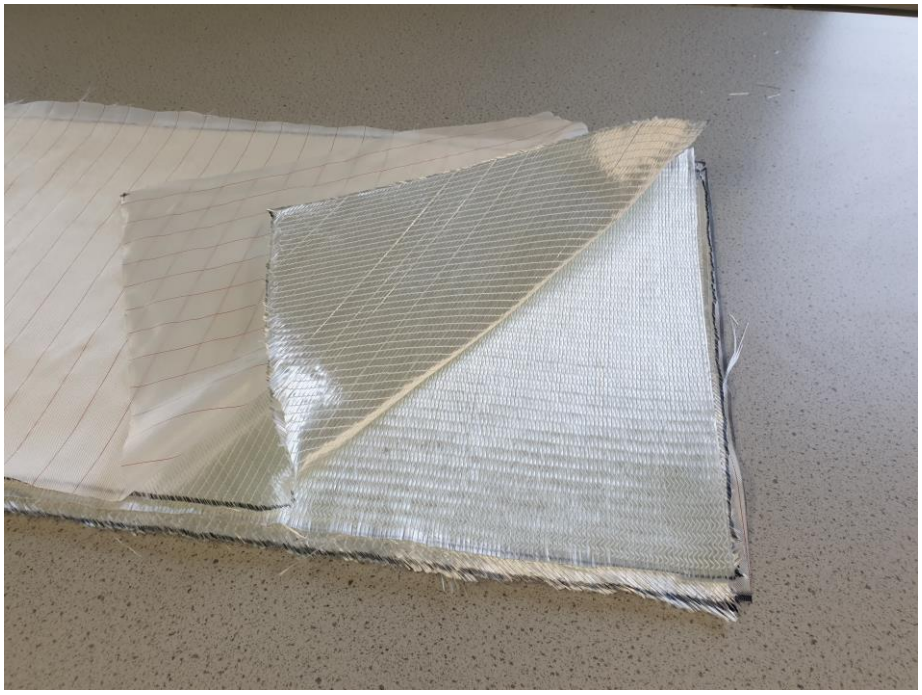

Figure 0.4: Glass Fibre Sheets – Layup

Figure 0.5: Mould with Tacky Tape Applied

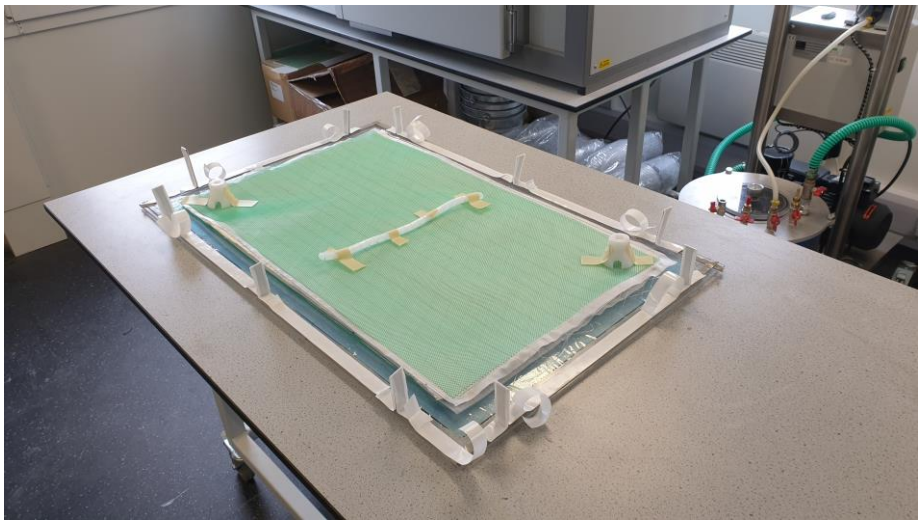

Figure 0.6: Prepared Setup Prior to Bagging

Figure 0.7: Resin Infusion Setup

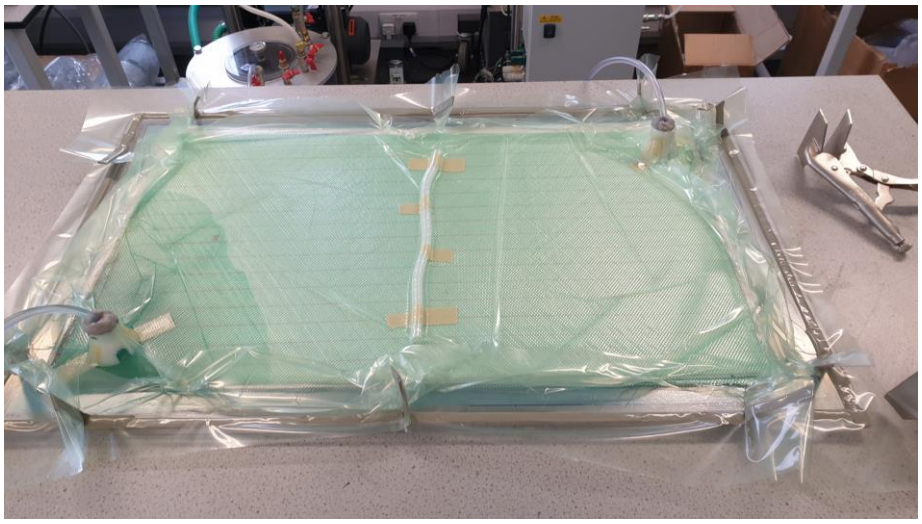

Figure 0.8: Resin Infusion Progression

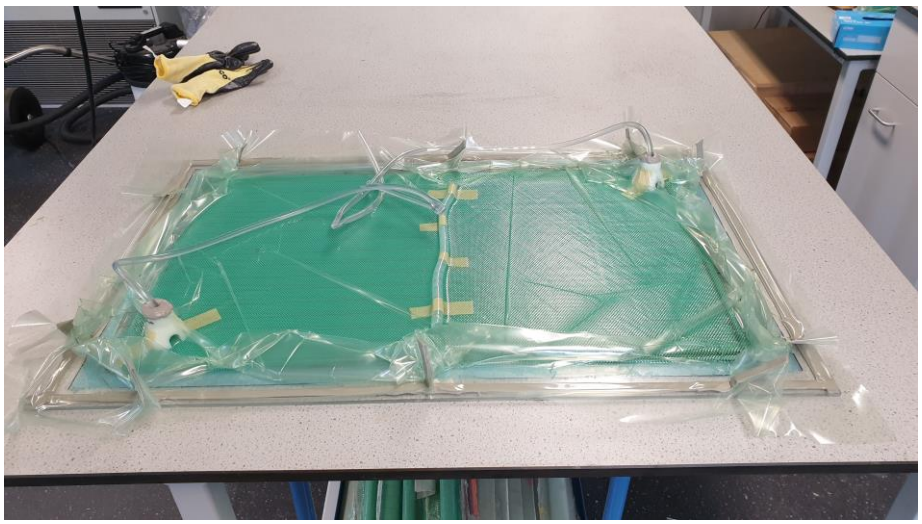

Figure 0.9: Post-cure, After Removal from the Oven

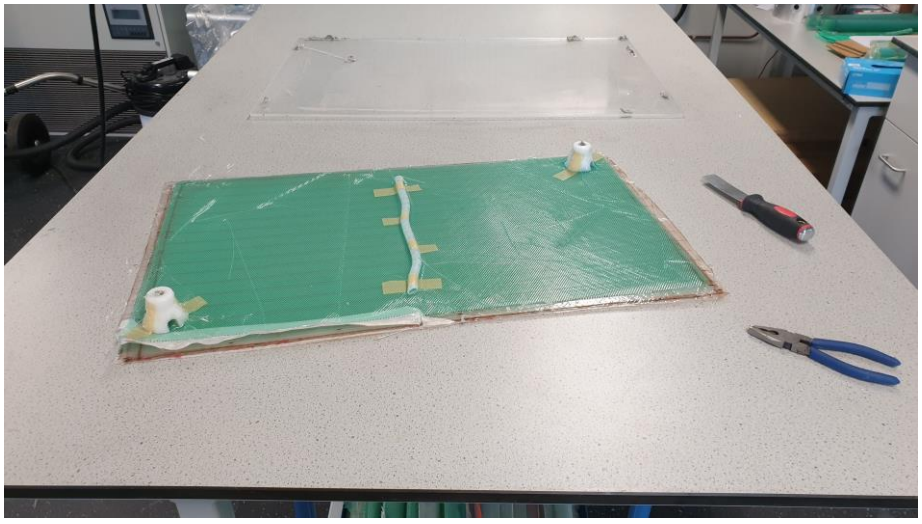

Figure 0.10: Removal of Bag and Mould

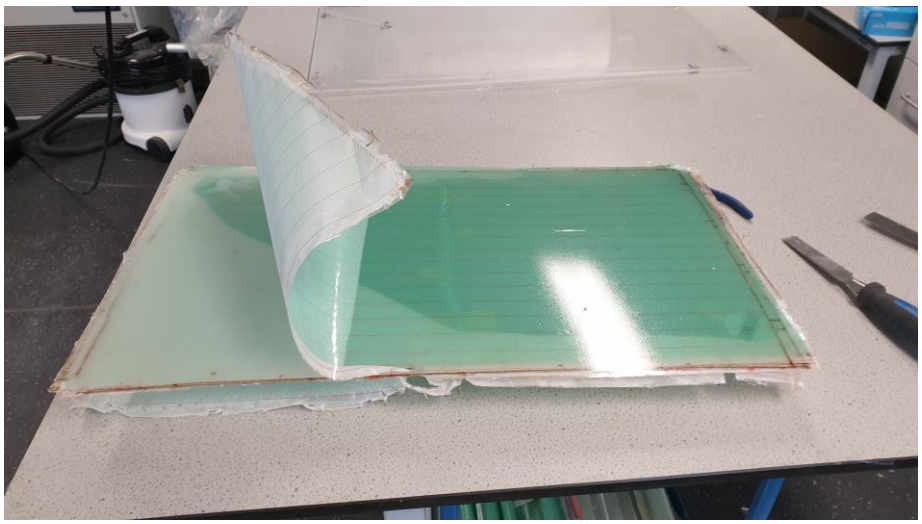

Figure 0.11: Removal of Peel Ply

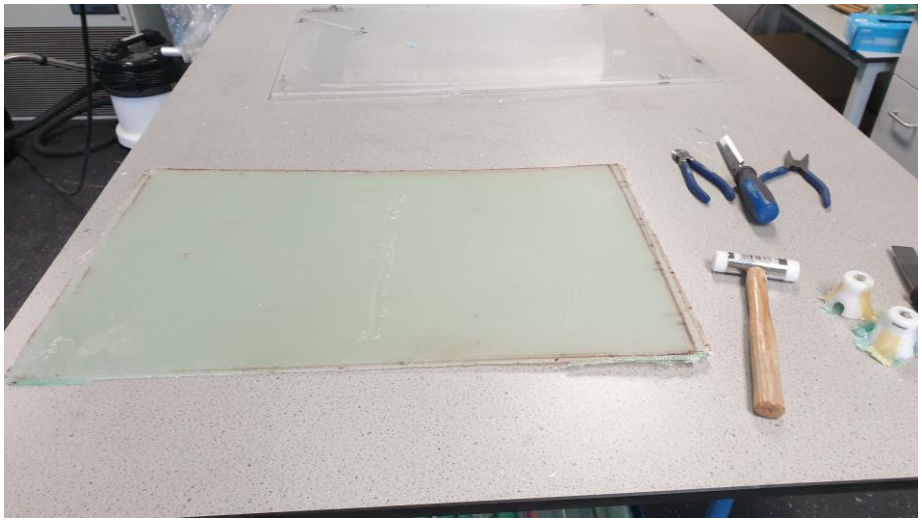

Figure 0.12: Finished Composite Panel

Appendix B - Weathering Intermediate Analysis: Photographs

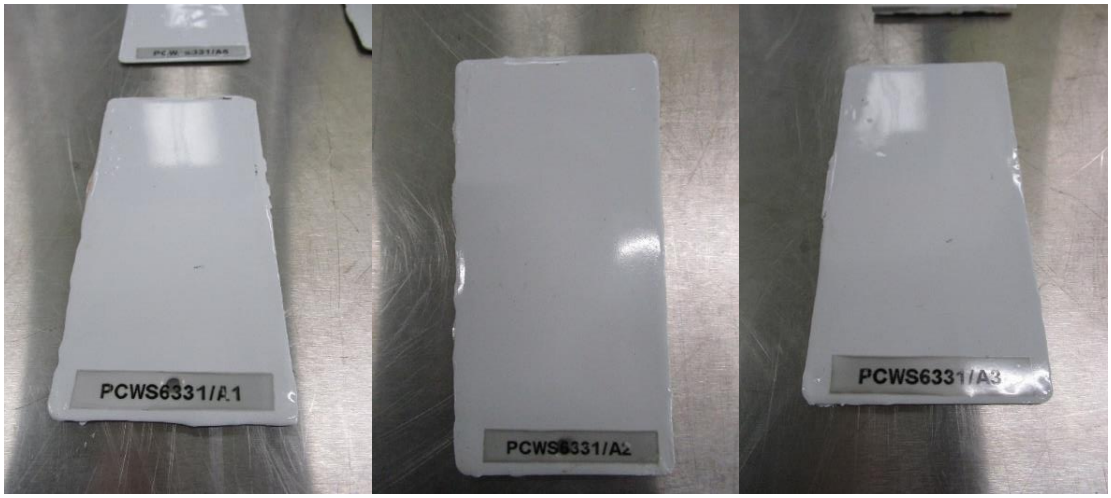

Figure 0.13: Coating C1, Aluminium Substrate, UVa, 3000hrs

Figure 0.14: Coating C2, Aluminium Substrate, UVa, 3000hrs

Figure 0.15: Coating C1, Composite Substrate, UVa, 3000hrs

Figure 0.16: Coating C2, Composite Substrate, UVa, 3000hrs

Figure 0.17: Coating C1, Aluminium Substrate, Xenon-Arc, 3500hrs

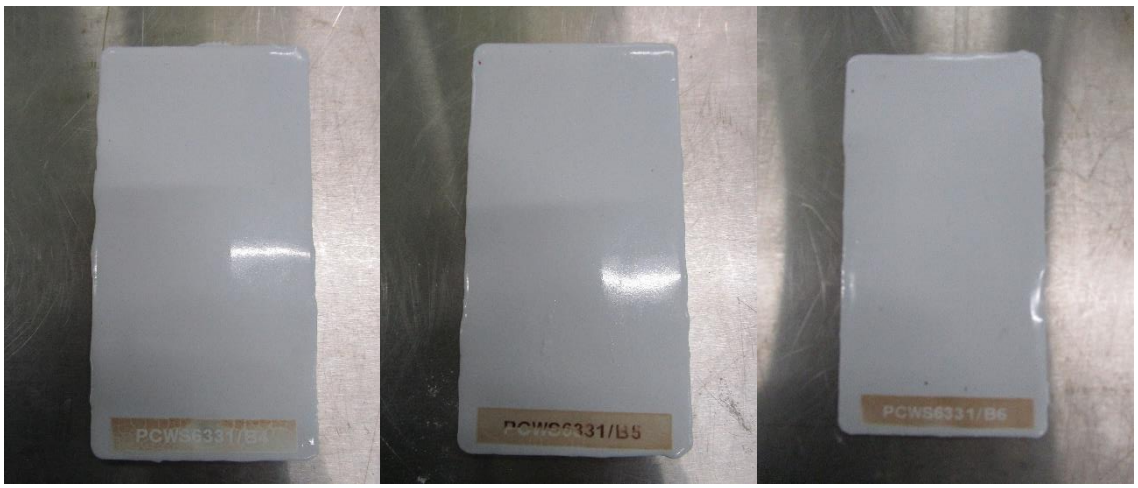

Figure 0.18: Coating C2, Aluminium Substrate, Xenon-Arc, 3500hrs

Figure 0.19: Coating C1, Composite Substrate, Xenon-Arc, 3500hrs

Figure 0.20: Coating C2, Composite Substrate, Xenon-Arc, 3500hrs

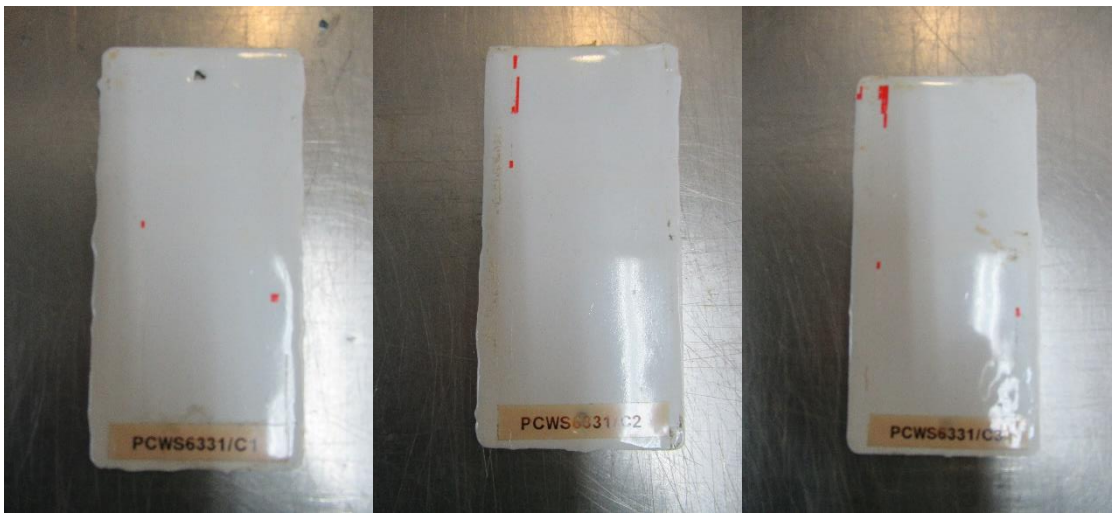

Figure 0.21: Coating C1, Aluminium Substrate, Natural Outdoors, 7000hrs

Figure 0.22: Coating C2, Aluminium Substrate, Natural Outdoors, 7000hrs

Appendix C - Weathering Intermediate Analysis: Colour Parameters

Hours	L	a	b	ΔE*
0	87.35	-0.49	0.89	-
500	87.25	-0.52	1.14	0.30
1000	87.04	-0.53	1.44	0.64
1500	87.16	-0.51	1.22	0.36
2000	87.25	-0.51	1.24	0.36
2500	87.35	-0.53	1.24	0.37
3000	87.00	-0.53	1.42	0.63

Figure 0.23: Coating B, Aluminium Substrate, UVa

Hours	L	a	b	ΔE*
0	-	-	-	0.00
500	-0.16	0.01	0.31	0.35
1000	-0.34	0.02	0.57	0.67
1500	-1.54	-1.35	7.28	0.71
2000	-0.33	-0.02	0.69	0.76
2500	-0.28	-0.02	0.61	0.67
3000	-0.38	-0.01	0.78	0.87
4000	-0.43	0.00	0.74	0.86
5000	-0.45	0.00	0.80	0.92
6000	-0.40	0.00	0.66	0.77
7500	-0.52	0.01	0.65	0.83

Figure 0.24: Coating C1, Aluminium Substrate, UVa

Hours	L	a	b	ΔE*
0	-	-	-	0.00
500	-0.03	0.00	0.24	0.25
1000	-0.14	-0.04	0.44	0.46
1500	-1.45	-1.35	7.20	0.58
2000	-0.30	-0.01	0.54	0.63
2500	-0.22	-0.01	0.54	0.59

3000	-0.24	-0.01	0.60	0.66
4000	-0.32	-0.01	0.60	0.69
5000	-0.25	-0.01	0.59	0.64
6000	-0.30	0.00	0.59	0.66
7500	-0.37	0.01	0.66	0.76

Figure 0.25: Coating C1, Composite Substrate, UVa

Hours	**L**	**a**	**b**	**∆E***
0	-	-	-	0.00
500	-0.15	-0.01	0.27	0.30
1000	-0.32	-0.02	0.48	0.57
1500	-1.59	-1.36	7.24	0.61
2000	-0.42	0.00	0.54	0.69
2500	-0.32	-0.02	0.52	0.61
3000	-0.37	-0.01	0.60	0.71
4000	-0.44	-0.01	0.60	0.74
5000	-0.44	-0.01	0.64	0.78
6000	-0.45	0.00	0.64	0.79
7500	-0.62	0.03	0.66	0.90

Figure 0.26: Coating C2, Aluminium Substrate, UVa

Hours	**L**	**a**	**b**	**∆E***
0	-	-	-	0.00
500	-0.09	-0.02	0.26	0.28
1000	-0.13	-0.03	0.36	0.38
1500	-1.61	-1.39	7.61	0.63
2000	-0.35	-0.05	0.82	0.89
2500	-0.33	-0.06	0.80	0.86
3000	-0.45	-0.04	0.86	0.97
4000	-0.59	-0.03	1.21	1.34
5000	-0.42	-0.05	0.82	0.92
6000	-0.42	-0.04	0.77	0.88
7500	-0.68	0.02	1.05	1.25

Figure 0.27: Coating C2, Composite Substrate, UVa

Hours	**L**	**a**	**b**	**∆E***

0	-	-	-	0.00
500	-0.06	0.03	0.10	0.12
1000	-0.16	0.03	0.14	0.23
1500	-0.22	0.05	0.23	0.32
2500	-0.25	0.05	0.22	0.34
3500	-0.27	0.04	0.25	0.37
4500	-0.31	0.05	0.25	0.41
6000	-0.41	0.05	0.25	0.48

Figure 0.28: Coating C1, Aluminium Substrate, Xenon-Arc

Hours	**L**	**a**	**b**	**∆E***
0	-	-	-	0.00
500	-0.04	0.02	0.07	0.09
1000	-0.10	0.02	0.09	0.14
1500	-0.11	0.04	0.14	0.19
2500	-0.24	0.04	0.16	0.30
3500	-0.23	0.03	0.20	0.31
4500	-0.34	0.04	0.23	0.42
6000	-0.38	0.03	0.23	0.45

Figure 0.29: Coating C1, Composite Substrate, Xenon-Arc

Hours	**L**	**a**	**b**	**∆E***
0	-	-	-	0.00
500	-0.05	0.02	0.06	0.09
1000	-0.25	0.02	0.20	0.32
1500	-0.23	0.03	0.20	0.31
2500	-0.28	0.03	0.19	0.34
3500	-0.31	0.01	0.22	0.38
4500	-0.34	0.03	0.23	0.40
6000	-0.48	0.04	0.26	0.54

Figure 0.30: Coating C2, Aluminium Substrate, Xenon-Arc

Hours	**L**	**a**	**b**	**∆E***
0	-	-	-	0.00
500	0.00	0.03	0.06	0.07
1000	-0.10	0.04	0.09	0.14

1500	-0.14	0.04	0.17	0.22
2500	-0.21	0.05	0.17	0.28
3500	-0.23	0.05	0.26	0.35
4500	-0.27	0.04	0.16	0.31
6000	-0.48	0.07	0.34	0.59

Figure 0.31: Coating C2, Composite Substrate, Xenon-Arc

Hours	**L**	**a**	**b**	**∆E***
0	-	-	-	0.00
500	-0.16	0.02	0.22	0.28
5000	-0.30	-0.01	0.33	0.44
5500	-2.23	-1.29	7.85	1.43
6000	-1.36	0.00	1.73	2.22
6500	-1.27	0.01	1.52	2.00
7000	-1.40	0.02	1.66	2.18
8500	-1.70	0.04	1.71	2.42
9500	-1.78	0.04	1.66	2.44
11000	-2.04	0.05	1.86	2.77
13500	-2.77	0.06	2.21	3.55

Figure 0.32: Coating C1, Aluminium Substrate, Natural Outdoors

Hours	**L**	**a**	**b**	**∆E***
0	-	-	-	0.00
500	-0.26	0.01	0.38	0.46
5000	-0.52	-0.01	0.51	0.74
5500	-2.43	-1.30	8.05	1.76
6000	-1.63	0.06	1.41	2.16
6500	-1.62	0.05	1.45	2.19
7000	-1.92	0.09	1.59	2.49
8500	-2.51	0.12	1.77	3.07
9500	-2.59	0.13	1.76	3.14
11000	-2.96	0.14	1.96	3.55
13500	-3.59	0.15	2.35	4.30

Figure 0.33: Coating C2, Aluminium Substrate, Natural Outdoors

Appendix D - Weathering Intermediate Analysis: Full FTIR Spectra (500nm – 4000nm/5000nm)

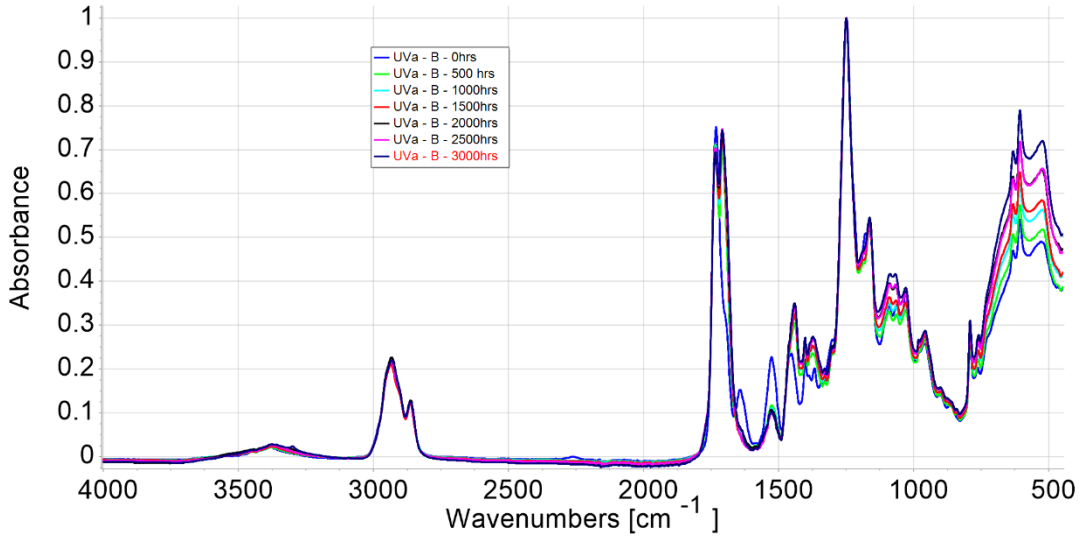

Figure 0.34: Coating B, UVa

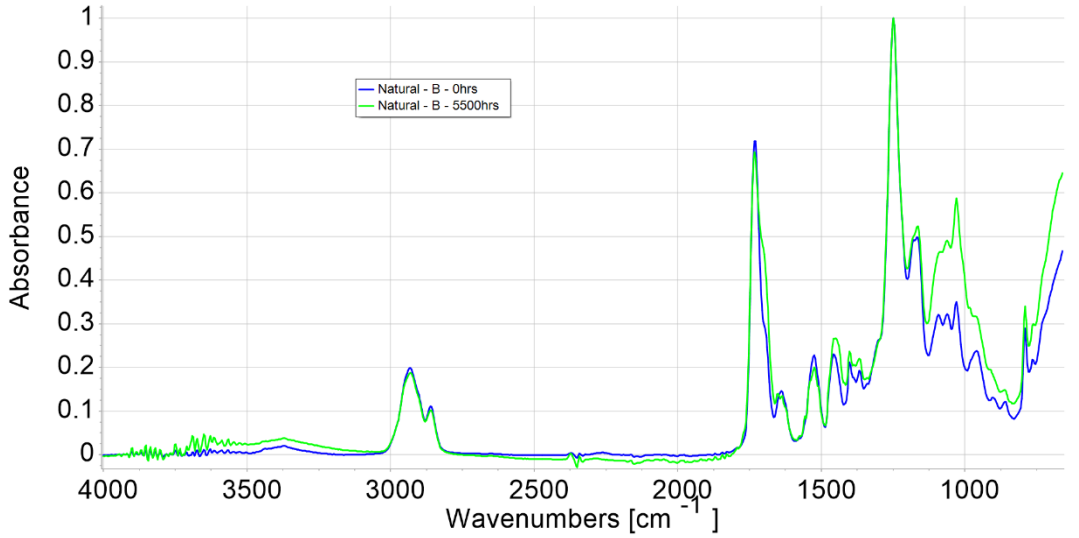

Figure 0.35: Coating B, Natural Outdoors

Appendix D - Weathering Intermediate Analysis: Full FTIR Spectra (500nm – 4000nm/5000nm)

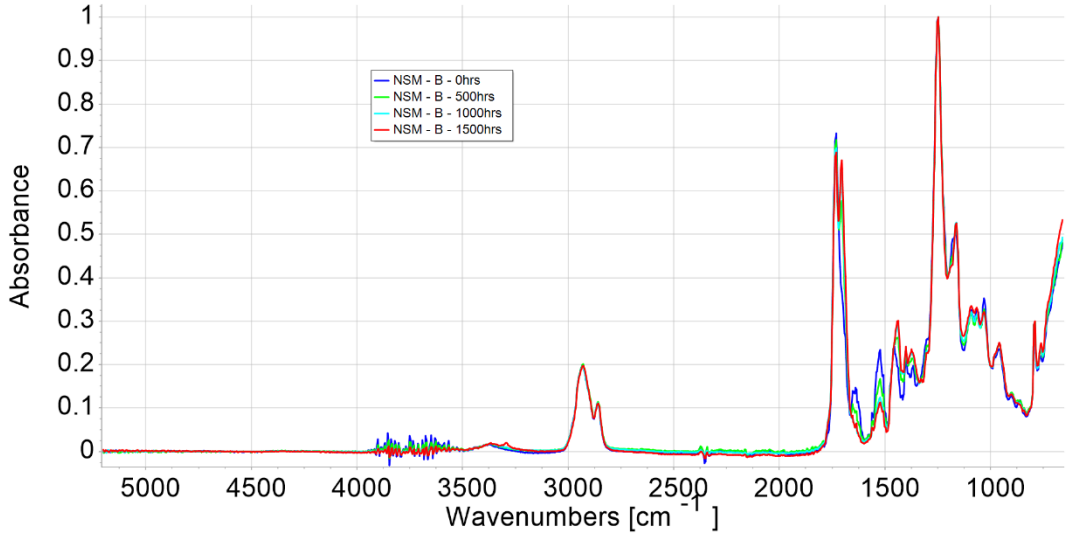

Figure 0.36: Coating B, NSM

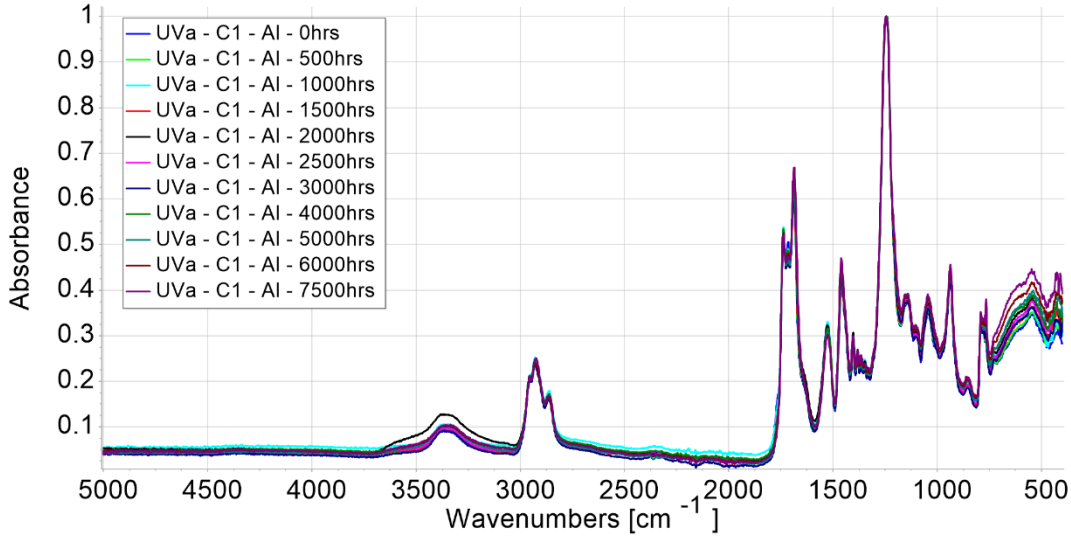

Figure 0.37: Coating C1, UVa

Appendix D - Weathering Intermediate Analysis: Full FTIR Spectra (500nm – 4000nm/5000nm)

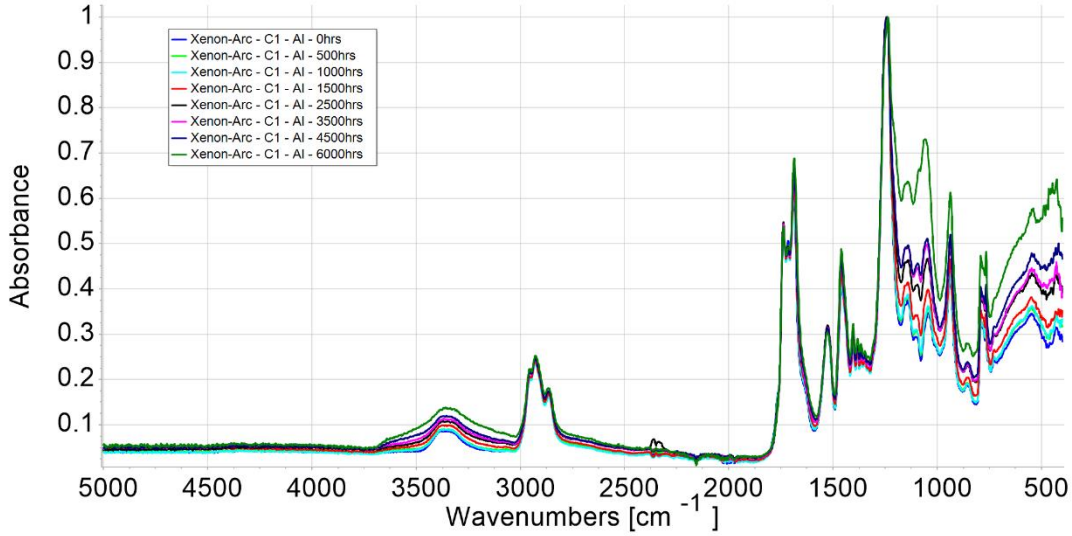

Figure 0.38: Coating C1, Xenon-Arc

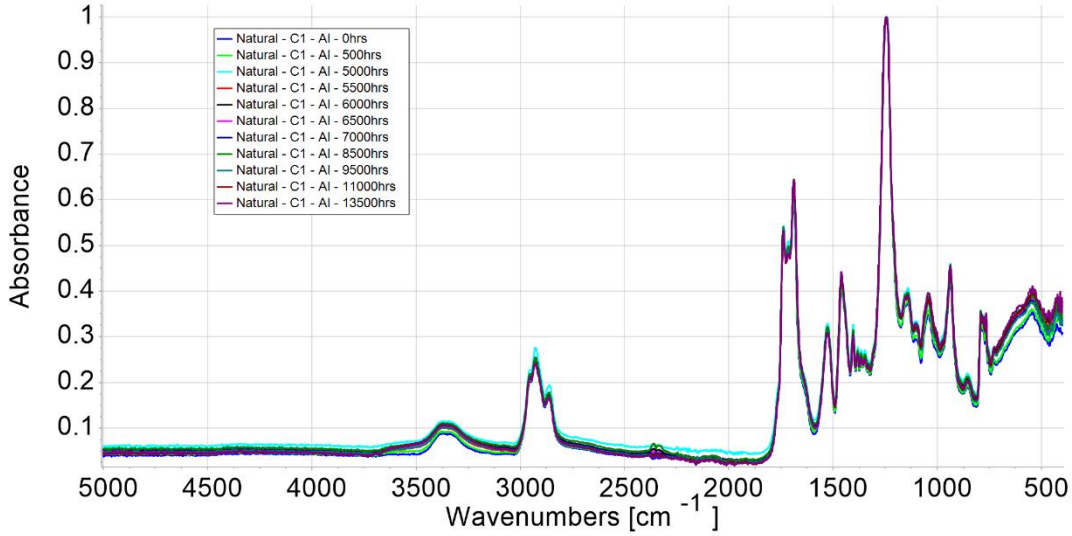

Figure 0.39: Coating C1, Natural Outdoors

Appendix D - Weathering Intermediate Analysis: Full FTIR Spectra (500nm – 4000nm/5000nm)

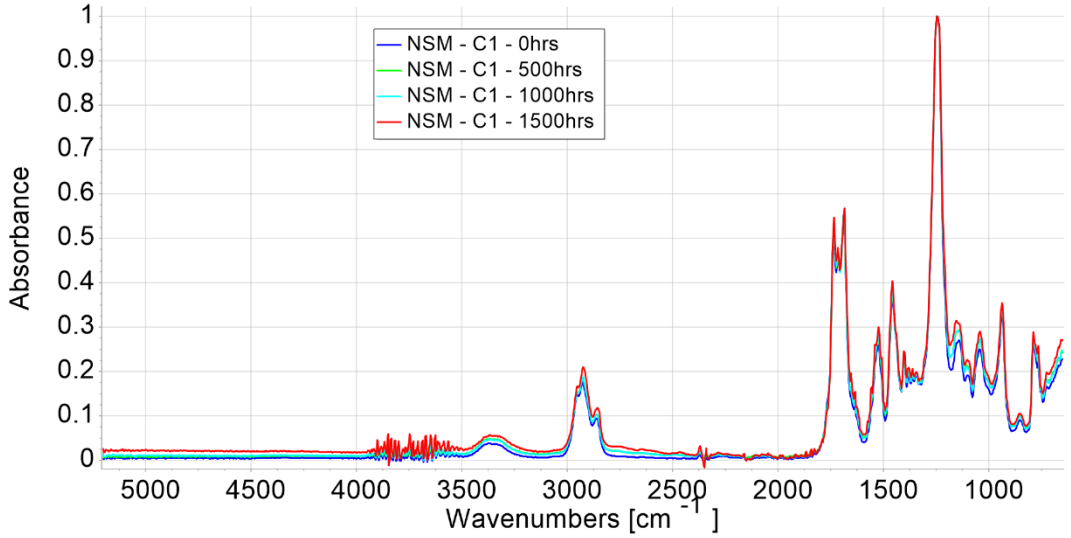

Figure 0.40: Coating C1, NSM

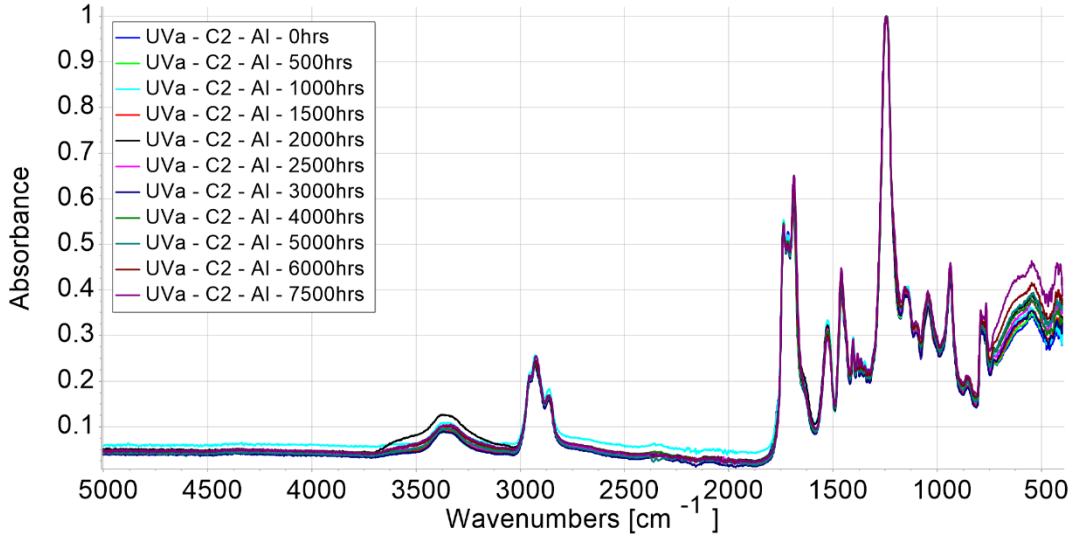

Figure 0.41: Coating C2, UVa

Appendix D - Weathering Intermediate Analysis: Full FTIR Spectra (500nm – 4000nm/5000nm)

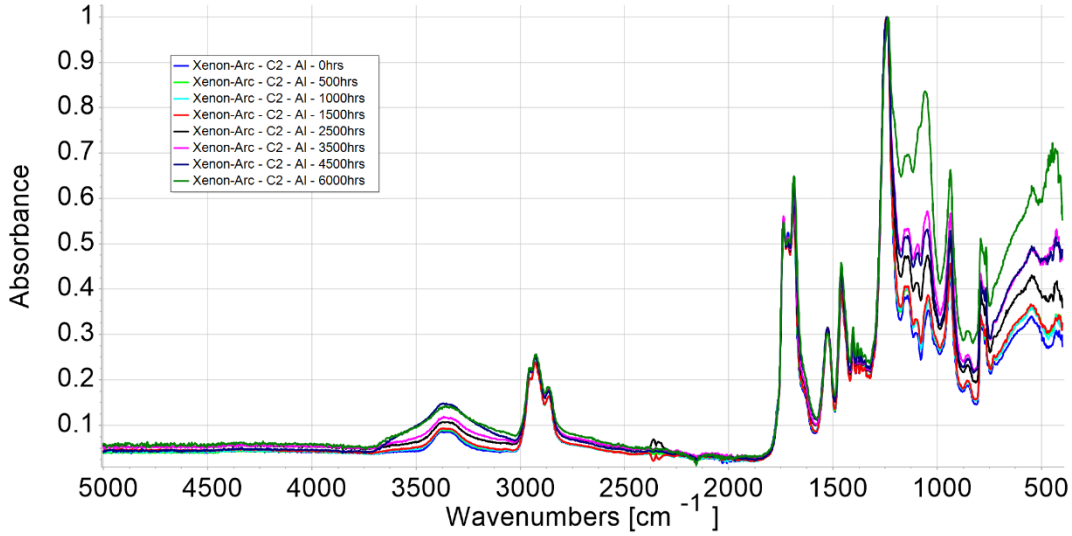

Figure 0.42: Coating C2, Xenon-Arc

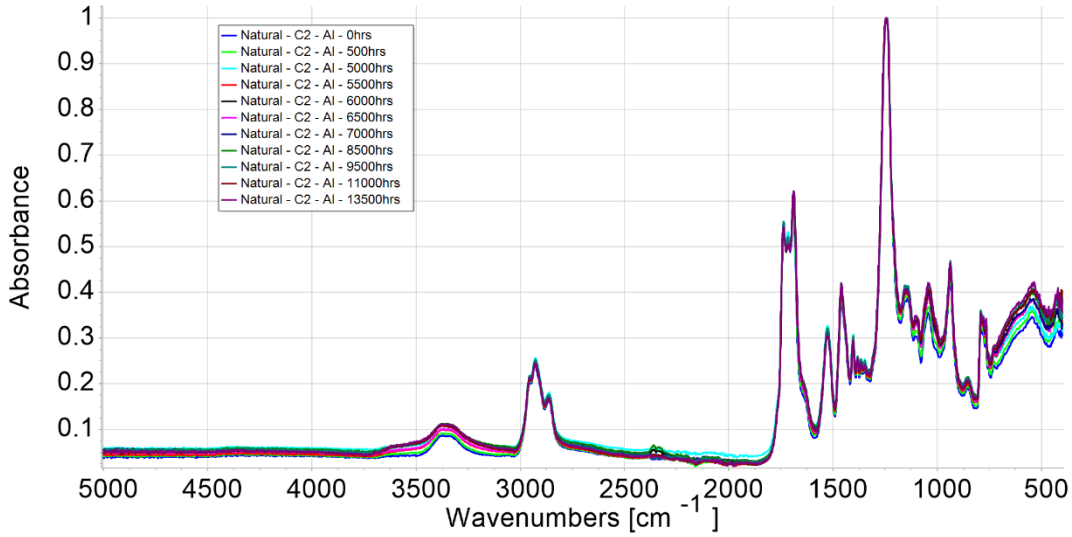

Figure 0.43: Coating C2, Natural Outdoors

Appendix D - Weathering Intermediate Analysis: Full FTIR Spectra (500nm – 4000nm/5000nm)

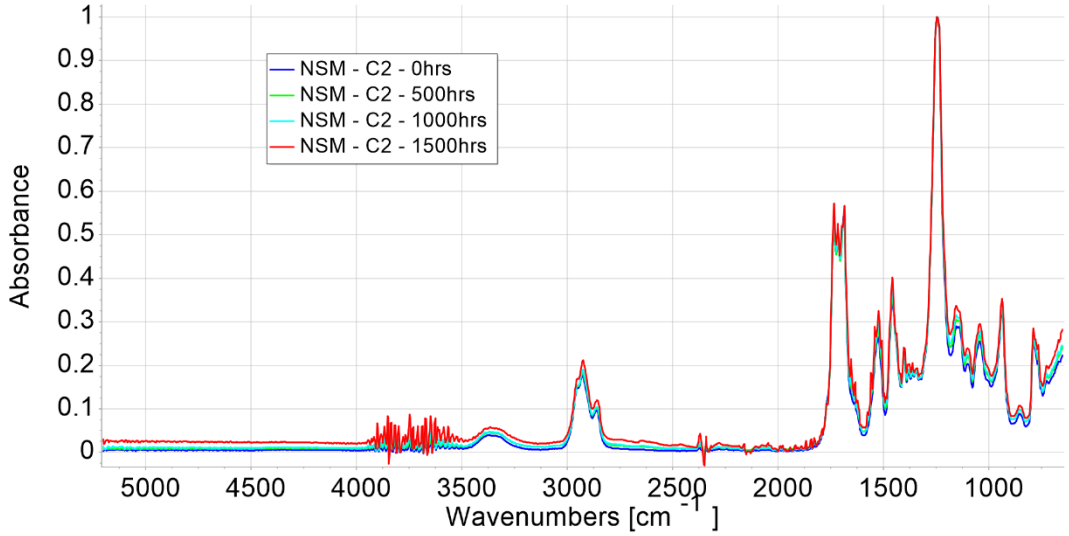

Figure 0.44: Coating C2, NSM

Appendix E - Combined RET & Weathering Analysis: Photographs

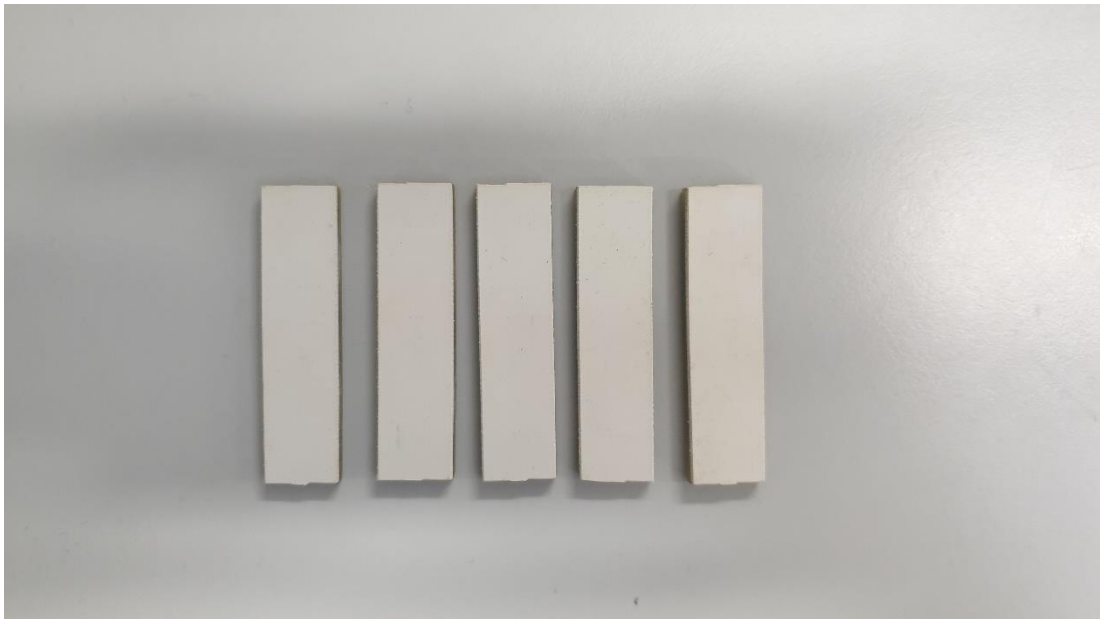

Figure 0.45: Coating B, Stage 2

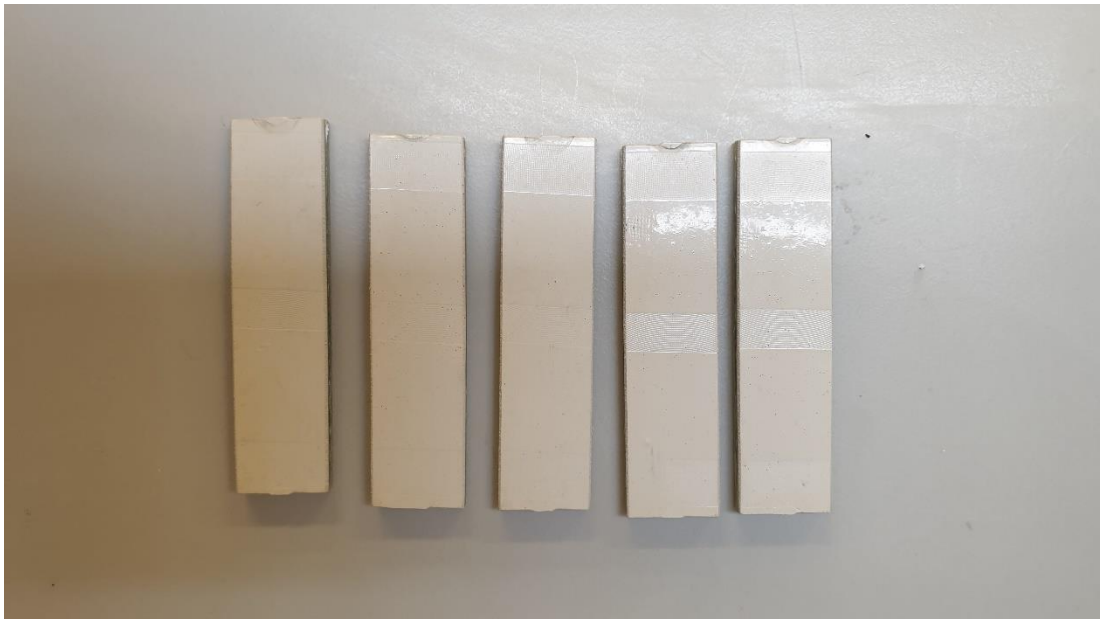

Figure 0.46: Coating B, Stage 3

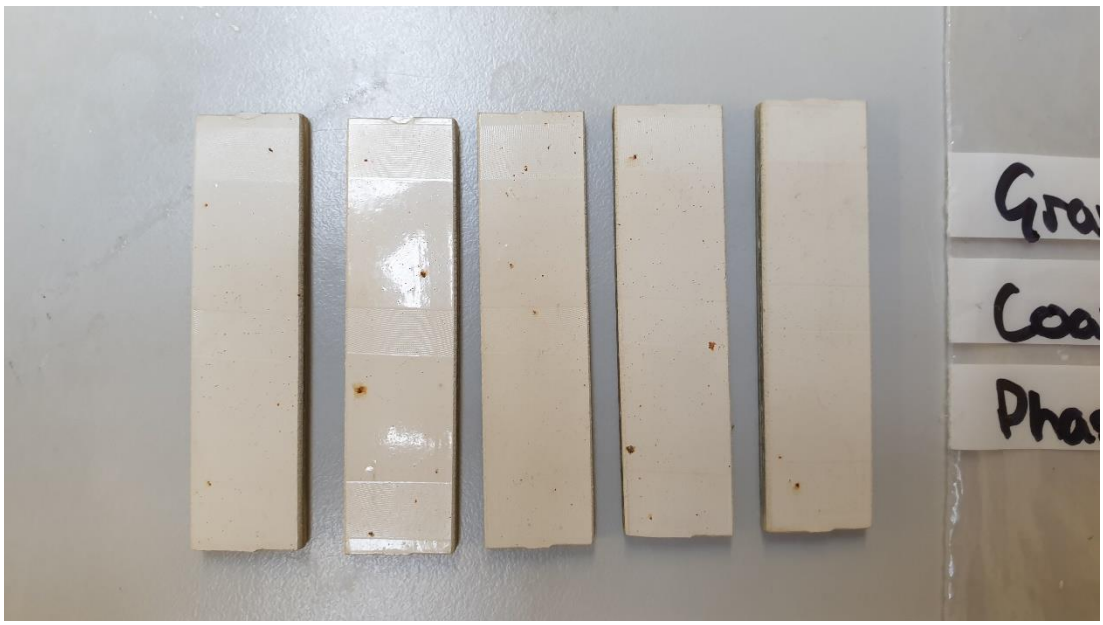

Figure 0.47: Coating B, Stage 4

Figure 0.48: Coating B, Stage 5

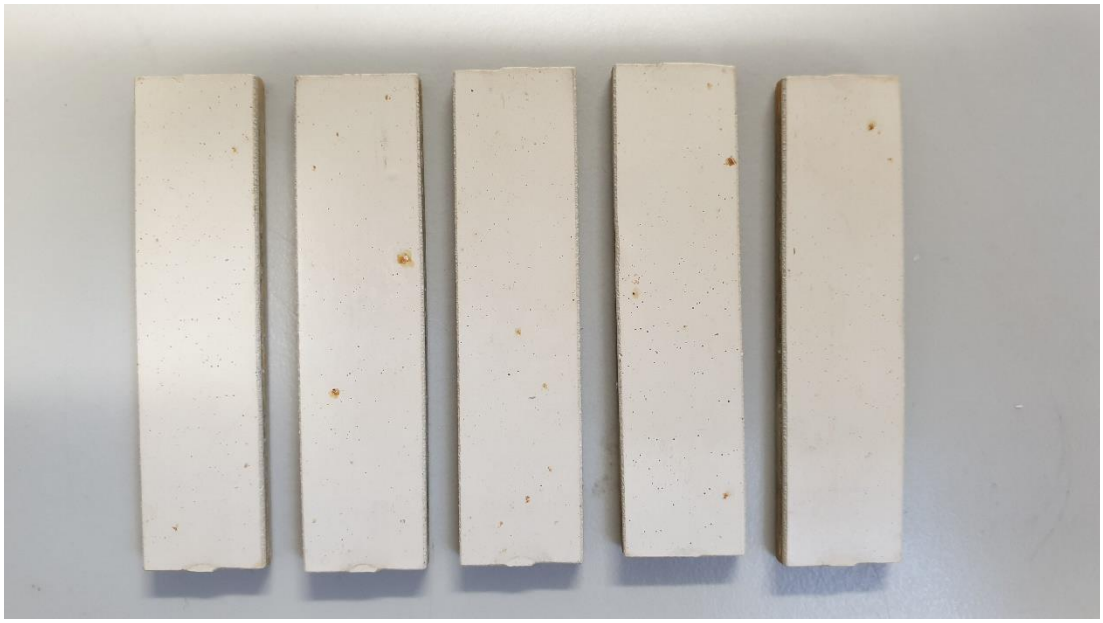

Figure 0.49: Coating B, Stage 6

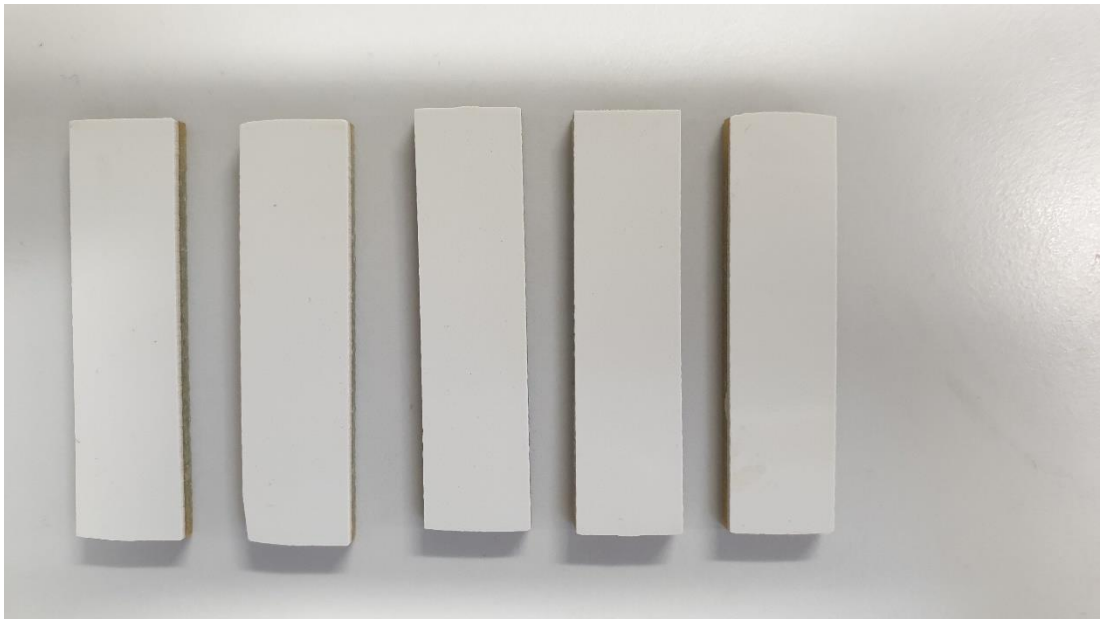

Figure 0.50: Coating C1, Stage 2

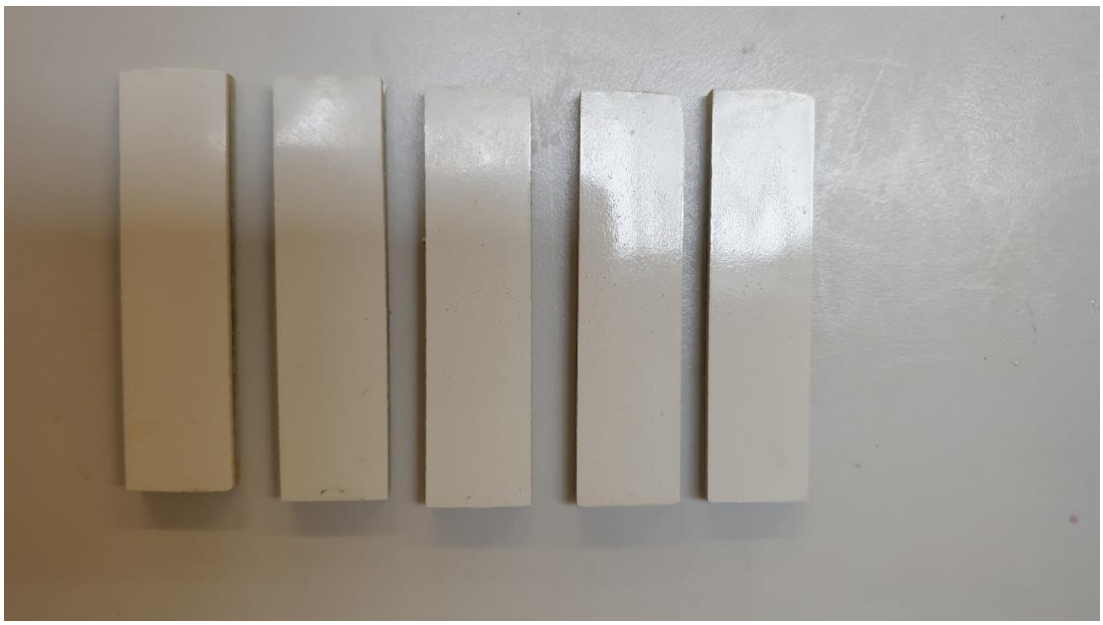

Figure 0.51: Coating C1, Stage 3

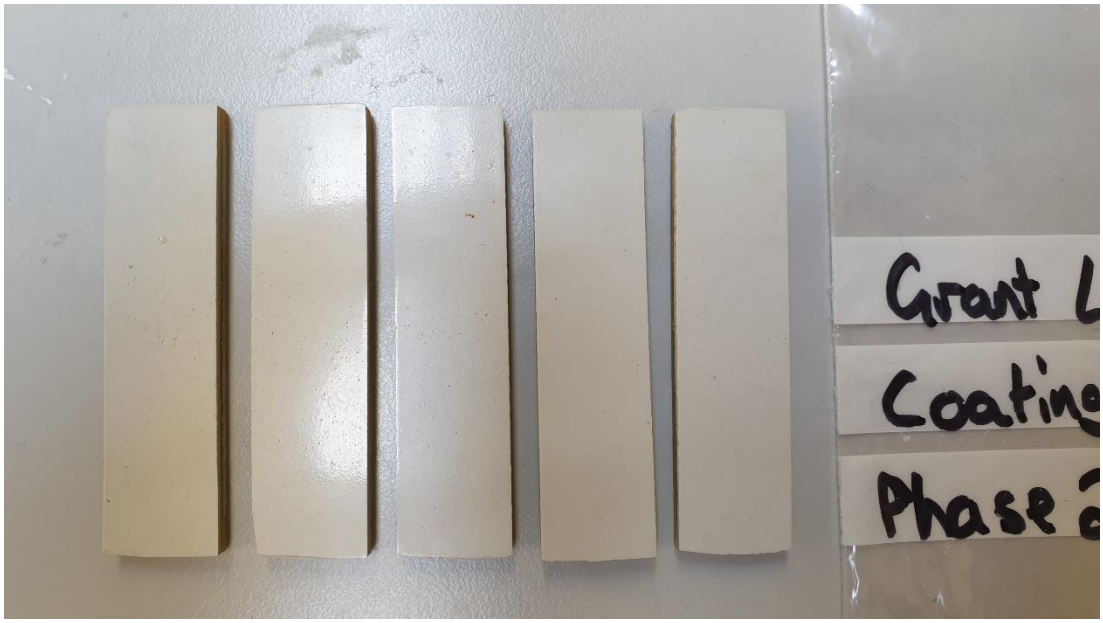

Figure 0.52: Coating C1, Stage 4

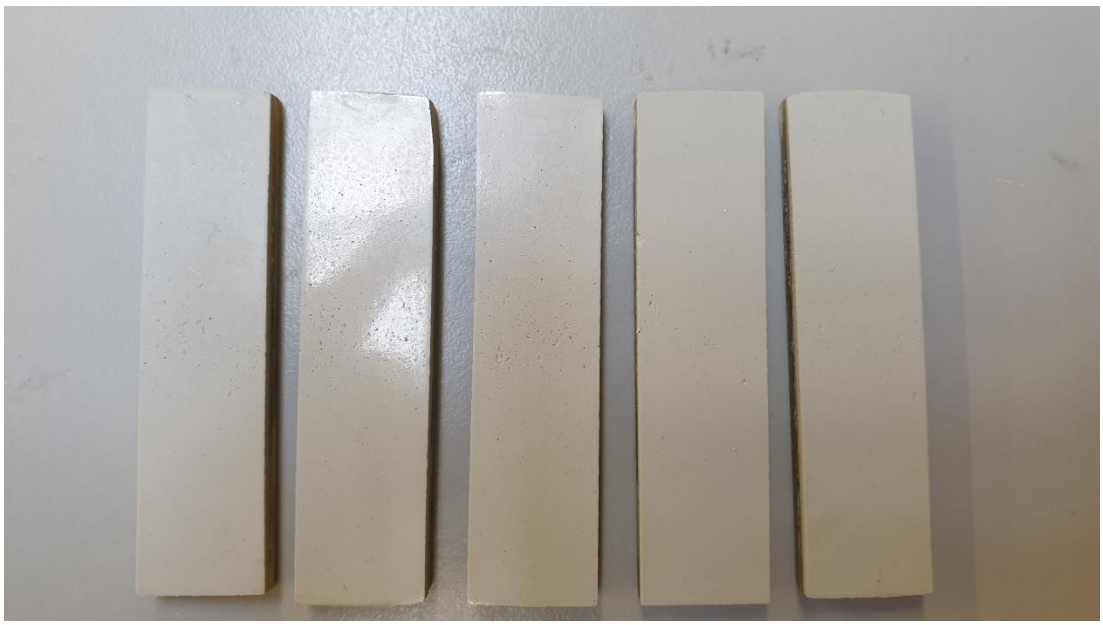

Figure 0.53: Coating C1, Stage 5

Figure 0.54: Coating C1, Stage 6

Appendix F - Combined RET & Weathering Analysis: Full FTIR Spectra (500nm – 5000nm)

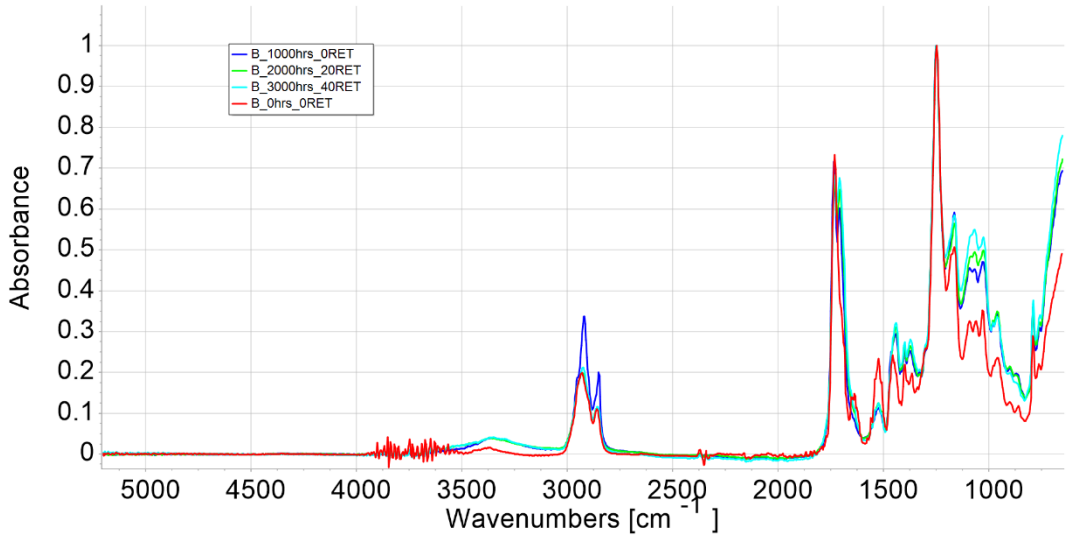

Figure 0.55: Coating B, Combined

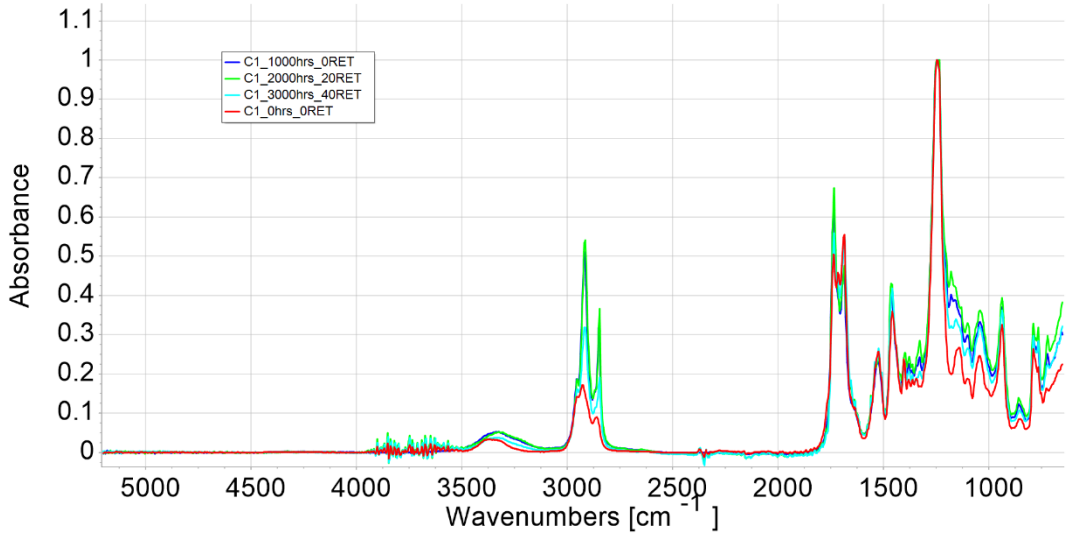

Figure 0.56: Coating C1, Combined